

Declaration

Planar, Fibre & Solitonic Devices

A thesis submitted for the degree
of Doctor of Philosophy of
the Australian National University

The research has been conducted under the supervision of Prof. J. D. Love and
Dr. Yu. S. Kivshov. However, I am specifically stating that the material
presented within this thesis is my own.

None of the work presented here has ever been submitted for any degree at this
or any other institution of higher learning.

Victoria V. Steblina

Canberra,
March 12, 1998

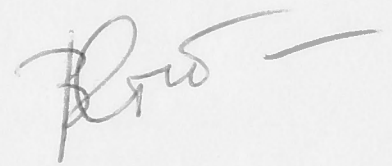


Declaration

This thesis is an account of research undertaken in the Optical Sciences Centre within the Research School of Physical Sciences and Engineering at the Australian National University between January 1995 and March 1998 while I was enrolled for the Doctor of Philosophy degree.

The research has been conducted under the supervision of Prof. J. D. Love and Dr. Yu. S. Kivshar. However, unless specifically stated otherwise, the material presented within this thesis is my own.

None of the work presented here has ever been submitted for any degree at this or any other institution of learning.



Victoria V. Steblina
March, 1998

Publications

Referenced Papers:

1. J. D. Love and V. V. Steblina, "High frequency waveguide devices", *Electronic Letters*, 30, 1953-1955, (1994).
2. V. V. Steblina, Yu. S. Kivshin, M. Hael, and R. A. Creswell, "Soliton beams in diffraction gratings: numerical analysis", *Optics Communications*, 118, 345-352, (1995).
3. A. V. Buryak, Yu. S. Kivshin, V. V. Steblina, and R. A. Creswell, "Soliton beams and parametric solitons in diffraction gratings", *Optics Letters*, 21, 52, 1670-1674, (1996).
4. S. J. Hewlett, J. D. Love, and V. V. Steblina, "Analysis and design of highly branched planar evanescent couplers", *Optical and Quantum Electronics*, 28, 71-81, (1996).
5. V. Tikhonenko, Yu. S. Kivshin, V. V. Steblina, and A. A. Zharov, "Soliton solitons in a saturable optical medium", *J. Opt. Soc. Am. B*, 13, 22-26, (1996).
6. V. V. Steblina, A. V. Buryak, and Yu. S. Kivshin, "Scattering and splitting of solitons in a bulk cylindrical medium", *Optics Letters*, 23, 156-158, (1998).
7. V. V. Steblina, J. D. Love, R. H. Stolen, and J-S. Wang, "Guiding mode degeneracy in bent W-fibers beyond cutoff", *Optics Communications*, (1998), in press.
8. V. V. Steblina, J. D. Love, R. H. Stolen, and J-S. Wang, "Bends in depressed-cladding and W-fibers: modal degeneracy", *Journal of Lightwave Technology*, (1997), submitted.
9. A. V. Buryak and V. V. Steblina, "Interactions of $\chi^{(3)}$ solitons", *J. Opt. Soc. Am. B*, (1996), submitted.

Conference Proceedings and Contract Reports:

1. J. D. Love and V. V. Steblina, "R&D investigations of planar optical waveguide devices". Stage 1 report. Telecom Australia Research Laboratories, Contract No 7356, 1994.

Publications

Refereed Papers:

1. J. D. Love and V. V. Steblina, "Highly broadband buried channel couplers", *Electronics Letters*, **30**, 1853-1855, (1994).
2. V. V. Steblina, Yu. S. Kivshar, M. Lisak, and B. A. Malomed, "Self-guided beams in diffractive $\chi^{(2)}$ medium: variational approach", *Optics Communications*, **118**, 345-352, (1995).
3. A. V. Buryak, Yu. S. Kivshar, and V. V. Steblina, "Self-trapping of light beams and parametric solitons in diffractive quadratic media", *Phys. Rev. A*, **52**, 1670-1674, (1995).
4. S. J. Hewlett, J. D. Love, and V. V. Steblina, "Analysis and design of highly-broadband planar evanescent couplers", *Optical and Quantum Electronics*, **28**, 71-81, (1996).
5. V. Tikhonenko, Yu. S. Kivshar, V. V. Steblina, and A. A. Zozulya, "Vortex solitons in a saturable optical medium", *J. Opt. Soc. Am. B*, **15**, 79-86, (1998).
6. V. V. Steblina, A. V. Buryak, and Yu. S. Kivshar, "Scattering and spiralling of solitons in a bulk quadratic medium", *Optics Letters*, **23**, 156-158, (1998).
7. V. V. Steblina, J. D. Love, R. H. Stolen, and J-S. Wang, "Cladding mode degeneracy in bent W-fibres beyond cutoff", *Optics Communications*, (1998), in press.
8. V. V. Steblina, J. D. Love, R. H. Stolen, and J-S. Wang, "Bends in depressed-cladding and W-fibres: modal degeneracy", *Journal of Lightwave Technology*, (1997), submitted.
9. A. V. Buryak and V. V. Steblina, "Interactions of $\chi^{(2)}$ solitons", *J. Opt. Soc. Am. B*, (1998), submitted.

Conference Proceedings and Contract Reports:

1. J. D. Love and V. V. Steblina. "R&D investigations of planar optical waveguides devices". Stage 1 report. **Telecom Australia Research Laboratories**. Contract N: 7356, 1994.

2. J. D. Love and V. V. Steblina, "Highly broadband buried channel couplers", Proceedings of **19th Australian Conference on Optical Fibre Technology**, pages 282-285, Melbourne, Australia, 1994.
3. V. V. Steblina, A. V. Buryak, and Yu. S. Kivshar, "Self-trapping of light beams and (2+1) solitons in $\chi^{(2)}$ media", **4th Workshop on Guided Wave Optics**, Sydney, Australia, 1995.
4. S. J. Hewlett, J. D. Love, and V. V. Steblina, "Analysis and design of highly broadband buried channel waveguide couplers", **9th International Conference on Ion Beam Modification of Materials, Workshop on Planar Optical Waveguides & Devices**, Bateman's Bay, NSW, Australia, 1995.
5. J. D. Love and V. V. Steblina. "R&D investigations of planar optical waveguides devices". Stage 2 report. **Telecom Australia Research Laboratories**. Contract N: 7356, 1995.
6. V. V. Steblina, J. D. Love, and F. Ladouceur, "Supermode analysis of fibre bend loss", Proceedings of **20th Australian Conference on Optical Fibre Technology**, pages 67-70, Coolum Beach, Queensland, Australia, 1995.
7. V. V. Steblina, J. D. Love, and S. J. Hewlett, "Analysis and design of highly broadband buried channel waveguide couplers", Proceedings of **32nd Australasian Applied Mathematics Conference**, Masterton, New Zealand, 1996.
8. V. V. Steblina, J. D. Love, R. H. Stolen, and J-S. Wang, "Bend birefringence in W-fibres", Proceedings of **21th Australian Conference on Optical Fibre Technology**, pages 237-240, Gold Coast, Queensland, Australia, 1996.
9. V. V. Steblina, Yu. S. Kivshar, and A. V. Buryak, "Collision, fusion, and spiralling of interacting solitons in a bulk quadratic medium", **Optical Guided Waves & Applications Meeting**, Canberra, Australia, 1997.
10. V. V. Steblina, J. D. Love, R. H. Stolen, and J-S. Wang, "Bend birefringence in finite-cladding W-fibres", Proceedings of **11th International Conference on Integrated Optics and Optical Fibre Communications / 23rd European Conference on Optical Communications**, pages 3.207-3.210, Edinburgh, UK, 1997.
11. V. V. Steblina, Yu. S. Kivshar, and A. V. Buryak "Collision, fusion and spiralling of interacting solitons in a bulk quadratic medium", **NATO Advanced Study Institute on Advanced Photonics with Second-Order Optically Nonlinear Processes**, Sozopol, Bulgaria, Sep 21 - Oct 3, 1997.
12. V. V. Steblina, A. V. Buryak and Yu. S. Kivshar, "Scattering and spiralling of solitons in a bulk quadratic medium", **Technical Digest on Nonlinear Guided-Wave Phenomena, 1998**, Optical Society of America, Washington D.C., 1998.

Abstract

The reader will find in this thesis part of the work I have done on planar, fibre, and solitonic devices over the last three years. After a brief introduction (Chapter 1), Chapter 2 presents the basic theory of buried channel optical waveguides (BCW) and couplers, and its relation to the design of actual waveguide devices. Chapter 3 presents a novel design approach of BCW couplers that realises dropping filters and power dividers with very broadband coupling responses. Chapters 4 and 5 concentrate on bend loss from finite-cladding single-mode fibres. In particular, in Chapter 4 we numerically quantify bend loss in practical telecommunication fibres and propose an experimentally feasible design for a bent-fibre attenuator. Chapter 5 lays down a theory of transmission beyond fundamental mode cutoff in bent W- and depressed cladding fibres. Experimental transmission spectra of slightly bent finite-cladding W-fibres are compared with theoretical results. Chapters 6 and 7 are dedicated to spatial solitons in materials with quadratic nonlinearity. In Chapter 6 we show that localised solutions describing two-wave self-guided beams (spatial optical solitons) in a diffractive nonlinear $\chi^{(2)}$ medium can be well approximated analytically using the variational approach. Chapter 7 concludes the thesis and presents a theory of soliton interactions in bulk $\chi^{(2)}$ crystals, which have potential application in all-optical switching devices.

Thanks to my friends and fellow students Elena Ostrovskaya, Daniel Saltrass and Robert Micallef for the great friendship and fun. I am sincerely grateful for your personal and scientific companionship over the past years, and hope that life won't separate us in future. A huge thanks to Dr. Alexander Buryak, my husband, friend, and colleague, whose help and energy kept me going for the last few months. The support and love I have received from him has been invaluable in sustaining me through my studies.

I must express my gratitude to Rebecca Pallavicini, Andrea Rolins and Helen McMartin for everything they have done for me, and for their optimism and humour that enlightened my days in the department.

Finally, I thank my parents for introducing me to the realm of physics. Their help and support in my life cannot be overestimated. This thesis would not have been possible without them.

Abstract

The reader will find in this thesis part of the work I have done on planar, three- and nonlinear, devices over the last three years. A brief introduction (Chapter 1), Chapter 2 reviews the basic theory of linear and optical waveguides (BOW) and compares and its relation to the design of actual waveguide devices. Chapter 3 presents a novel design approach of BOW coupled that raises coupling efficiency and power densities with very broadened coupling responses. Chapters 4 and 5 concentrate on point-to-point interconnecting structures. In particular, in Chapter 4, we numerically quantify bend loss in practical technological devices and propose an experimentally feasible design for a bend-free structure. Chapter 5 presents a theory of coupling between two-dimensional optical waveguides. Experimental studies are compared with theoretical results. Chapters 6 and 7 are dedicated to spatial solitons in materials with parabolic nonlinearity. In Chapter 6, we show that localized solitons (bright, dark and guided beams) (spatial optical solitons) in a nonlinear medium can be well approximated analytically using the variational approach. Chapter 7 considers the theory and presents a theory of soliton interactions in bulk media, which have potential application in all-optical switching devices.

11. V. V. Stenflo, *Journal of Applied Physics*, **87**, 1033 (1999).
12. V. V. Stenflo, *Journal of Applied Physics*, **87**, 1033 (1999).

Acknowledgements

This thesis would have never been possible without the ongoing dedication and support of my supervisors Prof. John Love and Dr. Yuri Kivshar. They have been invaluable to me both as supervisors and as colleagues, generously providing me with advice, encouragement, experience and a great deal of their time. Not to mention an atmosphere of friendship and enthusiasm whose equal is difficult to imagine. I shall always consider myself to have been exceptionally lucky in having worked with both of them.

Thanks to Dr. François Ladouceur, my “science and life” adviser, with whom I shared an office for three years. He helped greatly on computational matters and by reading and commenting upon the presentation of this thesis.

I am no less indebted to Marcella Faith from Telstra Research Laboratories, Dr. Simon Hewlett from Australian Optical Fibre Research, and Prof. Roger Stolen from AT&T Bell Laboratories for very fruitful collaboration at different stages of my Ph.D.

I would like to thank all members of the Optical Sciences Centre, with whom it was a pleasure at all times to work alongside. I am especially grateful to Prof. Allan Snyder for providing such a great work environment.

I gratefully acknowledge the support of the Australian Photonics Cooperative Research Centre through provision of a Photonics Research Scholarship, and subsequently the Australian National University for provision of an ANU Scholarship.

Thanks to my friends and fellow students Elena Ostrovskaya, Daniel Beltrami and Robert Micallef for the great friendship and fun. I am sincerely grateful for your personal and scientific companionship over the past years, and hope that life won't separate us in future. A huge thanks to Dr. Alexander Buryak, my husband, friend, and colleague, whose help and energy kept me going for the last few months. The support and love I have received from him has been invaluable in sustaining me through my studies.

I must express my gratitude to Rebecca Pallavicini, Andrea Robins and Helen McMartin for everything they have done for me, and for their optimism and humour that enlightened my days in the department.

Finally, I thank my parents for introducing me to the realms of physics. Their help and support in my life cannot be overestimated. This thesis would not have been possible without them.

Acknowledgements

This thesis would have never been possible without the ongoing discussion and support of my supervisors, Dr. John Love and Dr. Yan Aizawa. Their have been invaluable to me both as supervisors and as colleagues, generously providing me with advice, encouragement, and experience and a great deal of their time. Not to mention an atmosphere of friendship and enthusiasm which equal is difficult to imagine. I shall always consider myself to have been extraordinarily lucky in having worked with both of them.

Thanks to Dr. Francis Labounty, my "science and life" advisor, with whom I shared an office for three years. He helped greatly on conceptual matters and by reading and commenting upon the presentation of this thesis.

I am no less indebted to Marcella Hill from Technic Laboratory, Dr. Simon Hewlett from Australian Optical Fibre Research, and Paul Roger Sloan from A&T Bell Laboratories for very fruitful collaboration at different stages of my Ph.D.

I would like to thank all members of the Optical Sciences Centre, with whom it was a pleasure at all times to work alongside. I am especially grateful to Prof. Alan Snyder for providing such a great work environment.

I gratefully acknowledge the support of the Australian Photonics Cooperative Research Centre through provision of a Photonics Research Scholarship, and especially the Australian National University for provision of an ANU bursary.

Thanks to my friends and fellow students, Etsa Gavrylyuk, Daniel Bellamy and Robert Mihal for the great friendship and fun. I am especially grateful for your personal and scientific companionship over the past year, and hope that life won't separate us in future. A huge thanks to Dr. Alexander Buryk, my husband, friend, and colleague, whose help and energy kept me going for the last few months. The support and love I have received from him has been invaluable in sustaining me through my studies.

I must express my gratitude to Rebecca Palivich, Andrew Robins and Helen McManis for everything they have done for me, and for their optimism and humour that enlivened my days in the department.

Finally, I thank my parents for introducing me to the realm of physics. Their help and support in my life cannot be overestimated. This thesis would not have been possible without them.

Contents

1	Introduction	1
1.1	Research highlights	1
1.2	The subject of this thesis	4
2	Buried Channel Waveguides & Couplers	7
2.1	Advantages of planar couplers	7
2.2	Buried channel waveguide geometry	9
2.3	Fundamental equations of optical waveguide theory	10
2.4	Propagation through buried channel waveguides	11
2.4.1	Single-mode propagation	11
2.4.2	Bend loss	12
2.5	Analysis of planar couplers	13
2.5.1	Modal analysis	14
2.5.2	Uniform region	15
2.5.3	Non-uniform region	16
2.5.4	Excitation	18
2.5.5	Accumulated phase	18
2.5.6	Splitting ratio	19
2.5.7	3 dB splitters & wavelength demultiplexing couplers	20
2.6	Numerical modelling	21
2.6.1	Single-core BCW	22
2.6.2	Twin-core BCW coupler	22
2.6.3	3 dB splitters	24
2.6.4	Wavelength multiplexing/demultiplexing couplers	24
2.7	Application to practical optical coupler design.	26
2.7.1	Designs based on the plasma enhanced chemical vapour deposition (PECVD) fabrication technique.	27
2.7.2	Designs based on the flame hydrolysis fabrication technique.	31
2.8	Conclusions	34

3	Broadband Planar Couplers	35
3.1	Background	35
3.2	BCW wavelength-flattening strategies	36
3.2.1	Symmetric coupler	38
3.2.2	Asymmetric coupler	41
3.2.3	Second-mode cutoff	43
3.3	Highly broadband couplers – practical examples	45
3.3.1	Symmetric coupler	45
3.3.2	Asymmetric coupler	46
3.4	Conclusions	49
4	Bends in Finite-Cladding Practical Fibres	51
4.1	Bend loss in infinite-cladding fibres	51
4.1.1	Pure bend loss	51
4.1.2	Transition loss	55
4.2	Bend loss in practical fibres	56
4.2.1	Model of the fibre profile	56
4.2.2	Modified bend loss mechanism	58
4.2.3	Transformation to an equivalent straight waveguide	59
4.2.4	Variable curvature bends: numerical coupled mode analysis	60
4.2.5	Constant curvature bends	63
4.3	Conclusions	67
5	Bends in Depressed-Cladding and W-Fibres: modal degeneracy	69
5.1	Experimental results	70
5.2	Bent slab model	74
5.2.1	Finite coating model	76
5.2.2	Infinite coating model	77
5.3	Qualitative description	78
5.3.1	Propagation beyond fundamental mode cutoff	78
5.3.2	Attenuation mechanisms	78
5.3.3	Cladding mode degeneracy	80
5.4	Experiment simulation	85
5.4.1	Bend-induced asymmetry	85
5.4.2	Transmitted power	87
5.5	Conclusions	89
6	Self-guided beams in a diffractive $\chi^{(2)}$ medium: variational approach	91
6.1	Background	91
6.2	Mathematical model	91
6.3	Solitons in slab $\chi^{(2)}$ waveguides	93
6.3.1	Analytical solutions	94
6.3.2	Variational solutions	95

6.4	Solitons in bulk quadratic media	99
6.5	Conclusions	104
7	Interactions of $\chi^{(2)}$ solitons	105
7.1	Background	105
7.2	Mathematical model and integrals of motion	106
7.3	Summary of stability results	109
7.4	Soliton interactions: theory versus numerics	109
7.4.1	Effective particle approach	110
7.4.2	Power exchange between colliding solitons	115
7.5	Stability of spiralling configurations	117
7.6	Physical estimates	118
7.7	Conclusions	118

Appendices

A	Numerical methods	121
A.1	Fourier Decomposition Method (FDM)	121
A.2	Beam Propagation Method (BPM)	123
A.2.1	Linear BPM	123
A.2.2	Nonlinear BPM	125
A.3	Transfer Matrix Approach plus Staircase Approximation	126
A.4	Shooting and Relaxation Methods	129
B	Fractional Coupled Power	131
B.1	Power exchange in a coupler	131
B.2	Power exchange between modes of a bent fibre	134
C	Derivation of adiabatic equations of soliton interaction	135

23 6.4 Solitons in bulk quadratic media

25 6.5 Conclusions

26

27 Interactions of $\chi^{(2)}$ solitons

28 7.1 Background

29 7.2 Mathematical model and integrals of motion

30 7.3 Summary of analytic results

31 7.4 Soliton interactions: theory versus numerics

32 7.4.1 Effective particle approach

33 7.4.2 Power exchange between colliding solitons

34 7.5 Stability of splitting configurations

35 7.6 Physical estimates

36 7.7 Conclusions

37

38 Appendices

39

40 A Numerical methods

41 A.1 Fourier Decomposition Method (FDM)

42 A.2 Beam Propagation Method (BPM)

43 A.2.1 Beam Propagation Method (BPM)

44 A.2.2 Nonlinear BPM

45 A.3 Transfer Matrix Approach plus Staircase Approximation

46 A.4 Shooting and Relaxation Methods

47

48 B Fractional Coupled Power

49 B.1 Power exchange between modes of a pair

50 B.2 Power exchange between modes of a pair

51

52 C Derivation of adiabatic equations of soliton interaction

53

54

55

56

57

58

59

60

61

62

63

64

65

66

67

68

69

70

71

72

73

74

75

76

77

78

79

80

81

82

83

84

85

86

87

88

89

90

CHAPTER 1

Introduction

The communications network ... will enable the consciousness of our grandchildren to flicker like lightning back and forth across the face of this planet. They will be able to go anywhere and meet anyone at any time without stirring from their homes. All the museums and libraries of the world will be extensions of their living rooms.

Arthur C. Clarke, *Voices From The Sky*,
Harper & Row (1965)

1.1 Research highlights

The author of “*2001: A Space Odyssey*” would no doubt be pleased that his vision of a world connected by instantaneous communications did arrive as predicted. This leap from vision to reality has been exponential, not gradual. The most sweeping changes in communications over the past three decades have been compressed into the short space of the past few years. Bit by bit, the Earth’s surface is being criss-crossed by a network of optical fibres, connecting countries across oceans, and connecting cities across vast distances. In the modern “information society”, large capacity and reliable local, national and international telecommunications networks pave the way for the convergence of computers, advanced communications, information and entertainment. Before a national *information superhighway* can emerge, the “roads” must be widened and the “freight” – text, data, images, voice or video signals – must be digitalised, packaged and tagged so that it can be bussed speedily and accurately from end to end.

Modern telecommunications networks rely on the unmatched capacity of silica-based optical fibres to carry information. Currently optical fibre links are replacing traditional copper cabling in the nation’s infrastructure. Copper coaxial cables are inadequate for transmitting high-volume data, whereas optical fibres have essentially unlimited capacity. In a practical network, the majority of optical fibres are still interconnected by electronic devices, which provide necessary switching and signal processing functions. Therefore, significant limitations on the bit-rate capacity and

cost of these hybrid networks are imposed by the speed of electronic processing and the need to convert signals from light to electricity and back to light again. This is one reason why current optical fibre systems utilise only a minute fraction of available capacity.

An ultimate goal for fibre optics is the creation of *all-optical networks* that run entirely in glass. Unlike existing fibre optic networks, which convert light signals to electronic form in order to amplify or switch them, the *all-optical network is entirely photonic*. It will carry information-bearing laser-light pulses in dozens of wavelengths to create tens of thousands of channels that can be switched and guided by simple photonic devices.

Historically, the new era in photonics integrated research started in 1969, when the concept of *integrated optics* was proposed [1]. Research on optical integrated circuits (OIC), where certain electronic functions were replaced with photonic equivalents (see, e.g. Fig. 1.1), started in the early 1970s, when various materials and processing techniques for waveguides were investigated. Through this, the main features of glass, LiNbO_3 , polymer, and semiconductor waveguides were revealed. Recent developments in optical planar waveguides, especially in the buried channel waveguide (BCW) technology (see [2–4] to cite a few), represent a major step towards the super-capacity, super-fast “transparent” optical fibre networks of the future.

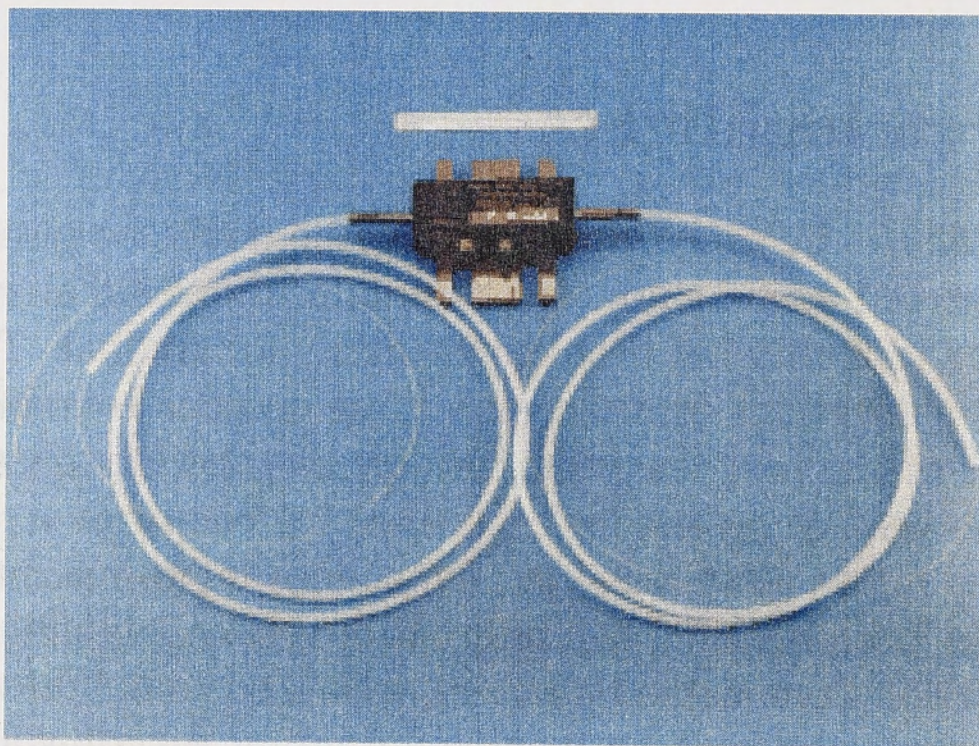


Figure 1.1: Integrated electro-optical modulator.

Nowadays the vast majority of optical fibres and passive optical processing elements are used as linear devices (i.e. their characteristics do not depend on the intensity of the incident signal) [5]. Linear optical devices are very versatile and cover a broad range of network applications including power splitting, coupling and wavelength multiplexing/demultiplexing of signals. Designs and principles of operation of novel linear waveguide structures, especially broadband, are still to be

suggested and thoroughly investigated. Further analysis and characterisation of existing fibre and integrated optical elements are needed both for fundamental and applied reasons.

Although ideal for some processing duties, linear waveguide devices are, by definition, unsuitable for power switching. The key to developing photonic switches is the discovery of nonlinear optical materials whose refractive index can vary rapidly in response to changing light intensity. Such materials must also be suitable for the production of low-loss optical waveguides which can be structured in an appropriate way to form an optical switch. For example, optical materials with a cubic nonlinear response (so-called Kerr or $\chi^{(3)}$ materials) have been proposed for ultra-high-speed signal processing [6]. By now many types of nonlinear all-optical devices (e.g. nonlinear optical couplers [7, 8], nonlinear Mach-Zehnder interferometers [9] and nonlinear mode-mixers [10] etc.) have been designed and implemented experimentally.

Apart from creating nonlinear analogs of existing linear devices, the futuristic concept of solitonic long-distance transmission line has been developed using so-called *temporal solitons* as non-spreading light pulses in nonlinear (silica glass) fibres [11, 12]. Because of the balance between the nonlinearity and dispersion, temporal solitons can propagate in a fibre without changing their shape. Despite recent successes of novel linear transmission schemes (e.g. recently suggested NRZ transmission regime [13, 14]), *the use of such solitons heralds a dramatic increase of the bit-rate capacity of optical fibres.*

More recently, the fundamental concept of *guiding light by light itself* has been suggested [15], taking advantage of *spatial solitons*, in other words – self-guiding optical beams, in this case existing due to the balance between diffraction and nonlinearity. Stable spatial solitons open up exciting prospects of creating *reconfigurable guiding structures* in nonlinear optical materials.

The overall material properties required for these applications are very stringent, and to date, only a few suitable materials have been identified. Unfortunately, the value of the positive Kerr-type nonlinearity of conventional (silica-based) optical materials is very small and this makes it difficult to design and produce highly efficient and compact nonlinear optical devices using acceptably low intensities. Among the organic $\chi^{(3)}$ optical materials (polymers) the situation is encouraging, but far from perfect: organic materials with high electronic Kerr nonlinearity are lossy and not environmentally stable. For this reason researchers have not been very optimistic about effective signal processing using Kerr-type nonlinear devices under realistic conditions.

However, recent studies of nonlinear wave propagation in a different medium, namely quadratic (or $\chi^{(2)}$) optical materials, have revealed similar spatial soliton phenomena, previously reported only for $\chi^{(3)}$ materials. The second-order nonlinearity is traditionally associated with second-harmonic generation [16], and was not, until recently, seen as a source of self-guiding and switching phenomena. This view has now changed, and it has been demonstrated [17] that under certain conditions $\chi^{(2)}$ nonlinear materials can behave very similarly to conventional Kerr materials due to so-called *cascaded* $\chi^{(2)}$ nonlinear effects, producing very high effective nonlin-

earities. The newly discovered cascading phenomenon is opening up opportunities for novel nonlinear switching schemes as well as soliton-based devices. Moreover, unlike self-guided beams in cubic nonlinear materials, stable $\chi^{(2)}$ spatial solitons can be found both for planar and bulk geometries [18–23], thus bringing the idea of reconfigurable waveguide chips closer to reality.

Starting from 1994, as a member of both the linear and nonlinear research teams at the Optical Sciences Centre, I have been addressing theoretical aspects of planar integrated optics waveguide design, practical optical fibres performance as well as fundamental problems of soliton-based all-optical switching. The original results obtained in this field with my direct participation form the basis of this thesis.

1.2 The subject of this thesis

This thesis is designed to provide basic insight into the physics of wave propagation through both linear and nonlinear waveguiding structures, with emphasis on theoretical analyses and numerical modelling. The choice of topics and overall thrust of the thesis have been determined by initial motivation to study both “real life” optical waveguides (i.e. linear integrated optics devices and optical fibres) and futuristic all-optical components (such as spatial soliton systems).

The first part of this thesis is dedicated to buried channel optical waveguides and devices. Attention is given to several types of devices, concentrating, on the one hand, on semi-analytical design and characterisation of conventional coupler devices, and, on the other hand, on introduction of novel techniques for highly broadband operation, that is strategically important for multi-wavelength channel lightwave networks. Most of the design ideas have been tested against experimental feasibility by collaborators.

The next two Chapters deal with bends in practical optical fibres. Since the problem of fibre bend loss is of fundamental importance to telecommunications, existing research on this topic has been extensive. Nevertheless, in some cases existing results are of limited value due to significant differences between “real fibre” and theoretical models, which have been used. We have generalised the existing models, accounting for such important factors as the finiteness of the cladding and absorption by protective jacket, to develop a qualitative theory explaining, e.g., non-monotonic losses in jacketed fibres, as well as unexpected experimental transmission spectra of single-mode W-fibres beyond fundamental mode cutoff.

The third, and last part of the thesis, extends into the nonlinear domain of quadratic solitons. This is a topical fundamental phenomenon of nonlinear materials and there has been substantial experimental interest in this subject. Extrapolating the success of theorists and experimentalists in this field, observation of the $\chi^{(2)}$ soliton switching should be around the corner! The last part of this thesis starts with a convenient approach to determining approximate analytical solutions for quadratic spatial solitons both in planar and bulk nonlinear media. An analysis of solitons’ interactions in bulk $\chi^{(2)}$ crystals, which has potential application in switching devices, concludes the thesis.

Finally, as well as providing further insight into the above topics, the presentation is general enough for specialists working in either linear or nonlinear fields to readily follow. Besides, this work could also be useful for a newcomer in this area of research, highlighting the importance of linear and advantages of future nonlinear all-optical telecommunications devices. For the purpose of clarity, most of the complex mathematical calculations and technical details (e.g., reviews of numerical methods used throughout this work), find their place in Appendices. Related facts that should be linked to this thesis are included in the Bibliography. As Fermat said, "The margin is too small to include all details...!"

2.1 Advantages of planar couplers

To send the same information to two (or more) recipients in an optical network, the optical signal has to be split into two (or more) possibly equal parts. The common device which can be used for this application is the 3 dB (i.e. 50% : 50%) splitter, based on a specially designed optical coupler comprising two silica fibre cores in close proximity (see Fig. 2.1). The light launched initially into one core is coupled across to the other core, with the fraction of the coupled power determined by the device geometry and the optical properties of the coupler's material. Using the directional coupler, switching with high extinction ratio (defined as the ratio of the maximum and minimum output levels) are possible.

The optical fibre coupler is an established device which has been refined continuously over the last 20 years, so that a wide variety of very low-loss couplers is now available for a diversity of optical splitting and combining purposes between different fibres and wavelength channels. However, there are several goals which the tapered fibre coupler has not yet achieved.

Firstly, there is an inherent lower limit to the overall dimensions of a single tapered coupler (24). Although the central coupling region of a well-tuned tapered fibre coupler is only of the order of a couple of millimetres in length, when combined with the necessarily length of the adiabatically tapered input and output fibres, this leads to an overall device length of several centimetres. Subsequent packaging results in a final length of around 10 cm.

Secondly, in a concatenation of fibre couplers, such as the simple tree shown in Fig. 2.2, the two output leads from the first coupler need to be spliced to the input parts of the second and third couplers, and there is also a lower limit on the bending radius of the order of centimetres, below which the joining leads cannot be bent in order to avoid significant loss from the fibres (see Chapters 4 and 5 for a detailed

The first part of the thesis is devoted to a general introduction to the subject of optical communications. It starts with a brief history of the field, followed by a discussion of the basic principles of light propagation and modulation. The second part of the thesis is devoted to a detailed study of the properties of optical fibers. It covers the theory of light propagation in fibers, the design of fiber structures, and the characteristics of fiber-based communication systems. The third part of the thesis is devoted to a study of the properties of optical waveguides. It covers the theory of light propagation in waveguides, the design of waveguide structures, and the characteristics of waveguide-based communication systems. The fourth part of the thesis is devoted to a study of the properties of optical amplifiers. It covers the theory of light amplification, the design of amplifier structures, and the characteristics of amplifier-based communication systems. The fifth part of the thesis is devoted to a study of the properties of optical modulators. It covers the theory of light modulation, the design of modulator structures, and the characteristics of modulator-based communication systems. The sixth part of the thesis is devoted to a study of the properties of optical detectors. It covers the theory of light detection, the design of detector structures, and the characteristics of detector-based communication systems. The seventh part of the thesis is devoted to a study of the properties of optical receivers. It covers the theory of light reception, the design of receiver structures, and the characteristics of receiver-based communication systems. The eighth part of the thesis is devoted to a study of the properties of optical transmitters. It covers the theory of light transmission, the design of transmitter structures, and the characteristics of transmitter-based communication systems. The ninth part of the thesis is devoted to a study of the properties of optical networks. It covers the theory of light networking, the design of network structures, and the characteristics of network-based communication systems. The tenth part of the thesis is devoted to a study of the properties of optical systems. It covers the theory of light system design, the design of system structures, and the characteristics of system-based communication systems.

CHAPTER 2. THEORETICAL ANALYSIS OF OPTICAL FIBERS

The first part of this chapter is devoted to a study of the basic principles of light propagation in optical fibers. It starts with a discussion of the wave equation for light propagation in a medium with a refractive index n . The wave equation is then solved for a cylindrical fiber structure, leading to the characteristic equation for the propagation constants. The second part of this chapter is devoted to a study of the properties of optical fibers. It covers the theory of light propagation in fibers, the design of fiber structures, and the characteristics of fiber-based communication systems. The third part of this chapter is devoted to a study of the properties of optical waveguides. It covers the theory of light propagation in waveguides, the design of waveguide structures, and the characteristics of waveguide-based communication systems. The fourth part of this chapter is devoted to a study of the properties of optical amplifiers. It covers the theory of light amplification, the design of amplifier structures, and the characteristics of amplifier-based communication systems. The fifth part of this chapter is devoted to a study of the properties of optical modulators. It covers the theory of light modulation, the design of modulator structures, and the characteristics of modulator-based communication systems. The sixth part of this chapter is devoted to a study of the properties of optical detectors. It covers the theory of light detection, the design of detector structures, and the characteristics of detector-based communication systems. The seventh part of this chapter is devoted to a study of the properties of optical receivers. It covers the theory of light reception, the design of receiver structures, and the characteristics of receiver-based communication systems. The eighth part of this chapter is devoted to a study of the properties of optical transmitters. It covers the theory of light transmission, the design of transmitter structures, and the characteristics of transmitter-based communication systems. The ninth part of this chapter is devoted to a study of the properties of optical networks. It covers the theory of light networking, the design of network structures, and the characteristics of network-based communication systems. The tenth part of this chapter is devoted to a study of the properties of optical systems. It covers the theory of light system design, the design of system structures, and the characteristics of system-based communication systems.

Buried Channel Waveguides & Couplers

This chapter is devoted to the basic theory of buried channel optical waveguides and its relation to the design of actual waveguide devices. A qualitative physical description combined with analytical and numerical techniques cover the important aspects of wave propagation in buried channel waveguides and couplers.

2.1 Advantages of planar couplers

To send the same information to two (or more) recipients in an optical network, the optical signal has to be split into two (or more) possibly equal parts. The common device which can be used for this application is the 3 dB (i.e. 50% : 50%) splitter, based on a specially designed optical coupler comprising two silica fibre cores in close proximity (see Fig. 2.1). The light launched initially into one core is coupled across to the other core, with the fraction of the coupled power determined by the device geometry and the optical properties of the coupler's material. Using the directional coupler, switching with high extinction ratio (defined as the ratio of the maximum and minimum output levels) are possible.

The optical fibre coupler is an established device which has been refined continuously over the last 20 years, so that a wide variety of very low-loss couplers is now available for a diversity of optical splitting and combining processes between different fibres and wavelength channels. However, there are several goals which the tapered fibre coupler has not yet achieved.

Firstly, there is an inherent lower limit to the overall dimensions of a single tapered coupler [24]. Although the central coupling region of a well-fused tapered fibre coupler is only of the order of a couple of millimetres in length, when combined with the necessarily length of the adiabatically tapered input and output fibres, this leads to an overall device length of several centimetres. Subsequent packaging results in a final length of around 10 cm.

Secondly, in a concatenation of fibre couplers, such as the simple tree shown in Fig. 2.2, the two output leads from the first coupler need to be spliced to the input ports of the second and third couplers, and there is also a lower limit on the bending radius, of the order of centimetres, below which the joining leads cannot be bent in order to avoid significant loss from the fibres (see Chapters 4 and 5 for a detailed

discussion of bend loss). This places a lower limit on the overall lateral dimension (i.e. vertical in Fig. 2.2) of the tree layout.

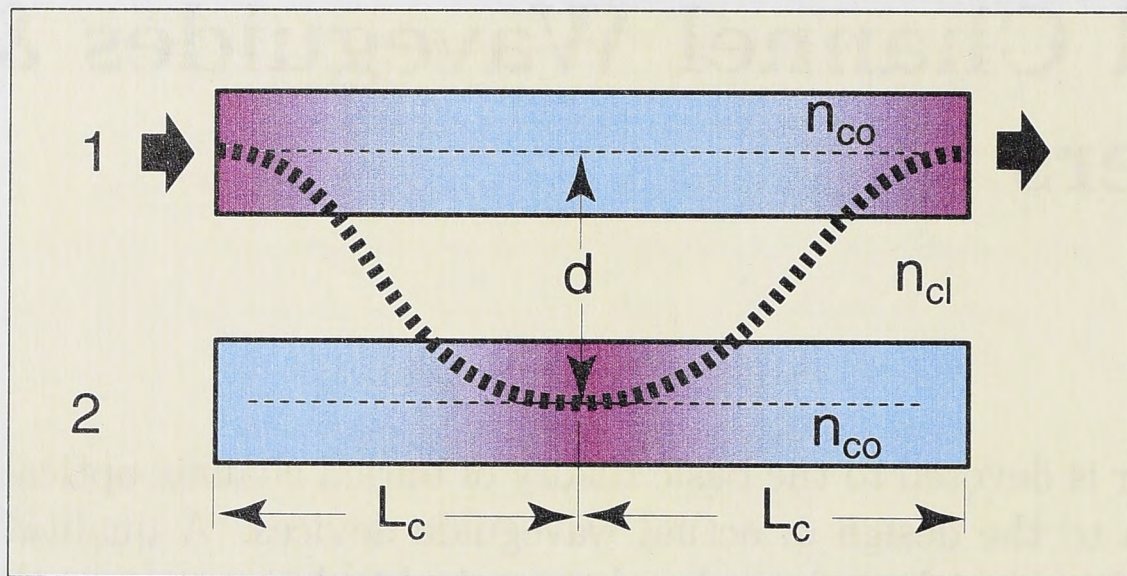


Figure 2.1: Schematic of a coupler. First and second coupler cores are marked by 1 and 2, n_{co} and n_{cl} are the refractive indices of the core and the cladding, respectively, d is the distance between the core axes. The broken bold line symbolises power transfer between the coupler cores, L_c being the distance at which complete transfer of power from core 1 to core 2 takes place.

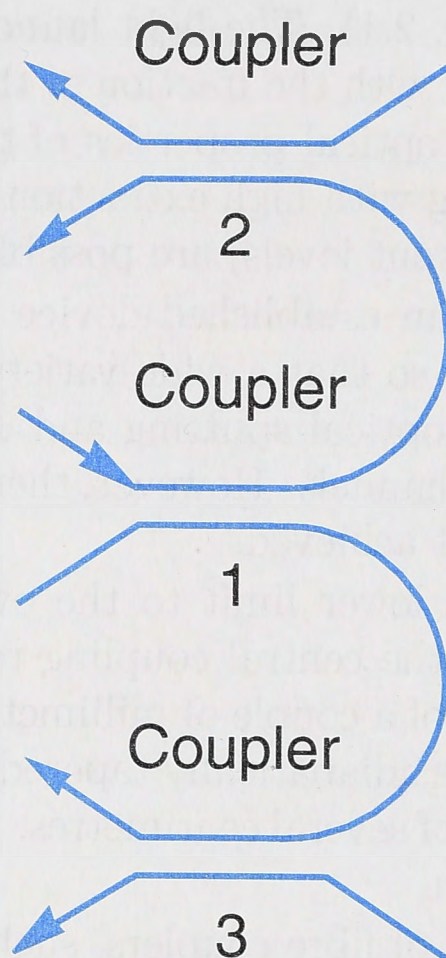


Figure 2.2: Concatenation of fibre couplers.

Both of these limitations can be overcome through the use of planar, or buried channel couplers. As will be shown later, the overall length of a planar coupler is much shorter than that of the corresponding fibre coupler. Although the length of the coupling region of the planar devices is usually somewhat larger than that of the tapered fibre coupler, this is more than compensated for by the much shorter length of the input and output channel waveguides. Furthermore, concatenations of planar couplers occupy a much smaller area, typically of the order of $1 \text{ cm} \times 2\text{-}3 \text{ cms}$, since the complete tree can be fabricated simultaneously.

In the next Section, aspects of propagation pertinent to buried channel waveguides are first summarised, followed by a discussion of relevant physical aspects of propagation through planar couplers, which are subsequently analysed and quantified in Section 2.6.

2.2 Buried channel waveguide geometry

The waveguides and devices considered in this Chapter are premised on the plasma deposition and etching processes used at ANU (see [25] for specifications and details), University of New South Wales and PIRI[†], which fabricate waveguides with essentially uniform core and cladding refractive indices, i.e. a step profile, and approximately square core cross-sections. Accordingly, the buried waveguide has the cross-section and profile shown in Fig. 2.3, where the cladding region is taken to be infinite in extent. The core has sides 2ρ and refractive index n_{co} , while the cladding index is n_{cl} .

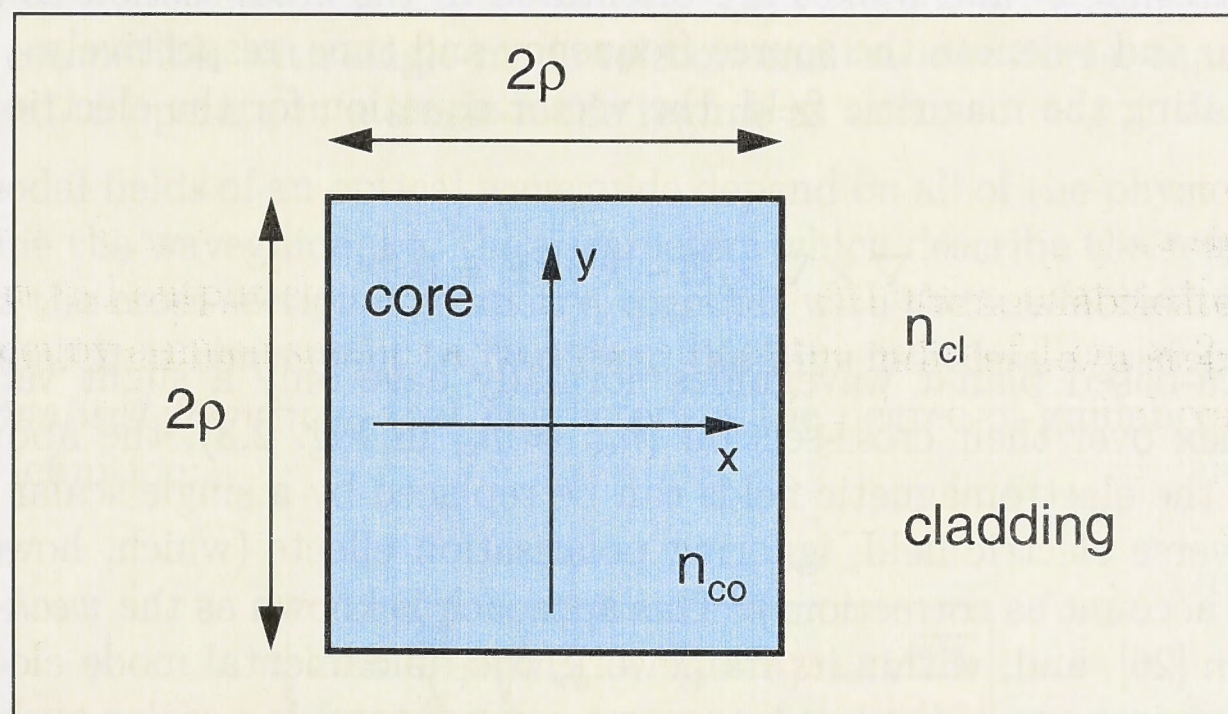


Figure 2.3: Cross-section of the square-core, step-profile buried channel waveguide. ρ is the waveguide half-width, n_{co} and n_{cl} are the refractive indices of the core and the cladding material, respectively.

[†]Photonic Integration Research, Inc.

2.3 Fundamental equations of optical waveguide theory

The electromagnetic wave propagation along optical waveguides is, in general, described by Maxwell equations, which, in rationalized MKS units, can be presented in the following form for a monochromatic source of excitation [5, Sectn. 30-1]:

$$\begin{aligned}\nabla \times \mathbf{E} &= ik \sqrt{\frac{\mu_0}{\epsilon_0}} \mathbf{H} \\ \nabla \times \mathbf{H} &= -ikn^2 \sqrt{\frac{\mu_0}{\epsilon_0}} \mathbf{E},\end{aligned}\tag{2.1}$$

where $\mathbf{E} = \mathbf{E}(x, y, z, t)$ and $\mathbf{H} = \mathbf{H}(x, y, z, t)$ are the (complex) vector electric field and vector magnetic field, respectively, ϵ_0 is the dielectric permittivity and μ_0 is magnetic permeability of free space, $k = 2\pi/\lambda$ is the wavenumber in terms of the source wavelength λ , and $n = n(x, y)$ is the refractive index. In the orthogonal coordinate system, a plane wave propagates along the z direction parallel to the waveguide axis with propagation constant β . Since the refractive index varies only in the transverse plane, the electromagnetic fields can be expressed in the separable forms:

$$\begin{aligned}\mathbf{E} &= \mathbf{e}(x, y)e^{i(\beta z - \omega t)} \\ \mathbf{H} &= \mathbf{h}(x, y)e^{i(\beta z - \omega t)},\end{aligned}\tag{2.2}$$

where the cartesian x - and y -axes are orientated in the cross-section as shown in Fig. 2.3 and ω and t denote the source frequency and time, respectively.

By eliminating the magnetic field, the vector equation for the electric field can be obtained:

$$\nabla \times \nabla \times \mathbf{E} - k^2 n^2 \mathbf{E} = 0.\tag{2.3}$$

Since silica-based planar waveguides normally have only a slight variation in refractive index over their cross-section ($n_{co} \approx n_{cl}$ in Fig. 2.3), the above vector equations for the electromagnetic fields can be replaced by a single scalar equation for the transverse electric field, ignoring polarisation effects (which, however, can be taken into account as corrections). This approach is known as the *weak-guidance approximation* [26], and, within its framework, the fundamental mode electric field E (which represents one of the two transverse components) is a scalar quantity with the separable form

$$E(x, y, z) = \psi(x, y)e^{i\beta z},\tag{2.4}$$

where $\psi(x, y)$ can be taken to be real in lossless materials and it is understood that $E(x, y, z)$ denotes the real part of the right hand side of Eqn. (2.4) for the linear problems in later chapters. Here $\psi(x, y)$ is the fundamental solution (with

the largest value of β) of the *scalar wave equation*

$$\left\{ \frac{\partial^2}{\partial x^2} + \frac{\partial^2}{\partial y^2} + k^2 n^2(x, y) - \beta^2 \right\} \psi = 0. \quad (2.5)$$

This equation, together with its boundary conditions, constitutes an eigenvalue problem that has both a discrete and a continuous spectrum. Eigenvectors corresponding to discrete eigenvalues of this problem determine the transverse electric fields $\psi(x, y)$ and the propagation constants β , respectively, corresponding to *bound modes* of the waveguide. In this Chapter we will be dealing with so-called *single-mode waveguides*, which support only one bound mode, the *fundamental mode*. The solutions of equation (2.5) for the BCW and planar coupler are discussed further in Section 2.6.

2.4 Propagation through buried channel waveguides

2.4.1 Single-mode propagation

To be compatible with single-mode telecommunications fibres, channel-type BCW's need to operate in a single-mode regime as well.

The modal fields of an optical waveguide depend on all of the physical quantities which define the waveguide, i.e. the parameters which describe the refractive index profile and the cross-sectional geometry, together with the wavelength of the source of excitation. It is convenient to introduce the dimensionless *waveguide parameter* V , or *normalised frequency*, that characterises the degree of guidance and has the following definition:

$$V = \frac{2\pi}{\lambda} \rho \sqrt{n_{\text{co}}^2 - n_{\text{cl}}^2} = k \rho n_{\text{co}} \sqrt{2\Delta} \quad (2.6)$$

where $\Delta = (n_{\text{co}}^2 - n_{\text{cl}}^2) / 2n_{\text{co}}^2$ is the relative index difference.

It is important to note, that the above definition is identical to that for a step-profile fibre of core radius ρ (see Fig. 2.4). This facilitates the generalisation of a criterion from fibre optics to derive a single-mode condition for buried channel (or planar) waveguides.

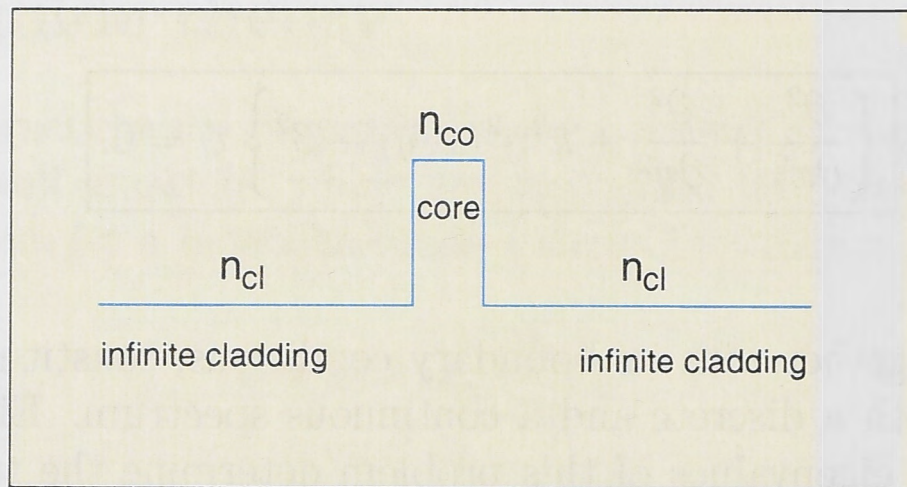


Figure 2.4: Refractive index profile of a step-profile optical fibre. n_{co} and n_{cl} are the refractive indices of the core and the cladding, respectively.

The condition for the square-core waveguide to be single-moded can be obtained from the cutoff V -value for the second mode of the corresponding step-profile fibre with the same core and cladding indices, i.e. $V = 2.41$ [5, Sectn. 12-9], by simply requiring that the areas of the circular and square cores be equal. Namely, if V_c denotes the cutoff V -value for the second mode of the square-core waveguide, then

$$V_c \simeq 2.41 \left(\frac{\pi}{4} \right)^{1/2} = 2.13 \quad (2.7)$$

as can be verified numerically [27].

In a single-mode waveguide with an infinite cladding, the fundamental mode does not have a cutoff wavelength provided the waveguide has a matched-cladding refractive index profile, i.e. the core index is greater than the uniform cladding index.

2.4.2 Bend loss

In a layout of planar waveguides and devices, it is often necessary to link successive devices with bent waveguides in order to minimise the overall dimensions of the design, and, in the case of the planar coupler, to be able to bring the two cores together, as will be discussed further. Since the length of individual planar devices is of the order of millimetres, the ideal bend radii are of similar magnitude and extreme care must be taken in the design to ensure that bend loss is not significant. Here we present only a brief introduction to the bend loss problem, while Chapters 4 and 5 provide more elaborate analysis.

The expression for the modal power attenuation coefficient γ due to pure bend loss in a square-core planar waveguide has the same dominant exponential dependence as for a fibre [28]

$$\gamma \sim \exp \left(-\frac{4}{3} \Delta \frac{R_b W^3}{\rho V^2} \right) \quad (2.8)$$

where ρ and R_b are the core half-width and the bend radius, respectively, V is determined by (2.6), and the cladding modal parameter W is defined by

$$W = \rho (\beta^2 - k^2 n_{cl}^2)^{1/2} \quad (2.9)$$

If Δ is increased (by decreasing ρ and keeping V and hence W constant), bend loss decreases because the modal field is more tightly confined to the bend, and, similarly, increasing the width of the waveguide in the plane of the bend has the same effect, as can be confirmed numerically [28].

2.5 Analysis of planar couplers

Currently, there is a wide range of fused-taper fibre couplers available commercially, covering such optical processes as splitting, coupling, and wavelength multiplexing and demultiplexing. In principle, all of these types of fibre couplers can be paralleled by an equivalent planar coupler, such as the one illustrated schematically in Fig. 2.5.

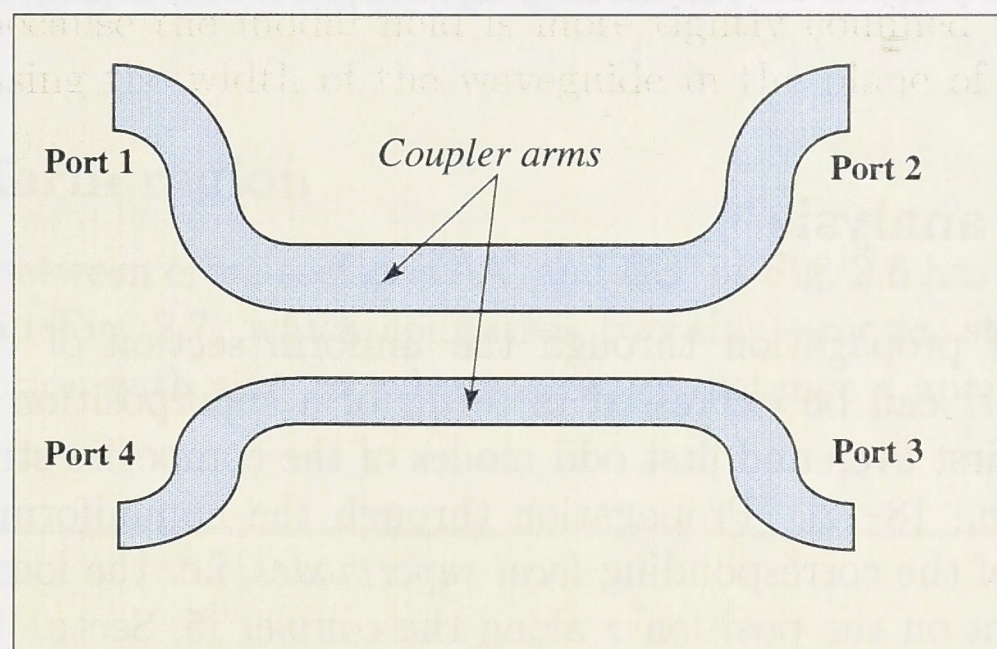


Figure 2.5: Schematic of a planar coupler.

However, planar couplers differ from their fibre counterparts in two significant respects. Firstly, fused taper couplers rely on interference between cladding modes, i.e. modes whose effective-index values ($n_{\text{eff}} = \beta/k$) are below the cladding index, for their operation, whereas planar couplers are essentially untapered devices with an infinite cladding, and rely on interference between core modes. In the former case, the coupling length between cores is reduced to millimetres through tapering, whereas in the latter case, a similar effect can be achieved by designing the cores to be arbitrarily close as shown in Fig. 2.5, although the reduction in coupling length is not so pronounced.

In terms of fabrication of couplers with specific properties, the fused-taper process has the advantage that the response of the fibre coupler can be monitored during the drawing process. Thus, essentially no pre-design is required, whereas

planar couplers cannot be monitored at all during fabrication and it is therefore necessary, not only to accurately predetermine all dimensions and parameter values for the type of design in Fig. 2.5, but also to have sufficient control over the fabrication processes to reproduce the requisite design reasonably accurately. Put another way, planar coupler design should take advantage of those parameters whose values have the least effect on propagation. The thrust of this Chapter is to address the design and tolerance aspects of two types of planar coupler, namely the 3 dB splitter at a specified wavelength, and the wavelength multiplexer/demultiplexer.

The analysis of propagation through and the design of planar couplers with specific splitting/combining properties would be very straightforward if the coupling action occurred only in the two parallel cores in Fig. 2.5. However, because the pairs of input and output arms must necessarily come close together at the beginning and end, respectively, of the central straight region, propagation in both pairs will contribute to coupling. In other words, the coupler analysis and design must allow for all three regions. This Section introduces two distinct approaches to the problem, one which is semi-analytical and based on the propagation of the superposition of a pair of supermodes along the length of the coupler, and the other one which is purely numerical and based on the beam propagation method (BPM).

2.5.1 Modal analysis

The analysis of propagation through the uniform section of the symmetric, single-mode coupler[†] can be expressed in terms of a superposition of its two *supermodes*, i.e. the first even and first odd modes of the composite straight two-core waveguide [5, Sectn. 18–12]. Propagation through the nonuniform section is expressible in terms of the corresponding *local supermodes*, i.e. the local fundamental solutions, dependent on the position z along the coupler [5, Sectn. 19–6]. Accordingly, it is convenient to examine the three regions of the coupler separately, as delineated in Fig. 2.6.

The input region to the left of the cross-section AA' and the output region to the right of BB' are assumed to consist of bends of constant radius R_b which is chosen to be sufficiently large to avoid any losses due to bending, i.e. for given values of the indices and core size

$$R_b \gg \frac{\rho V^2}{\Delta W^3} \quad (2.10)$$

on rearranging the exponent in Eqn. (2.8).

[†]Strictly speaking, couplers are, in general, two-moded. The terminology refers to the two single-moded waveguides (in isolation from each other), comprising the coupler.

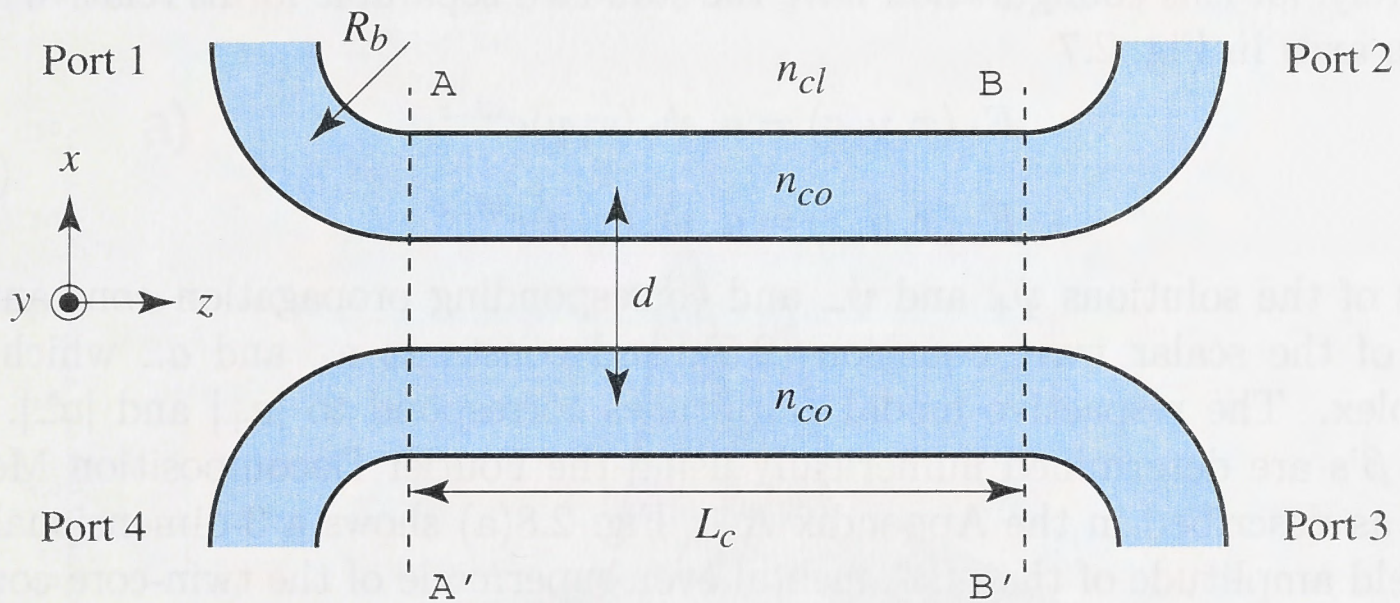


Figure 2.6: Division of the coupler into three regions. R_b denotes the bend radius of the coupler arms, n_{co} and n_{cl} are the refractive indices of the core and the cladding, respectively, d is the separation between the core axes, and L_c is the length of the straight coupling section.

2.5.2 Uniform region

The region between cross-sections AA' and BB' in Fig. 2.6 has the uniform cross-section shown in Fig. 2.7, which comprises two single-mode, step-profile cores of square cross-section with side 2ρ , whose axes are distance d apart.

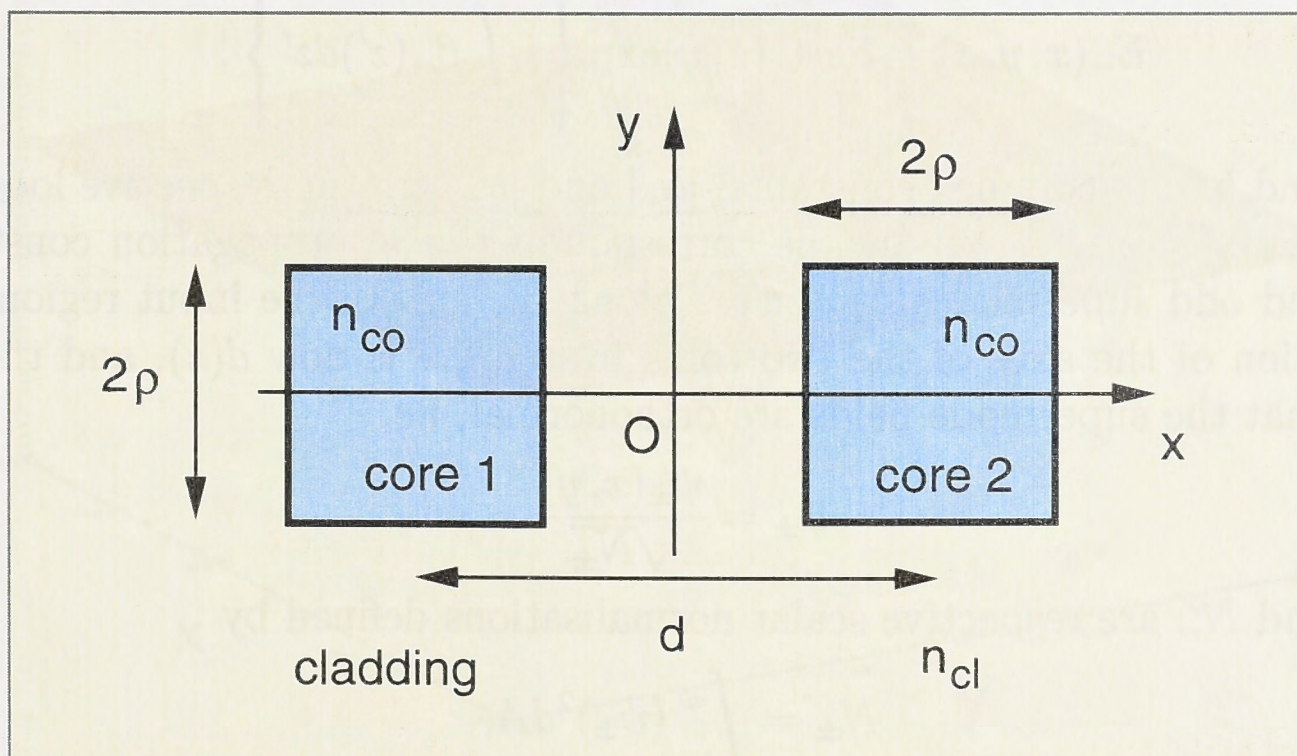


Figure 2.7: Cross-section of the central region of the coupler. n_{co} and n_{cl} are the refractive indices of the core and the cladding, respectively, d is the separation between the core axes, ρ is the core half-width.

The scalar transverse electric fields E_+ and E_- of the even and odd supermodes, respectively, for this configuration have the standard separable forms relative to the cartesian axes in Fig. 2.7

$$\begin{aligned} E_+(x, y, z) &= a_+ \psi_+(x, y) e^{i\beta_+ z} \\ E_-(x, y, z) &= a_- \psi_-(x, y) e^{i\beta_- z} \end{aligned} \quad (2.11)$$

in terms of the solutions ψ_+ and ψ_- and corresponding propagation constants β_+ and β_- of the scalar wave equation (2.5), and constants a_+ and a_- which may be complex. The respective modal amplitudes correspond to $|a_+|$ and $|a_-|$. The ψ 's and β 's are determined numerically using the Fourier Decomposition Method (FDM), as described in the Appendix A.1. Fig. 2.8(a) shows a 3-dimensional plot of the field amplitude of the fundamental even supermode of the twin-core coupler, while the field of the second-order odd supermode is plotted in Fig. 2.8(b).

2.5.3 Non-uniform region

Propagation along the curved input and output arms to the left and right of the cross-sections AA' and BB', respectively, in Fig. 2.6 can be described in general by a superposition of the even and odd local supermodes to account for the continuous variation in separation between the two cores along z . This description is equivalent to assuming that evolution of each supermode is adiabatic and its power, and therefore amplitude, is conserved [5, Sectn. 28-3]. The forms of the local modes are generalisations of Eqn. (2.11)

$$\begin{aligned} E_+(x, y, z) &= b_+ \hat{\psi}_+(x, y) \exp \left\{ i \int_0^z \beta_+(z') dz' \right\} \\ E_-(x, y, z) &= b_- \hat{\psi}_-(x, y) \exp \left\{ i \int_0^z \beta_-(z') dz' \right\}, \end{aligned} \quad (2.12)$$

where b_+ and b_- are complex constants, $|b_+|$ and $|b_-|$ are the respective local mode amplitudes, $\beta_+(z)$ and $\beta_-(z)$ are the corresponding local propagation constants of the even and odd supermodes distance z along the axis of the input region, where the separation of the axes of the two cores in Fig. 2.7 is now $d(z)$, and the "hat" indicates that the supermode fields are orthonormal, i.e.

$$\hat{\psi}_\pm = \frac{\psi_\pm(x, y)}{\sqrt{N_\pm}} \quad (2.13)$$

Here N_+ and N_- are respective scalar normalisations defined by

$$N_\pm = \int_{A_\infty} (\psi_\pm)^2 dA,$$

where the integration is over the infinite cross-section of the coupler. The ψ 's and β 's are calculated for each value of core separation at each position z along the input arms using the FDM, and the phase integrals in Eqn. (2.12) can then be calculated numerically.

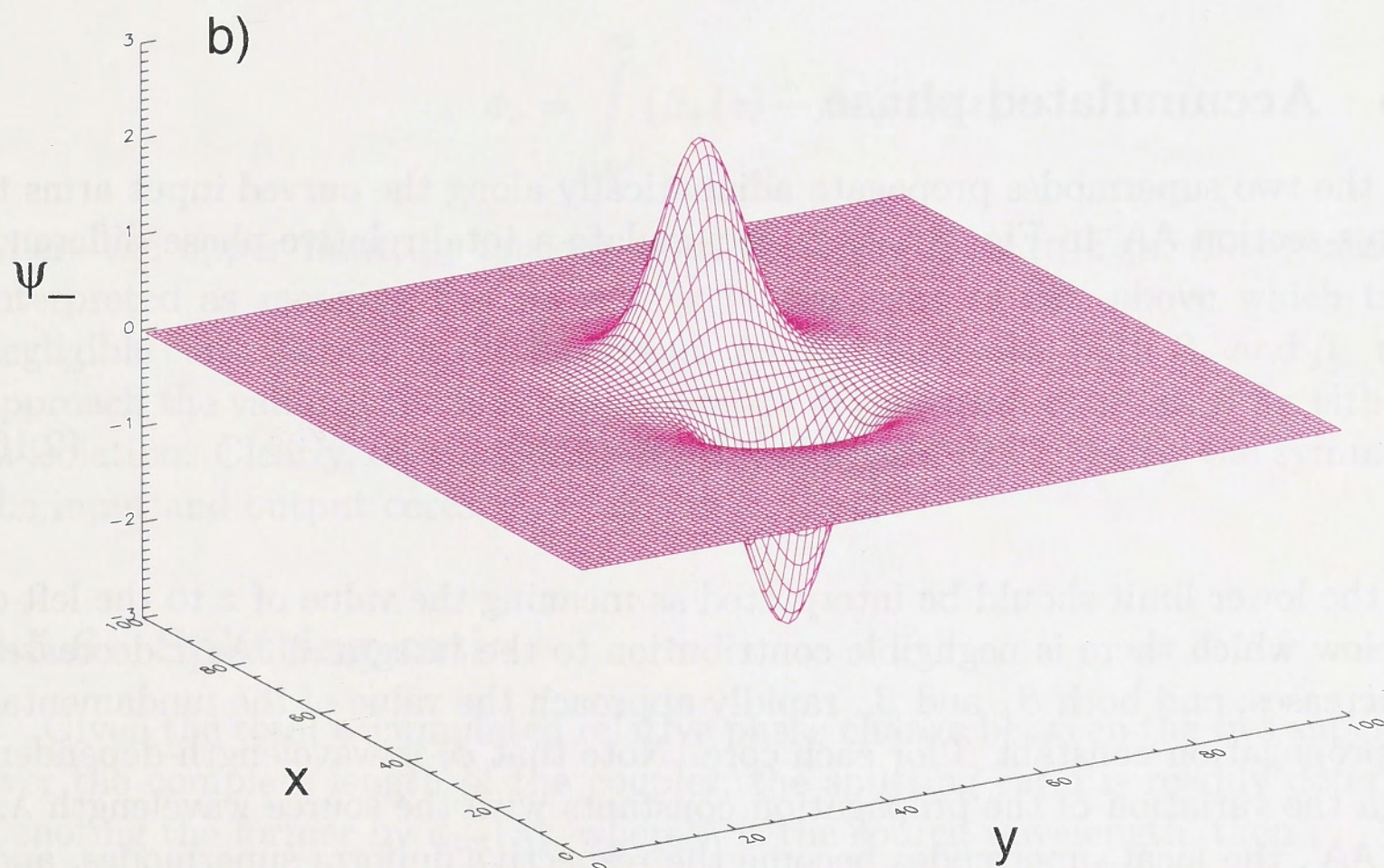
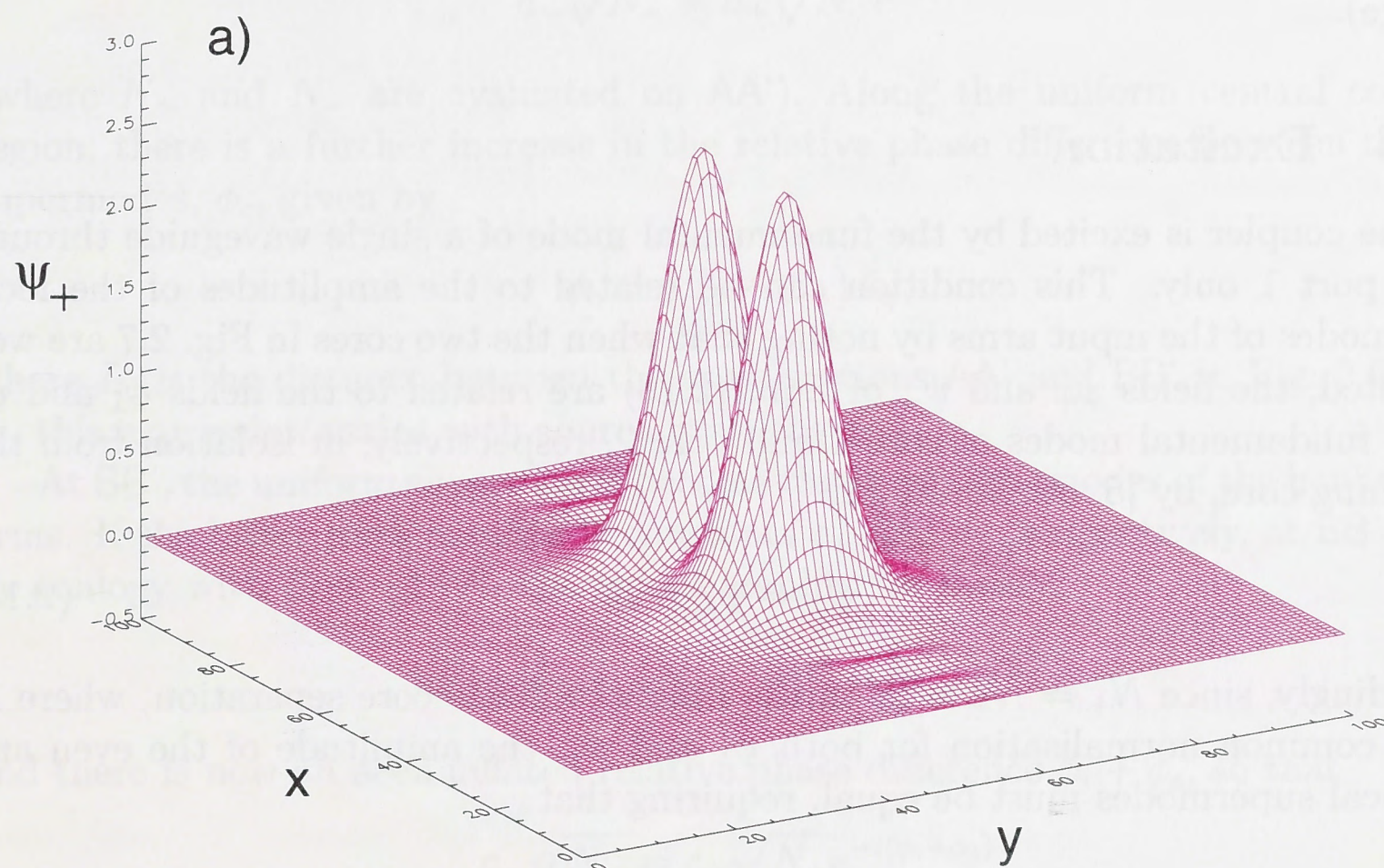


Figure 2.8: Plots of the FDM fields of the a) fundamental even mode and b) second-order odd mode of the twin-core BCW, where the horizontal and the vertical scales are in arbitrary units.

Physically, the orthonormality of the fields in Eqn. (2.12) is equivalent to power conservation of each local supermode, i.e. each mode is assumed to propagate adiabatically through the tapered region where the two curved cores converge (or diverge).

2.5.4 Excitation

The coupler is excited by the fundamental mode of a single waveguide through input port 1 only. This condition can be related to the amplitudes of the local supermodes of the input arms by noting that when the two cores in Fig. 2.7 are well separated, the fields ψ_+ and ψ_- of Eqn. (2.13) are related to the fields ψ_1 and ψ_2 of the fundamental modes of core 1 and core 2, respectively, in isolation from the remaining core, by [5, Sectn. 18-12]

$$\psi_{\pm} = \psi_1 \pm \psi_2 \quad (2.14)$$

Accordingly, since $N_+ = N_- = N$ in the limit of infinite core separation, where N is the common normalisation for both ψ_1 and ψ_2 , the amplitude of the even and odd local supermodes must be equal, requiring that

$$|b_+| = |b_-| \quad (2.15)$$

in Eqn. (2.12).

2.5.5 Accumulated phase

As the two supermodes propagate adiabatically along the curved input arms to the cross-section AA' in Fig. 2.6, they accumulate a total relative phase difference ϕ_i

$$\phi_i = \int_{-\infty}^{AA'} \{\beta_+(z) - \beta_-(z)\} dz, \quad (2.16)$$

where the lower limit should be interpreted as meaning the value of z to the left of AA' below which there is negligible contribution to the integrand. As z decreases, $d(z)$ increases, and both β_+ and β_- rapidly approach the value of the fundamental-mode propagation constant β for each core. Note that ϕ_i is wavelength-dependent through the variation of the propagation constants with the source wavelength λ .

At AA', the local supermodes become the respective uniform supermodes, and, since the modal amplitudes are constant in the respective regions, it follows from Eqns. (2.11)-(2.13) that

$$|a_+| = \frac{|b_+|}{\sqrt{N_+}}; \quad |a_-| = \frac{|b_-|}{\sqrt{N_-}} \quad (2.17)$$

Furthermore, since there is the relative phase difference ϕ_i between the b 's on AA', it follows that there is the same relative phase difference between the a 's, i.e.

$$a_- \sqrt{N_-} = a_+ \sqrt{N_+} e^{-i\phi_i} \quad (2.18)$$

(where N_+ and N_- are evaluated on AA'). Along the uniform central coupling region, there is a further increase in the relative phase difference between the two supermodes, ϕ_c , given by

$$\phi_c = \{\beta_+ - \beta_-\} L_c, \quad (2.19)$$

where L_c is the distance between the cross-sections AA' and BB' in Fig. 2.6. Like ϕ_i , this expression varies with source wavelength.

At BB', the uniform supermodes become the local supermodes of the bent output arms. If the latter have amplitude constants c_+ and c_- , respectively, at BB', then, by analogy with Eqn. (2.17), the modal amplitudes satisfy

$$|c_+| = |a_+| \sqrt{N_+}; \quad |c_-| = |a_-| \sqrt{N_-} \quad (2.20)$$

and there is now an accumulated relative phase difference $\phi_i + \phi_c$, so that

$$c_- \sqrt{N_-} = c_+ \sqrt{N_+} e^{-i(\phi_i + \phi_c)} \quad (2.21)$$

Finally, by analogy with Eqn. (2.16), the total accumulated relative phase difference along the output arms, ϕ_o , is given by

$$\phi_o = \int_{BB'}^{\infty} \{\beta_+(z) - \beta_-(z)\} dz, \quad (2.22)$$

where the upper limit, by analogy with the lower limit in Eqn. (2.16), should be interpreted as meaning the value of z to the right of BB' above which there is negligible contribution to the integrand. As $d(z)$ increases, both β_+ and β_- rapidly approach the value of the fundamental-mode propagation constant β for either core in isolation. Clearly, on comparing Eqns. (2.16) and (2.22), or by the symmetry of the input and output cores, $\phi_o = \phi_i$.

2.5.6 Splitting ratio

Given the total accumulated relative phase change between the two supermodes over the complete length of the coupler, the splitting ratio is readily determined. Denoting the former by $\phi_{\text{tot}}(\lambda)$, where λ is the source wavelength, then

$$\phi_{\text{tot}}(\lambda) = \phi_i + \phi_c + \phi_o = 2\phi_i + \phi_c, \quad (2.23)$$

where ϕ_i , ϕ_c and ϕ_o are evaluated from Eqns. (2.16), (2.19) and (2.22), respectively. Recalling that unit power enters port 1 of Fig. 2.6, then it follows from Eqns. (2.15), (2.17) and (2.20), that the amplitudes of the local supermodes sufficiently far to

the right of BB' in Fig. 2.6 are equal, i.e. $|c_+| = |c_-|$ and there is a relative phase between the modal constants, expressible as

$$c_- = c_+ e^{-i\phi_{\text{tot}}(\lambda)} \quad (2.24)$$

Hence, on expressing ψ_+ and ψ_- in terms of ψ_1 and ψ_2 through Eqn. (2.14), and suppressing common phase and normalisation N of the fundamental modes in cores 1 and 2, then the fields in the output arms 2 and 3 of Fig. 2.6 are both proportional to

$$A_2 = (1 + e^{-i\phi_{\text{tot}}(\lambda)})\psi_1; \quad A_3 = (1 - e^{-i\phi_{\text{tot}}(\lambda)})\psi_2 \quad (2.25)$$

respectively. Consequently, the corresponding output powers P_2 and P_3 are proportional to the squares of the moduli in Eqn. (2.25), since ψ_1 and ψ_2 both have the same functional form. Imposing power conservation, so that the total output and input powers are equal, leads to

$$P_2 = \frac{1 + \cos[\phi_{\text{tot}}(\lambda)]}{2}; \quad P_3 = \frac{1 - \cos[\phi_{\text{tot}}(\lambda)]}{2}, \quad (2.26)$$

so that the *splitting ratio depends solely on the total accumulated relative phase change* between the even and odd supermodes over the entire length of the coupler.

2.5.7 3 dB splitters & wavelength demultiplexing couplers

The single-mode planar coupler will act as a *3 dB splitter* at a given input wavelength λ , with equal power outputs from ports 2 and 3, provided that in Eqn. (2.26) the total accumulated phase satisfies

$$\phi_{\text{tot}}(\lambda) = \frac{2m + 1}{2}\pi \quad (2.27)$$

for $m = 0, 1, 2, \dots$. This is a transcendental equation which is solved numerically in Subsection 2.6.3 in order to determine a range of wavelength and coupler parameter values for which equal splitting can occur.

For a coupler which will *wavelength demultiplex* and, by reciprocity, *multiplex* signals at different wavelengths, it is necessary that the superposition of the two signals entering port 1 in Fig. 2.6 be split such that one wavelength exits from port 2 and the other from port 3. Since practical fibre exhibits minimum losses around 1.3 and 1.55 μm wavelength [29], most of telecommunications devices are designed to operate in these wavelength windows. Accordingly, the coupler parameters must take values such as to satisfy simultaneously the two conditions

$$\phi_{\text{tot}}^{(\lambda=1.3)} = 2p\pi; \quad \phi_{\text{tot}}^{(\lambda=1.55)} = (2q + 1)\pi \quad (2.28)$$

where p and q are positive integers. Like Eqn. (2.27), these conditions must be solved numerically; practical examples are given in Subsection 2.6.4.

2.6 Numerical modelling

In order to satisfy the phase conditions derived in Eqns. (2.27) and (2.28) of Subsection 2.5.7 for the various types of symmetric planar couplers, numerical quantification of the values of the supermode and local supermode propagation constants is required, which in turn are determined by the values of coupler parameters, such as bend radius, core separation, relative index difference, etc, and the source wavelength. Below we simulate the response of the complete coupler using a well-tried and straightforward method for this purpose - the *Fourier Decomposition Method* (FDM) and check its validity by another purely numerical approach - the *Beam Propagation Method* (BPM). Both methods are described in detail in Appendix A.

The computations were based on the following parameter values for the single-core BCW:

wavelength	$\lambda = 1.3 \mu\text{m}$
cladding index	$n_{\text{cl}} = 1.447$
relative index difference	$\Delta = 0.003$
core half-width	$\rho = 3.6808 \mu\text{m}$

On substituting these values into Eqn. (2.6), $V \simeq 2$, thereby ensuring that each core in isolation is single-moded ($V < 2.13$).

Fourier Decomposition Method

This method solves linear eigenvalue/eigenvector problems, such as (2.5). It is based on a decomposition of a modal field into a complete set of sinusoidal basis functions [30]. For the purpose of clarity, we will concentrate only on the results, obtained using this approach, and refer the reader to Appendix A.1 for a technical discussion.

Beam Propagation Method

This method is now well established as a powerful technique for studying propagation along both uniform (i.e. translationally invariant) and non-uniform (i.e. z -dependent) waveguides and devices. In the weak-guidance approximation, it is based on the scalar wave equation for the scalar transverse electric field. Given a specified initial field in the (x, y) cross-section, it propagates this field incrementally along the z axis using forward and backward Fourier transforms, and then determines the correction to the field in the next cross-section before repeating the whole process. Accordingly, the field is determined in successive cross-sectional planes, including both the guided and radiated portions (see Appendix A.2 for a comprehensive description).

2.6.1 Single-core BCW

For a simple comparison between the results of the FDM and the BPM, both were used to determine W^2 , where W is the cladding mode parameter of Eqn. (2.9) for the fundamental mode of the single-core BCW of Fig. 2.3. If $N = N_m = N_n$ in Eqn. (A.2) denotes the number of harmonics used in the FDM, then the convergence of the method with increasing N can be gauged from the Table I,

N	10	20	30	40	50	60
W^2	1.63192	1.91460	1.92815	1.93019	1.93210	1.93243

Table I: Convergence of parameter W^2 with increasing number of harmonics in FDM.

where 50 harmonics was found to be adequate for the accuracy required, and the lengths of the sides of the bounding square are prescribed by $L_x = L_y = 256\rho/15$ in Fig. A.1. The BPM for the same situation launched the Gaussian field approximation to the fundamental mode at the beginning of the BCW and propagated it a distance of 4 cm, generating the correct field after only 0.75 mm. The relative error between the BPM ($W^2 = 1.98 \pm 0.05$) and FDM ($N = 60$) values of W^2 was about 2%. We attribute this error to the uncertainty in defining exact core dimensions, e.g. for this calculation only 30 points have been allocated for the core region in each dimension (compared to 256 points for the whole domain).

2.6.2 Twin-core BCW coupler

The application of the FDM to the twin-cores of Fig. 2.7 uses $L_x = \rho(256 + 15d/\rho)/15$ and $L_y = 256\rho/15$, together with 48 harmonics in the Y -direction and 80 in the X -direction to obtain satisfactory convergence. A 3-dimensional plot of the field amplitude of the even and odd coupler supermodes obtained using FDM was already shown in Fig. 2.8.

The values of W_+^2 and W_-^2 for the even and odd supermodes, respectively, where W_+ and W_- are defined through Eqn. (2.9) with β replaced by β_+ and β_- , respectively, are listed in Table II as a function of normalised separation of the two cores d/ρ , using the parameter values defined in the beginning of this Section.

Note how the pairs of values approach one another rapidly with increasing separation of the cores. The smallest value $d = 2\rho$ corresponds to the two cores at contact. Also listed in Table III are the propagation constants and the corresponding beat length z_b for the two modes, which is defined by

$$z_b = \frac{2\pi}{\beta_+ - \beta_-} \quad (2.29)$$

and increases very rapidly with increasing separation, indicating the need to keep the two cores as close together as possible to minimise device length.

d/ρ	W_+^2	W_-^2
2.0	2.557623	1.462328
2.5	2.186061	1.687472
3.0	2.046272	1.815250
3.5	1.985326	1.877608
4.0	1.957325	1.906749
4.5	1.944204	1.920266
5.0	1.937936	1.926566
5.5	1.934888	1.929570
6.0	1.933497	1.930916
6.5	1.932767	1.931504
7.0	1.932377	1.931846
7.5	1.932232	1.931928
8.0	1.932120	1.931997
8.5	1.932085	1.932021
9.0	1.932067	1.932032
9.5	1.932058	1.932042
10.0	1.9320455	1.9320455

Table II. Values of the square of the cladding modal parameter for the two supermodes as a function of normalised separation.

d/ρ	β_+, m^{-1}	β_-, m^{-1}	z_b, mm
2.5	7004956.0	7002330.0	2.39
3.0	7004218.0	7003004.0	5.18
3.5	7003899.0	7003330.0	11.04
4.0	7003749.0	7003485.0	23.73
4.5	7003681.0	7003554.0	49.59
5.0	7003648.0	7003588.0	105.96
5.5	7003632.0	7003603.0	218.17

Table III. Values of the propagation constants for the two supermodes and the beat length of the twin square-core coupler as a function of normalised separation.

2.6.3 3 dB splitters

The single-mode planar coupler will act as a 3 dB splitter with a given input into port 1 at wavelength λ and equal power outputs from ports 2 and 3, if the accumulated phase ϕ_{tot} satisfies Eqn. (2.27). The shortest such coupler then corresponds to $m = 0$. A bend radius of $R_b = 10$ mm was chosen for the curved input and output ports in Fig. 2.6 to ensure negligible bend loss. Using the parameters defined in the beginning of this Section, the value of the exponential term in Eqn. 2.8 is 6.85×10^{-4} . In evaluating the phase integrals in Eqns. (2.16) and (2.22), which are identical, we found that the contribution to the integral was only significant within a distance $\delta z = \sqrt{6R_b\rho}$ from each end of the straight coupling region when the core axes are separated by 8ρ . For the core dimension $\rho = 3.68 \mu\text{m}$ and the above bend radius, $\delta z = 0.47$ mm.

Two cases were considered. In the first case the cores in the central region of Fig. 2.6 are touching, i.e. $d/\rho = 2$ and the core cross-section is rectangular with aspect ratio 2, and in the second case, $d/\rho = 4$, i.e. the cores are separated by one core width. In both cases, the propagation constants $\beta_+(z)$ and $\beta_-(z)$ were evaluated numerically everywhere along the coupler using the FDM, and the integrals in Eqns. (2.16) and (2.22) were also evaluated numerically. When the cores are in contact, virtually all the coupling occurs in the input and output arms and $L_c = 0.37 \mu\text{m}$, i.e. the coupler is just two circular arcs at contact. In the second case, there is significant coupling in the central region and $L_c = 5.616$ mm.

2.6.4 Wavelength multiplexing/demultiplexing couplers

For the multiplexing coupler, the phase conditions were derived in Subsection 2.5.7. The two wavelengths are input through port 1 in Fig 2.6, the longer $1.55 \mu\text{m}$ wavelength is assumed to emerge out of port 2 and the shorter $1.3 \mu\text{m}$ wavelength out of port 3. This is equivalent to imposing the two phase conditions given by Eqn. (2.28). The values of the integers p and q need to be kept as small as possible to minimise the length of the coupler. This is desirable to maximise the yield of planar devices in any fabrication process.

The length L_c of a coupler satisfying each condition in Eqn. (2.28) for the two cases is plotted as a function of the core half-width ρ in Fig. 2.9, where the thick and thin curves correspond to the $1.55 \mu\text{m}$ and $1.3 \mu\text{m}$ wavelengths, respectively. The crossing points of the pairs of curves define the length L_c of the central region of the demultiplexing coupler. For $d/\rho = 2$, the smallest values of p and q for which the curves cross correspond to $p = 8$, $q = 8$ and $L_c = 6.792$ mm, $\rho = 2.93 \mu\text{m}$. These relatively large values arise from the long interaction lengths in the input and output ports. In the second case, $d/\rho = 4$, a solution exists for $p = 0$, $q = 1$, giving $L_c = 8.019$ mm and $\rho = 3.44 \mu\text{m}$.

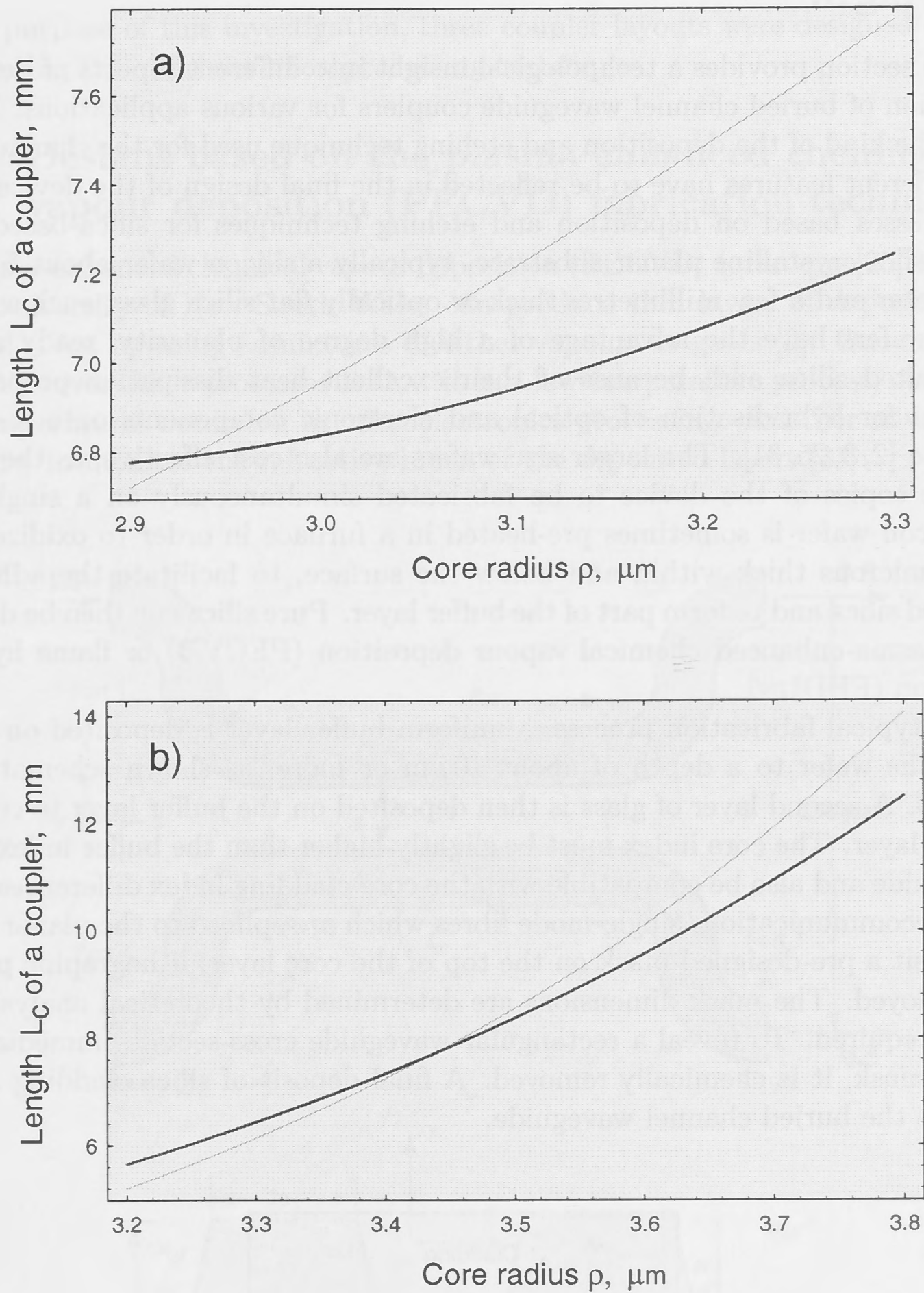


Figure 2.9: Length L_c of a coupler (mm) as a function of core radius ρ (microns) for (a) $d/\rho = 2$ and (b) $d/\rho = 4$ in the central coupling region. Thick and thin curves correspond to 1.55 μm and 1.3 μm wavelengths, respectively.

2.7 Application to practical optical coupler design.

This section provides a technological insight into different aspects of design and fabrication of buried channel waveguide couplers for various applications. Depending on the kind of the deposition and etching technique used for the channel formation, different features have to be reflected in the final design of the device.

Processes based on deposition and etching techniques for silica-based glasses start with a crystalline planar substrate, typically a silicon wafer about 5 – 20 cm in diameter and a few millimetres thick or optically flat silica glass, such as quartz. Silicon wafers have the advantage of a high degree of planarity, ready adhesion of deposited silica and, because of their excellent heat dissipation property, the potential for hybridisation of optical and electronic components onto a common substrate [2, 3, 25, 31]. The larger size wafers are also cost effective, as they enable multiple copies of the device to be fabricated simultaneously on a single wafer. The silicon wafer is sometimes pre-heated in a furnace in order to oxidize a layer several microns thick within and below the surface, to facilitate the adhesion of deposited silica and to form part of the buffer layer. Pure silica can then be deposited using plasma-enhanced chemical vapour deposition (PECVD) or flame hydrolysis deposition (FHD).

In a typical fabrication process, a uniform buffer layer is deposited on the surface of the wafer to a depth of about $10\ \mu\text{m}$ or more, as shown schematically in Fig. 2.10. A second layer of glass is then deposited on the buffer layer to constitute the core layer. The core index must be slightly higher than the buffer index to form a waveguide and also be compatible with the core-cladding index differences of standard telecommunications single-mode fibres which are spliced to the planar devices. To deposit a pre-designed mask on the top of the core layer, lithographic processes are employed. The mask dimensions are determined by theoretical analysis of the devices required. To reveal a rectangular waveguide cross-section immediately below the mask, it is chemically removed. A final deposit of silica cladding material produces the buried channel waveguide.

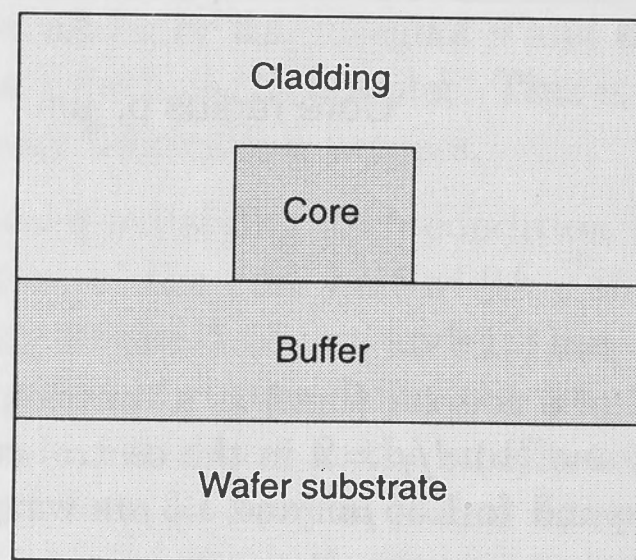


Figure 2.10: Schematic of a buried channel waveguide.

For the purpose of this investigation, three coupler layouts were designed and fabricated using two different microprocessing techniques.

2.7.1 Designs based on the plasma enhanced chemical vapour deposition (PECVD) fabrication technique.

Plasma-enhanced chemical vapour deposition (PECVD) technique [25] employed in the University of New South Wales can produce thin layers of deposited silica or doped silica by using admixtures of either vapours or gases [2]. One advantage of PECVD over other processes is that it is a low-temperature process, compatible with temperatures occurring in microelectronics processing. Another advantage is the ability to monitor the refractive index of the deposited layers [31].

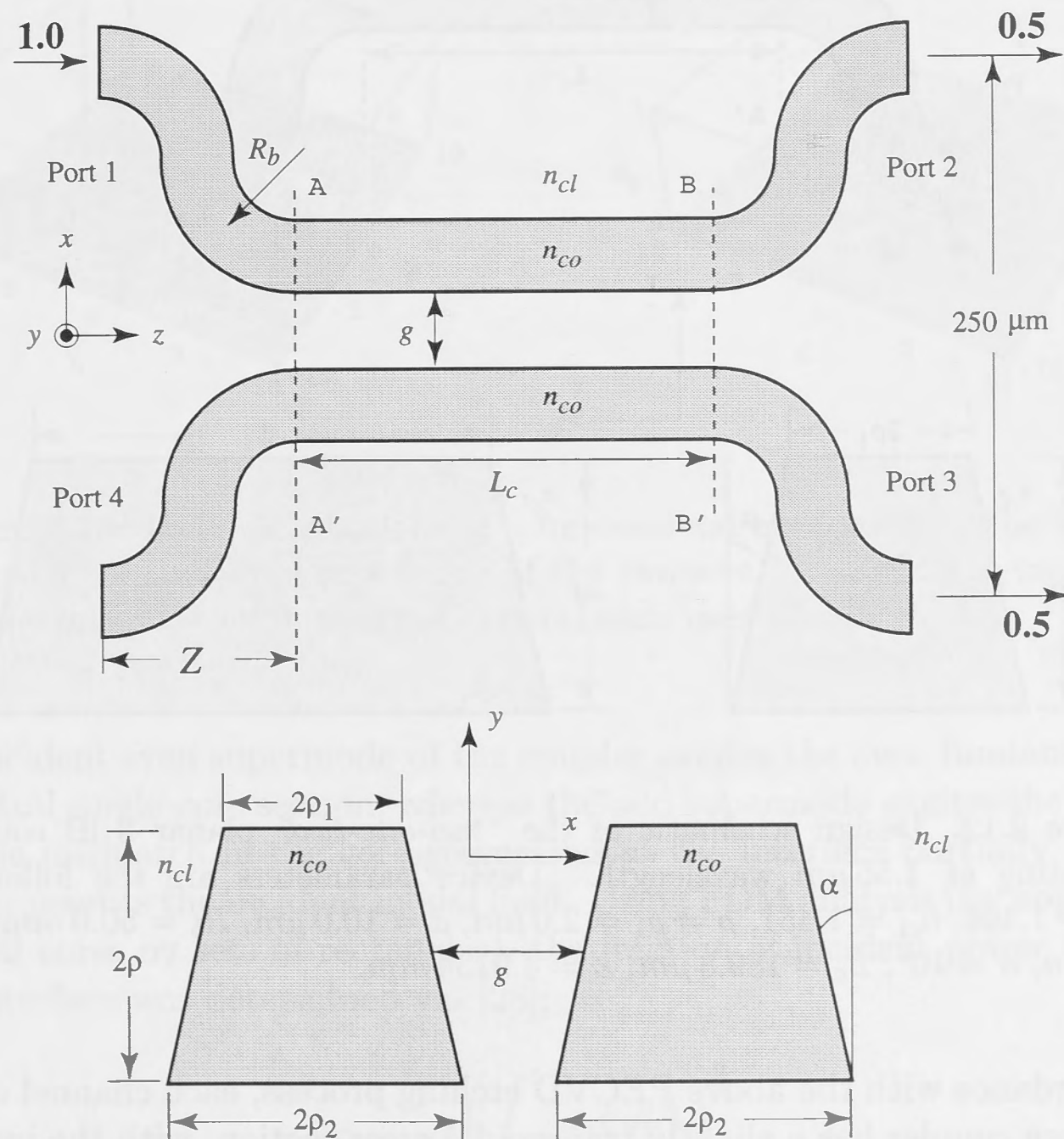


Figure 2.11: Design schematic of a conventional planar 3 dB coupler, operating at $1.55 \mu\text{m}$ wavelength. Device parameters are the following: $n_{co} = 1.468$, $n_{cl} = 1.451$, $\rho = \rho_1 = 2.0 \mu\text{m}$, $\rho_2 = \rho_1 + 2\rho_1 \tan \alpha = 2.7 \mu\text{m}$, $R_b = 50.0 \text{ mm}$, $g = 3.0 \mu\text{m}$, $\alpha = 10^\circ$, $L_c = 250.0 \mu\text{m}$, $Z = 4.9224 \text{ mm}$.

Figures 2.11 and 2.12 present two coupler designs optimised for the PECVD grown silica/silicon parameters configured for a 3dB split at the $1.55\ \mu\text{m}$ carrier wavelength. The coupler layout is shown with the corresponding cross-sectional geometry and parameters delineated in the figure captions. The performance of both couplers was judged against the sensitivity to variations in physical dimensions and value of the transition losses, with the best design to form the basis of a planar dispersion compensator (upon writing of grating in one of the coupler arms).

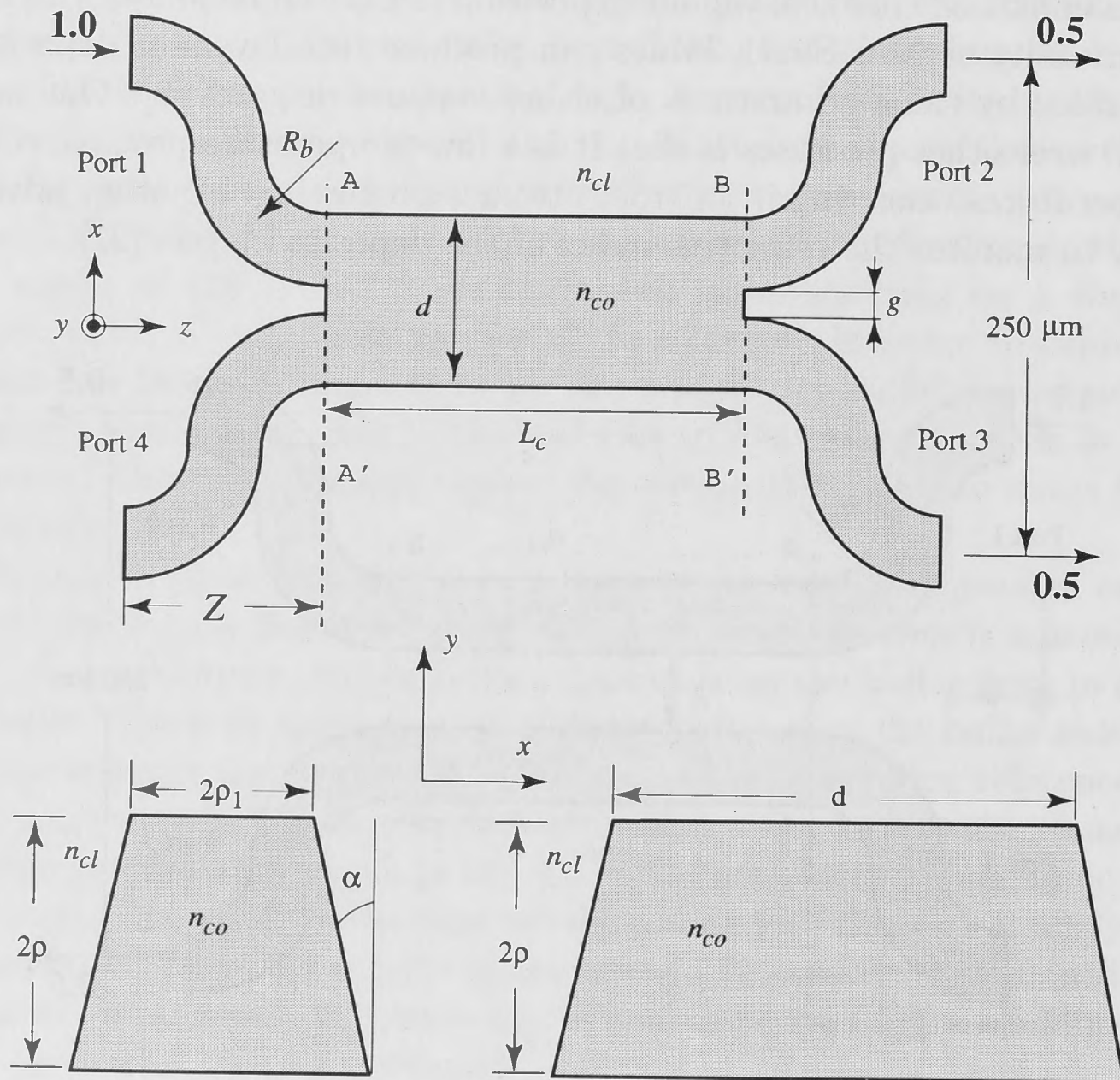


Figure 2.12: Design schematic of the “two-one-two” planar 3 dB coupler, operating at $1.55\ \mu\text{m}$ wavelength. Device parameters are the following: $n_{co} = 1.468$, $n_{cl} = 1.451$, $\rho = \rho_1 = 2.0\ \mu\text{m}$, $d = 10.0\ \mu\text{m}$, $R_b = 50.0\ \text{mm}$, $g = 2.0\ \mu\text{m}$, $\alpha = 10^\circ$, $L_c = 189.8\ \mu\text{m}$, $Z = 4.9134\ \text{mm}$.

In accordance with the above PECVD etching process, each channel comprising the twin-core coupler has a slightly trapezoidal cross-section, with the incline angle α adjusted between 5 and 15 degrees. In the following modelling $\alpha = 10^\circ$ was used. The arms of the coupler are converging and diverging symmetrically to match standard jacketed single-mode fibres.

The designs should allow for several uncertainties in the fabrication process, such as: ± 0.0005 variation in the refractive index value of step-profile waveguides,

square core half-width error $\pm 2 - 3\%$, and height (depth) uniformity margin of $\pm 1.5\%$ over 10 cm (i.e. wafer diameter). Since our goal is to produce a design which is least sensitive to the largest error, the "two-one-two scheme" in Fig. 2.12 seems attractive.

Because of the presence of the transition region between the two single-moded channels and the two-moded straight waveguide of approximately double cross-sectional area, this structure would incur transition losses [28] at the two interfaces AA' and BB'. Figure 2.13 plots the fundamental mode field of the central section and the even supermode field of the coupler at the interface.

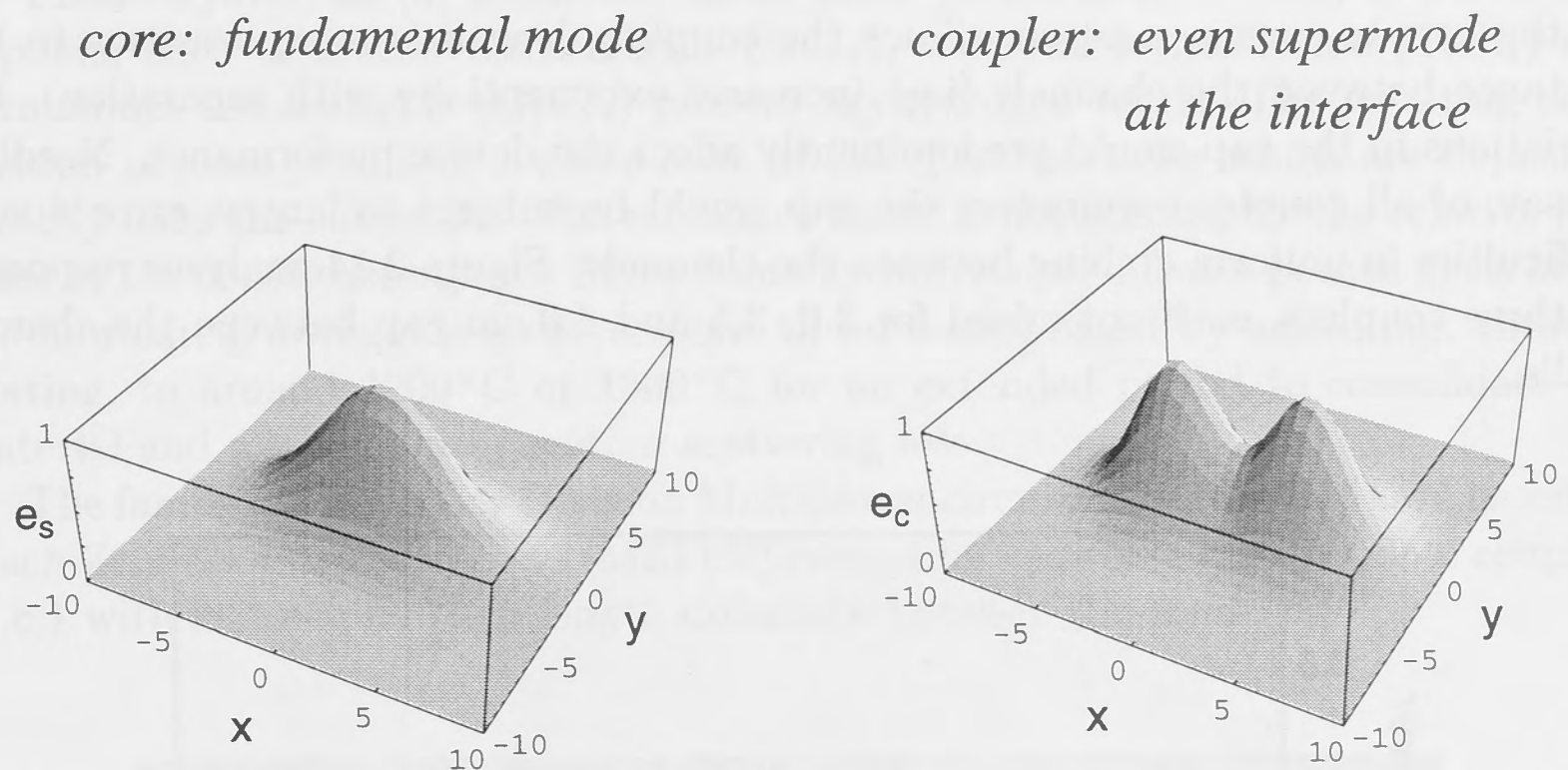


Figure 2.13: Field distributions of a fundamental even mode of the central core and the first even supermode of the two-core coupler at the interface. Horizontal scales are in microns, vertical scale uses arbitrary units.

The incident even supermode of the coupler excites the even fundamental mode of the central single-core section, whereas the odd supermode excites the odd second mode. The mismatch in the core geometries at the interface partially reflects and partially transmits the incident modal field. Using FDM analysis (by approximating trapezoidal cores by sets of rectangles), the fraction of incident power transmitted at each interface was determined via [28]:

$$\frac{P_s}{P_c} = \frac{\left(\int_{A_\infty} e_c e_s dA \right)^2}{\int_{A_\infty} e_c^2 dA \int_{A_\infty} e_s^2 dA}, \quad (2.30)$$

where P_c is the incident power in the supermode of the coupler before the interface, P_s is the power transmitted to the corresponding mode of the single-core central

section after the interface, A_∞ is the infinite cross-section and e_c and e_s are the solutions of the scalar wave equation for the transverse electric field dependence for the coupler and the single central core, respectively. The overlap integral between the two modes is evaluated at the interfaces AA' and BB'.

For the parameters of the design 2.12, the fraction of power entering the straight section at AA' was $P_s/P_c = 0.842$ and $P_s/P_c = 0.991$ for the even supermode and odd supermode of the coupler, respectively. Because of the symmetry, the same ratio would apply at the second interface BB'. A loss of 17% at each interface is significant; therefore only the first coupler design shown in Fig. 2.11 was found to be suitable.

Coupler response has been also verified with respect to variations in the value of the core-to-core separation. Since the coupling length is most sensitive to the distance between the channels (i.e. increases exponentially with separation), the variations in the gap would predominantly affect the device performance. Needless to say, of all coupler parameters the gap would be subject to largest error due to difficulties in uniform etching between the channels. Figure 2.14 analyses responses of three couplers, each optimised for 3.0, 3.5 and 4.0 μm gap between the channel walls.

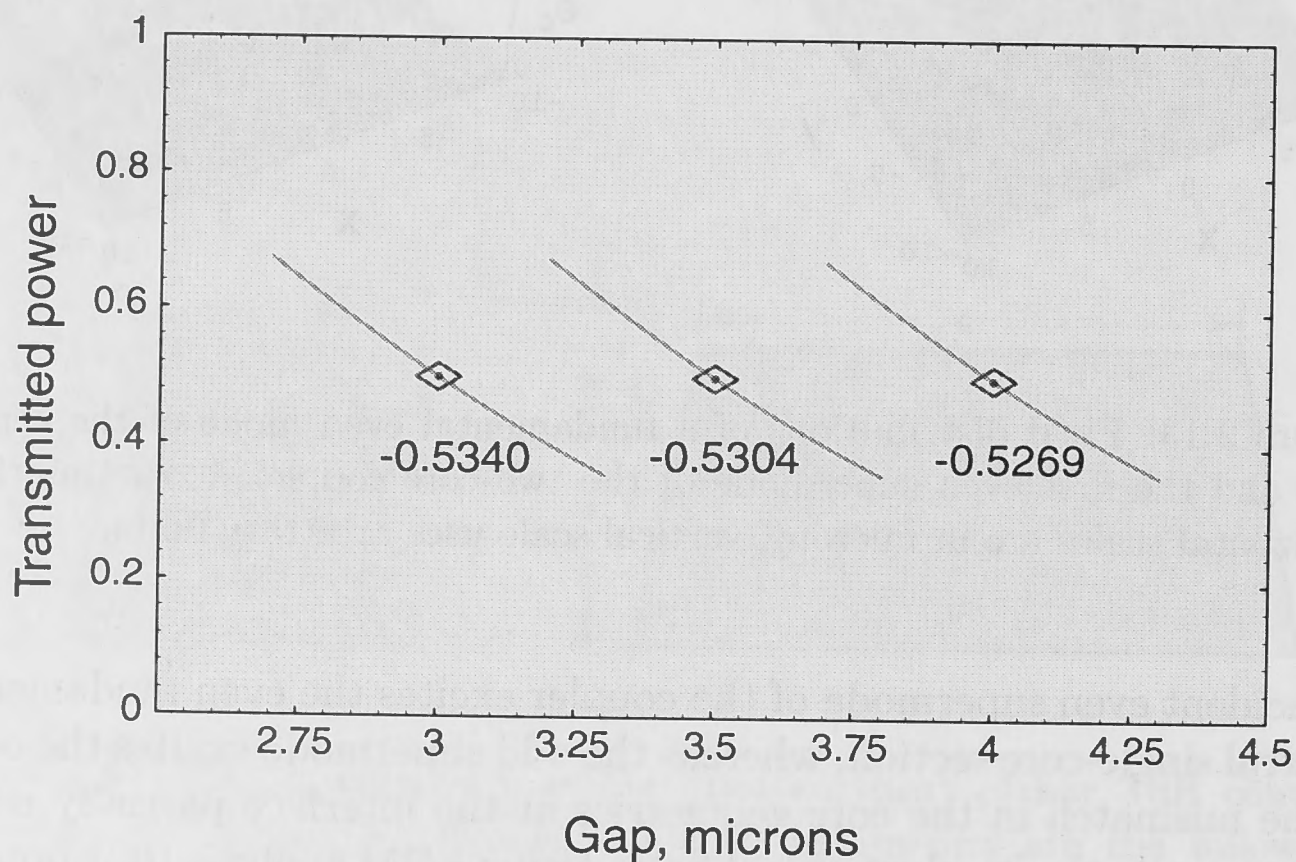


Figure 2.14: Coupler responses as a function of gap g between the channel walls. Three curves correspond to three different couplers, optimised for $g = 3.0, 3.5$ and $4.0 \mu\text{m}$, respectively. Diamonds correspond to exact 50% splitting ratios at prescribed values of g , the slope's value reflects the degree of sensitivity to variations in g .

Assuming average fabrication error of the order of $0.1 \mu\text{m}$, corresponding slopes of transmitted power vs. gap were calculated using Fourier Decomposition Method.

Negative numbers beneath each slope represent values of derivatives with respect to separation, the largest absolute number highlighting the most sensitive design. The estimated departures from an exact 50% splitting ratio are quantified in Fig. 2.14, showing no significant advantages of having larger separation. Therefore, the design with the smallest feasible gap (providing shorter coupling length) has been incorporated into the mask for the planar dispersion compensator.

2.7.2 Designs based on the flame hydrolysis fabrication technique.

Flame hydrolysis [3] generates small glass particles by feeding a mixture of vapours, such as silicon tetrachloride (SiCl_4), titanium tetrachloride (TiCl_4) and germanium tetrachloride (GeCl_4) into an oxyhydrogen torch. The resulting combustion process produces a white soot of fine glass particles which are deposited directly onto the substrate. The refractive index is determined by the relative flow rates of the constituent gases. Since flame hydrolysis produces a porous glass layer, the fabricated waveguide structure has to be consolidated by annealing, through heating, to around 1200°C or 1300°C for an extended period to consolidate the material and minimise propagation scattering loss.

The family of Frequency Division Multiplexer circuits (see Fig. 2.15) are based on Mach-Zehnder interferometers (MZ) [32] consisting of two 3 dB directional couplers (d.c.) with an unequal path length difference between the arms.

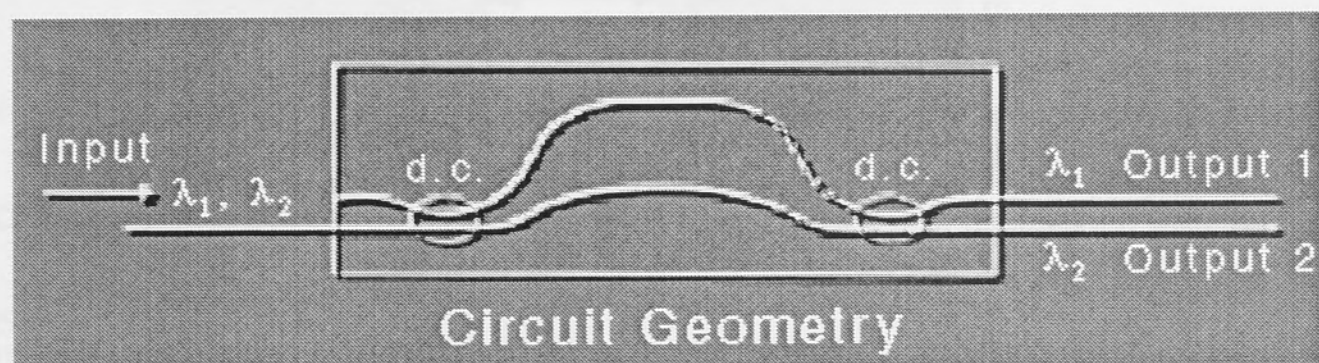


Figure 2.15: Schematics of a Frequency Division Multiplexer circuit. λ_1 and λ_2 are the different channel wavelengths.

The devices function as multi-demultiplexers for nanometre order channel spacings. Half-wavelength plates can be hybridised into the waveguide arms to eliminate polarisation dependency. A set of devices (mostly Mach-Zehnder interferometers), based on the 3 dB coupler design in Figure 2.16, have been made in collaboration with Telstra Research Laboratories at Photonic Integration Research, Inc. (PIRI), using their foundry service.

A so-called *high delta* PIRI material was used for the devices because of its uniformity and low loss. The optimisation program, based on the Fourier Decomposition Method, was modified for a square core geometry and PIRI refractive index values.

Since 2 – 3 microns trench spacing was the fabrication limit and the length of the coupling region was not critical, coupling arm spacing could be traded off for length. The first round of devices was designed for 1.55 microns operating wavelength and have been used in test bed experiments at Telstra Research Laboratories.

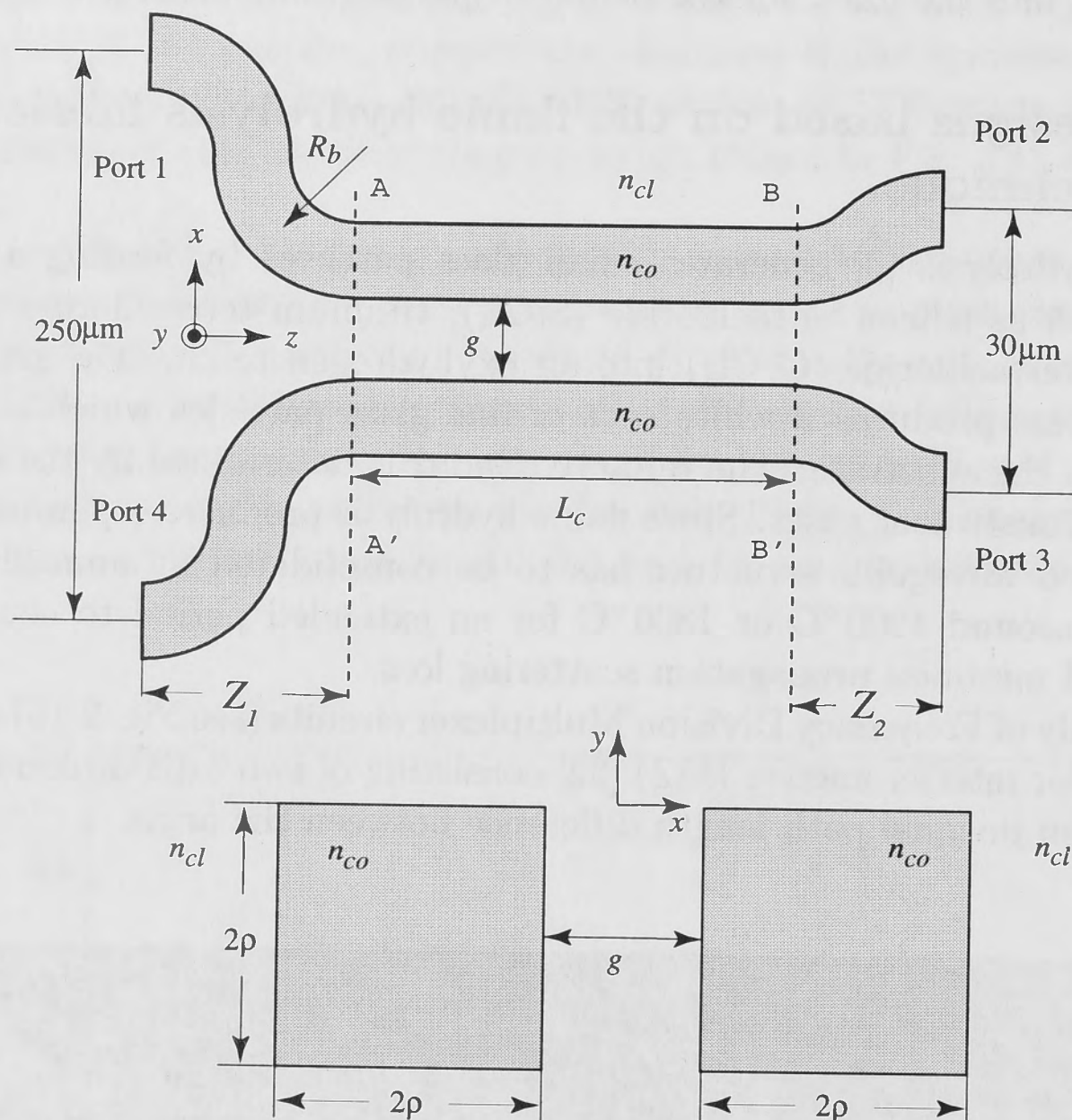


Figure 2.16: 3 dB coupler design and parameters for the high delta PIRI material. Device parameters are the following: $\lambda = 1.55\ \mu\text{m}$, $n_{co} = 1.454$, $n_{cl} = 1.444$, $\rho = 3.0\ \mu\text{m}$, $R_b = 50.0\ \text{mm}$, $g = 3.6\ \mu\text{m}$, $L_c = 505.6\ \mu\text{m}$, $Z_1 = 4.9031\ \text{mm}$, $Z_2 = 1.4283\ \text{mm}$.

Several Mach-Zehnders have been produced on a single chip. A round wafer shown in Fig. 2.17 accommodated four masks: C1 and C5 had 1 MZ each, R1 and R2 had 8 a piece. Fig. 2.18 includes some data on the extinction of the balanced MZ's. The trend is fairly convincing: the devices in the centre are the best, closer to the edge the performance (deviation of a coupler from 3 dB) degrades rapidly. This appeared to be due to the wafer's radial non-uniformity. The devices in the centre were very close to 3 dB (off by $\simeq 0.4\ \text{dB}$) which is suitable. The best extinction for a Mach-Zehnder (again in the centre) was $\simeq 20\ \text{dB}$.

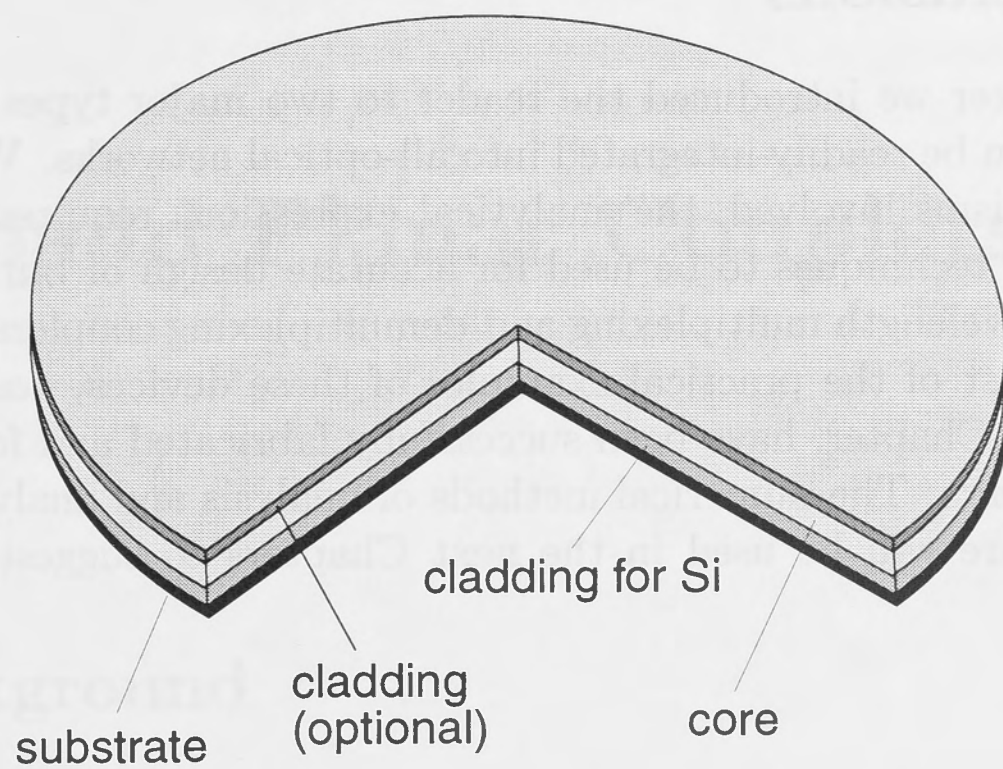


Figure 2.17: PIRI wafer geometry.

Variation of extinction ratio for Balanced Mach-Zehnder
 $cl=491$

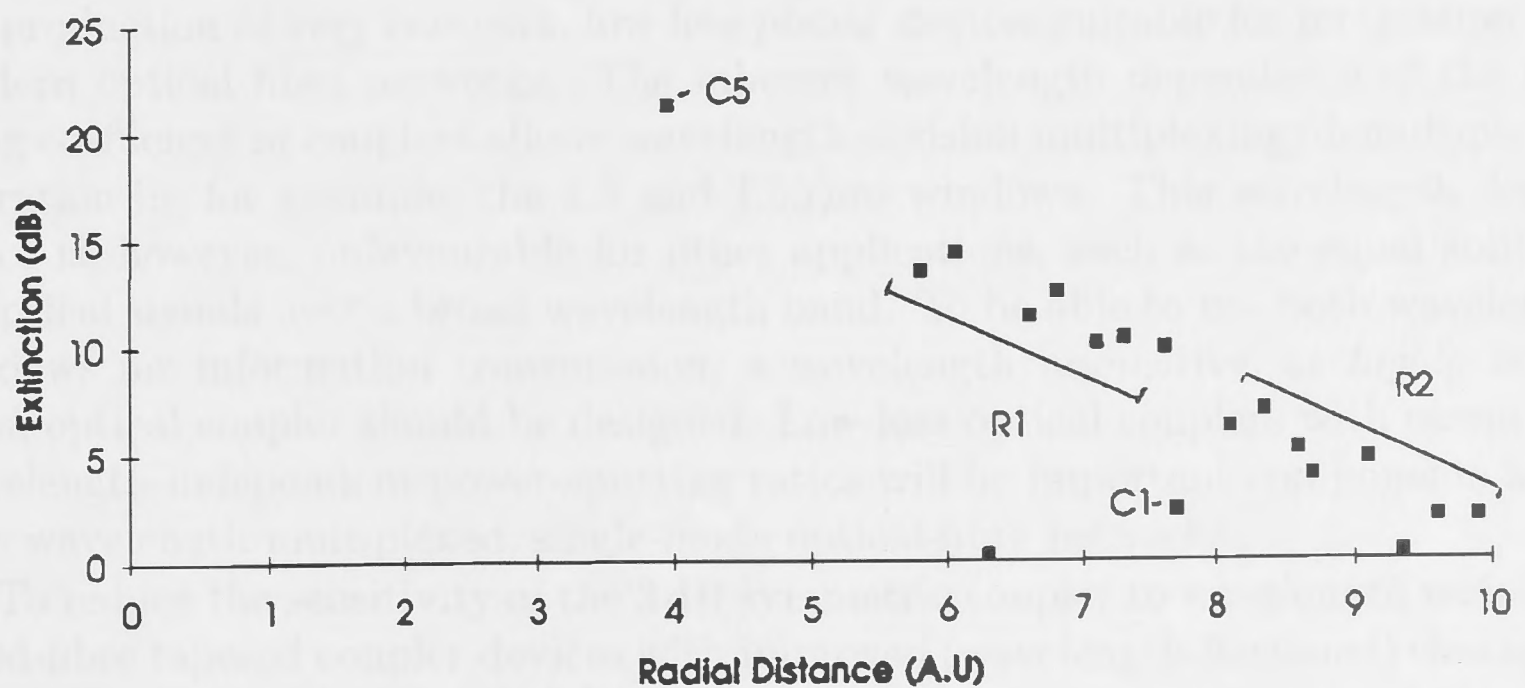


Figure 2.18: Extinction ratios of the balanced Mach-Zehnder interferometers vs distance across the wafer. Labels denote four masks: C1 and C5 had 1 MZ each, R1 and R2 had 8 a piece.

2.8 Conclusions

In this Chapter we introduced the reader to two major types of linear optical devices which can be readily integrated into all-optical networks. We delineated the physical mechanisms involved, the analytical expressions required and the appropriate numerical techniques to be used for accurate design of buried channel 3dB couplers, and wavelength multiplexing and demultiplexing couplers. It is important to note, that most of the practical examples of these devices, designed by us and described in this Chapter, have been successfully fabricated and found their use in further experiments. The numerical methods of analysis and analytical approaches demonstrated here will be used in the next Chapters to suggest and investigate novel devices.

Broadband Planar Couplers

3.1 Background

Advances in information and communications technology, especially broadband communication, are leading to “multimedia” equipment and applications, combining two-way exchanges of data in the form of television-type images carried optically at 1.55 microns wavelength as well as more conventional electronic information transmitted at 1.3 microns wavelength. Many of the information services have originated on traditional “*narrowband*” telecommunications networks, but have the potential to be enhanced using broadband networks. “*Broadband*” simply means a network capable of transferring large amounts of information quickly, ideally in both directions.

As it has been demonstrated in the previous Chapter, recent advances in the development of buried channel waveguide (BCW) technology have made possible the production of very compact, low-loss planar devices suitable for integration into modern optical fibre networks. The inherent wavelength dependence of the coupling coefficient in couplers allows wavelength-division multiplexing/demultiplexing operation in, for example, the 1.3 and 1.55 μm windows. This wavelength dependence is, however, unfavourable for other applications, such as the equal splitting of optical signals over a broad wavelength band. To be able to use both wavelength windows for information transmission, a wavelength insensitive, or *highly broadband*, optical coupler should be designed. Low-loss optical couplers with essentially wavelength-independent power-splitting ratios will be important components in future wavelength-multiplexed, single-mode optical-fibre networks.

To reduce the sensitivity of the 3 dB symmetric coupler to wavelength variation, fused-fibre tapered coupler devices with improved (wavelength-flattened) characteristics have been reported [33, 34]. The broader response is achieved by fusing and pulling two fibres with slightly different diameters or by using a slightly unbalanced all-fiber Mach-Zehnder interferometer made with identical single-mode fibers. This technique has some limitations in terms of control over the fabricated coupler shape and suitability for integrated optical circuitry. Broadband evanescent couplers have also been developed using buried channel waveguide (BCW) technology [4, 35, 36] but their wavelength-flattened characteristics are still far from ideal, with typical power-splitting ratios of $50\% \pm 5\%$ over the wavelength range 1.3 to 1.55 μm [4]. In

this Chapter we will demonstrate how the spectral dependence of the coupling coefficient can be used to significantly improve the wavelength-flattened characteristics of symmetric and asymmetric BCW directional couplers [37, 38].

3.2 BCW wavelength-flattening strategies

We begin by considering the BCW directional coupler shown schematically in Figure 3.1. The coupler comprises two cores with the curved input/output arms of constant bend radius, R_b , which lead to a uniform central region of length L_c and centre-to-centre core separation d . A step refractive-index profile is assumed with core and cladding indices n_{co} and n_{cl} , respectively. In general, the coupler design should take into account the contribution to coupling from the curved input and output arms, as well as from the central region where the coupling is strongest. Furthermore, the bend radius, R_b , should be large enough to avoid significant bend loss and the coupler should operate in the two-moded régime (see Section 3.2.3). We include all these considerations in our analysis in Section 3.3.

To begin with, however, we concentrate on the uniform coupling region in Figure 3.1(a) which is delineated by the lines AA' and BB'. Figure 3.1(b) shows the cross-sectional geometry of the asymmetric coupler within this region. The two waveguide cores are rectangular in cross-section and are assumed to be single-moded in isolation. They have a common height 2ρ , which is dictated by the deposition and etching PECVD fabrication process used at the Australian National University [25], while the respective widths of core 1 and core 2 are $2\rho_1$ and $2\rho_2$. We also define the width-to-height, or core aspect ratios as $\varepsilon_1 = \rho_1/\rho$ and $\varepsilon_2 = \rho_2/\rho$, respectively.

The coupling between two parallel, uniform waveguides of arbitrary cross-section and refractive-index profile is well understood and can be described using either coupled-mode theory [5, Sectn. 29–2] or the supermode approach [5, Sectn. 18–12]. With reference to Figure 3.1, if the excitation conditions are such that unit power is launched into port 1 and zero power is launched into port 4 at AA' ($z = 0$), the fractional powers exiting ports 2 and 3 at BB' ($z = L_c$) are described by the analytical expressions:

$$P_2 = 1 - F^2 \sin^2 \phi, \quad (3.1a)$$

$$P_3 = F^2 \sin^2 \phi, \quad (3.1b)$$

where

$$\phi = \frac{CL_c}{F} = \left(\frac{\beta_+ - \beta_-}{2} \right) L_c, \quad (3.2)$$

and

$$F^2 = 1 - \left(\frac{\beta_1 - \beta_2}{\beta_+ - \beta_-} \right)^2. \quad (3.3)$$

Here, β_1 and β_2 denote the propagation constants of the fundamental modes of cores 1 and 2 in isolation, respectively, while β_+ and β_- are the propagation constants of the two (orthogonal) supermodes of the composite twin-core waveguide.

The parameter F^2 represents the maximum fractional power transfer between cores and the coupling coefficient, C , decreases exponentially with increasing core separation.

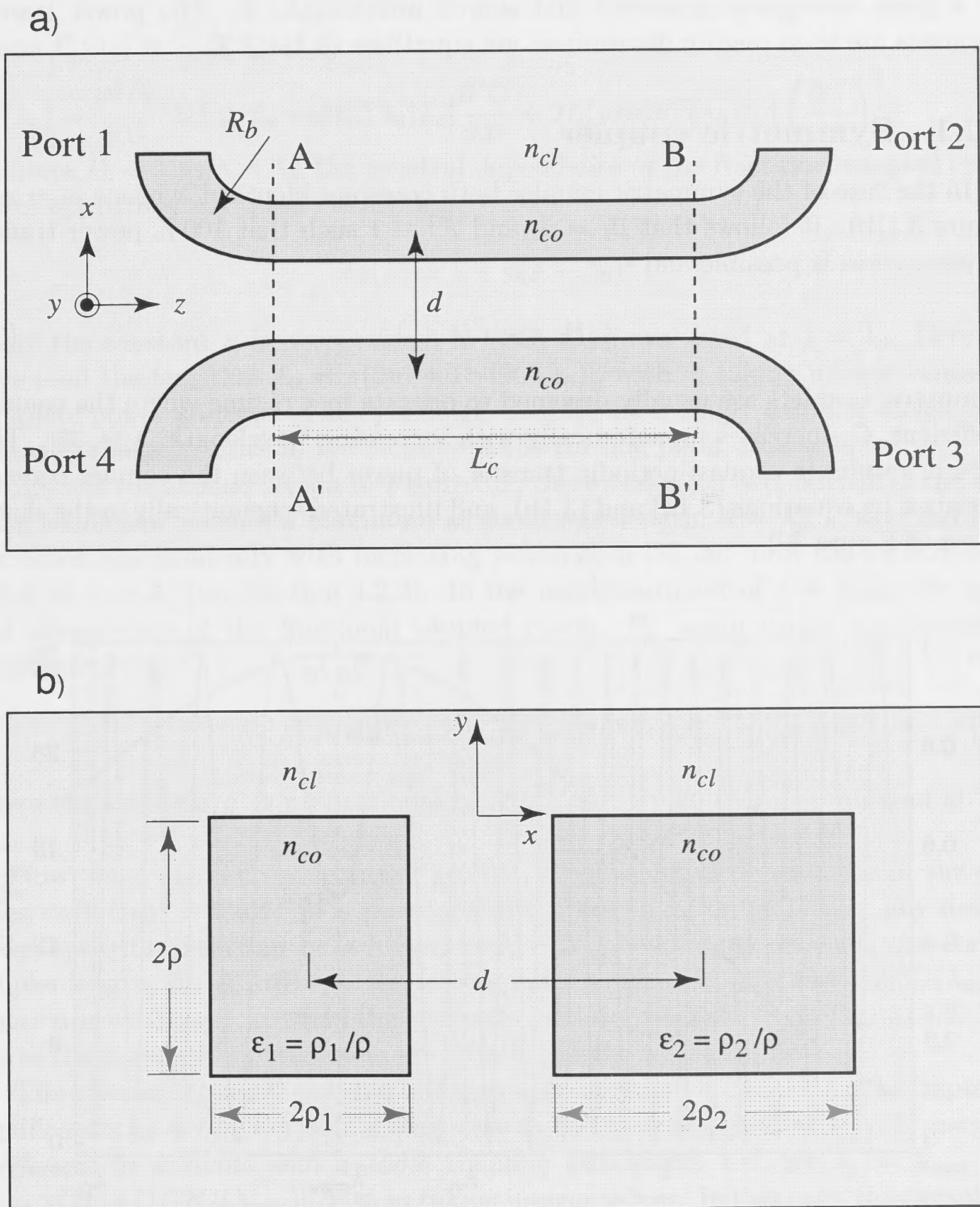


Figure 3.1: (a) Schematic diagram of a planar evanescent coupler showing the curved input/output arms leading to a uniform central coupling region. (b) Cross-sectional geometry of an asymmetric directional coupler in the mid-waist coupling region.

It should be noted that each of these parameters are wavelength-dependent and the waveguide cores are assumed to be similar in the above formulation. If the cores are not sufficiently similar, then negligible coupling will occur.

Throughout this Chapter, we use the Fourier Decomposition Method (FDM) (see Chapter 2), described in Appendix A.1, to calculate β_+ , β_- , β_1 and β_2 numerically for a given waveguide geometry and source wavelength, λ . The power transfer dynamics are then readily determined via equations (3.1)–(3.3).

3.2.1 Symmetric coupler

In the case of the symmetric coupler both cores are identical, whence $\rho_1 = \rho_2$ in Figure 3.1(b). It follows that $\beta_1 = \beta_2$ and $F^2 \equiv 1$ such that 100% power transfer between cores is possible and

$$P_3 = \sin^2(CL_c). \quad (3.4)$$

Symmetric couplers are usually designed to operate in a régime where the coupling coefficient, C , increases monotonically with increasing wavelength, λ [4, 35]. This, in turn, results in a quasi-periodic transfer of power between the coupler cores, as described by equations (3.1a) and (3.1b), and illustrated schematically in the shaded region of Figure 3.2.

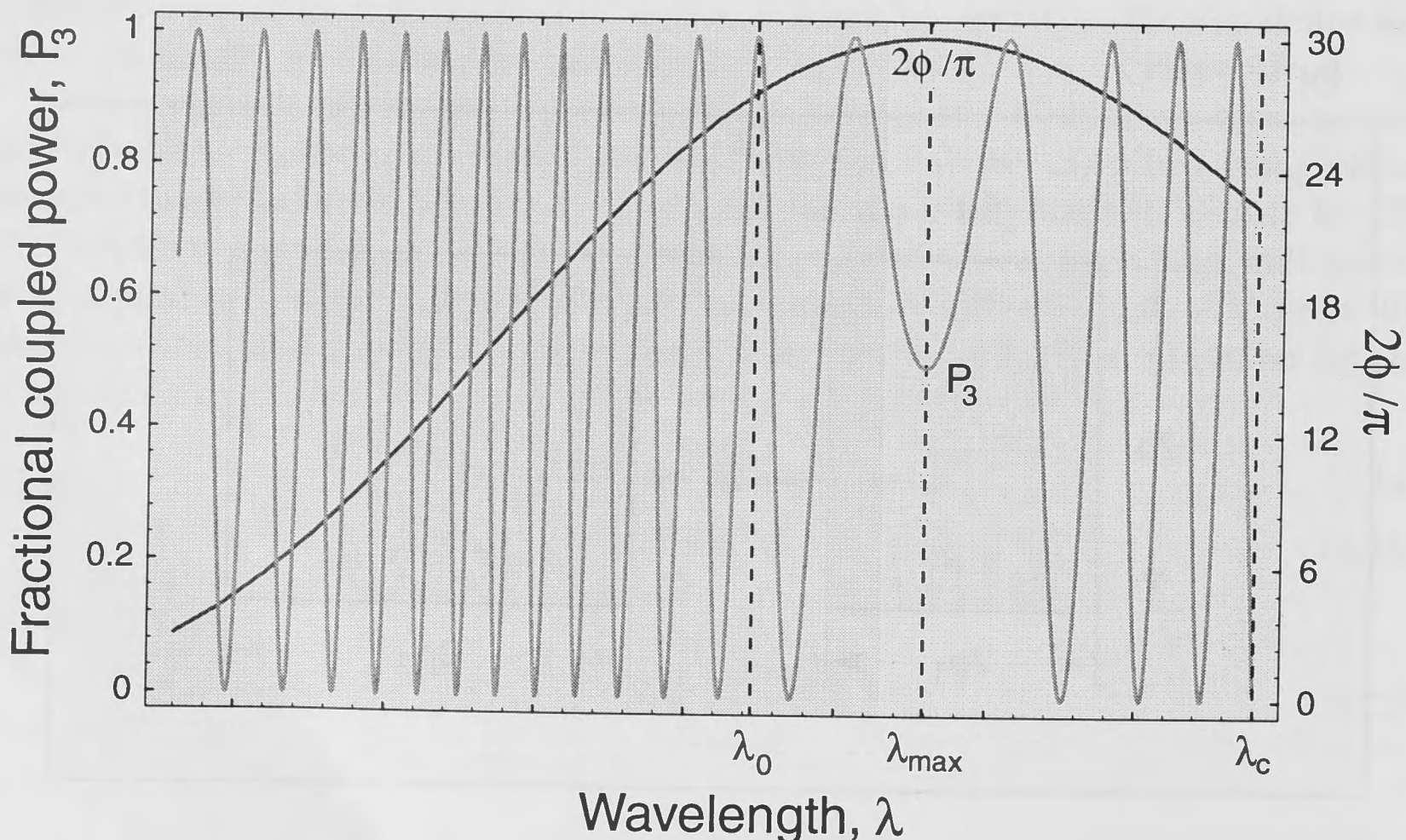


Figure 3.2: Schematic showing the spectral dependence of the fractional coupled power, P_3 (oscillating curve), and the parameter $2\phi/\pi$ (slowly-varying curve) for a uniform symmetric coupler.

Expanding P_3 in Taylor series in the vicinity of the 100% coupling wavelength $\lambda = \lambda_0$, we obtain

$$P_3(\lambda) = P_3(\lambda_0) + P_3'(\lambda_0)(\lambda - \lambda_0) + \frac{1}{2}P_3''(\lambda_0)(\lambda - \lambda_0)^2 + \dots, \quad (3.5)$$

where $P_3'(\lambda_0) = \frac{\partial P_3}{\partial \lambda}(\lambda_0) = 0$, and

$$P_3''(\lambda_0) = \frac{\partial^2 P_3}{\partial \lambda^2}(\lambda_0) = L_c \sin[2C(\lambda_0)L_c] \frac{\partial^2 C}{\partial \lambda^2} + 2L_c^2 \cos[2C(\lambda_0)L_c] \left(\frac{\partial C}{\partial \lambda} \right)^2.$$

Since $P_3 = 1$ at $\lambda = \lambda_0$, the spectral dependence of the fractional coupled power varies approximately quadratically as:

$$P_3(\lambda) \simeq 1 - \kappa(\lambda - \lambda_0)^2, \quad (3.6)$$

where the constant κ is proportional to $(\partial C/\partial \lambda)^2$, evaluated at $\lambda = \lambda_0$. Here, we have used the fact that $L_c = \pi(2m+1)/[2C(\lambda_0)]$, with m taking integer values for complete power transfer. The symmetric coupler accordingly exhibits wavelength-flattened characteristics in the vicinity of the turning point at $\lambda = \lambda_0$.

Beyond the shaded region in Figure 3.2, the wavelength dependence of the coupling coefficient reaches a maximum at some wavelength, $\lambda = \lambda_{\max}$, say, and then decreases monotonically with increasing wavelength [36, 39] until the second-mode cutoff at $\lambda = \lambda_c$ (see Section 3.2.3). In the neighbourhood of $\lambda = \lambda_{\max}$, the spectral dependence of the fractional coupled power, P_3 , again varies approximately quadratically as:

$$P_3(\lambda) \simeq \sin^2[C(\lambda_{\max})L_c] + \sigma(\lambda - \lambda_{\max})^2, \quad (3.7)$$

where the constant σ is proportional to $(\partial^2 C/\partial \lambda^2) \sin[2C(\lambda)L_c]$, evaluated at $\lambda = \lambda_{\max}$.

Now, for a given cross-sectional geometry, the spectral dependence of the coupling coefficient is fixed. It is therefore clear from equation (3.7) that any desired power-splitting ratio can be achieved at $\lambda = \lambda_{\max}$ by simply choosing the correct coupler length, L_c . A 3 dB splitter, for example, requires $L_c = \pi(2n+1)/[4C(\lambda_{\max})]$, where n is an integer, to yield the spectral characteristics shown in Figure 3.3. Values of the simulation parameters are detailed in the figure caption.

The wavelength-flattened characteristics of a symmetric coupler can be improved significantly by *arranging for the maximum in the spectral dependence of the coupling coefficient to coincide with a 100% coupling wavelength*, i.e., for $\lambda_0 = \lambda_{\max}$ and $L_c = \pi(2m+1)/[2C(\lambda_{\max})]$, with m taking integer values. In this case, the parameter $\kappa = 0$ in equation (3.6) and the spectral dependence of the fractional coupled power, P_3 , now exhibits a *quartic behaviour*:

$$\boxed{P_3(\lambda) = 1 - \mu(\lambda - \lambda_0)^4}, \quad (3.8)$$

where the constant μ is proportional to $(\partial^2 C/\partial \lambda^2)^2$, evaluated at $\lambda = \lambda_0 = \lambda_{\max}$.

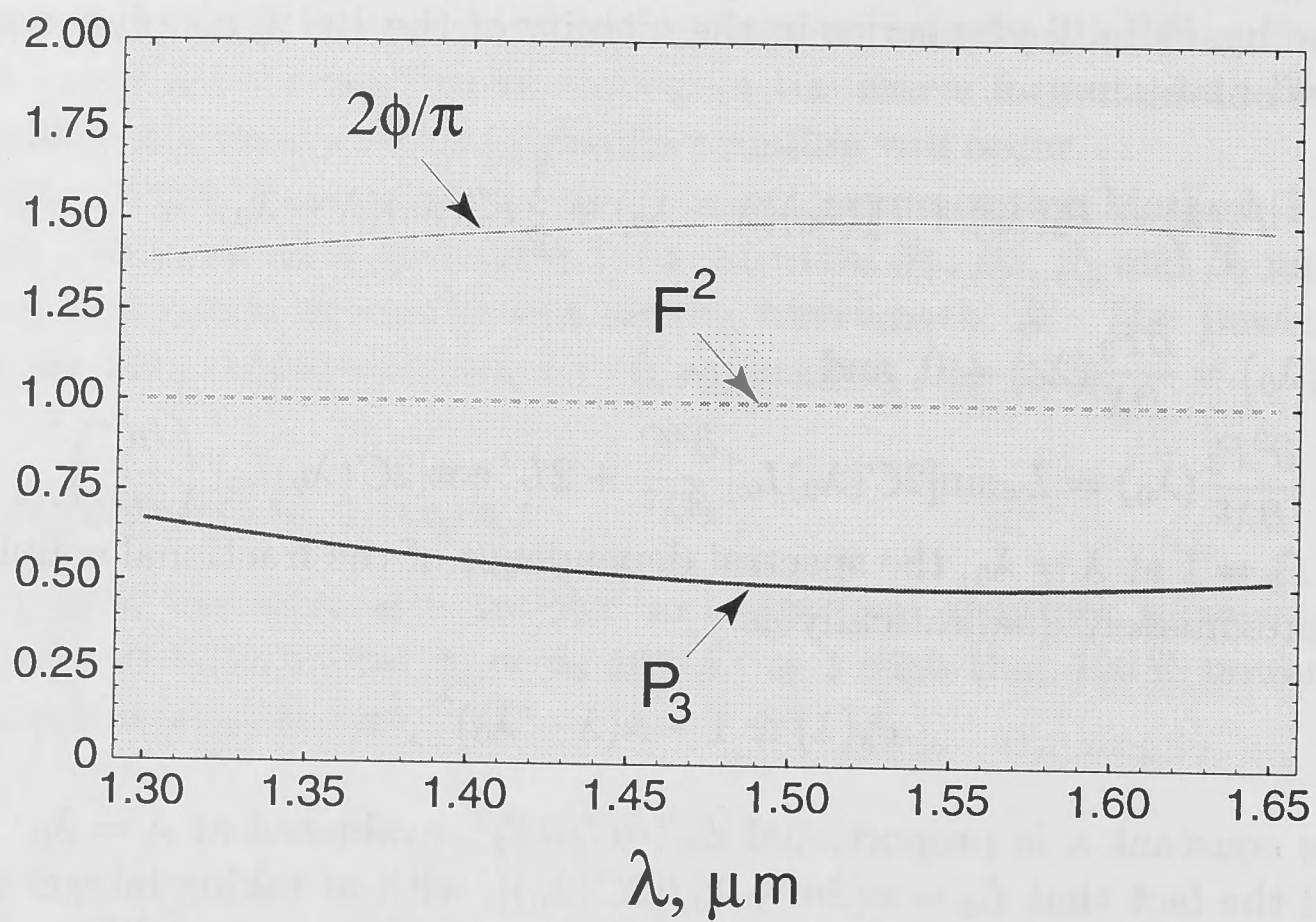


Figure 3.3: Spectral dependence of the fractional coupled power, P_3 , and the parameters F^2 and $2\phi/\pi$ for a uniform symmetric 3 dB splitter in the $1.55 \mu\text{m}$ window. The simulation parameters correspond to: $\Delta = [1 - (n_{cl}/n_{co})^2]/2 = 0.003$, $n_{cl} = 1.447$, $\rho_1 = \rho_2 = \rho = 2.9 \mu\text{m}$, $L_c = 3\pi/[4C(1.55)] = 0.997 \text{ mm}$ and $d = 7.25 \mu\text{m}$.

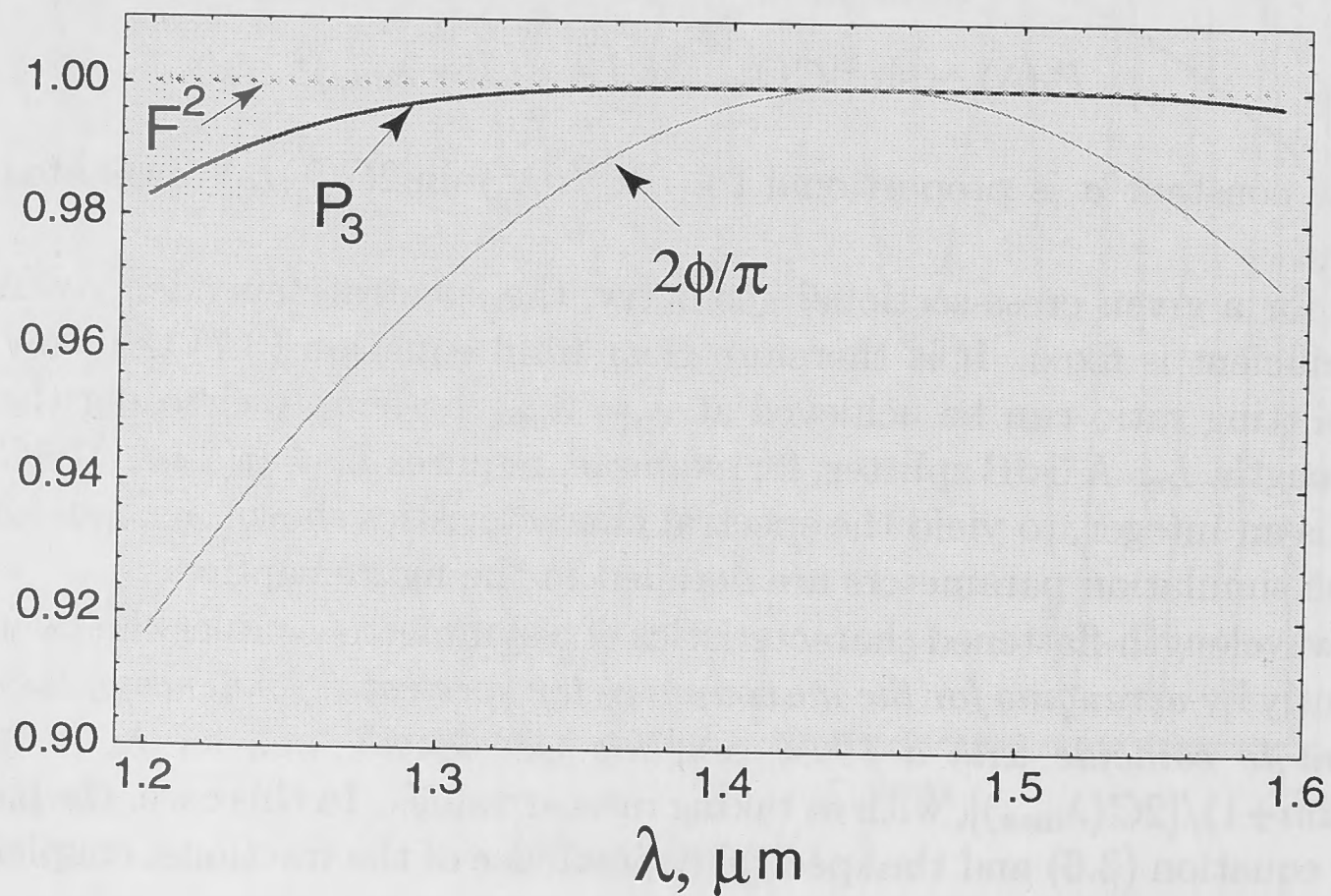


Figure 3.4: Spectral dependence of the fractional coupled power, P_3 , and the parameters F^2 and $2\phi/\pi$ for a *broadband* symmetric coupler with 100% power transfer. The simulation parameters correspond to: $\Delta = 0.003$, $n_{cl} = 1.447$, $\rho_1 = \rho_2 = \rho = 2.7 \mu\text{m}$, $L_c = 0.6164 \text{ mm}$ and $d = 6.75 \mu\text{m}$.

As a result, the 100% coupling region is considerably more flattened, as illustrated in Figure 3.4 where we present the spectral characteristics of a typical broadband symmetric coupler, or *dropping filter*. Values of the simulation parameters are detailed in the figure caption. The power-splitting ratio exhibits a departure of only 0.6% from 100% over the broadband wavelength range 1.26 – 1.59 μm .

The realisation of such a coupler in practice, like the designs in Section 2.7, would have to take account of fluctuations in the fabrication parameters and possibly temperature effects.

3.2.2 Asymmetric coupler

Conventional symmetric, single-mode couplers have a maximum wavelength sensitivity at precisely those wavelengths where 50% coupling occurs and are thus, in general, unsuitable as broadband 3 dB power splitters. To reduce this sensitivity to wavelength, slightly asymmetric fused-fibre tapered couplers have been developed [33] which can provide approximately 3 dB splitting over the 1.3 and/or 1.55 μm windows. Asymmetric BCW couplers have also been designed and fabricated with comparable spectral responses to their fused-fibre counterparts [4, 35].

The basic principle behind asymmetric coupler design is to detune the symmetric coupler by making its component cores slightly different, as illustrated in Figure 3.1(b). This can be achieved by changing the cross-sectional geometry, refractive index profile, or both, but the difference between β_1 and β_2 in equation (3.3) must be sufficiently small to permit power transfer between the cores over reasonable lengths. In the case of an asymmetric-coupler 3 dB splitter, for example, all the light entering port 1 is to be split equally at the output ports 2 and 3 in the vicinity of some wavelength $\lambda = \lambda_0$, say. This condition is conventionally achieved by designing the coupler such that, in the vicinity of $\lambda = \lambda_0$, $F^2 \simeq 1/2$ and $\sin^2 \phi \simeq 1$ in equations (1)–(3.3). Figure 3.5 illustrates the spectral characteristics of such a 3 dB splitter in the 1.3 μm window. Values of the simulation parameters are detailed in the figure caption.

As in previously reported designs [4, 33, 35], the parameters F^2 and $2\phi/\pi$ are monotonically increasing functions of wavelength. Typical power-splitting ratios of $50\% \pm 5\%$ are then readily achieved over a 0.25 μm wavelength band [4]. However, *by taking advantage of the maximum that occurs in the parameter ϕ when the BCW cores are in close proximity, this range can be significantly broadened to yield a much flatter wavelength response* [37, 38].

This claim is demonstrated in Figure 3.6 where, in the neighbourhood of the peak value of ϕ , the term $\sin^2 \phi$ has a parabolic variation with increasing wavelength, while F^2 is monotonic increasing. By judicious choice of parameter values, it is possible to combine these spectral characteristics to produce a *quasi-cubic* dependence of the power-splitting ratio, P_3 , as illustrated in Figure 3.6. This shows a wavelength-flattened response with a variation of only 1.2% over the range 1.15 – 1.69 μm . Values of the simulation parameters are detailed in the figure caption.

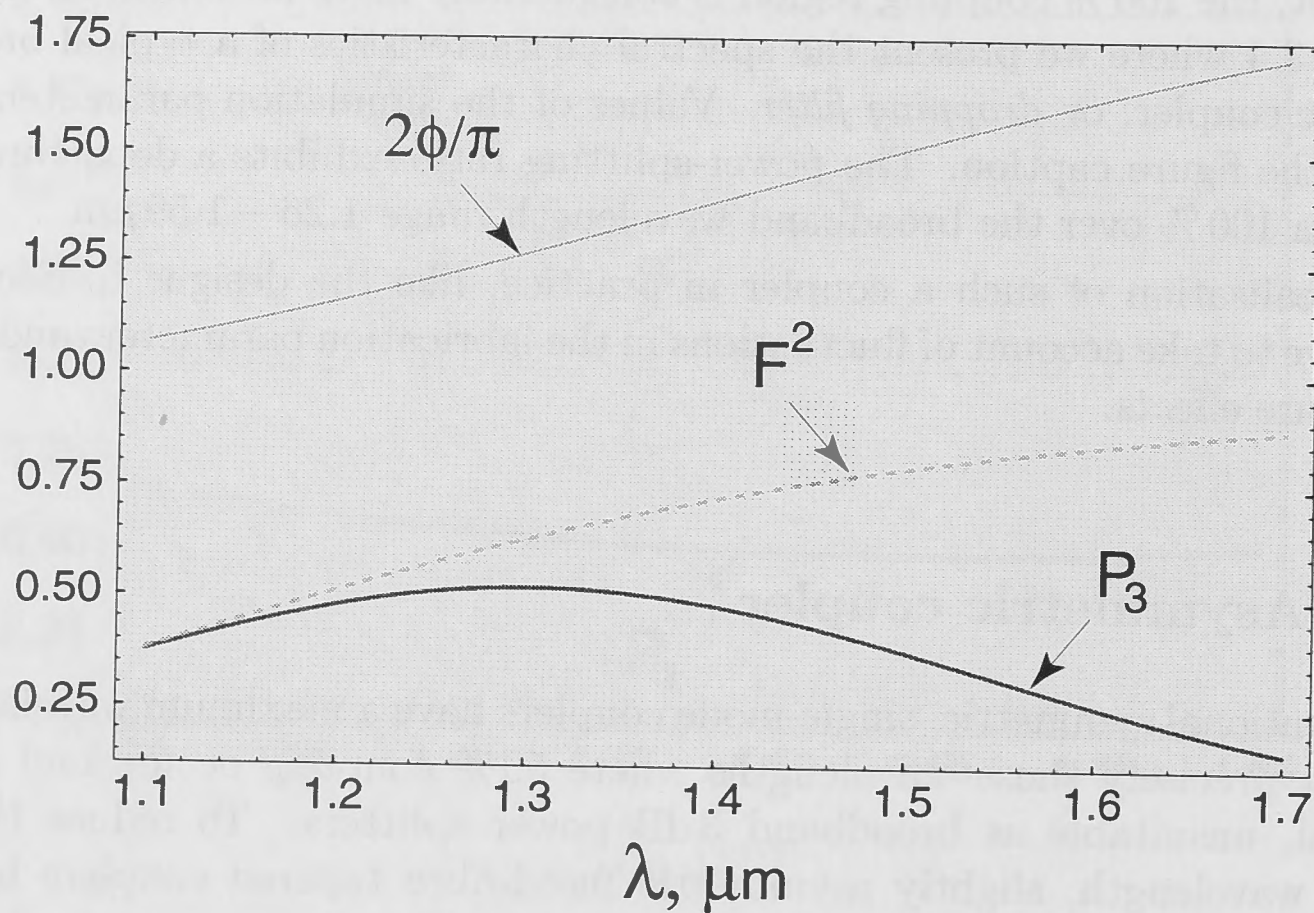


Figure 3.5: Spectral dependence of the fractional coupled power, P_3 , and the parameters F^2 and $2\phi/\pi$ for a conventional asymmetric-coupler 3 dB splitter in the $1.3 \mu\text{m}$ window. The simulation parameters correspond to: $\Delta = 0.003$, $n_{cl} = 1.447$, $\rho_1 = \rho = 3.6 \mu\text{m}$, $\rho_2 = 3.0 \mu\text{m}$, $L_c = 1.935 \text{ mm}$ and $d = 10.23 \mu\text{m}$.

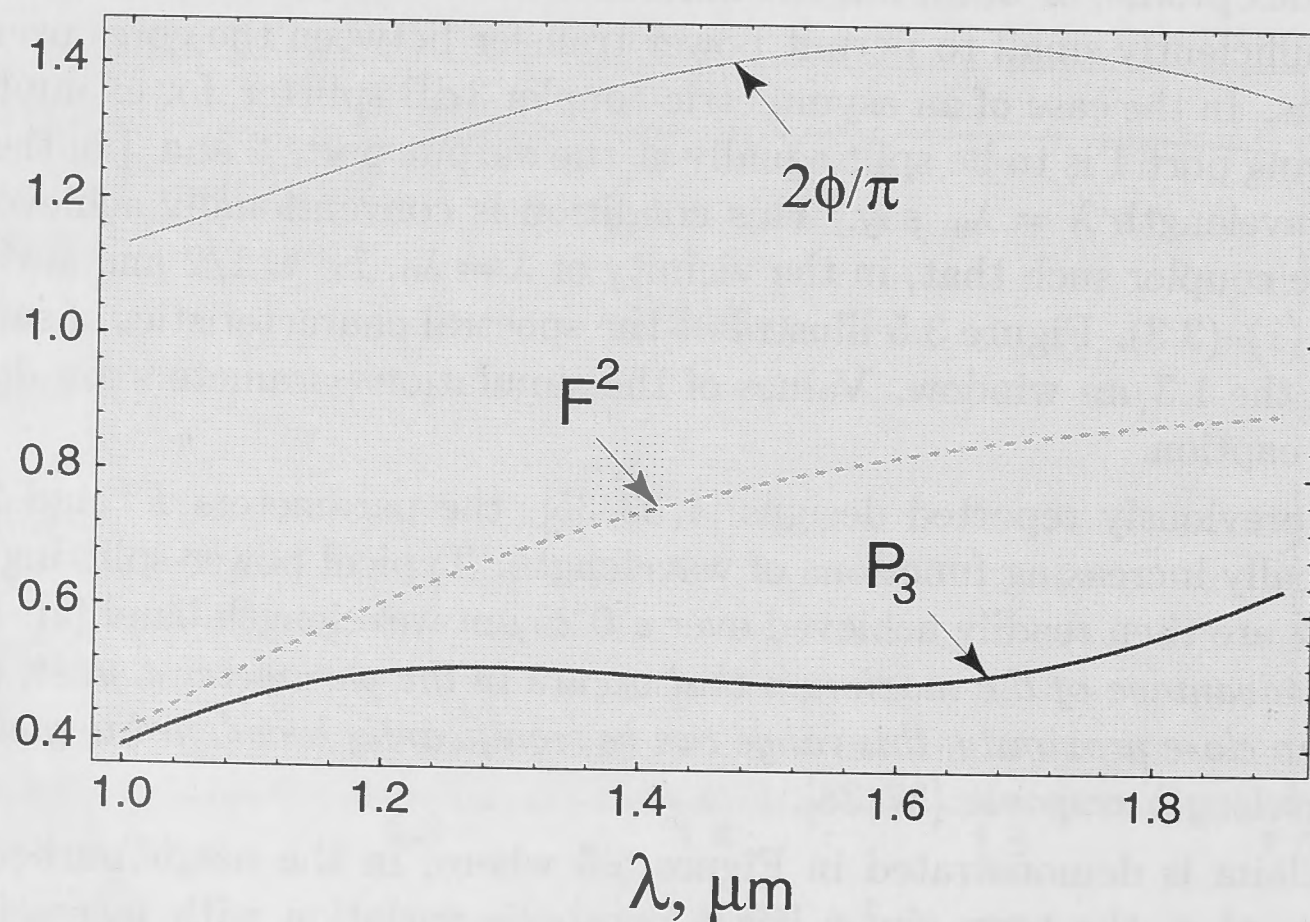


Figure 3.6: Spectral dependence of the fractional coupled power, P_3 , and the parameters F^2 and $2\phi/\pi$ for a broadband 3 dB splitter with a *quasi-cubic* spectral dependence. The simulation parameters correspond to: $\Delta = 0.003$, $n_{cl} = 1.447$, $\rho_1 = \rho = 3.6 \mu\text{m}$, $\rho_2 = 2.5 \mu\text{m}$, $L_c = 0.9106 \text{ mm}$ and $d = 7.63 \mu\text{m}$.

3.2.3 Second-mode cutoff

The fundamental supermode of a composite twin-core waveguide will propagate for any value of source wavelength when the refractive-index profile throughout both cores is higher than the surrounding cladding index, i.e., when the waveguide has a matched cladding. In contrast, *the second mode will always have a finite cutoff wavelength* [40, 41] by analogy with the second mode of a single-core optical fibre or buried channel waveguide. *This cutoff wavelength, λ_c , is a critical parameter in the design of planar, evanescent couplers operating in the two-moded régime.* Since no exact analytical solution is available for square- or rectangular-core couplers, approximate analytical expressions [42] or numerical techniques must accordingly be employed.

Although the Fourier Decomposition Method used in the preceding Sections is particularly suited for analysis of rectangular-core or layered waveguides, it only can be used to calculate modal field distributions that are reasonably well confined to the core region, i.e. sufficiently far above cutoff. As cutoff is approached when the modal effective index $n_{\text{eff}} = \beta/k$ becomes similar to the cladding refractive index n_{cl} , the modal field spreads farther into the cladding and the implicit assumption of zero field at the domain boundary (see Appendix A.1 for details) requires a prohibitively large bounding box. This drastically increases the computation time and memory requirements to achieve satisfactory convergence. In this Section we use the Modified version of the Fourier Decomposition Method (MFDM) [43] which is accurate down to and including modal cutoff. The need for an artificial bounding box is avoided in MFDM by mapping the whole (x, y) plane onto the unit square by means of a suitable transformation [28].

The second-mode cutoff V -value, V_c , is calculated numerically for the waveguide illustrated in Figure 3.1(b). This parameter is directly related to the cutoff wavelength, λ_c , via the expression [42]:

$$V_c = \frac{2\pi\bar{\rho}}{\lambda_c} \sqrt{n_{\text{co}}^2 - n_{\text{cl}}^2}, \quad (3.9)$$

where $\bar{\rho}$ is chosen to be a representative dimension of the waveguide under consideration. For presentation purposes, we introduce the normalised core separation, $D = 2d/(\rho_1 + \rho_2)$, such that $D = 2$ when the cores are touching and $D \rightarrow \infty$ as $d \rightarrow \infty$. Since neither the normalised core separation, D , nor the core aspect ratios, ε_1 and ε_2 , appear explicitly in equation (3.9), the cutoff V -value of the second mode must depend on them implicitly, as we now quantify.

In the case of the symmetric coupler both cores are identical, whence $\varepsilon_1 = \varepsilon_2$ in Figure 3.1(b), and the second mode then possesses odd symmetry about the x -axis and even symmetry about the y -axis. Figure 3.7 plots the cutoff V -value, V_c , of the second mode as a function of the normalised core separation, D , for various values of core aspect ratio, $\varepsilon_1 = \varepsilon_2$. Values of the simulation parameters are detailed in the figure caption. As $D \rightarrow \infty$, $V_c \rightarrow 0$ regardless of the core aspect ratio, and when $D \rightarrow 2$, V_c approaches the cutoff value for a rectangular-core waveguide with aspect ratio $\varepsilon = 2\varepsilon_1 = 2\varepsilon_2$.

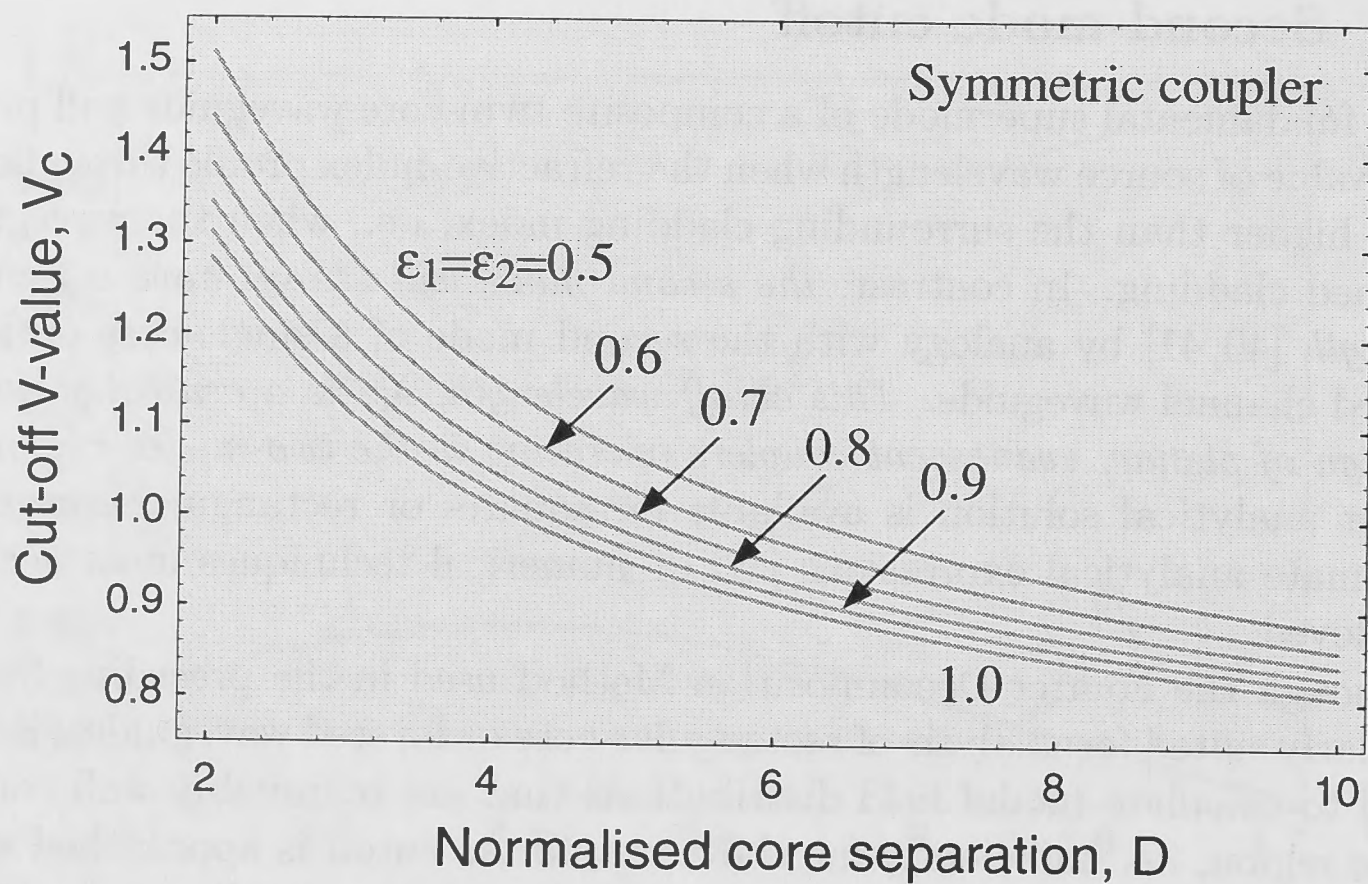


Figure 3.7: Second-mode cutoff V -value, V_c , of a symmetric coupler as a function of the normalized core separation, D , for various values of core aspect ratio, $\epsilon_1 = \epsilon_2$. The simulation parameters correspond to: $\Delta = 0.003$, $n_{cl} = 1.447$, $\rho = 3.6808 \mu\text{m}$ and $\bar{\rho} = \rho\sqrt{\epsilon_1} = \rho\sqrt{\epsilon_2}$. For a square-core coupler with $\epsilon_1 = \epsilon_2 = 1$, these parameters give $V = (2\pi/\lambda)\rho\sqrt{n_{co}^2 - n_{cl}^2} = 2$ when $\lambda = 1.3 \mu\text{m}$.

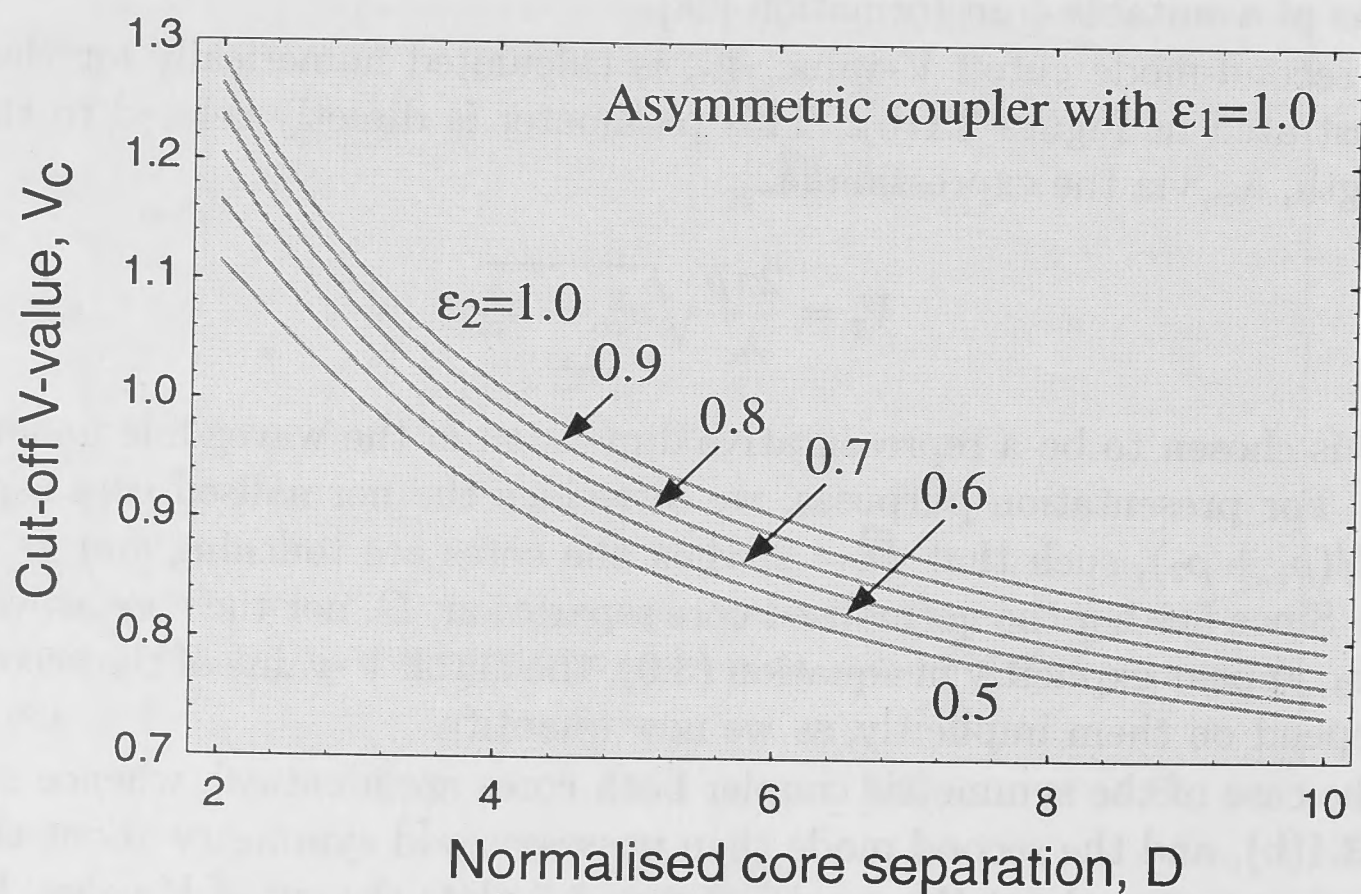


Figure 3.8: Second-mode cutoff V -value, V_c , of an asymmetric coupler as a function of the normalized core separation, D , for various aspect ratios, ϵ_2 , of core 2. The simulation parameters correspond to: $\Delta = 0.003$, $n_{cl} = 1.447$, $\rho = 3.6808 \mu\text{m}$, $\bar{\rho} = \rho\sqrt{\epsilon_2}$ and $\epsilon_1 = 1$, so that $V = 2$ for the square core when $\lambda = 1.3 \mu\text{m}$.

In the case of an asymmetric coupler, $\varepsilon_1 \neq \varepsilon_2$ in Figure 3.1(b), and the second mode then possesses even symmetry about the y -axis and is asymmetric about the x -axis. We concentrate, in particular, on the case when core 1 remains square (i.e., $\varepsilon_1 = 1$) while the aspect ratio of the second core, ε_2 , is varied. Figure 3.8 plots the cutoff V -value of the second mode as a function of the normalised core separation, D , for various aspect ratios, ε_2 , of core 2. Values of the simulation parameters are detailed in the figure caption. Again, as $D \rightarrow \infty$, $V_c \rightarrow 0$ independent of ε_2 , and when $D = 2$, V_c approaches the cutoff value for a rectangular-core waveguide with aspect ratio $1 + \varepsilon_2$.

3.3 Highly broadband couplers – practical examples

Practical planar couplers have curved input and output arms in addition to the straight central coupling region, as illustrated schematically in Figure 3.1(a). Although coupling occurs predominantly in the central region, there is also some additional coupling between the converging and diverging arms until the core separation becomes sufficiently large. In this section, we include the effect of this additional coupling and present examples of highly broadband buried channel couplers. Numerical quantification indicates that the *additional coupling does not affect the basic spectral-broadening phenomenon being reported*, but influences slightly the width of the wavelength-flattened region [37, 38].

3.3.1 Symmetric coupler

Propagation through a nonuniform symmetric coupler has been described analytically in Chapter 2 as a superposition of the local supermodes of the composite twin-core structure. In this approach, each local supermode is assumed to propagate adiabatically such that its power, and therefore its amplitude, are conserved along the coupler. This condition requires the curved paths to have bend radii that are large enough to incur negligible losses to radiation. We accordingly set $R_b = 22$ mm, with an estimated maximum bend loss of the order of 0.1 dB for all four curved paths.

With reference to Chapter 2, the total accumulated relative phase difference between the two supermodes over the complete length of the coupler is given by

$$\phi_{\text{tot}} = \phi_i + \phi_c + \phi_o = 2\phi_i + \phi_c, \quad (3.10)$$

where ϕ_i , ϕ_c and ϕ_o are the accumulated relative phase differences along the input arms, uniform central region and output arms, defined by (2.16), (2.19) and (2.22), respectively. The fractional power transfer equations are readily shown to be [5, Sectn. 19–6]:

$$P_2 = \cos^2 \left(\frac{\phi_{\text{tot}}}{2} \right) \quad \text{and} \quad P_3 = \sin^2 \left(\frac{\phi_{\text{tot}}}{2} \right). \quad (3.11)$$

Figure 3.9 plots the spectral dependence of the fractional coupled power, P_3 , for a highly broadband square-core symmetric coupler (or “dropping filter”) with the curved input/output arms included. Values of the simulation parameters are detailed in the figure caption. There is a departure of only 4.4% from 100% coupling over the wavelength range 1.3 – 1.58 μm . Beyond $\lambda_c = 1.58 \mu\text{m}$, the second, or odd supermode of the composite twin-core structure is cutoff, and coupling cannot occur.

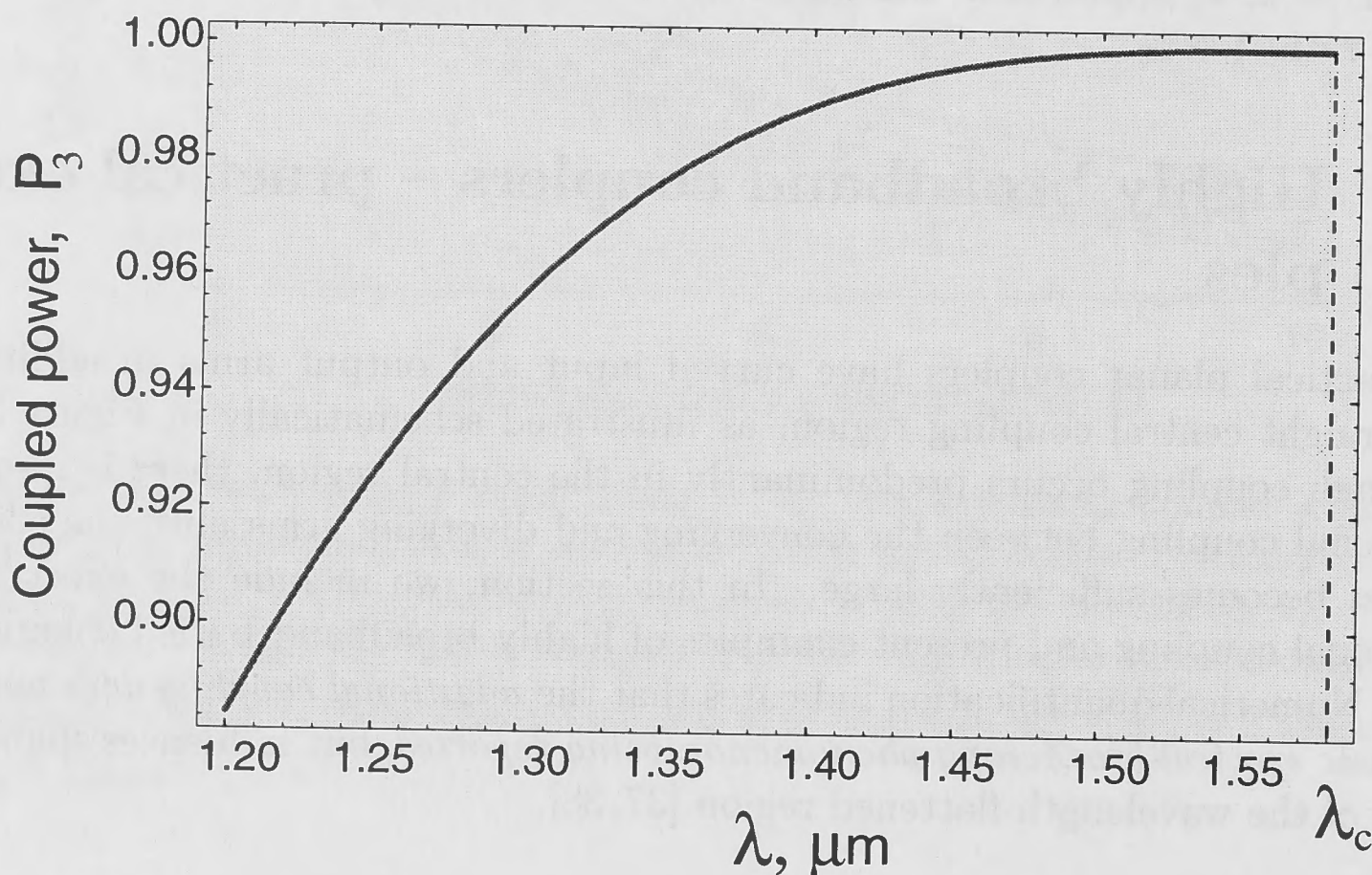


Figure 3.9: Spectral dependence of the fractional coupled power, P_3 , for a symmetric coupler with the curved input/output arms included. The simulation parameters correspond to: $\Delta = 0.003$, $n_{cl} = 1.447$, $\rho_1 = \rho_2 = \rho = 2.7 \mu\text{m}$, $L_c = 0.0522 \text{ mm}$, $d = 6.48 \mu\text{m}$ and $R_b = 22 \text{ mm}$.

3.3.2 Asymmetric coupler

In the case of the asymmetric coupler, the complexity of the problem makes it difficult to achieve a general analytic description of the coupling process. To this end, we seek a numerical solution and use the coupled local-mode approach discussed in Appendix B.

The following coupler parameters were varied: the half-width of the second core, ρ_2 , the centre-to-centre core separation d , and the length of the uniform central region, L_c . In all cases, the two-moded régime had to be maintained within the uniform central region over the entire range of operating wavelengths (see Section 3.2.3). FDM calculations were performed to determine the dependence of β_1 , β_2 , β_+ and β_- on both the propagation distance, z , and the source wavelength, λ . To illustrate the idea behind the coupler parameters optimisation, Figure 3.10 plots

the accumulated difference $\beta_+ - \beta_-$ as a function of wavelength and distance along the coupler for fixed core sizes and separation.

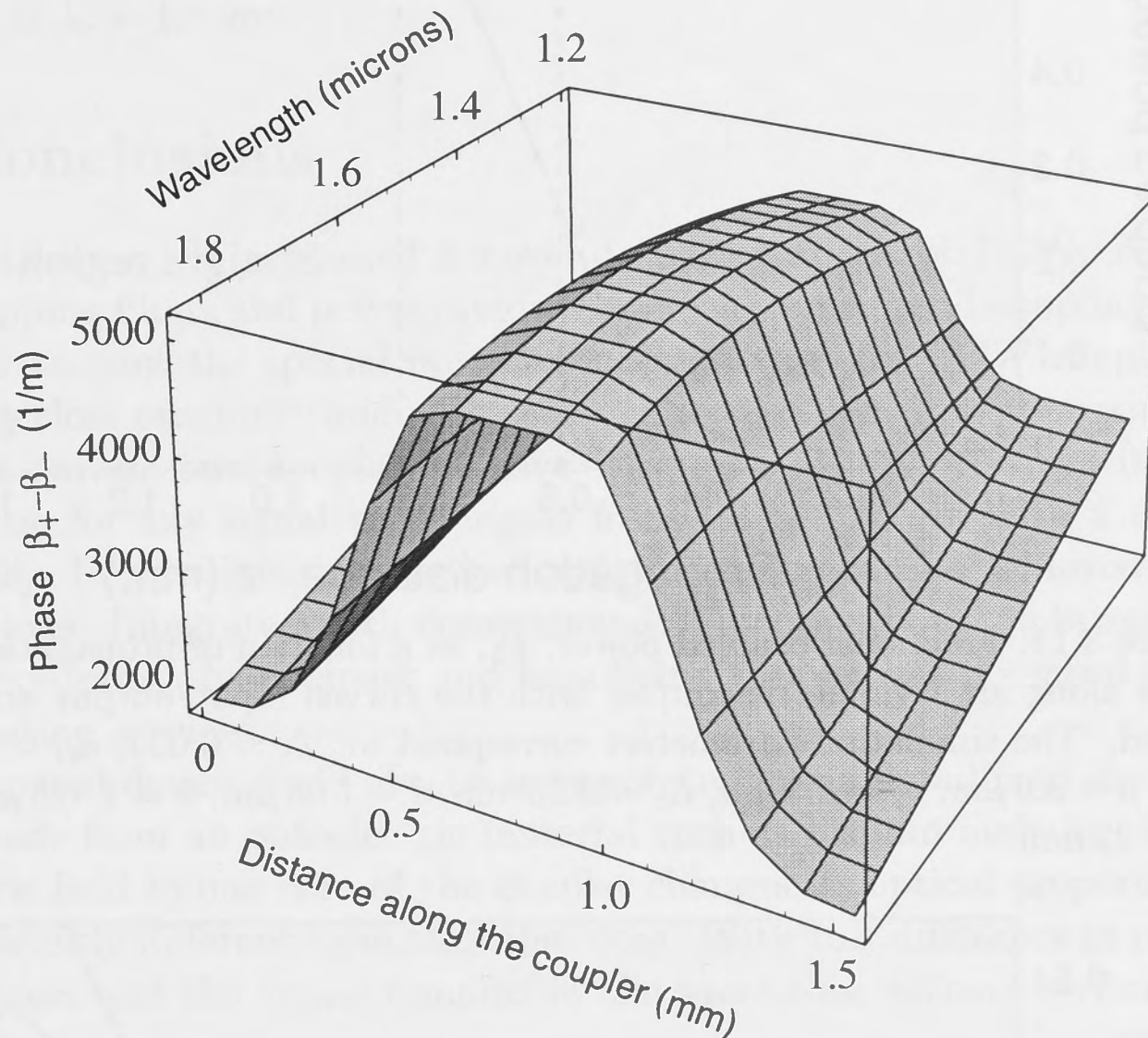


Figure 3.10: Accumulated “phase term”, $\beta_+ - \beta_-$, as a function of source wavelength λ and propagation distance z along an asymmetric coupler with the curved input/output arms included. The simulation parameters correspond to: $\Delta = 0.003$, $n_{c1} = 1.447$, $\rho_1 = \rho = 3.6 \mu\text{m}$, $\rho_2 = 2.4 \mu\text{m}$, $L_c = 0.323 \text{ mm}$, $d = 7.2 \mu\text{m}$ and $R_b = 22 \text{ mm}$.

The fractional coupled power, $P_3(z)$, was evaluated numerically using the procedure outlined in Appendix B. As a particular example, Figure 3.11 plots the fractional coupled power, P_3 , as a function of the propagation distance, z , along an asymmetric highly broadband coupler with the curved input/output arms included. Values of the simulation parameters are detailed in the figure caption. The position $z = 0$ is sufficiently far from the central coupling region to ensure that negligible coupling occurs.

Two broadband coupler designs are compared in Figure 3.12. The solid curve, ‘A’, includes the contribution to coupling from the curved input/output arms in Figure 3.1(a), and shows a wavelength-flattened response with a variation of only $50\% \pm 1.6\%$ over the wavelength range $1.3\text{--}1.67 \mu\text{m}$. Values of the simulation parameters are detailed in the figure caption.

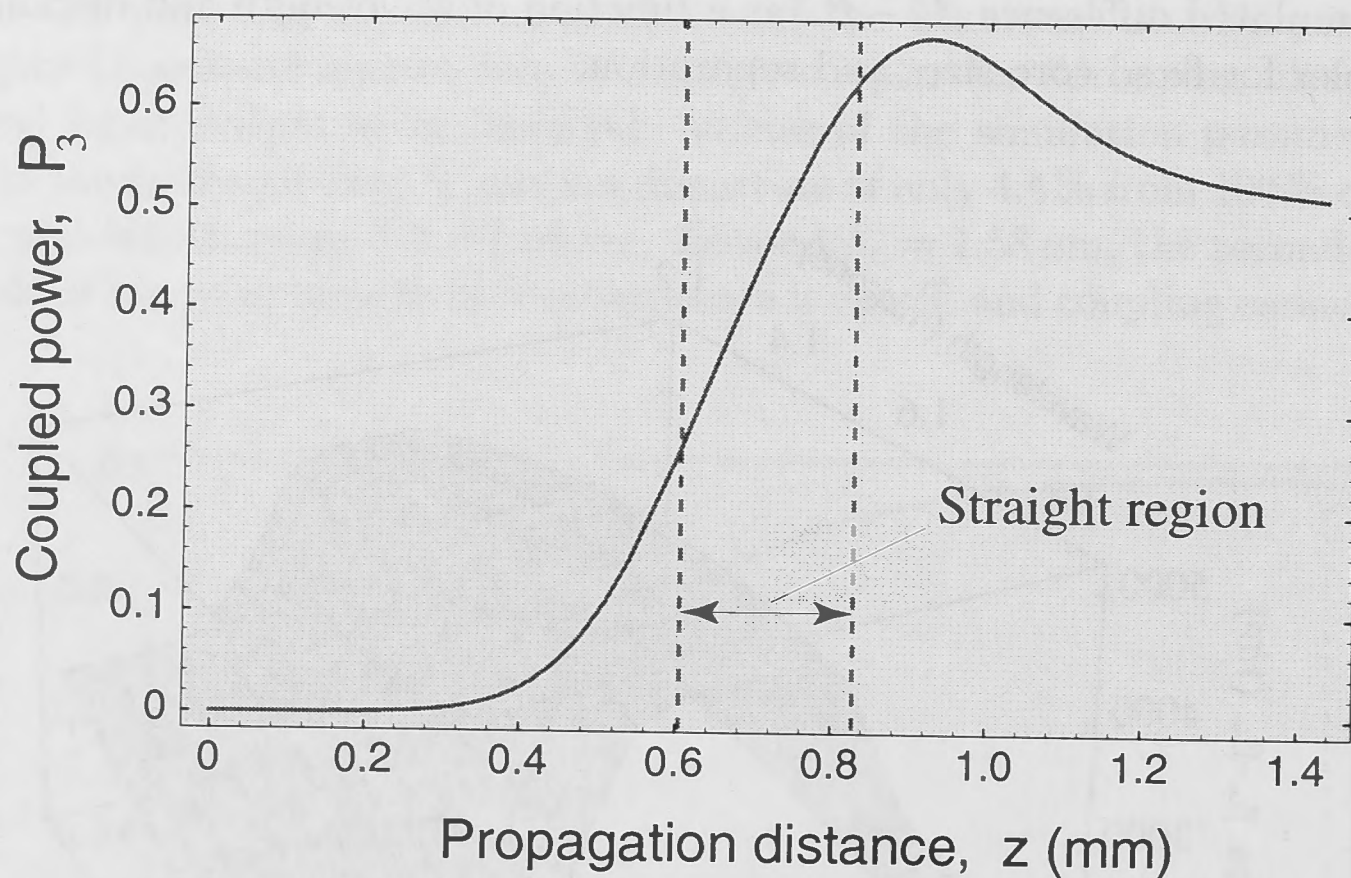


Figure 3.11: Fractional coupled power, P_3 , as a function of propagation distance along an asymmetric coupler with the curved input/output arms included. The simulation parameters correspond to: $\Delta = 0.003$, $n_{cl} = 1.447$, $\rho_1 = \rho = 3.6 \mu\text{m}$, $\rho_2 = 2.3 \mu\text{m}$, $L_c = 0.23 \text{ mm}$, $d = 7.08 \mu\text{m}$, $\lambda = 1.425 \mu\text{m}$ and $R_b = 22 \text{ mm}$.

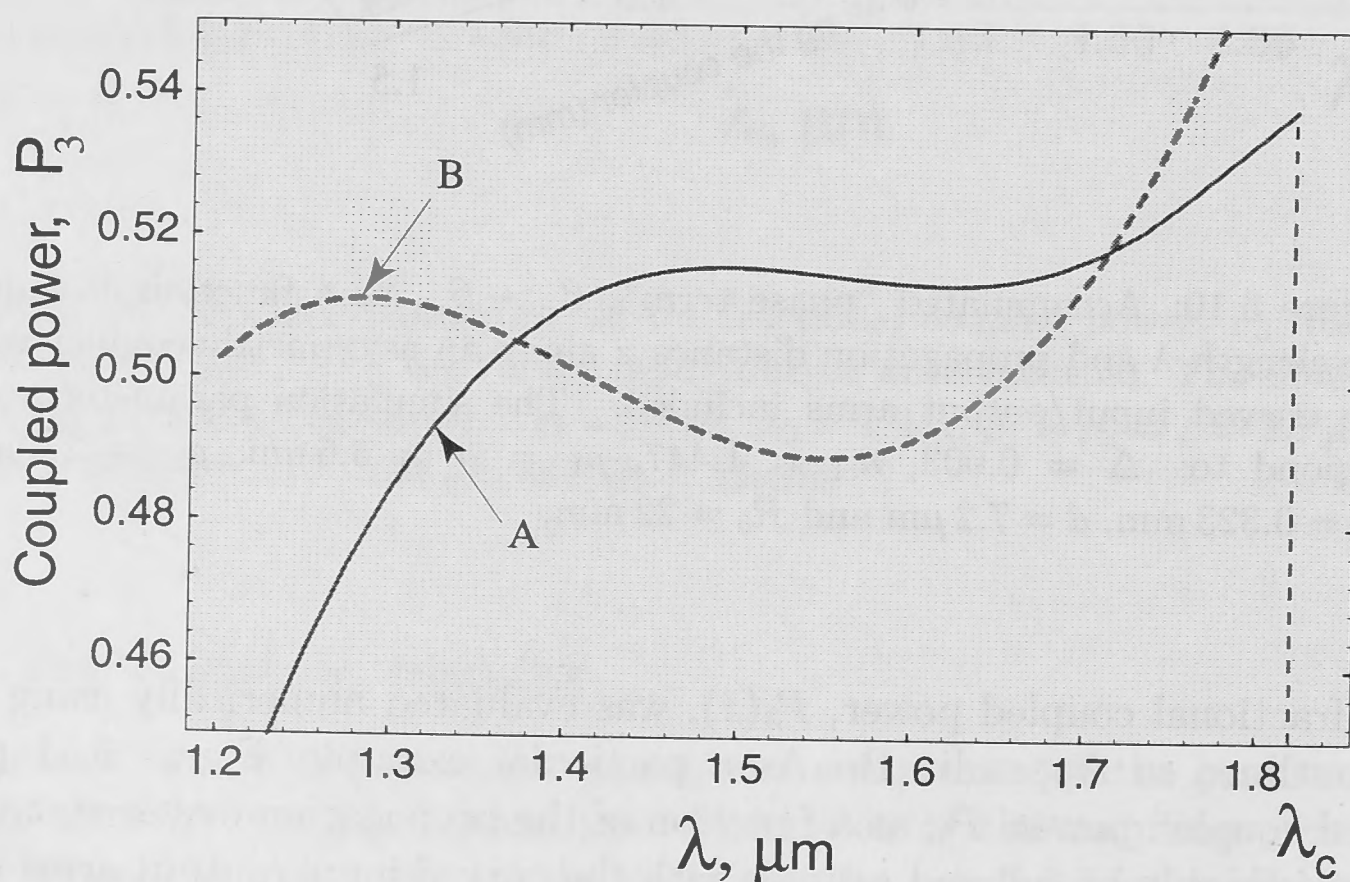


Figure 3.12: Spectral dependence of the fractional coupled power, P_3 , for a broadband 3 dB splitter. The solid curve, 'A', includes the contribution to coupling from the curved input/output arms and corresponds to the simulation parameters: $\Delta = 0.003$, $n_{cl} = 1.447$, $\rho_1 = \rho = 3.6 \mu\text{m}$, $\rho_2 = 2.3 \mu\text{m}$, $L_c = 0.23 \text{ mm}$, $d = 7.08 \mu\text{m}$ and $R_b = 22 \text{ mm}$. The broken curve, 'B', is for the straight coupler design without the bends and corresponds to the simulation parameters: $\Delta = 0.003$, $n_{cl} = 1.447$, $\rho_1 = \rho = 3.6 \mu\text{m}$, $\rho_2 = 2.5 \mu\text{m}$, $L_c = 0.91 \text{ mm}$ and $d = 7.625 \mu\text{m}$.

Beyond $\lambda_c = 1.82 \mu\text{m}$, the second supermode of the composite twin-core structure is cutoff and coupling ceases. A bend loss of approximately 0.1 dB is estimated for the entire coupler. The broken curve, 'B', in Figure 3.12 shows the analogous response for the straight coupler design without the bends. In this case, the cutoff wavelength is $\lambda_c = 1.9 \mu\text{m}$.

3.4 Conclusions

In this Chapter we presented a novel design approach of BCW couplers that realises dropping filters and power dividers with very broadband coupling responses. Taking into account the special optical characteristics of a BCW coupler with its cores in very close proximity and with cross-sectional dimensions approximately half of those of a conventional coupler, we have designed a practical device with 50–50% splitting ratio for any signal wavelengths from 1.3 to $1.67 \mu\text{m}$ with a tolerance of 1.6% [37, 38]. In principle, any desired splitting ratios can be achieved depending on applications. Integrated with conventional Y-junction power splitters placed at the coupler outputs, the compact and broadband coupler has potential application for broadcasting services.

The proposed device could also be incorporated into a broadband electro-optical switch if made from an optoelectric material such as lithium niobate. Application of an electric field to one core of the coupler changes its optical properties making them significantly different from the other core. With this difference in parameters, coupling ceases and the signal remains in the same core without switching to the other core.

4.1 Bend loss in infinite-cladding fibres

When light propagates in the fundamental mode of a perfectly straight and uniform single-mode fibre, it suffers only a slight attenuation of total power due to scattering and absorption by the constituent glass materials of the fibre core and cladding. However, if a bend is introduced into the fibre, a third loss mechanism appears and power is lost by radiation from the fundamental mode. The nature of bend loss is relatively well understood, and can be described conveniently in terms of two distinct physical mechanisms [3, Sects. 23].

4.1.1 Pure bend loss

The term pure bend loss is used to describe the power radiated from the fundamental mode of the straight fibre when it is bent into a planar curve of constant radius, R_b , relative to the centre of the bend C , such as that illustrated in Fig. 4.1.

Beyond $\lambda = 1.82 \mu\text{m}$, the second response of the composite twin-core structure is cutoff and coupling ceases. A band loss of approximately 0.1 dB is estimated for the same coupler. The broken curve in Figure 3.12 shows the analogous response for the straight coupler design without the bands. In this case, the cutoff wavelength is $\lambda = 1.8 \mu\text{m}$.

3.4 - Conclusions

In this Chapter we presented a novel design approach to BCC couplers that realizes coupling near and power division with very broadband constant responses. Taking into account the special optical characteristics of a BCC coupler with its core in very close proximity and with cross-sectional dimensions approximately half of those of a conventional coupler, we have designed a practical device with 50-50% splitting ratio for any signal wavelengths from 1.5 to 1.8 μm with a tolerance of $\pm 0.5 \mu\text{m}$. In practice, any desired splitting ratio can be achieved depending on application. Compared with conventional 2-function power splitters placed at the coupler output, the proposed and presented coupler has several advantages for broadband systems.

The proposed device could also be incorporated into a broadband electro-optical switch if made from an electrooptic material such as lithium niobate. Application of an electric field to one core of the coupler changes its optical properties making them significantly different from the other core. With this difference in parameters, coupling ceases and the signal remains in the same core without returning to the other core.



Figure 3.12: Coupling coefficient K versus wavelength λ in micrometers for a BCC coupler. The solid line shows the response of the proposed coupler with a 50-50% splitting ratio, which is constant across the wavelength range from 1.5 to 1.8 μm . The broken line shows the response of a straight coupler design without the bands, which has a narrower bandwidth and a lower coupling coefficient.

Bends in Finite-Cladding Practical Fibres

Interest in all-fibre optical components, such as polarisers, couplers, filters, gratings and tapers, has been stimulated by recent developments in the applications of optical fibre amplifiers. Many of these components involve interactions of the core-guided modes with modes of the whole finite-cladding practical fibre cross-section, for example in gain-flattening using forward-coupling Bragg gratings. Accordingly, there is an increasing need to understand the propagation characteristics of fibres in such situations.

In this Chapter we concentrate on bend loss from finite-cladding practical single-mode fibres. This research has been initiated through the collaboration with Telstra Research Laboratories (TRL), where the bent fibre attenuator was originally designed and fabricated. This design was based on the conventional assumption of the infinite fibre cladding, and, in practice, did not perform according to expectations. The finite-cladding analysis presented here provides an explanation to the unpredicted behaviour of the TRL-designed bent fibre attenuator, as well as suggests a novel practical design approach [44].

4.1 Bend loss in infinite-cladding fibres

When light propagates in the fundamental mode of a perfectly straight and uniform single-mode fibre, it suffers only a slight attenuation of total power due to scattering and absorption by the constituent glass materials of the fibre core and cladding. However, if a bend is introduced into the fibre, a third loss mechanism appears and power is lost by radiation from the fundamental mode. The nature of bend loss is relatively well understood, and can be described conveniently in terms of two distinct physical mechanisms [5, Sectn. 23].

4.1.1 Pure bend loss

The term *pure bend loss* is used to describe the power radiated from the fundamental mode of the straight fibre when it is bent into a planar curve of constant radius, R_b , relative to the centre of the bend C , such as that illustrated in Fig. 4.1.

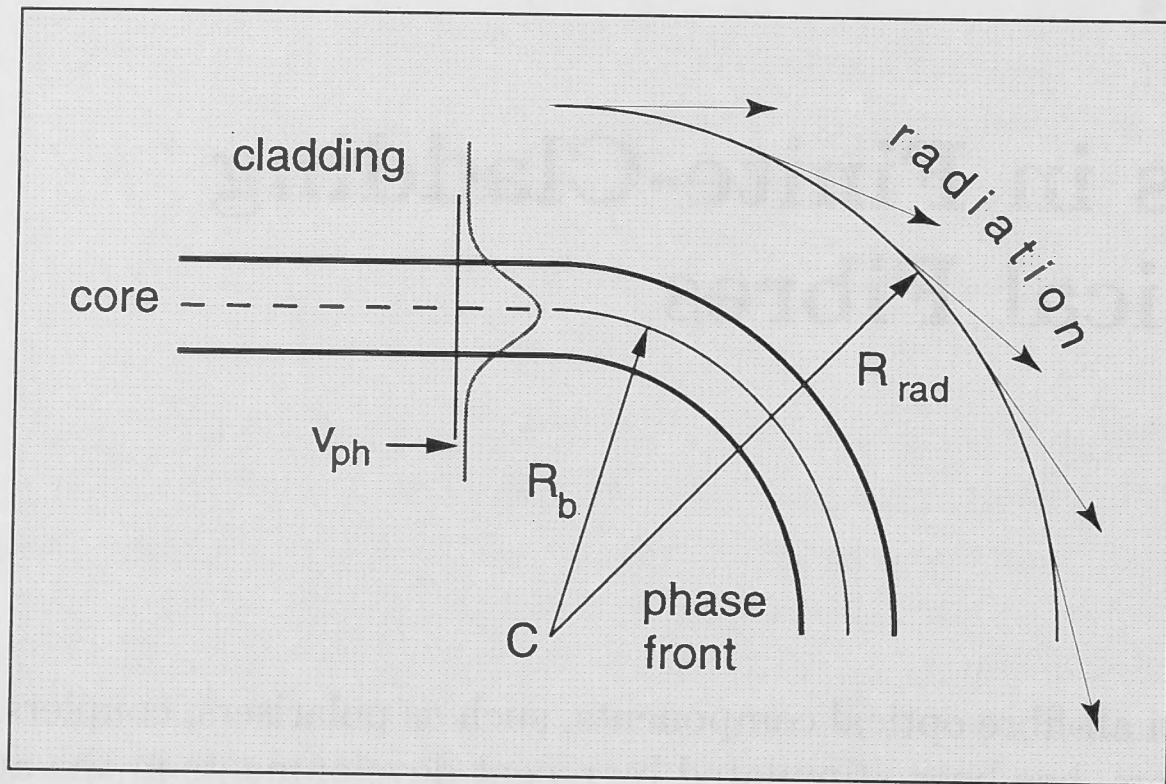


Figure 4.1: Fundamental-mode phase fronts on the straight and bent fibre, and the radiation caustic. R_b is the bend radius, the curve $R = R_{\text{rad}}$ defines the radiation caustic and v_{ph} is the phase velocity.

On the straight fibre, the transverse electric field of the fundamental mode is expressible in the separable form (see Chapters 2,3):

$$E(r, z) = \psi(r)e^{i\beta z} \quad (4.1)$$

where, assuming weak guidance, $\psi(r)$ is the fundamental solution of the scalar wave equation and β is the corresponding propagation constant. An implicit time dependence $\exp(-i\omega t)$ is assumed in the field expression, where ω is the source angular frequency.

On the straight fibre, the modal phase front is a plane perpendicular to the fibre axis, as shown in Fig. 4.1. This front propagates along the fibre with phase velocity v_{ph} defined by

$$v_{\text{ph}} = \frac{\omega}{\beta}. \quad (4.2)$$

Around the bend, the fundamental mode phase front is a plane rotating about the axis of the bend through C with angular velocity Ω . By matching the phase velocities of the mode of the straight and bent fibre on its axis at the beginning of the bend, we have

$$\Omega = \frac{\omega}{\beta R_b}. \quad (4.3)$$

If we draw a radial line in the rotating phase front, the phase velocity increases linearly with distance from C , until at radius R_{rad} , the phase velocity is equal to

the speed of light in the cladding, c/n_{cl} . Thus we deduce from Eqn. (4.3) that

$$\Omega R_{rad} = \frac{c}{n_{cl}}. \quad (4.4)$$

Beyond R_{rad} , the modal phase velocity cannot exceed c/n_{cl} , and consequently the modal field radiates as shown in Fig. 4.1. Accordingly, R_{rad} can be regarded as the apparent origin of radiation, and the curve $R = R_{rad}$ defines the *radiation caustic*. On setting $c = \omega/k$ in Eqn. (4.4) and substituting for Ω from Eqn. (4.3)

$$R_{rad} = R_b \frac{\beta}{kn_{cl}}. \quad (4.5)$$

Thus the distance of the radiation caustic from the fibre axis, d , is given by

$$d = R_{rad} - R_b = \frac{\beta - kn_{cl}}{kn_{cl}} R_b. \quad (4.6)$$

Thus, if the source wavelength and hence β remain fixed, the radiation caustic moves closer to the fibre axis as the bend radius decreases, and, intuitively, the radiated power increases. Similarly, if the bend radius remains fixed, the radiation caustic moves closer to the core as the source wavelength increases and β decreases, and the radiated power again increases.

Magnitude of bend loss

In order to quantify the magnitude of the pure bend loss, we introduce a *power attenuation coefficient* γ , so that if $P(z)$ denotes the total guided power in the fundamental mode distance z along the bend (measured along the fibre axis from the beginning of the bend), then

$$P(z) = P(0)e^{-\gamma z} \quad (4.7)$$

where $P(0)$ is the power at the beginning of the bend. An analytical expression for γ can be derived for a step-profile fibre (see Fig. 2.4, Chapter 2) using the thin-wire approximation to radiation from the fundamental mode. In this model the fibre is approximated by a current carrying antenna of infinitesimal thickness which radiates in an infinite medium of index equal to the cladding index n_{cl} . In terms of the modal parameters U and W , core radius ρ and fibre parameter V [5, Sectn. 23-5]:

$$\gamma = \left(\frac{\pi\rho}{R_b} \right)^{1/2} \frac{V^2 W^{1/2}}{2\rho U^2} \exp \left\{ -\frac{4}{3} \Delta \frac{R_b W^3}{\rho V^2} \right\}, \quad (4.8)$$

$$U = \rho \sqrt{k^2 n_{co}^2 - \beta^2}, \quad W = \rho \sqrt{\beta^2 - k^2 n_{cl}^2}, \quad V = k\rho \sqrt{n_{co}^2 - n_{cl}^2},$$

where $k = 2\pi/\lambda$ is the wavenumber, λ the source free-space wavelength, n_{co} the core index, n_{cl} the cladding index, and $\Delta = (n_{co}^2 - n_{cl}^2)/2n_{co}^2$ the relative index difference. It is clear from Eqn. (4.7) that pure bend loss is most sensitive to the expression in the exponent of Eqn. (4.8), and for a given wavelength decreases very rapidly with increasing bend radius.

Bent single-mode fibre

Assuming representative parameter values: $\Delta = 0.3\%$, $V = 2.3$, $W = 1.6$ and $\rho = 3\mu\text{m}$, then the fraction of power lost in one loop of fibre of radius R_b as illustrated in Fig. 4.2 is given by

$$P_{\text{rad}} = 10^4 e^{-500R_b} \% \quad (4.9)$$

where R_b is in metres.

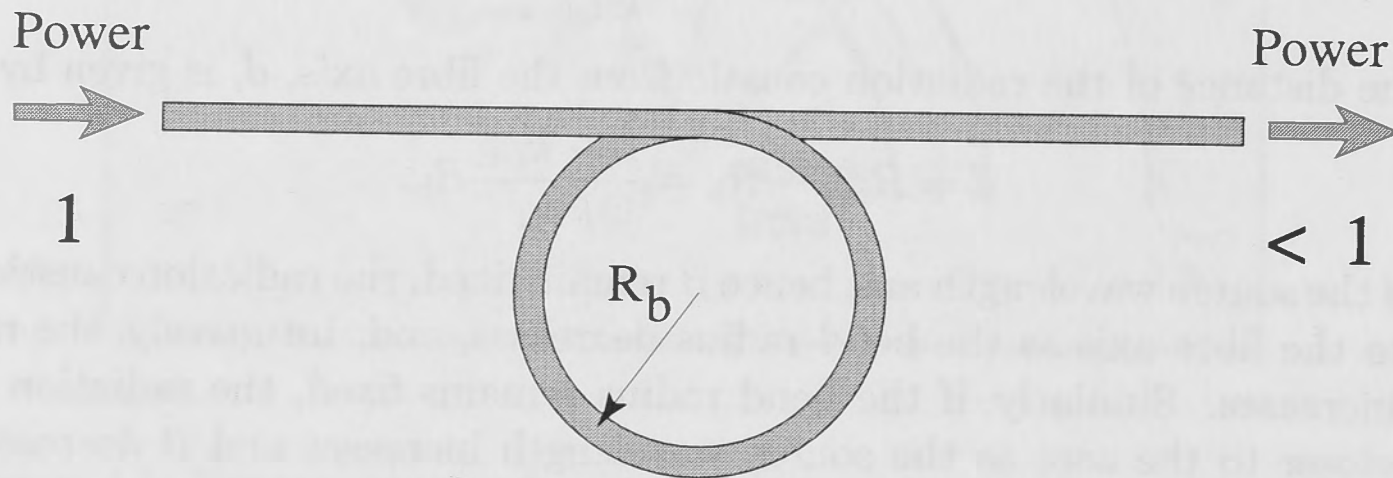


Figure 4.2: Single loop of fibre of radius R_b .

Thus, for example, if $R_b = 1\text{ cm}$, then 67% of fundamental mode power is lost in one loop, whereas if $R_b = 15\text{ cm}$ (the radius of a standard drum of fibre) then the loss of $10^{-29}\%$ is totally negligible.

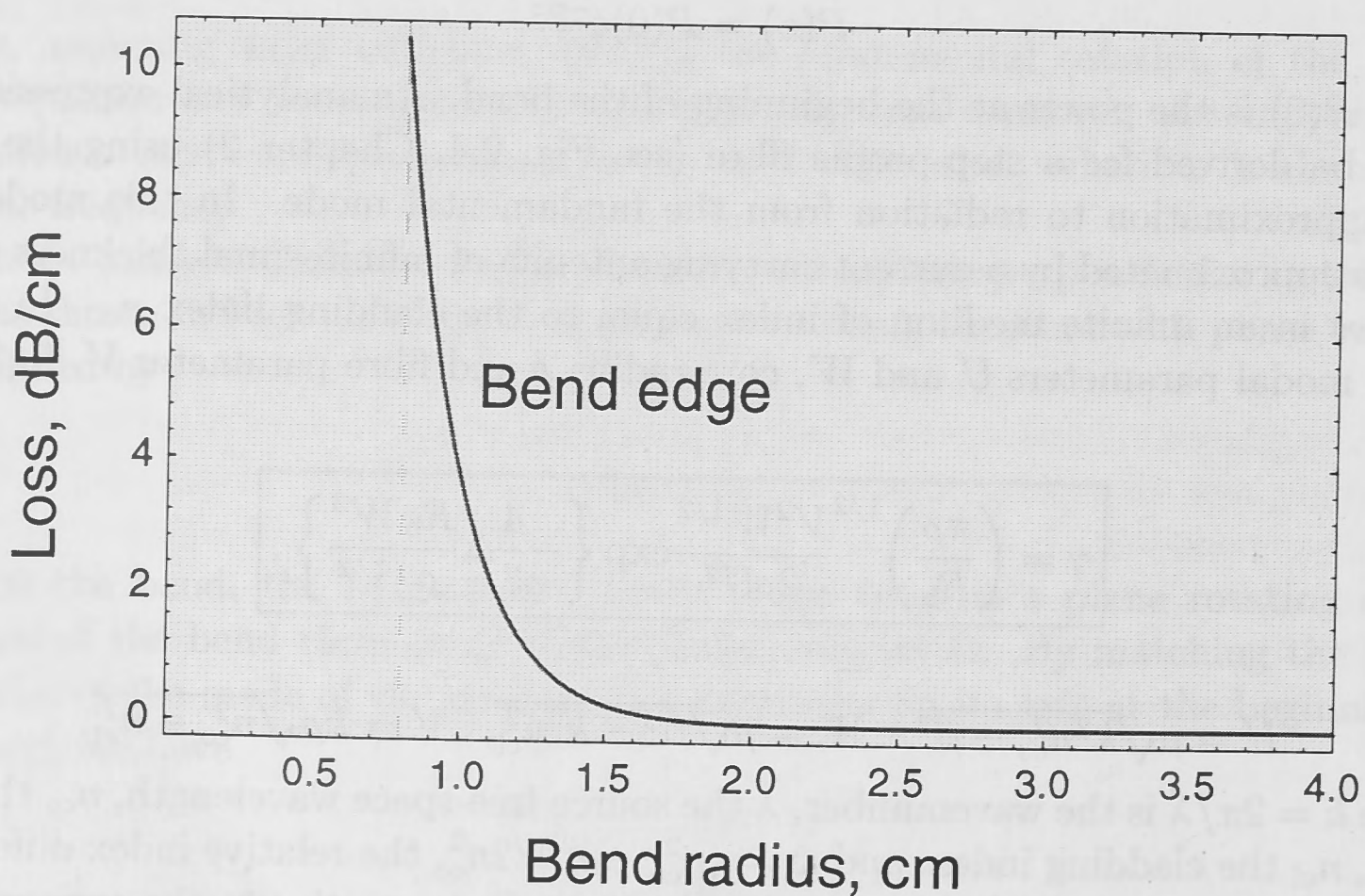


Figure 4.3: Pure bend loss (attenuation coefficient) as a function of radius.

Rapid decrease of bend loss with increasing radius, as illustrated schematically in Fig. 4.3, is often referred to as a *bend edge*. It is customary to express the fibre loss in units of dB/cm by using the relation

$$\gamma_{dB} = -\frac{10}{L} \log \left[\frac{P(L)}{P(0)} \right], \quad (4.10)$$

where $P(L)$ is the transmitted power at the end of fibre of length L .

Radiation from the bent fibre originates predominantly from the plane of the bend through the centre of curvature C and the fibre axis. In any other plane through the fibre axis, the radius of curvature is larger, and the power radiated is considerably reduced. Accordingly, it is often adequate to use a *bent slab model* in order to determine the magnitude of bend loss. As we see later, the slab model leads to a considerable simplification in the analysis of bend loss from real fibres.

4.1.2 Transition loss

In Section 4.1 we quantified fundamental mode attenuation due to pure bend loss when the radius of curvature of the fibre is fixed. There is a second bend loss mechanism which needs to be taken into account, arising from the change from the straight fibre to the bent fibre in Fig. 4.1, and is often referred to as *transition loss*. This loss arises because the fundamental mode field of the bent fibre is slightly shifted outwards in the plane of the bend and does not match the corresponding field of the straight fibre [5, Sectn. 36–14], as seen in Figure 4.4.

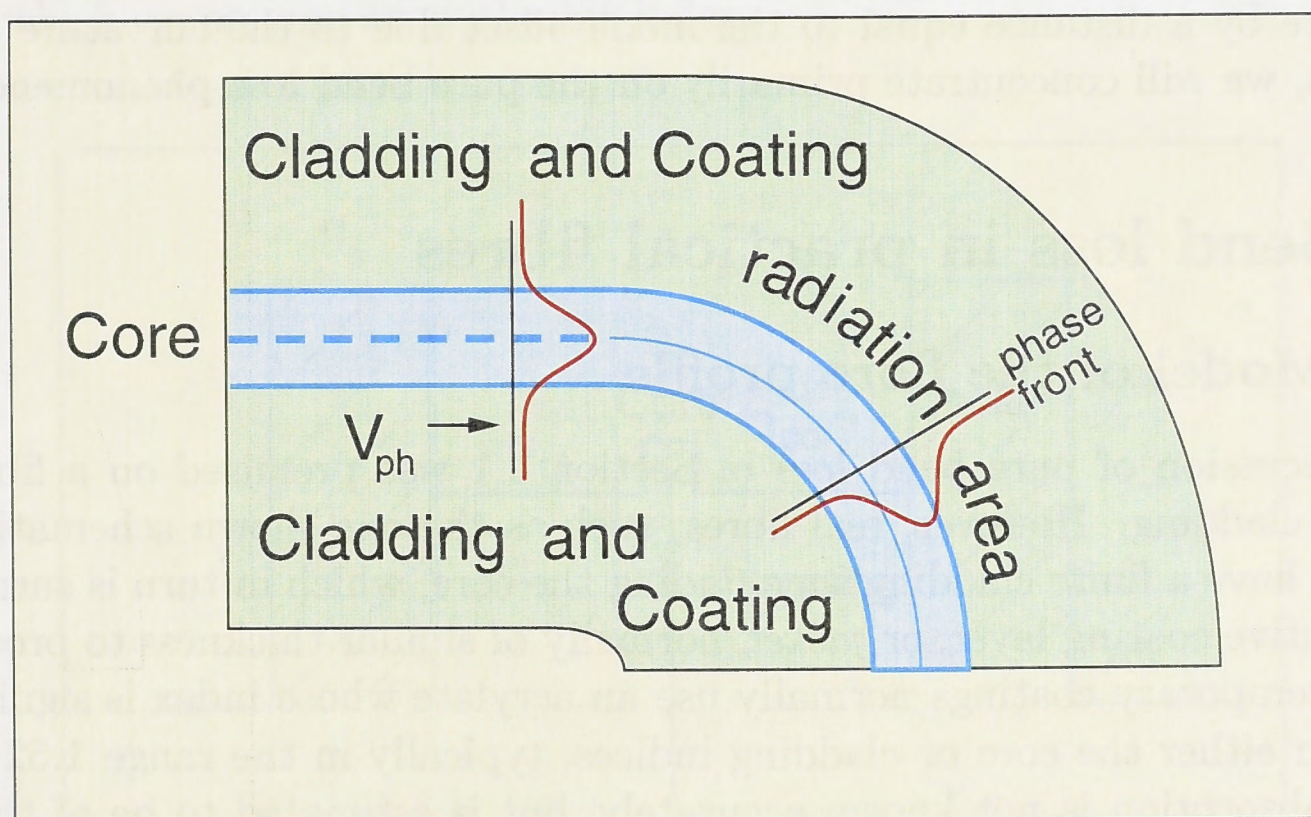


Figure 4.4: Modal field shift in the bent fibre.

Thus, if there is an abrupt change in curvature, as at the junction between the straight and bent fibre in Fig. 4.1, there will be a transition loss, and not all of the

power in the fundamental mode of the straight fibre will excite the fundamental mode of the bent fibre, the difference being lost as radiation into the cladding. Expressions for the radiated power, P_{rad} , have been derived, and, within the Gaussian approximation, the fraction of modal power loss can be expressed in closed form as [28, Sectn. 10.7].

$$\frac{P_{\text{rad}}}{P(0)} = \left[1 - \exp \left(-\frac{V^4 s^6}{8\Delta^2 \rho^4 R_b^2} \right) \right] \simeq \frac{V^4 s^6}{8\Delta^2 \rho^4 R_b^2} \quad (4.11)$$

in terms of parameters defined above, and the spot size s of the fundamental mode field. The approximation applies when the loss is small. Thus for the parameter values $V = 2.3$, $\Delta = 0.003$, $\rho = 3 \mu\text{m}$ and assuming a spot size comparable to the core size, we have

$$\frac{P_{\text{rad}}}{P(0)} \simeq \frac{3.5}{R_b^2}, \quad (4.12)$$

where R_b is in mm. Thus for a bend radius of 150 mm, there is a 0.016% power loss, increasing to 3.5% for a 10 mm radius bend. These results assume an abrupt change in curvature from the straight to the bent fibre, whereas the change in curvature for practical fibres will be more gradual. Clearly, in the limit in which there is a sufficiently slow change in curvature at the beginning of the bend, the transition loss could be made arbitrarily small. Thus, for present purposes, Eqn. (4.11) provides an upper bound on the actual transition loss. There are well-understood ways to decrease the transition loss by shifting the straight fibre slightly with respect to the curved fibre by a distance equal to the mode offset due to the curvature [45]. In this Thesis, we will concentrate primarily on the pure bend loss phenomenon.

4.2 Bend loss in practical fibres

4.2.1 Model of the fibre profile

The discussion of pure bend loss in Section 4.1 was premised on a fibre with an infinite cladding. However, real fibres, such as the one shown schematically in Figure 4.5, have a finite cladding surrounding the core, which in turn is surrounded by a protective coating layer, or *jacket*, normally of similar thickness to protect the fibre. Contemporary coatings normally use an acrylate whose index is significantly higher than either the core or cladding indices, typically in the range 1.52 – 1.54. The bulk absorption is not known accurately, but is estimated to be of the order 1 – 10 dB/cm, corresponding to a maximum imaginary part of the coating index of order 10^{-4} . For large bend radii, the finite cladding and jacket have negligible effect on pure bend loss, but for smaller bend radii, as we show below, they can radically change the power attenuation coefficient given by Eqn. (4.8). Furthermore, the absorption and scattering in the jacket dramatically modify the physical description of bend loss. Both of these effects are discussed further in detail.

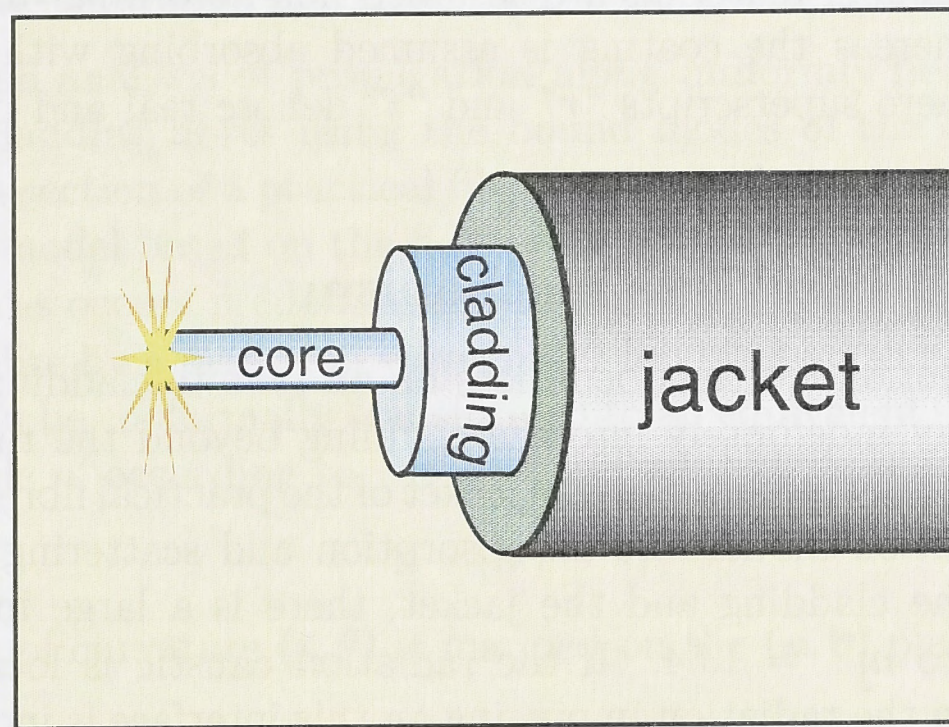


Figure 4.5: Jacketed optical fibre.

For convenience and simplicity we retain the step profile core-cladding used in the infinite-cladding model, and now add the finite cladding and jacket to arrive at the refractive index profile illustrated in Fig. 4.6. We assume core index $n_{co} = 1.44846$ and radius $\rho = 6 \mu\text{m}$, surrounded by a finite cladding of index $n_{cl} = 1.447$ occupying the region $\rho < r < \sigma$, where r is the polar radius relative to the axis of the bent fibre and the outer cladding radius $\sigma = 62.5 \mu\text{m}$. The jacket of index $n_j^{(r)} = 1.54$ and $n_j^{(i)} = 0.0001$ fills the region $\sigma < r < \tau$, where the outer coating radius $\tau = 125 \mu\text{m}$, beyond which we assume air with unit index.

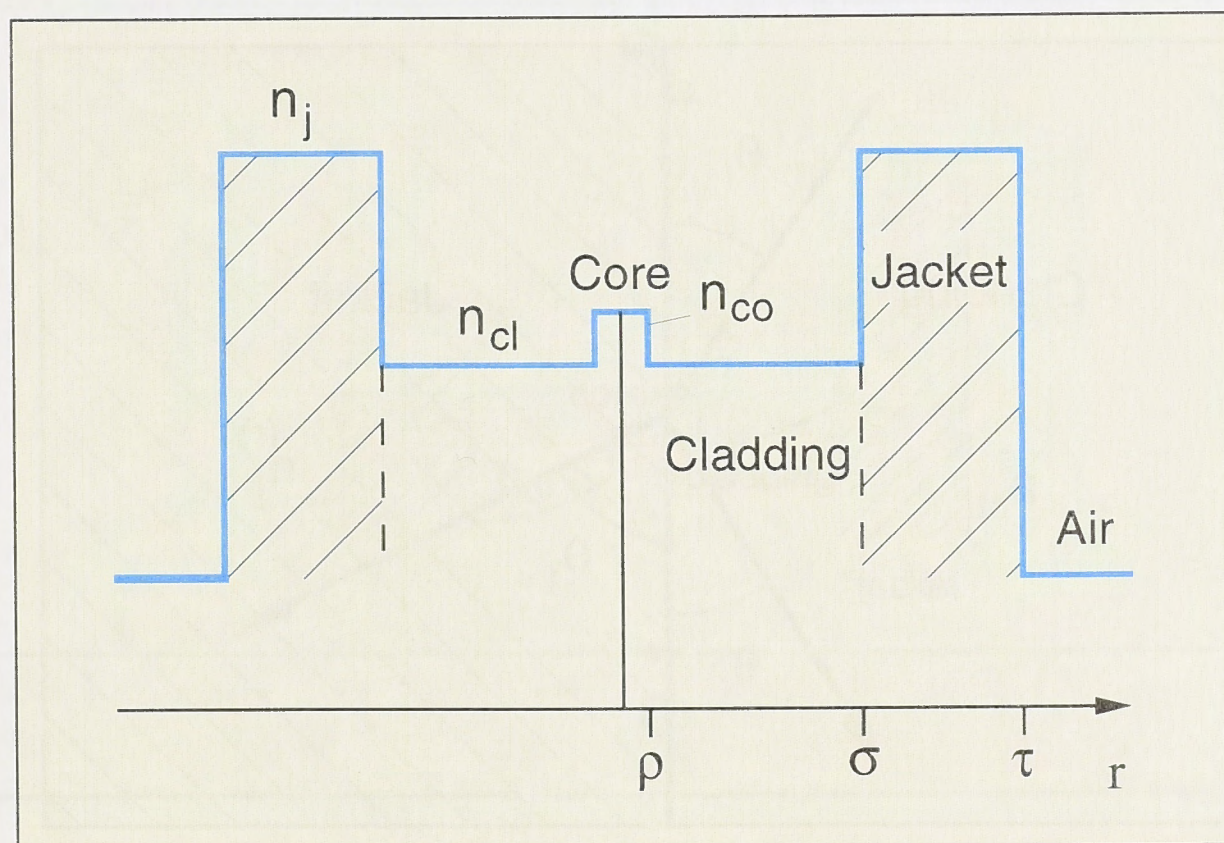


Figure 4.6: Schematic of the cross-section of the finite-cladding fibre, showing the index values and radii bounding each region.

The core and cladding materials are assumed non-absorbing, in which case the indices are real, whereas the coating is assumed absorbing with complex index $n_j = n_j^{(r)} + in_j^{(i)}$, where superscripts "r" and "i" denote real and imaginary parts, respectively.

4.2.2 Modified bend loss mechanism

We showed in Section 4.1 that bend loss on an infinite-cladding fibre is due to power radiating away indefinitely into the cladding beyond the radiation caustic. This situation is radically modified by the jacket of the practical fibre, and essentially transforms the radiation model into an absorption and scattering model. At the interface between the cladding and the jacket, there is a large increase in index from $n_{cl}^{(r)} = 1.447$ to $n_j^{(r)} = 1.54$. If the radiation caustic is located within the cladding region, then the radiation impinging on this interface is incident at a small angle relative to the interface.

To lowest order, the cladding-jacket interface acts as a partial reflector. Hence some of the radiation arriving at this interface is reflected back into the cladding (see Fig. 4.7). Secondly, the large index difference between the jacket (1.54) and air (1.0) tightly confines the refracted field to the absorbing jacket material.

This effect radically modifies the power attenuation coefficient given by Eqn. (4.8) for smaller bend radii. A finite cladding thickness leads to an oscillatory behaviour of the bend loss as a function of the bend radius and the wavelength [46]. This is caused by interference between the whispering gallery (WG) modes [46] within the cladding, guided by the cladding-jacket and/or jacket-air interfaces, and the core fundamental mode. The period of the oscillations depends on the beat length between the WG and core-guided modes.

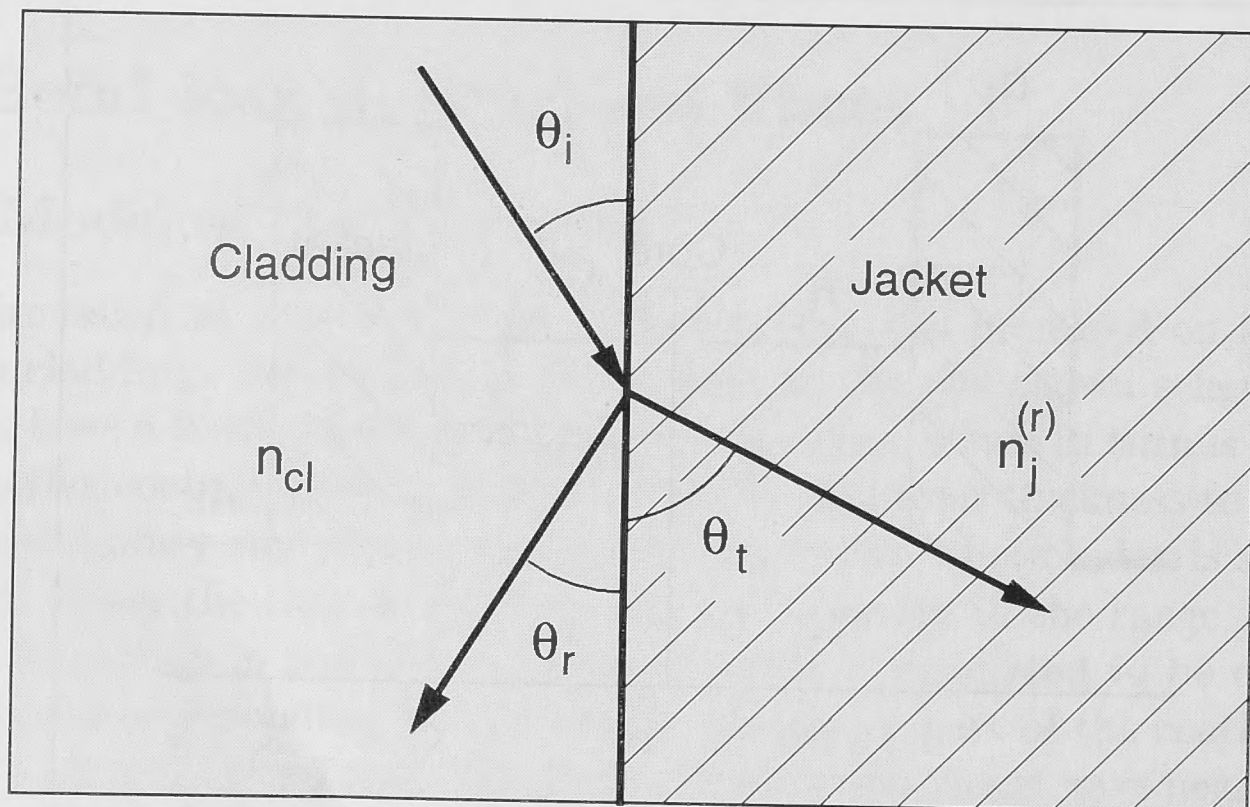


Figure 4.7: Cladding-jacket interface.

The effective waveguide core diameter in the (u, v) plane is

$$D = R_b \ln \left(\frac{R_b + \rho}{R_b - \rho} \right). \quad (4.15)$$

Thus, the piecewise step profile in Fig. 4.8(a) is transformed into the profile shown in Fig. 4.8(b).

This transformation provides a clear insight into the problem and lends itself into a convenient numerical implementation (see Appendix A.3 for more detail). Using this formalism and the transfer matrix approach [52], the eigenmodes of the bent waveguide are readily determined numerically. As an example, Figure 4.9 shows the field distribution of the fundamental core-guided mode and first two cladding modes of a straight fibre for $\lambda = 1.3 \mu\text{m}$ (a) and $\lambda = 1.55 \mu\text{m}$ (b) signal wavelengths.

4.2.4 Variable curvature bends: numerical coupled mode analysis

If we take the full core-cladding-jacket structure into account, then it is quite clear that, in addition to the modes guided in the core, discrete modes can propagate in the fibre cladding. Due to the perturbation caused by variable bending, substantial power can be transferred from the core-guided mode to the cladding-guided modes when the resonant condition is satisfied (i.e. when the phase velocities of the modes become identical) [5, Sectn. 27–3]. In the first approximation we can assume, that the highly absorbing jacket ($\gamma > 1000 \text{ dB/km}$) does not significantly affect the propagation constants of the cladding modes, and we ignore any interactions with coating modes, i.e. modes guided predominantly by the cladding-coating-air part of the profile.

In order to estimate the magnitude of the loss in the core-guided mode due to mode coupling, we use the coupled mode theory approach [5]. It results in a set of coupled-wave equations, which find their detailed description in Appendix B:

$$\begin{cases} \frac{db_1}{dz} - i(\beta_1 + D_{11})b_1 = iD_{12}b_2, \\ \frac{db_2}{dz} - i(\beta_2 + D_{22})b_2 = iD_{21}b_1, \end{cases} \quad (4.16)$$

where $b_1(z)$ and $b_2(z)$ are the coefficients of the normalised core and cladding modes, involved in the power exchange process, $\beta_1(z)$ and $\beta_2(z)$ are the propagation constants of the core and cladding modes of the unperturbed (straight) fibre, respectively, and $D_{ij}(z)$ is z -dependent coupling coefficient. To determine the coupling coefficients, which are proportional to the rate of change in bend radius, we calculate numerically overlap integrals (B.12) [see Appendix B.2]. Only the coupling between the even fundamental core mode and the odd first cladding mode of the transformed profile is taken into account, since coupling associated with the even second cladding mode is found to be negligible on symmetry grounds.

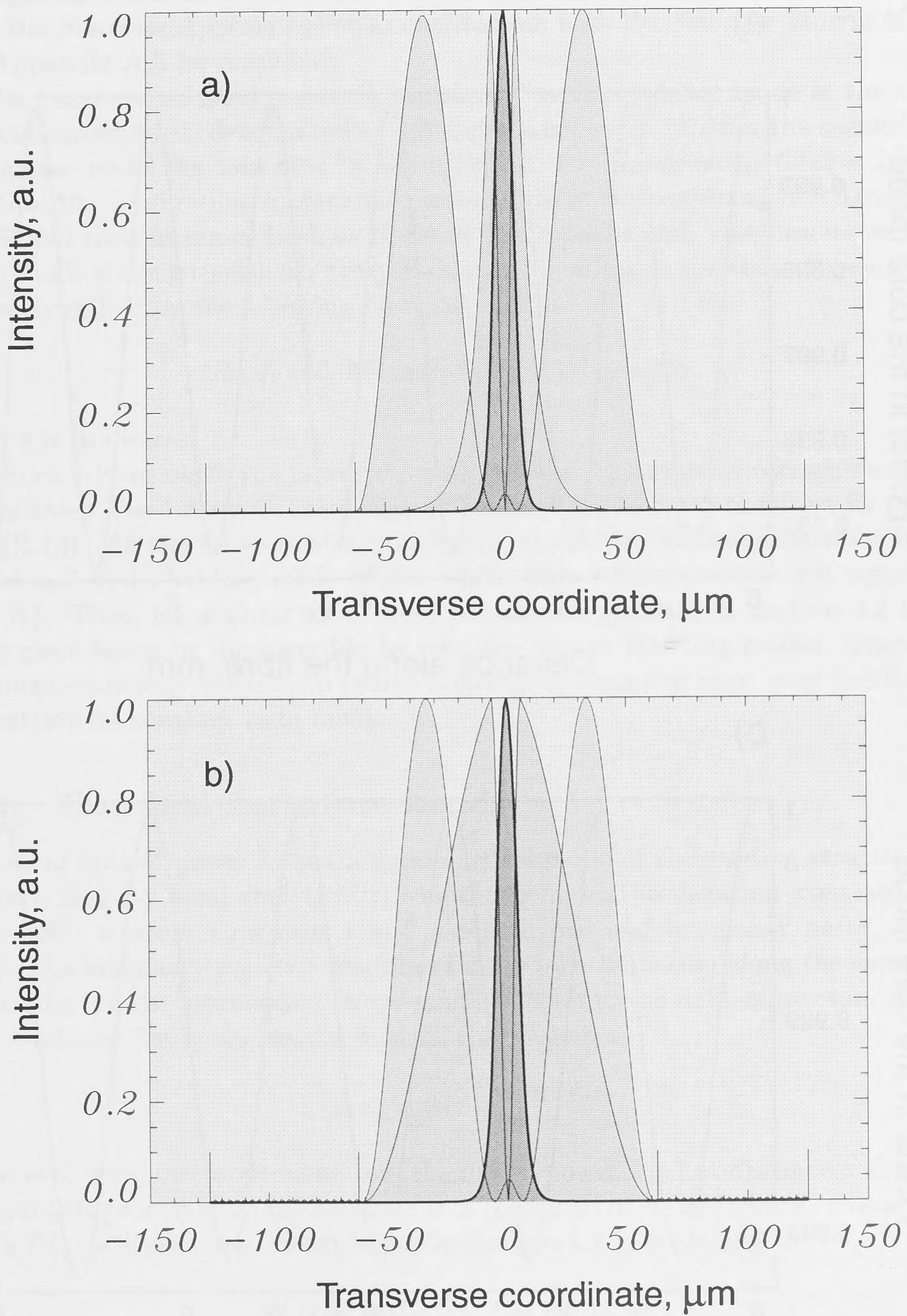


Figure 4.9: Fields of the core mode (darker) and first two cladding modes at (a) 1.3 and (b) 1.55 μm wavelengths.

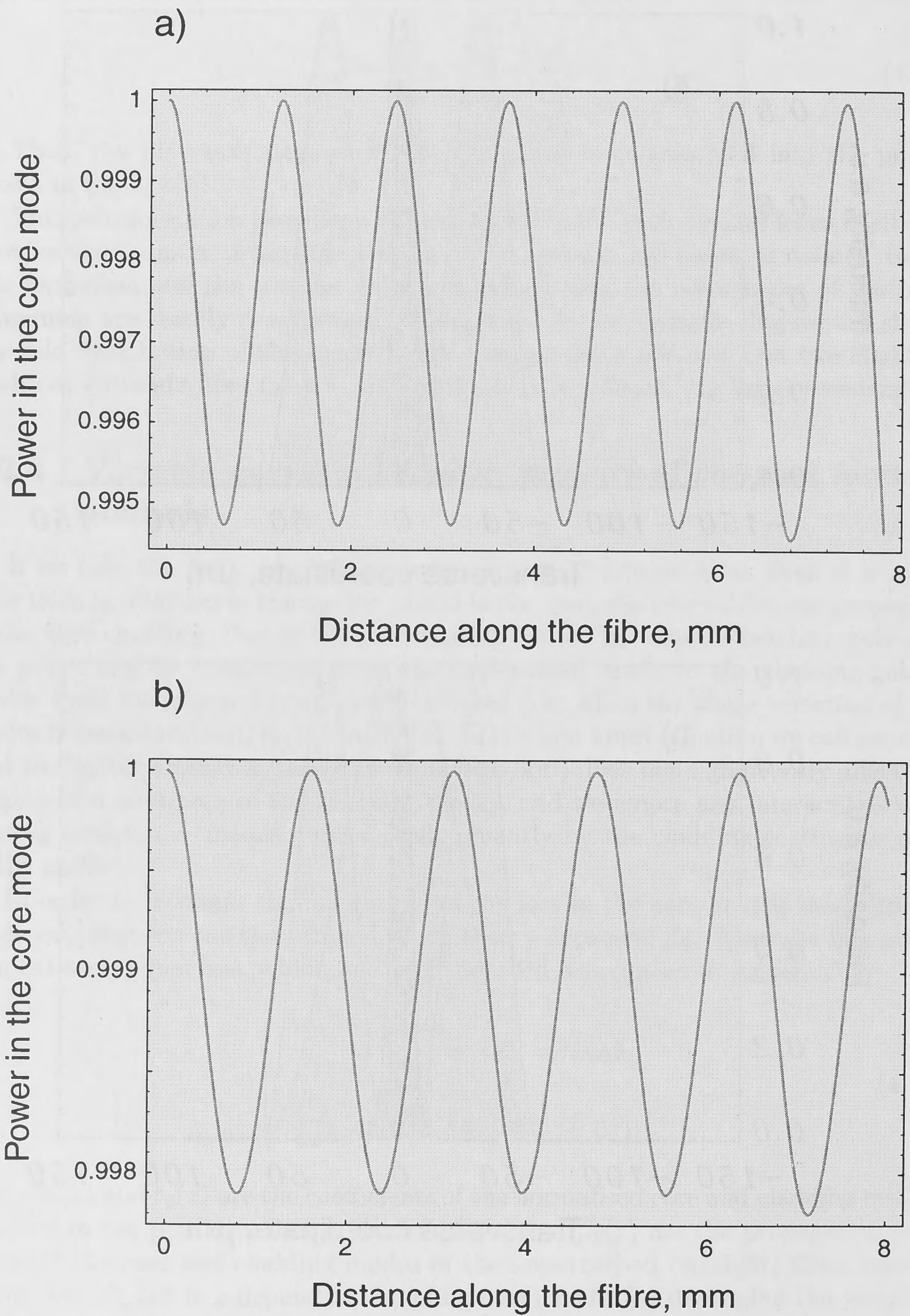


Figure 4.10: Fundamental mode power dynamics at (a) 1.3 and (b) 1.55 μm wavelengths.

Propagation constants of the core and cladding modes β_1 and β_2 are readily obtained using the *Staircase Approximation* in conjunction with the *Transfer Matrix Method* (see Appendix A.3 for a review).

The fractional coupled power P_2 transferred to the cladding mode at the end of the bent waveguide is determined by solving equations (B.13). For the quantitative analysis we model the bent fibre by an arc with z -varying curvature $C(z) = 1/R_b(z)$ such that the bend radius R_b decreases from 10 cm at the beginning to 0.5 cm in the middle and then increases back to 10 cm at the opposite end. Continuous variation of bend radius along the length z of a fibre, corresponding to the above arc geometry, can be described by the following function $R_b(z)$:

$$R_b(z) = 0.095 \tanh(500z - 4)^2 + 0.005, \quad (4.17)$$

where z is in metres.

Figure 4.10 presents the power dynamics of the fundamental core-guided mode for the cases $\lambda = 1.3 \mu\text{m}$ (a) and $\lambda = 1.55 \mu\text{m}$ (b), which are obtained by solving Eqs. (B.13). As can be seen from this figure, the power exchange between fundamental and first cladding mode of the whole fibre cross-section is not significant ($< 1\%$). Thus, for a given set of fibre parameters (defined in Section 4.2.1), we can neglect losses in the core due to coupling to the cladding modes. Since this coupling occurs only when bend radius is changing along the fibre, next Section will concentrate on constant radii bends.

4.2.5 Constant curvature bends

Loss of optical power from the fundamental mode of the guiding structure can be accounted for semi-analytically, via the complex propagation constant $\beta = \beta^{(r)} + i\beta^{(i)}$, where superscripts r and i denote real and imaginary parts, respectively. The imaginary part $\beta^{(i)}$ describes for modal attenuation along the waveguide by introducing the attenuation factor $\exp(-\beta^{(i)}z)$ into the field expression. Within weak-guidance, the scalar modal field $E(x, z)$ becomes

$$E(x, z) = \psi(x)e^{i\beta^{(r)}z - \beta^{(i)}z}. \quad (4.18)$$

In the weak-guidance approximation, the modal power $P(z)$ at distance z along the waveguide is proportional to the integral of $|E(x, z)|^2$ over the infinite cross-section. Hence $P(z)$ will decrease, as explained in Section 4.1.1, according to

$$P(z) = P(0)e^{-2\beta^{(i)}z} = P(0)e^{-\gamma z}, \quad (4.19)$$

where

$$\gamma = 2\beta^{(i)}. \quad (4.20)$$

To quantify pure bend loss in finite-cladding fibres (as shown in Figures 4.5 and 4.6), we first approximated the bent fibre by a straight slab waveguide with a

modified refractive index profile using conformal transformation introduced in Section 4.2.3. To find numerically fields and propagation constants of the fundamental core-guided mode of the transformed structure we used the *Staircase Approximation* together with the *Transfer Matrix Approach* [52–54], delineated in Appendix A.3. For our purposes we were interested only in the imaginary part $\beta^{(i)}$ of the propagation constant of the fundamental core-guided mode and obtained the attenuation coefficient γ via expression (4.20).

Fig. 4.11 shows the attenuation coefficient γ in dB/cm [see relation (4.10) for a definition of decibel units] as a function of bend radius for a single mode fibre operating at $\lambda = 1.55 \mu\text{m}$ wavelength with parameter values: $n_{\text{co}} = 1.47303$, $n_{\text{cl}} = 1.46943$, $n_j^{(r)} = 1.54$, $n_j^{(i)} = 0.0001$, $\rho = 4.15 \mu\text{m}$, $\sigma = 62.5 \mu\text{m}$, $\tau = 125 \mu\text{m}$.

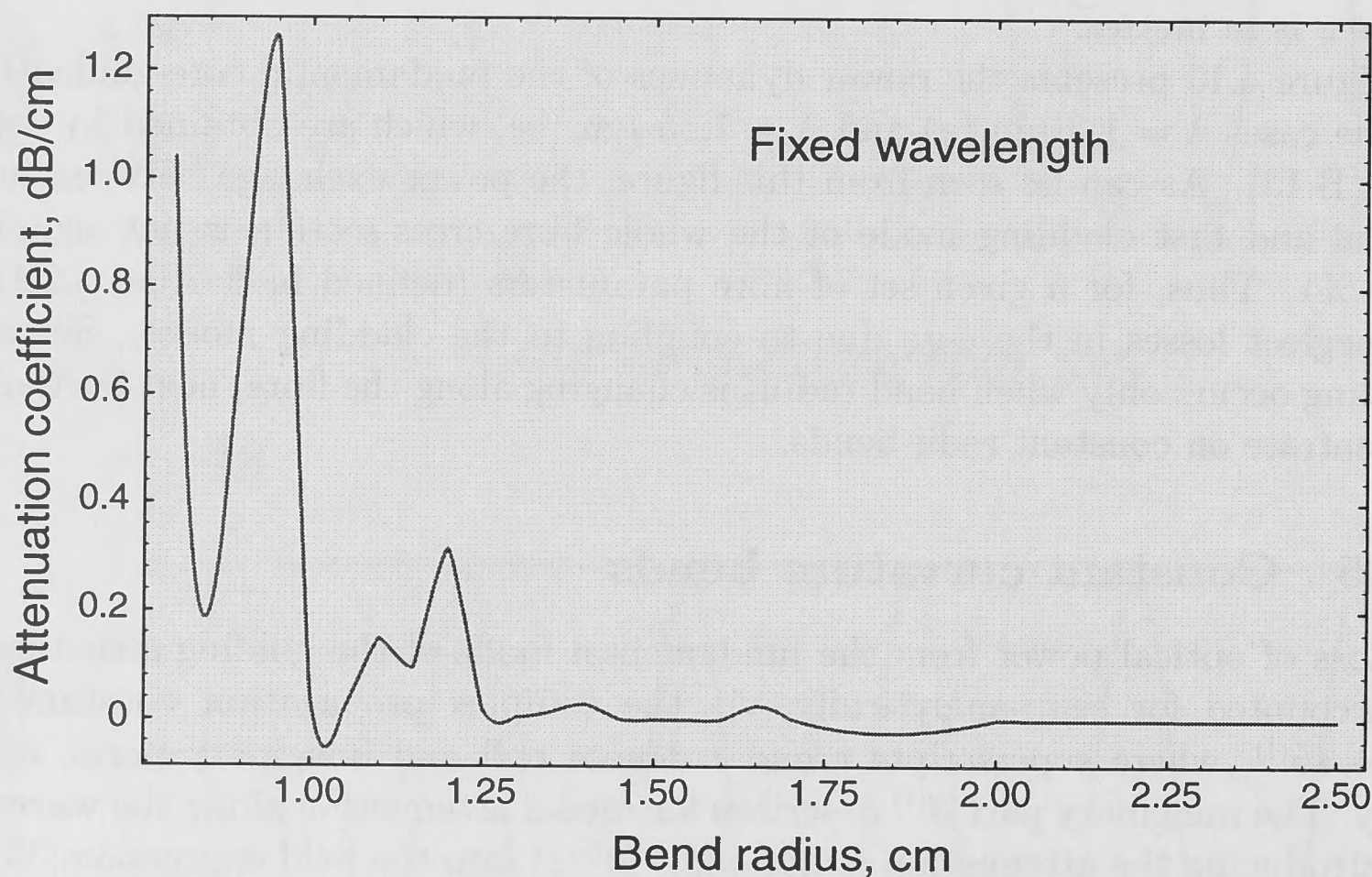


Figure 4.11: Attenuation coefficient γ as a function of bend radius for a waveguide with finite cladding and jacket.

The values of bend loss in Figure 4.11 are lower than that predicted by the infinite-cladding expression of Eqn. (4.8), and show oscillations that increase in amplitude as the radius of the bend is reduced [44]. Such oscillations have been observed experimentally [46], and occur due to reflections from cladding-jacket interface. Dips and peaks in the loss curve correspond to constructive and destructive interference of the field reflected from the cladding-jacket interface with the core field as bend radius varies.

Since the quantitative expression (4.8) for the attenuation coefficient was obtained in the frame of the infinite-cladding model of the circular fibre, and we are currently working in the slab waveguide model, we should now seek an expression

for modal attenuation in a bent slab. The theoretical value, which accounts for the mode field shift on the bend (as shown in Figure 4.4), is given by [55]:

$$\gamma = \frac{U^2 W^2 e^{2W}}{k n_{\text{eff}} \rho^2 (1+W) V^2} \exp \left\{ -\frac{4}{3} \Delta \frac{R_b W^3}{\rho V^2} \right\}, \quad (4.21)$$

where $U = \rho \sqrt{k^2 n_{\text{co}}^2 - \beta^2}$, $W = \rho \sqrt{\beta^2 - k^2 n_{\text{cl}}^2}$, $V = k \rho \sqrt{n_{\text{co}}^2 - n_{\text{cl}}^2}$, $k = 2\pi/\lambda$ is the wavenumber, λ the source free-space wavelength, n_{co} the core index, n_{cl} the cladding index, and $\Delta = (n_{\text{co}}^2 - n_{\text{cl}}^2)/2n_{\text{co}}^2$ the relative index difference, β and $n_{\text{eff}} = \beta/k$ are the propagation constant and the effective index of the fundamental mode of the straight waveguide, respectively.

Oscillations in the bend loss response make it difficult to characterise and optimise fibre performance for certain applications that require monotonic increase in loss with decrease in bend radius (e.g., variable bent fibre attenuators). Since these oscillations are a direct result of reflections at the cladding-coating interface, we should first investigate how changes in refractive index of the coating affect the bend loss response. Put another way, the boundary between the two regions should be made as “transparent” as possible to minimise reflected light. Furthermore, high jacket absorption would also inhibit radiation coming back into the core area after reflecting from the coating-air interface.

To test the bend loss response at $1.3 \mu\text{m}$ wavelength we use the same fibre parameters as in Figure 4.11, except that the imaginary part of the coating refractive index is now greater: $n_{\text{co}} = 1.47303$, $n_{\text{cl}} = 1.46943$, $n_j^{(r)} = 1.46943$, $n_j^{(i)} = 0.0004$, $\rho = 4.15 \mu\text{m}$, $\sigma = 62.5 \mu\text{m}$, $\tau = 145 \mu\text{m}$. By increasing $n_j^{(i)}$, we effectively increase absorption in the jacket, thereby bringing our model closer to the infinite-cladding approximation, in which all radiated light is assumed to be lost in the cladding. However, $n_j^{(i)}$ cannot be arbitrarily increased to provide the desired degree of absorption, since the transition from zero value in the cladding to non-zero value in the jacket also sets up an internal boundary and causes reflections. We found that the *oscillations in the bend loss from the fundamental mode can be eliminated entirely or significantly reduced* by closely matching the real part of the refractive index of the coating to that of the cladding and increasing its imaginary part to achieve a balance between absorption and reflection [44] (for our set of parameters an increase of $n_j^{(i)}$ from 0.0001 to 0.0004 proved sufficient). The pure bend loss will then be a maximum and approach the theoretical value of Eqn. (4.21), as is illustrated in Fig. 4.12.

To give an insight into the sensitivity of the attenuation coefficient to deviations from exact index-matching conditions, we calculated numerically a series of bend loss curves for several values of index mismatch. For the optimised response plotted in Fig. 4.13 by the thick line, we used the following fibre parameters for a $1.3 \mu\text{m}$ carrier wavelength: $n_{\text{co}} = 1.44846$, $n_{\text{cl}} = 1.447$, $n_j^{(r)} = 1.447$, $n_j^{(i)} = 0.0004$, $\rho = 6 \mu\text{m}$, $\sigma = 62.5 \mu\text{m}$, $\tau = 145 \mu\text{m}$. This case corresponds to exact matching of the cladding and jacket real refractive indices, with a relatively high absorption in the jacket region ($n_j^{(i)} = 0.0004$).

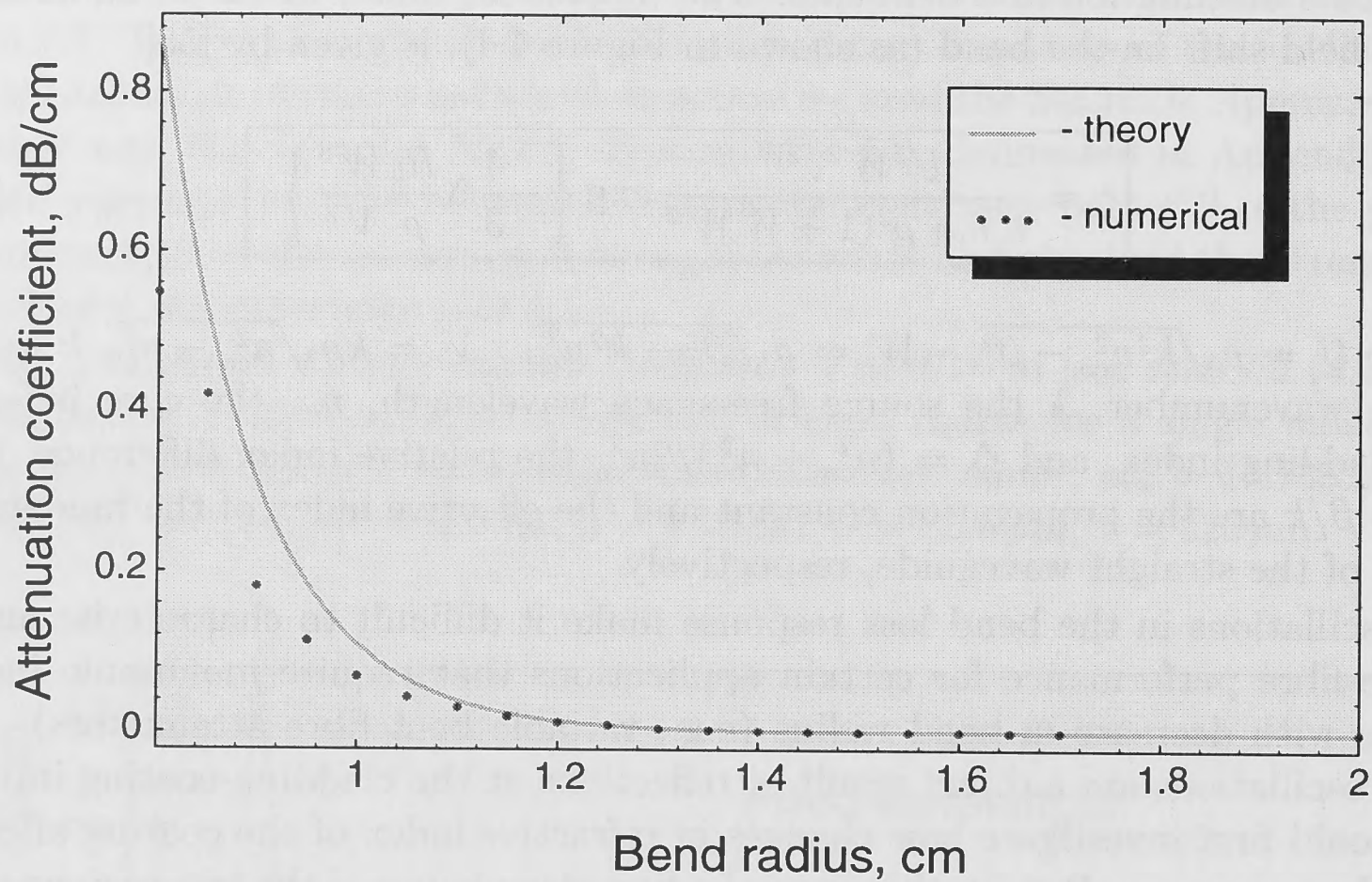


Figure 4.12: Comparison between numerically obtained values of attenuation coefficient γ and theoretical results.

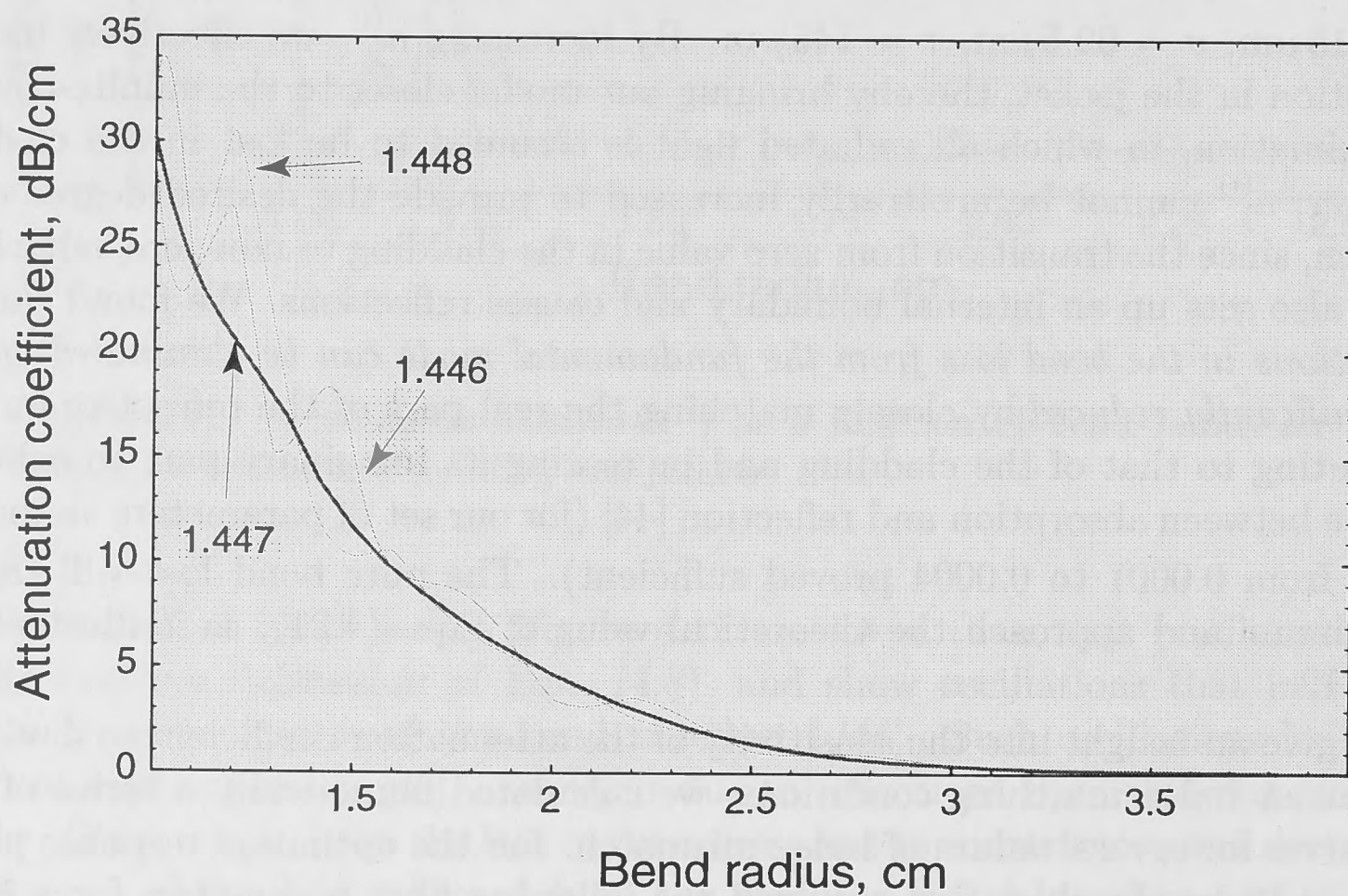


Figure 4.13: Attenuation coefficient γ vs. bend radius for exact (thick line, $n_{cl} = n_j^{(r)} = 1.447$) and approximate index matching (thin lines) for two cases of mismatch ($n_j^{(r)} = 1.446$ and $n_j^{(r)} = 1.448$).

This combination of parameter values *significantly dampens oscillations in the bend loss curves* shown by thin lines [44], which correspond to a slight mismatch between cladding and coating indices. Clearly, the difference of only 0.001 between n_{cl} and $n_j^{(r)}$ results in significant oscillations only for very tight bends ($R_b < 1.5$ cm in Fig. 4.13). For larger bend radii, no significant changes compared to the exact matching case were observed, which suggests an experimentally feasible fibre design for a variable bent-fibre attenuator.

4.3 Conclusions

In this Chapter we have covered several aspects pertinent to bent finite-cladding practical fibres, ranging from background theory to coupled mode analysis of variable curvature bends, and numerical quantification of bend loss behaviour of constant curvature bent fibres for possible practical applications. We have demonstrated that for our set of parameters loss from the fundamental mode due to coupling to cladding modes is negligible, and numerically quantified bend loss in practical finite cladding fibres, including the oscillatory behaviour of the attenuation coefficient at small bend radii. An experimentally feasible technique of matching the coating and cladding indices and increasing the coating absorption has been proposed to suppress these oscillations and suggests a simple design for a bent-fibre attenuator [44]. The suggested device should overcome the shortcomings of an attenuator based on bend loss from a single-mode fibre with unmatched cladding and coating indices.



Figure 4.14: Electric field profile of an infinite-cladding fibre, showing essentially the fundamental core-guided mode.

The combination of parameter values simultaneously displays deviations in the bend loss curves shown by the lines (1), which correspond to a sharp mismatch between cladding and coating indices. Clearly, the differences of only 0.01 between n_1 and n_2 result in significant variations only for very tight bends ($R < 1$ cm). Fig. 4.13. Exaggerated bend radii, to significant changes compared to the exact matching case are shown, which suggests an experimentally feasible fibre design for a variable bend-tightness attenuator.

4.3 Conclusions

In this Chapter we have covered several aspects pertinent to bent finite-cladding practical fibres ranging from background theory to empirical and analytical available curvature bends, and numerical quantification of bend loss behaviour of constant curvature bend fibres for possible practical applications. We have demonstrated that for a given set of parameters loss from the fundamental mode due to coupling to cladding modes is negligible, and numerically quantified bend loss in practical finite cladding fibres exhibiting the oscillatory behaviour of the attenuation coefficient at small bend radii. An experimentally feasible technique of matching the coating and cladding indices and their variation with respect to constant bend loss proposed to suppress these oscillations and suggest a simple design for a bend-tightness attenuator based on bend loss from a single mode fibre with mismatched cladding and coating indices.

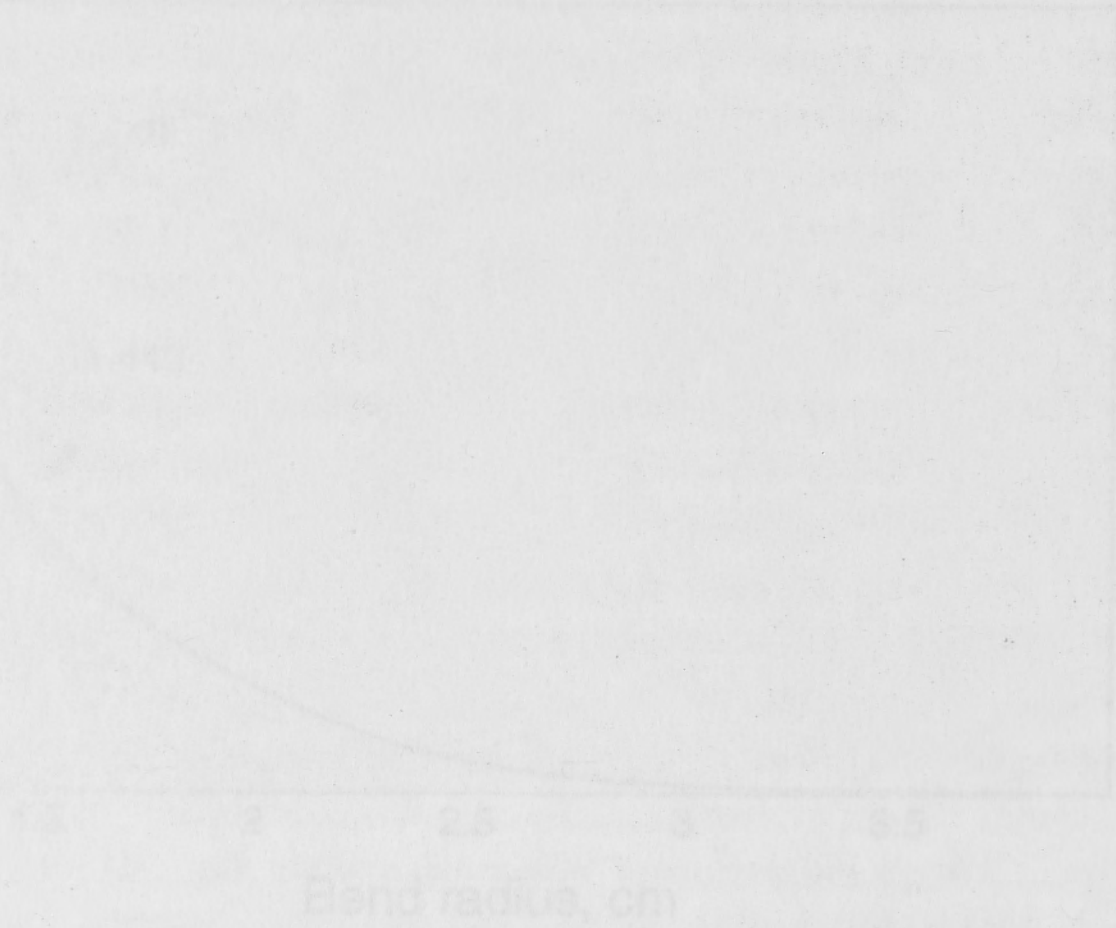


Figure 4.13. Exaggerated bend radii for exact (1) and mismatched (2) cladding and coating indices. The y-axis represents the bend loss coefficient α in dB/cm. The x-axis represents the bend radius R in cm. The parameters are $n_1 = 1.448$, $n_2 = 1.447$, $n_c = 1.449$, $n_{cl} = 1.448$, $\lambda = 1.55 \mu\text{m}$, $a = 2.5 \mu\text{m}$, $b = 1.25 \mu\text{m}$.

Bends in Depressed-Cladding and W-Fibres: modal degeneracy

On matched-cladding fibres, described in the previous Chapter, where there are no depressions in the refractive index profile, the fundamental mode does not have a finite cutoff wavelength if the cladding were unbounded (as in Fig. 5.1). In practical fibres, of course, the cladding has a finite thickness, typically about $60\ \mu\text{m}$. In some cases, such as fused fibre taper couplers [24], the core-guided modes propagate beyond their normal cutoff wavelengths. If the source wavelength were continuously increased, the effective index $n_{\text{eff}} = \beta/k$ of the fundamental mode would eventually decrease below the cladding index, i.e. be cut off. It would then propagate as a cladding mode with its field located predominantly in the cladding and its power would be gradually attenuated by the adjacent fibre coating. In other words, the fundamental mode would behave very much like a leaky mode in an unbounded cladding, and its attenuation would increase as the wavelength increases.

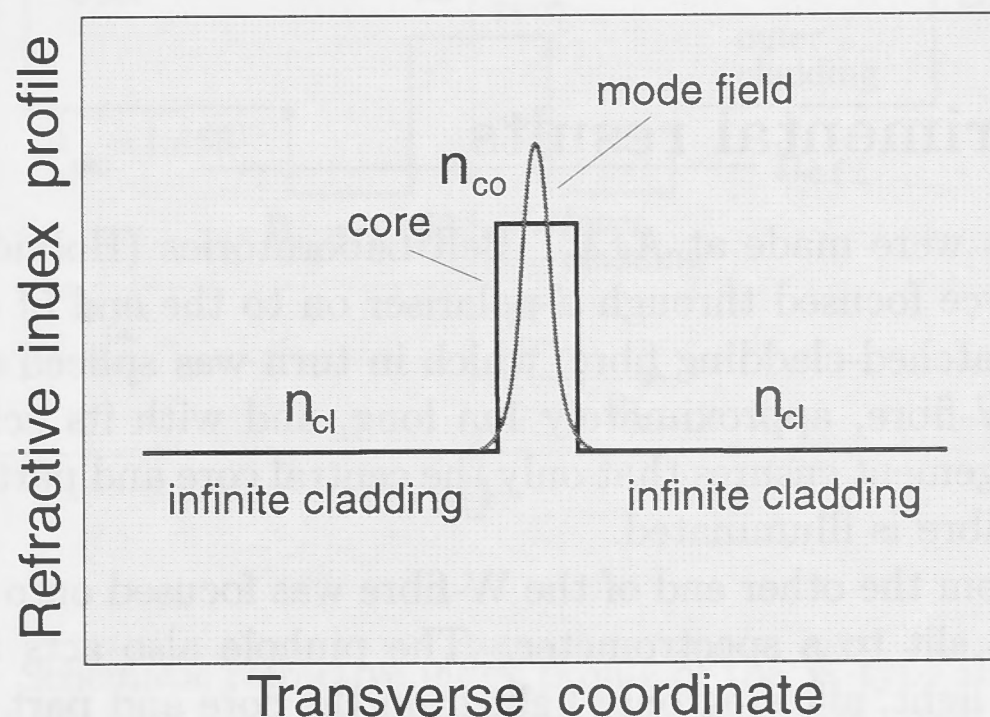


Figure 5.1: Refractive index profile of an infinite-cladding fibre, showing schematically the fundamental core-guided mode.

In the case of depressed-cladding and W-fibres, both of which have a depressed region between the core and the cladding, the situation can be very different. Existing work on whole fibre effects beyond the fundamental-mode cutoff wavelength in such fibres has focused on anomalous loss peaks, or, equivalently, transmission dips when the fibre is laid straight [56]. A basic study of the mechanism responsible for these transmission dips has been discussed elsewhere [57, 58], showing that, as the source wavelength increases beyond the normal fundamental mode cutoff, the dips can be explained in terms of abrupt changes in the power propagating in the core due to successive core mode-to-cladding mode, and cladding mode-to-core mode transitions with increasing source wavelength.

This Chapter examines changes to the above transmission characteristics which occur when the depressed-cladding and W-fibres are slightly bent. The literature describing the effects of bends and micro-bends on fibres is extensive, but the majority of these studies assume fibres with unbounded claddings and address primarily radiation loss from the fundamental mode [47, 59, 60]. The degeneracy of the fundamental mode associated with bending is hardly affected unless the bend radius is extremely small, close to the breaking point of the fibre. However, as we will demonstrate both experimentally and theoretically in this Chapter, bend-induced break of the cladding modes' degeneracy can be significant even at relatively large bend radii of the order of a metre or more [61, 62]. This effect is evident through splitting of the transmission dips of the fundamental mode transmission spectrum beyond the cutoff wavelength.

In Section 5.1, the experiment arrangements are described and the basic measured data presented. Section 5.2 introduces an equivalent straight slab waveguide for modelling the phenomenon. Section 5.3 explains the qualitative mechanisms, and Section 5.4 provides a simulation of the experiment, quantifying the location and strength of the transmission dips, and the splitting of these dips due to bending.

5.1 Experimental results

Measurements were made at AT&T Bell Laboratories (Holmdel, U.S.A.) with a white light source focused through a polariser on to the end of a straight length of single-mode matched-cladding fibre, which in turn was spliced symmetrically to a graded-index W-fibre, approximately 1 m long, and with its acrylate coating in place. This arrangement ensures that only the central core and part of the depressed region of the W-fibre is illuminated.

The output from the other end of the W-fibre was focused onto a pinhole, which acts as the input slit to a spectrometer. The pinhole also acts to filter out any residual cladding light, allowing only light from the core and part of the depressed region to be transmitted. The detected power measurements were made with a silicon detector, which cuts off beyond 1100 nm.

The profile of the particular W-fibre used in the experiment is graded across both the core and depression. Whilst, in principle, the measured profile could be analysed for the effective indices of its fundamental core and cladding modes, uncertainties

in the profile measurement in the core and depression regions generate uncertainties in the effective index values, which makes it difficult to resolve the positions of the dips accurately. However, as this paper is mainly concerned with the splitting of the cladding mode effective index, it is not necessary to know the precise profile. Accordingly, we prefer to work with a piecewise step profile. For the same reason, we use a slab model to investigate the cladding modes' behaviour.

Thus, we adopt the profile illustrated in Fig. 5.2, where the core index $n_{co} = 1.461$, the inner cladding or depression has index $n_{ic} = 1.453$, and the outer cladding index is $n_{oc} = 1.458$. The coating surrounding the outer cladding has real and imaginary index values $n_{coat}^{(r)} = 1.54$ and $n_{coat}^{(i)} = 0.0001$, respectively, to simulate the effect of the acrylate fibre coating. Beyond the coating is air. The corresponding positions of the core–inner cladding, inner cladding–outer cladding, outer cladding–coating and coating–air interfaces are

$$\rho_{co} = 2.5 \mu m, \rho_{ic} = 8.5 \mu m, \rho_{oc} = 52.0 \mu m \text{ and } \rho_{coat} = 114.5 \mu m,$$

respectively, relative to the transverse x axis.

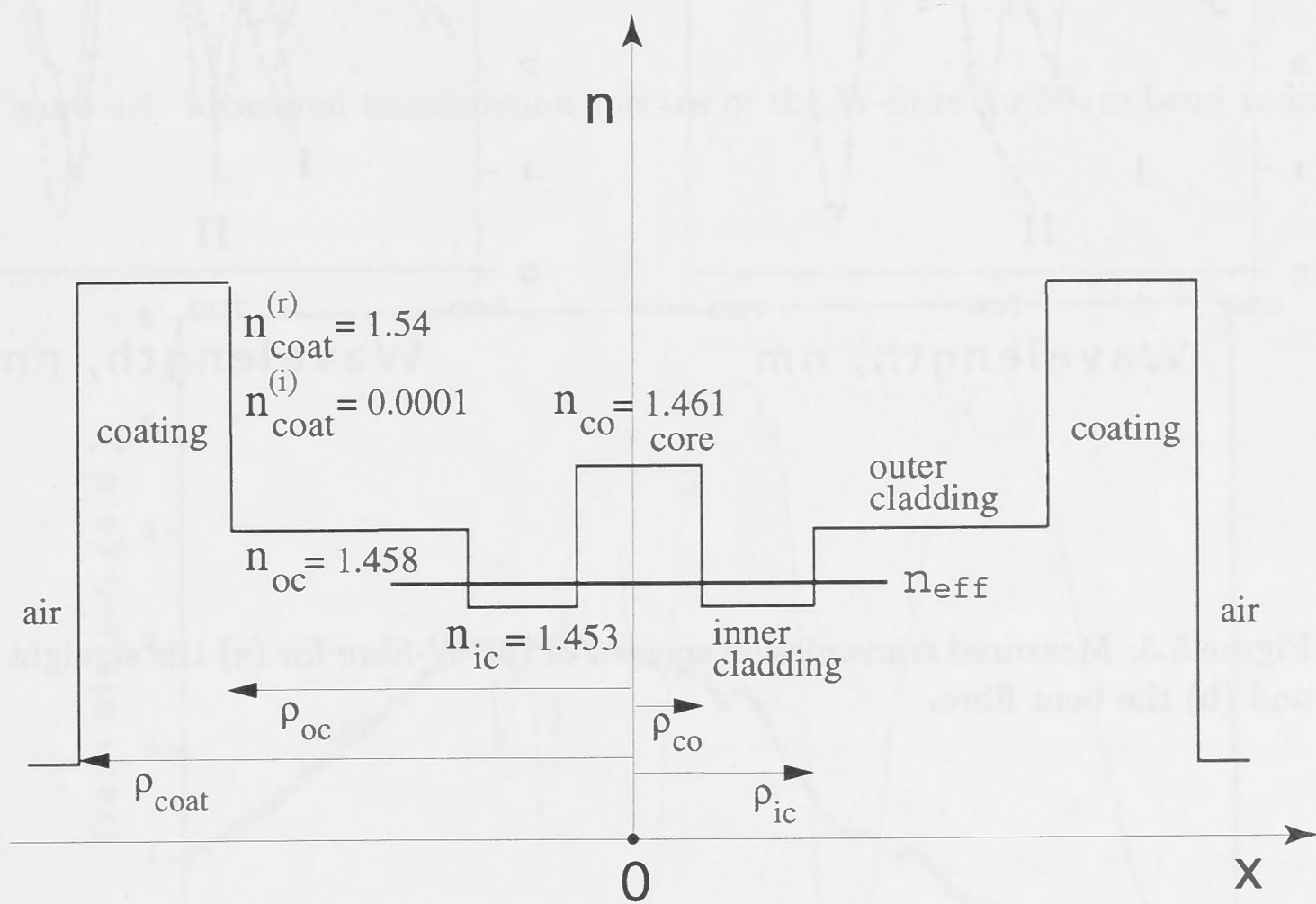


Figure 5.2: Schematic refractive index profile of the W-type slab waveguide with finite coating.

The measured power transmission spectrum of the straight W-fibre beyond the cutoff wavelength of the fundamental mode is plotted in arbitrary units in Fig. 5.3(a) as a function of source wavelength. As the source wavelength increases, transmission

dips are observed at discrete wavelengths of approximately 680, 700 and 730 nm, and the separation and depth of these dips increases with increasing wavelength. The same fibre is now realigned into a very gentle bend of approximately 150 cm radius, and the measurements repeated. This leads to the plot in Fig. 5.3(b). On comparing this plot with Fig. 5.3(a) (shown dotted), it is evident that the first depression (I) around 680 nm has been replaced by a shallower double dip, whereas the second (II) and third dips in Figs. 5.3(a) and (b) do not show this feature, but are shifted to slightly lower wavelengths.

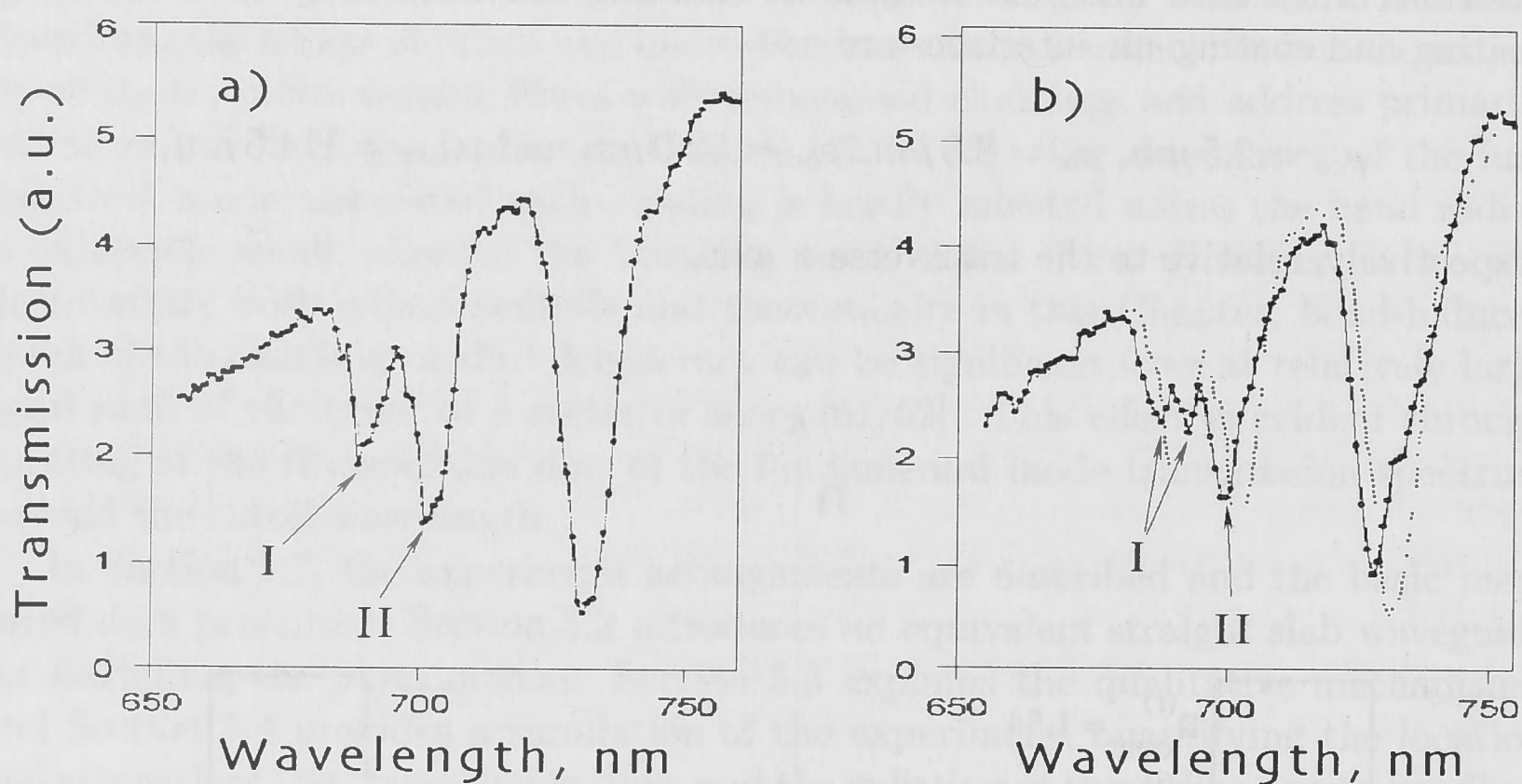


Figure 5.3: Measured transmission spectra of the W-fibre for (a) the straight and (b) the bent fibre.

The bend radius of the fibre was further reduced to about 50 cm, and the corresponding transmission spectrum is plotted in Fig. 5.4. Some new features are now evident. As well as the splitting of the first dip (I), seen in Fig. 5.3(b), similar splitting of the second transmission dip (II) and higher-order dips is observed, and new single dips at around 760 and 825 nm have appeared. Finally, if the bend radius is reduced to 4.5 cm by winding the fibre around a mandrel, the transmission spectrum of the fibre now appears as the smoothed-out curve in Fig. 5.5.

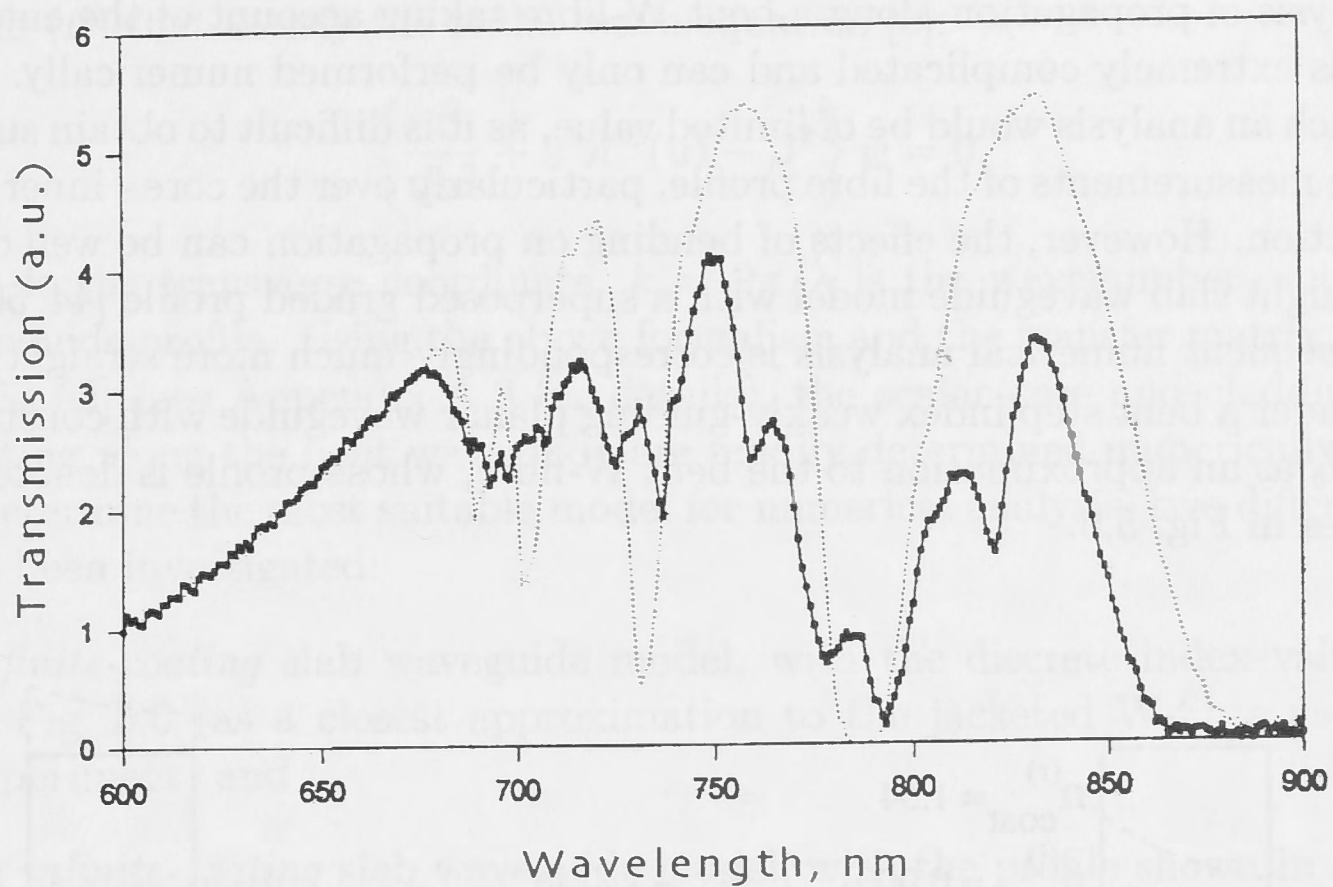


Figure 5.4: Measured transmission spectra of the W-fibre for 50 cm bend radius.

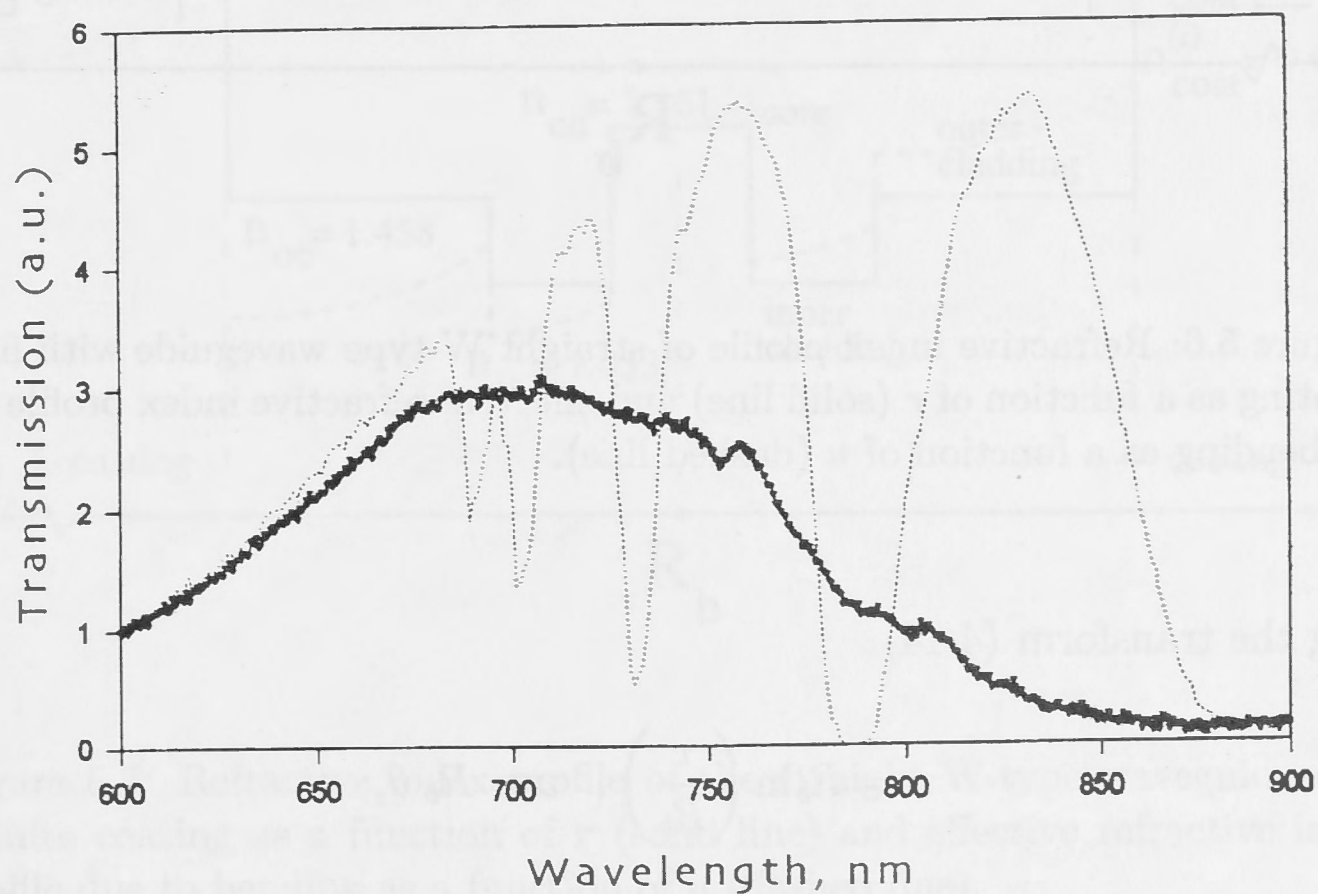


Figure 5.5: Measured transmission spectra of the W-fibre for 4.5 cm bend radius.

5.2 Bent slab model

Analysis of propagation along a bent W-fibre taking account of the entire cross-section is extremely complicated and can only be performed numerically. Furthermore, such an analysis would be of limited value, as it is difficult to obtain sufficiently accurate measurements of the fibre profile, particularly over the core - inner cladding cross-section. However, the effects of bending on propagation can be well described by a straight slab waveguide model with a superposed graded profile [44, 50, 53, 63]. The subsequent numerical analysis is correspondingly much more straightforward.

Consider a bent step index weakly-guiding planar waveguide with constant bend radius R_b as an approximation to the bent W-fibre, whose profile is denoted by the solid lines in Fig. 5.6.

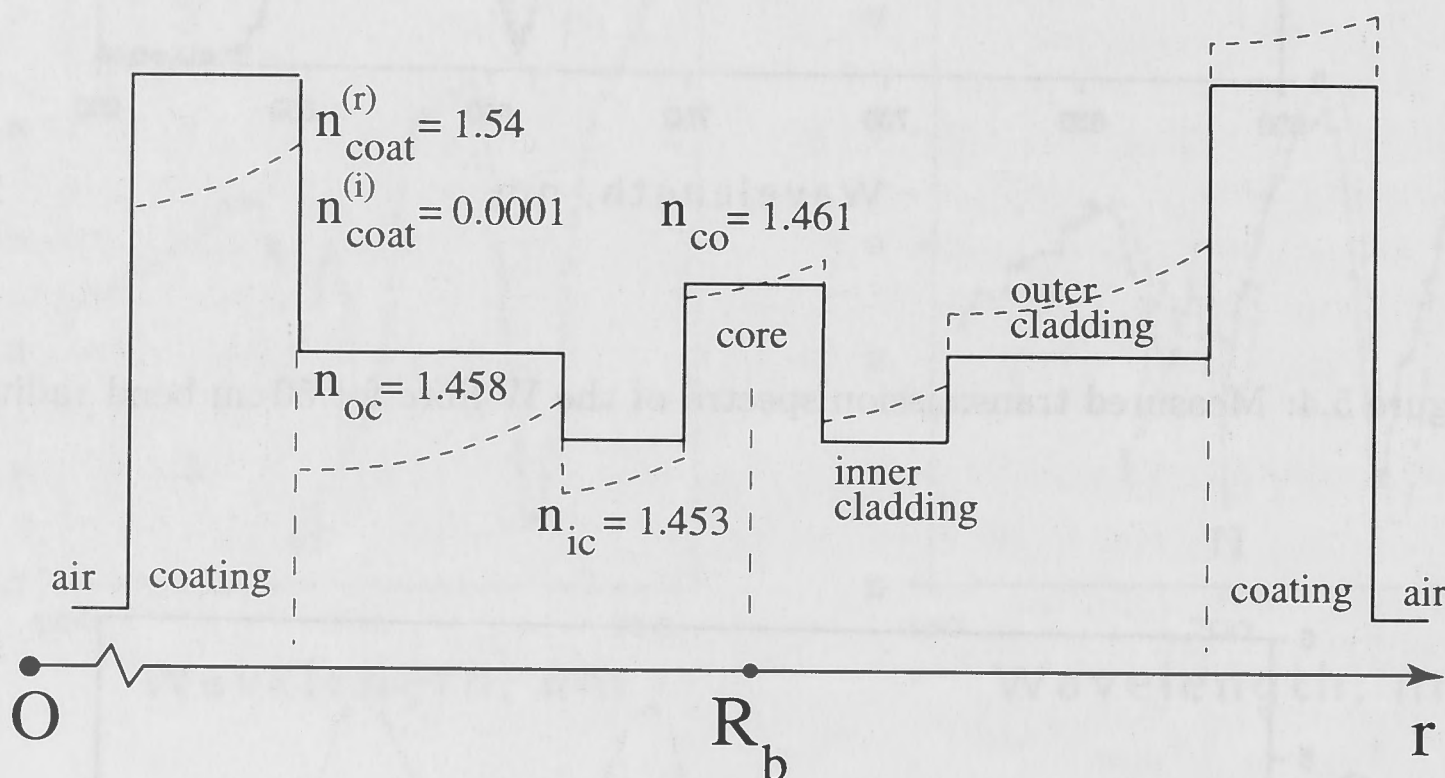


Figure 5.6: Refractive index profile of straight W-type waveguide with finite coating as a function of r (solid line) and effective refractive index profile due to bending as a function of u (dashed line).

Using the transform (4.14)

$$u = R_b \ln \left(\frac{r}{R_b} \right), \quad v = R_b \theta, \quad (5.1)$$

and mapping conformally the plane of curvature described in polar coordinates (r, θ) on to cartesian coordinates (u, v) [51], i.e. the bent waveguide onto a straight waveguide with a superposed graded index profile n' , we again obtain the result:

$$n' = n e^{u/R_b}, \quad (5.2)$$

indicated by the dashed curve. The transverse electric fields of the scalar modes of the waveguide have the form $E(u, v) = \psi(u) e^{i\beta v}$ with fields (ψ) and propagation constants (β) that satisfy the scalar wave equation [5]:

$$\left\{ \frac{d^2}{du^2} + k^2 n'^2(u) - \beta^2 \right\} \psi = 0, \quad (5.3)$$

where u is the transverse coordinate, $k = 2\pi/\lambda$ is the wavenumber, and $n'(u)$ is the waveguide profile. Using the above formalism and the transfer matrix approach [52–54, 64, 65] (see Appendix A.3 for details), the scalar core and cladding modes propagating along the bent waveguide are readily determined numerically.

To determine the most suitable model for numerical analysis, two different models have been investigated:

- a *finite-coating* slab waveguide model, with the discrete index values given in Fig. 5.6 (as a closest approximation to the jacketed W-fibre used in the experiment) and
- an *infinite-coating* slab waveguide model, with the profile shown in Fig. 5.7.

Note that the equivalent profile, shown dashed, also includes the coating regions.

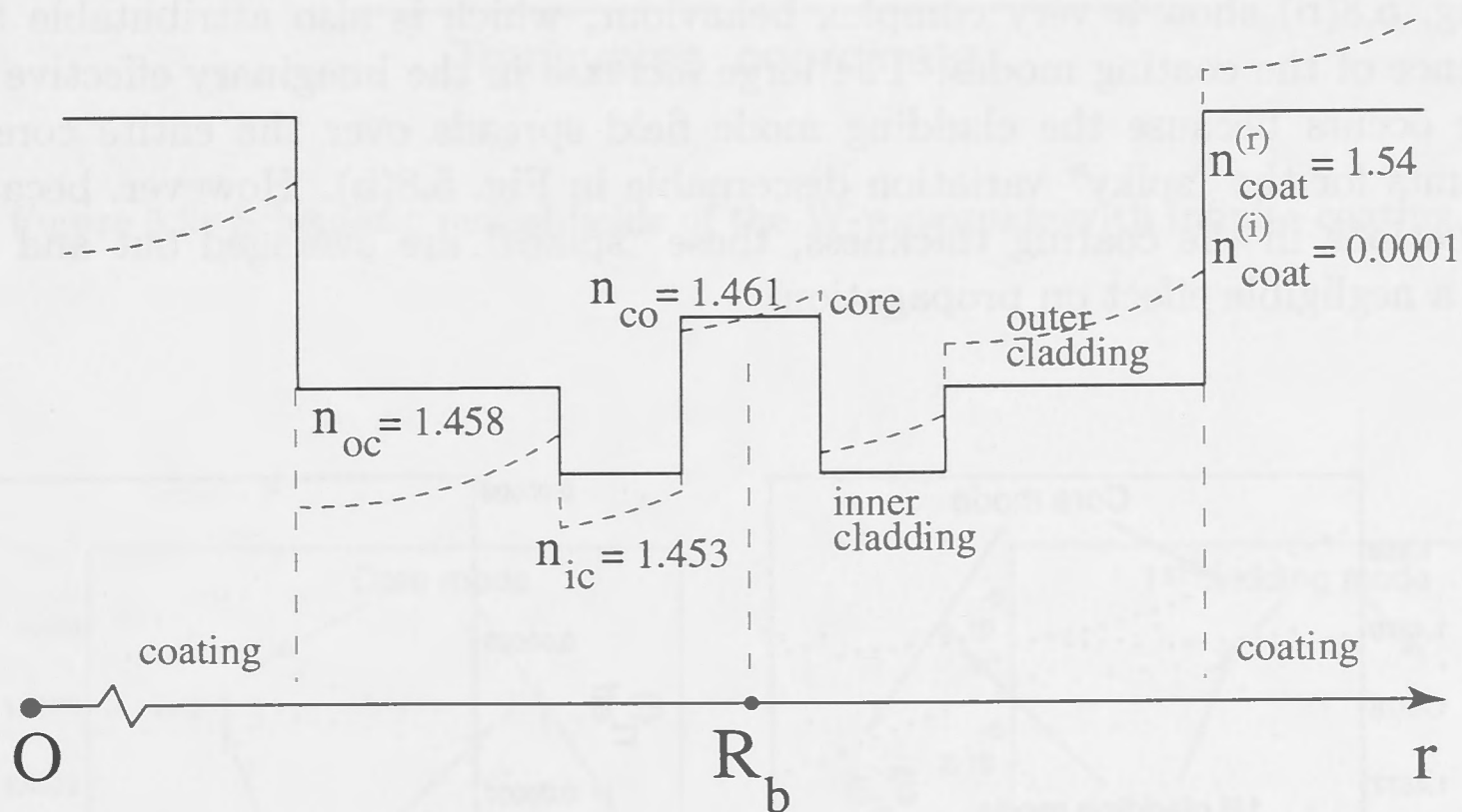


Figure 5.7: Refractive index profile of the straight W-type waveguide with infinite coating as a function of r (solid line) and effective refractive index profile due to bending as a function of u (dashed line).

The core, inner cladding and outer cladding are assumed non-absorbing with real refractive index values n_{co} , n_{ic} and n_{oc} , respectively, while the surrounding coating is absorbing and scattering with a complex index $n_{coat}^{(r)} + in_{coat}^{(i)}$; the small imaginary

part accounting for absorption and scattering. The real part of the coating dielectric constant is assumed to be much higher than that of the outer cladding, as in practice with acrylic coatings. The depression is assumed to be sufficiently large to ensure that the fundamental mode has a finite “cutoff” wavelength.

5.2.1 Finite coating model

Numerical solution of the scalar wave equation for a straight slab waveguide with a finite coating surrounded by air reveals multiple sets of eigenmodes of the whole structure that can be successively ascribed to the core region (fundamental mode), outer cladding (guided by the inner cladding - outer cladding area) and coating (bound by the protective absorbing jacket). In Figs. 5.8(a) and (b) we plot the real and imaginary parts of the fundamental and first cladding mode effective indices vs. the source wavelength, respectively. The real parts in Fig. 5.8(a) generally follow the expected evolution with wavelength, where the fundamental mode evolves into the first cladding mode and vice versa around $1.675 \mu\text{m}$ wavelength where the effective indices of the two modes are approximately equal. The small departures from this smooth evolution are attributable to the effects of coating modes, i.e. modes guided by the outer cladding - coating - air waveguide, which can significantly modify the first cladding mode at specific wavelengths. The plots of the imaginary part in Fig. 5.8(b) show a very complex behaviour, which is also attributable to the presence of the coating modes. The large increase in the imaginary effective index value occurs because the cladding mode field spreads over the entire core, and accounts for the “spiky” variation discernable in Fig. 5.8(b). However, because of fluctuations in the coating thickness, these “spikes” are averaged out and hence have a negligible effect on propagation.

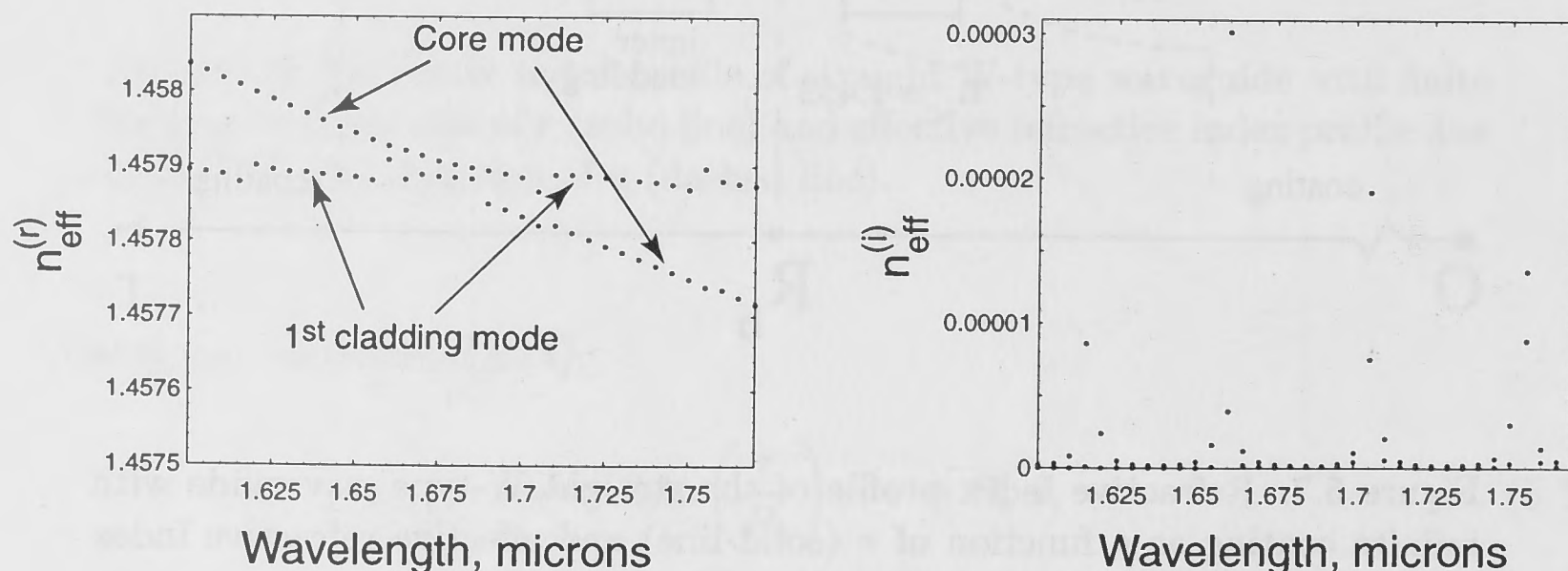


Figure 5.8: Effective index values vs. wavelength of the W-waveguide with finite coating; (a) real part and (b) imaginary part.

5.2.2 Infinite coating model

In contrast, the assumption of an infinite-coating slab waveguide model leads to a much smoother eigenmode distribution with modes located predominantly in the depression-cladding region, as in Fig. 5.9. With increasing wavelength, the fundamental mode with initially higher effective index in Fig. 5.8(a) continuously transforms into the first order cladding mode, and, similarly, the first cladding mode at lower wavelengths becomes the fundamental core-guided mode at relatively higher wavelengths as shown in Fig. 5.10(a).

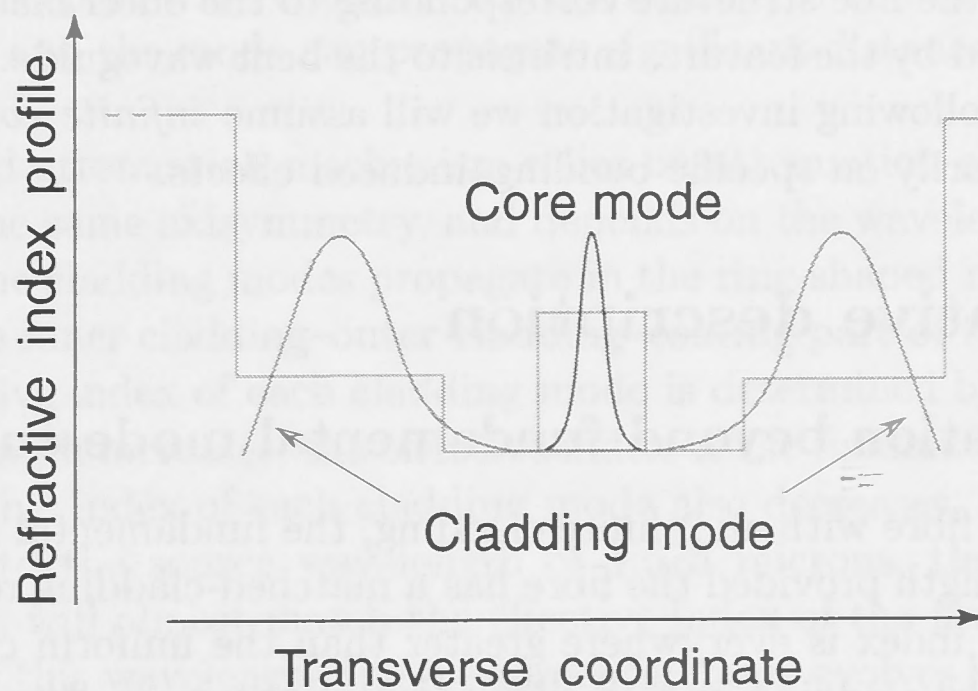


Figure 5.9: Schematic modal fields of the W-waveguide with infinite coating.

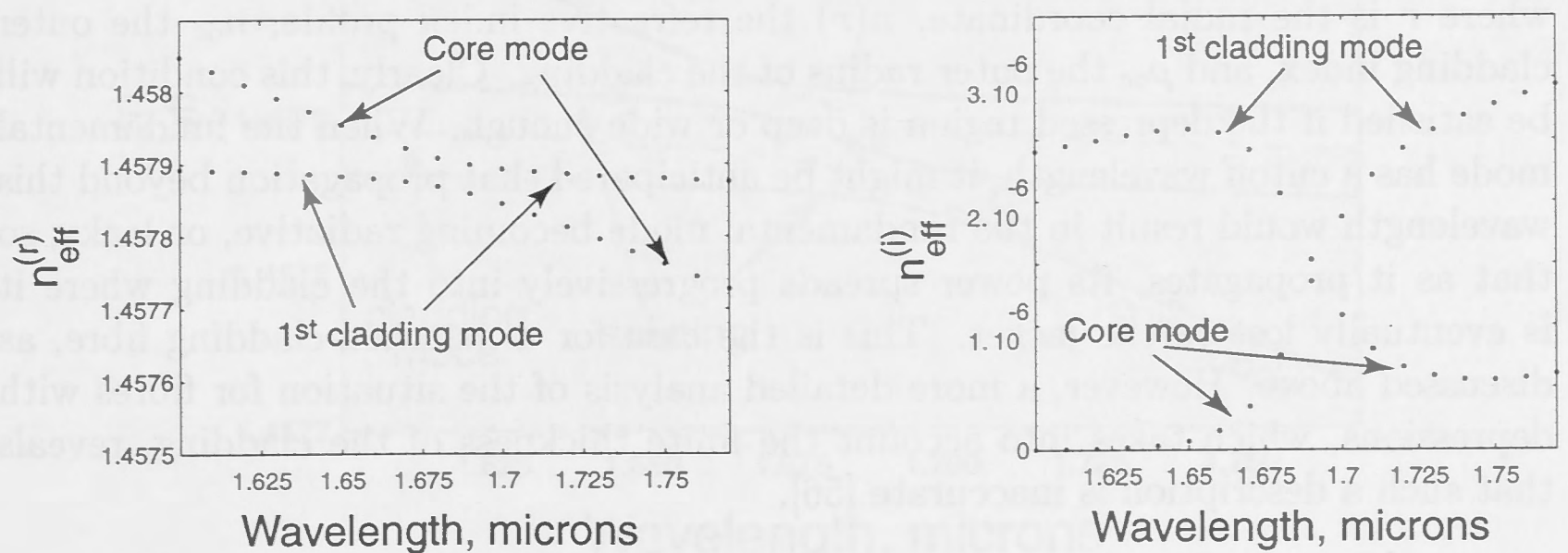


Figure 5.10: Effective index values vs. wavelength of the W-waveguide with infinite coating; (a) real part and (b) imaginary part.

The same trend is observed for modal attenuation which is characterised by the imaginary parts of the effective index plotted in Fig. 5.10(b). The power loss from the fundamental mode due to absorption and scattering in the coating is much less compared to the cladding mode attenuation because of tight confinement of the fundamental mode field to the core.

Accordingly, we adopt the infinite-coating model to avoid computational complexity. In practice, the fluctuations in Fig. 5.8 are probably averaged out because of variations in coating thickness and consistency along the length of the fibre, and the imaginary effective index values given in Fig. 5.10(b) will be a reasonable approximation. Furthermore, bending will introduce further splitting of modal characteristics, and the fine structure corresponding to the outer cladding - coating modes will be masked by the features intrinsic to the bent waveguide. Therefore, for the purpose of the following investigation we will assume *infinite coating geometry* to concentrate primarily on specific bending-induced effects.

5.3 Qualitative description

5.3.1 Propagation beyond fundamental mode cutoff

In a single-mode fibre with an infinite cladding, the fundamental mode does not have a cutoff wavelength provided the fibre has a matched-cladding refractive index profile, i.e. the core index is everywhere greater than the uniform cladding index. However, in depressed-cladding and W-fibres, where there are depressed layers in which the refractive index is below the cladding index, the fundamental mode will have a finite cutoff wavelength relative to the outer cladding index provided the complete refractive index profile of the fibre satisfies the inequality

$$\int_{-\rho_{oc}}^{\rho_{oc}} (n^2(r) - n_{oc}^2) r dr \leq 0, \quad (5.4)$$

where r is the radial coordinate, $n(r)$ the refractive index profile, n_{oc} the outer cladding index, and ρ_{oc} the outer radius of the cladding. Clearly, this condition will be satisfied if the depressed region is deep or wide enough. When the fundamental mode has a cutoff wavelength, it might be anticipated that propagation beyond this wavelength would result in the fundamental mode becoming radiative, or leaky, so that as it propagates, its power spreads progressively into the cladding where it is eventually lost to the jacket. This is the case for a matched-cladding fibre, as discussed above. However, a more detailed analysis of the situation for fibres with depressions, which takes into account the finite thickness of the cladding, reveals that such a description is inaccurate [56].

5.3.2 Attenuation mechanisms

Consider the schematic refractive index profile illustrated in Fig. 5.2. When the fundamental mode propagates beyond its cutoff wavelength, its effective index

$n_{\text{eff}} = \beta/k$ lies in the range $n_{\text{eff}} < n_{\text{oc}}$, denoted by the horizontal line. To understand the propagation characteristics of this mode, consider the core and depression part of the profile as constituting an effective matched-cladding fibre with core index n_{co} and cladding index n_{ic} . The fundamental mode is guided by this profile, even though it is formally beyond its cutoff wavelength. There are two loss mechanisms which attenuate this mode.

First, the tail of its evanescent field extends across the outer cladding and into the coating. In these two regions, the field amplitude decreases only algebraically ($\sim 1/\sqrt{r}$), because its effective index is below both the cladding and coating indices, and as the coating material is absorbing, the mode will be attenuated. Provided the depression is deep or wide enough, this attenuation of the fundamental mode will be only slight and the mode can propagate significant distances without noticeable loss of power.

The second attenuation mechanism relies on attenuation of individual cladding modes with the same axisymmetry, and depends on the wavelength of the source of excitation. The cladding modes propagate in the ring-shaped multimode waveguide defined by the inner cladding–outer cladding–coating part of the profile in Fig. 5.2, and the effective index of each cladding mode is determined by this profile. As the source wavelength increases, the effective index of the fundamental mode decreases, and the effective index of each cladding mode also decreases, but relatively slowly. Hence, close to the source wavelength of 1.675 microns, the fundamental mode effective index will almost match the effective index of the first cladding mode. In the vicinity of this wavelength the fundamental mode evolves into the first cladding mode, and, simultaneously, the cladding mode evolves into the fundamental mode, as depicted by the upper and lower dashed curves in Fig. 5.11.

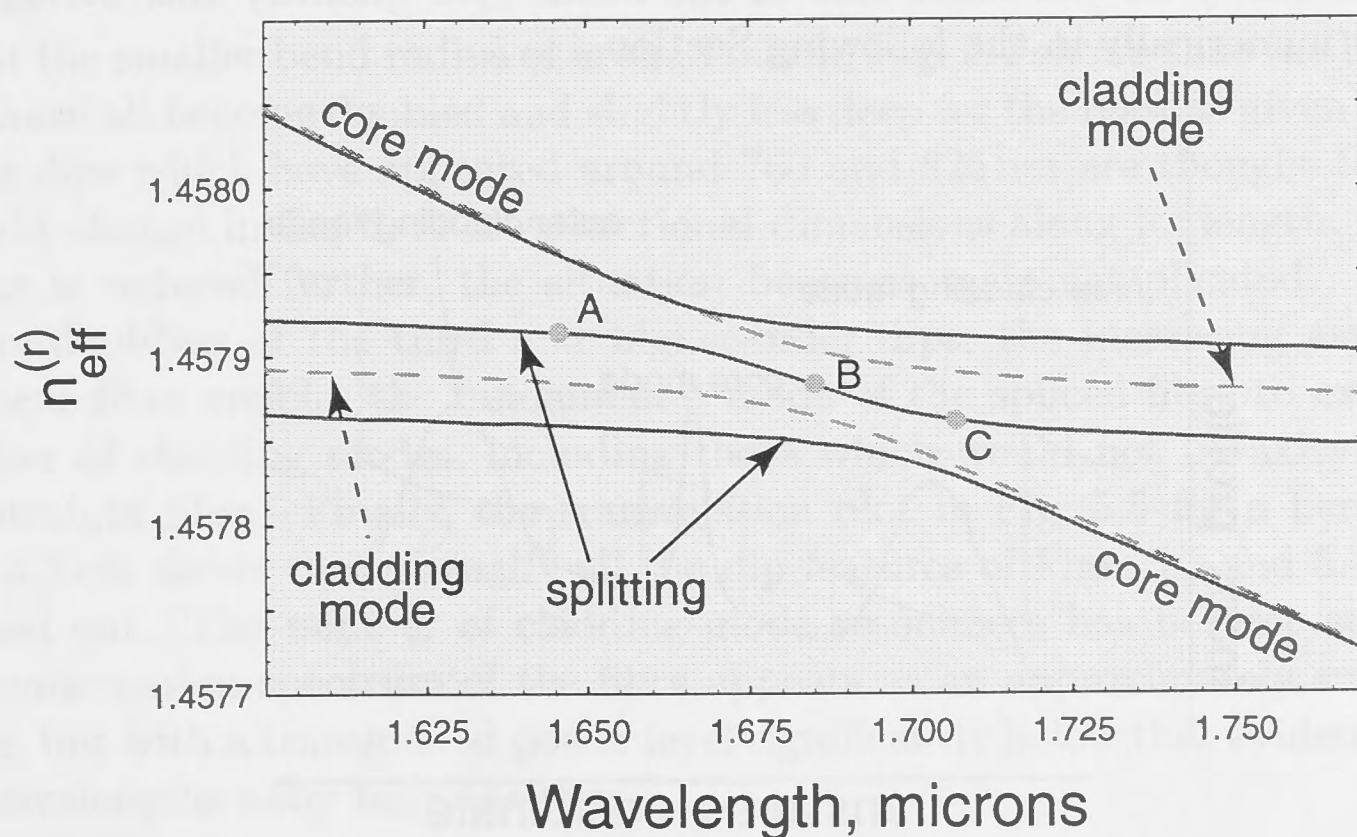


Figure 5.11: Real part of the effective index for modes of the bent (solid curves) and straight (dashed curves) waveguide.

In other words, the Gaussian-shaped fundamental mode field evolves into the single-humped cladding mode field and vice versa. However, in the immediate neighbourhood of the $1.675 \mu\text{m}$ wavelength, both modal fields extend over the entire core-depression-cladding cross-section. Since the source power is essentially invariant within the slight change in wavelength, the fraction of modal power entering the core-depression region is significantly reduced, accounting for the first dip in Fig. 5.3(a). As the source wavelength increases, there will be a series of deep dips in the spectral dependence of the power transmitted in the fundamental mode [56]. Three of these dips are evident in Fig. 5.3(a).

5.3.3 Cladding mode degeneracy

On the straight fibre, the circularly symmetric fundamental and cladding modes are degenerate and their two polarisation states, with a common propagation constant, constitute any pair of orthogonal directions in the fibre cross-section. With the introduction of bending, this degeneracy is broken because the bend introduces an effective asymmetry into the fibre cross-section. Normally this effect is negligible for the core-guided fundamental mode, unless the bend radius is extremely small, i.e. of the order of a cm or less. However, in the case of the cladding modes, the effect is significant at quite large bend radii because their modal fields are spread over the entire core - inner cladding - outer cladding cross-section of the fibre [61, 62].

The bending breaks the degeneracy of the symmetric cladding modes, so that each mode is replaced by two cladding modes with closely-spaced effective indices as shown in figures 5.11 and 5.12. The cladding mode with the slightly higher effective index has a field which lies predominantly on the outer side of the bent waveguide, while the cladding mode with the slightly lower effective index has a field which lies predominantly on the inner side of the bend. We quantify this breaking of degeneracy numerically in the following Section.

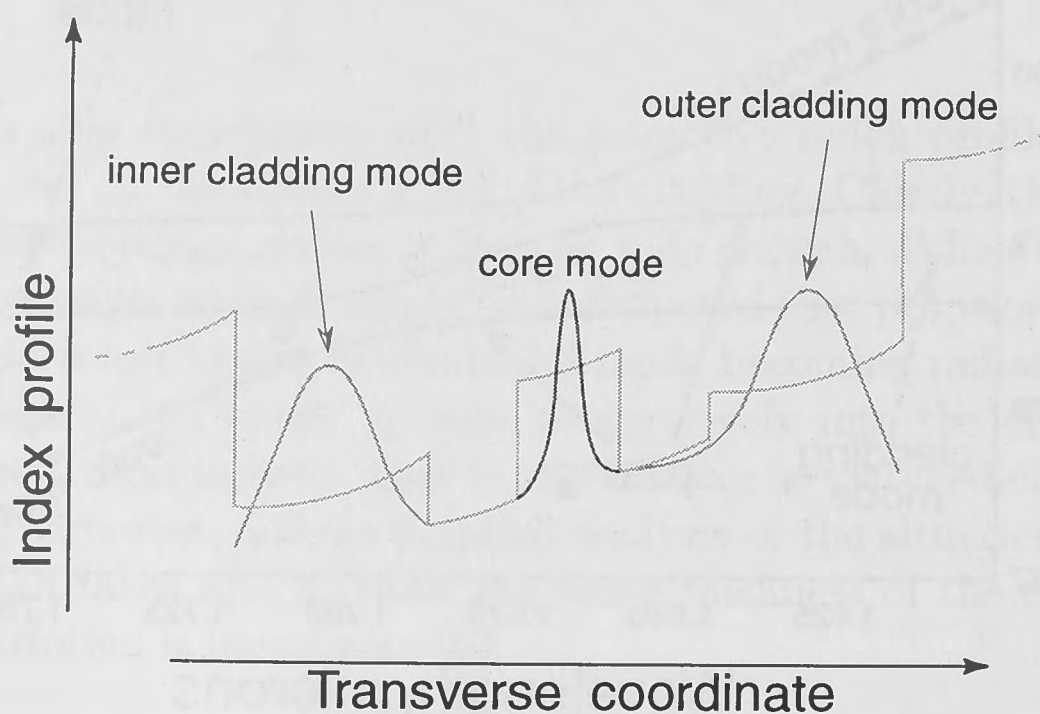


Figure 5.12: Schematic of modal fields of the slightly bent W-waveguide with infinite coating. Effective refractive index profile due to bending is shown as a function of the transverse coordinate u .

With the introduction of slight bending, the splitting of the first cladding mode resonance is evident from the doubling of the first dip (I) in Figs. 5.3(a) and (b). The core mode evolves into the first cladding mode having the slightly higher effective index, depicted by the upper solid curve in Fig. 5.11. Simultaneously, the cladding mode with the slightly higher effective index evolves into the cladding mode with the slightly lower effective index, corresponding to the more horizontal solid line with the S-shaped centre, and the cladding mode with the slightly lower effective index evolves into the fundamental mode, corresponding to the lower solid curve. The evolution of the modal fields for the top and bottom solid curves in Fig. 5.11 is similar to that for the straight fibre, while the field evolution of the middle solid curve at points A, B and C is quantified in Fig. 5.13, showing a portion of core-guided field at B, which accounts for the rise in transmitted power between dips in the first double-dip in Fig. 5.3(b). It is also noticeable that the depth of the double dips is smaller than that of the corresponding single dip, because of reduced excitation of the asymmetric cladding modes compared with the symmetric, straight fibre case.

The splitting of the second dip (II) in Figs. 5.3(a) and (b) is not discernable at this radius, because of the structure of the higher-order cladding mode fields. The effective index plots for the second dip in Fig. 5.3(b) is similar to that of Fig. 5.11, but the second-order inner and outer cladding mode fields display a different behaviour to those in Fig. 5.13. With reference to Fig. 5.11, the fields at A, B and C are plotted in Fig. 5.14 and display the characteristic double peak associated with the second cladding mode, but there is no core field present at B. In other words, there will be no double-dip present. There is a slight but apparent shift of the second dip to lower wavelengths, which is also confirmed numerically. However, when the bend radius is reduced to 50 cm, the corresponding fields plots in Fig. 5.15 now reveal a core field at B and hence account for the second double-dip in Fig. 5.4 at 700 nm.

At the smaller bend radius of around 50 cm, Fig. 5.4 shows that the higher-order dips have all become doubled and slightly less deep for the reasons given above. The single dips which have appeared around 760 and 825 nm are thought to be due to a slight change in the fibre cross-sectional dimensions along its length. If the bend radius is reduced further, the situation becomes more complicated. In addition to the doubling of the third and higher-order dips, the increasing asymmetry of the bent fibre enables the fundamental mode of the spliced fibre to excite a large number of cladding modes, including those which would not be axisymmetric on the straight fibre. Finally, the transmission plot in Fig. 5.5 for a bend radius of only 4.5 cm shows that virtually all the dip features of Figs. 5.3 and 5.4 have been washed out. The number of cladding-mode resonances has become so large that the transmission spectrum of the fibre appears as an approximately smoothed-out curve, but with a transmitted power level significantly below that evident in Fig. 5.3 for wavelengths away from the dips.

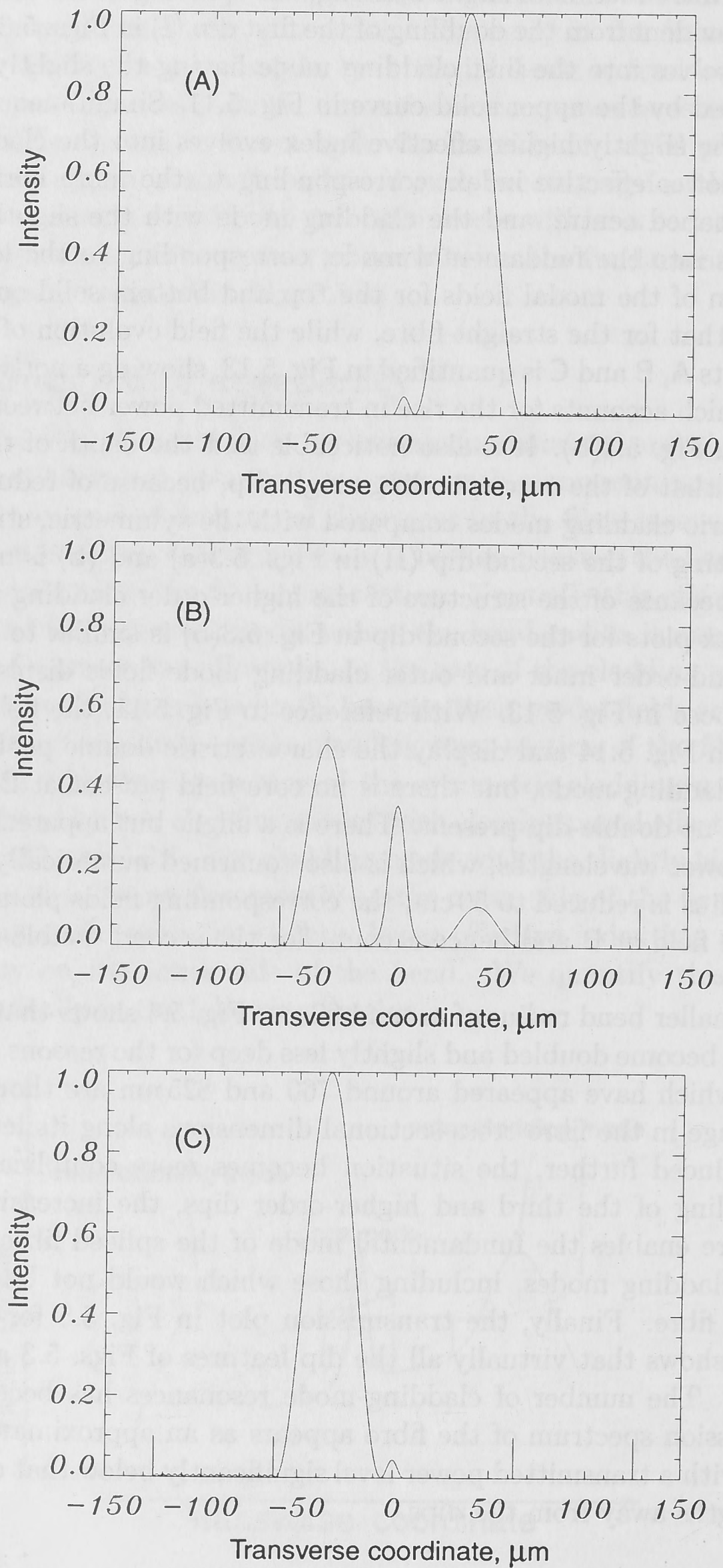


Figure 5.13: Characteristic field evolution of the first-order cladding mode vs. wavelength, corresponding to the points A, B and C in Fig. 5.11 ($R_b = 150\text{cm}$).

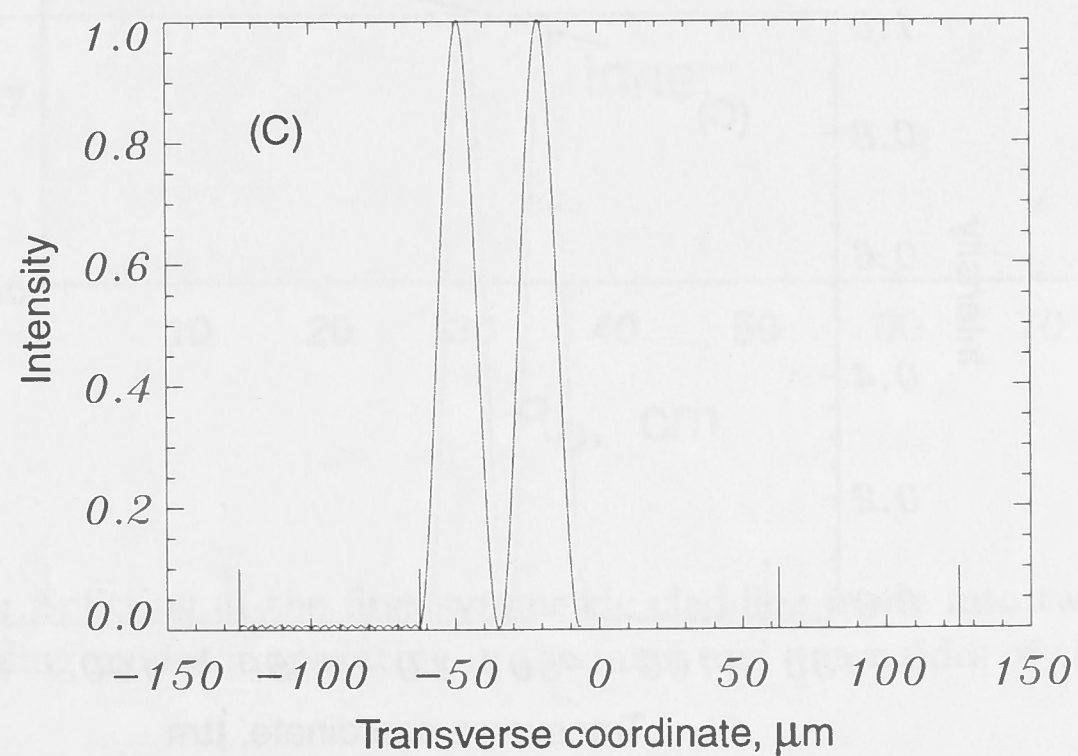
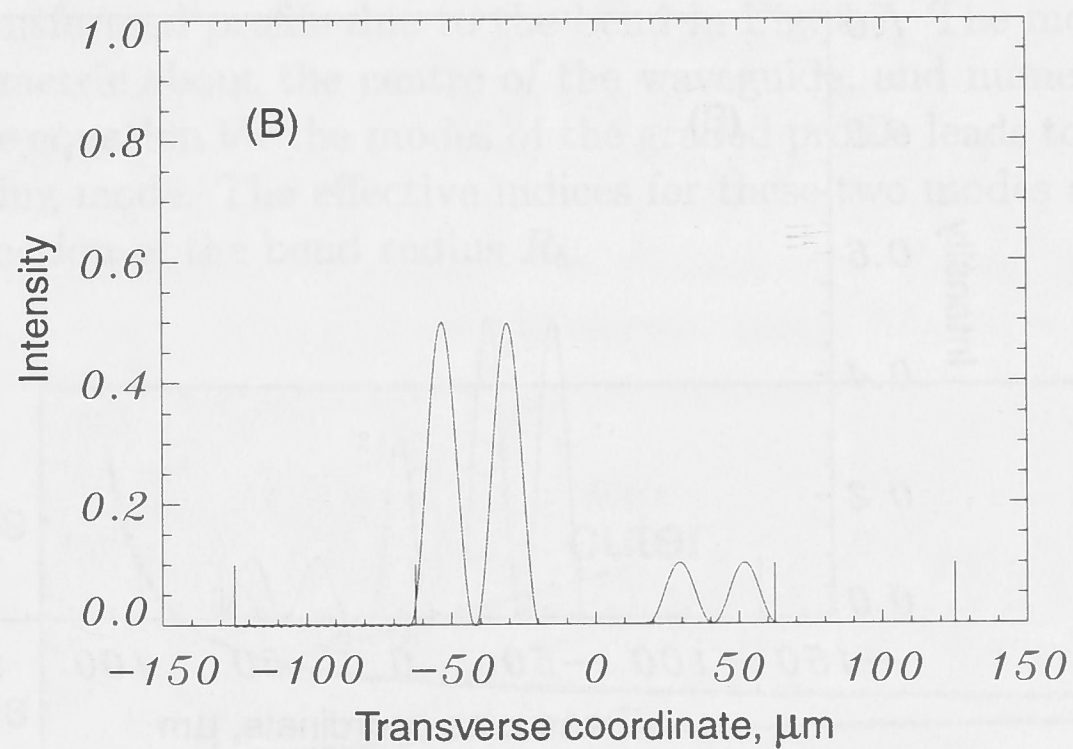
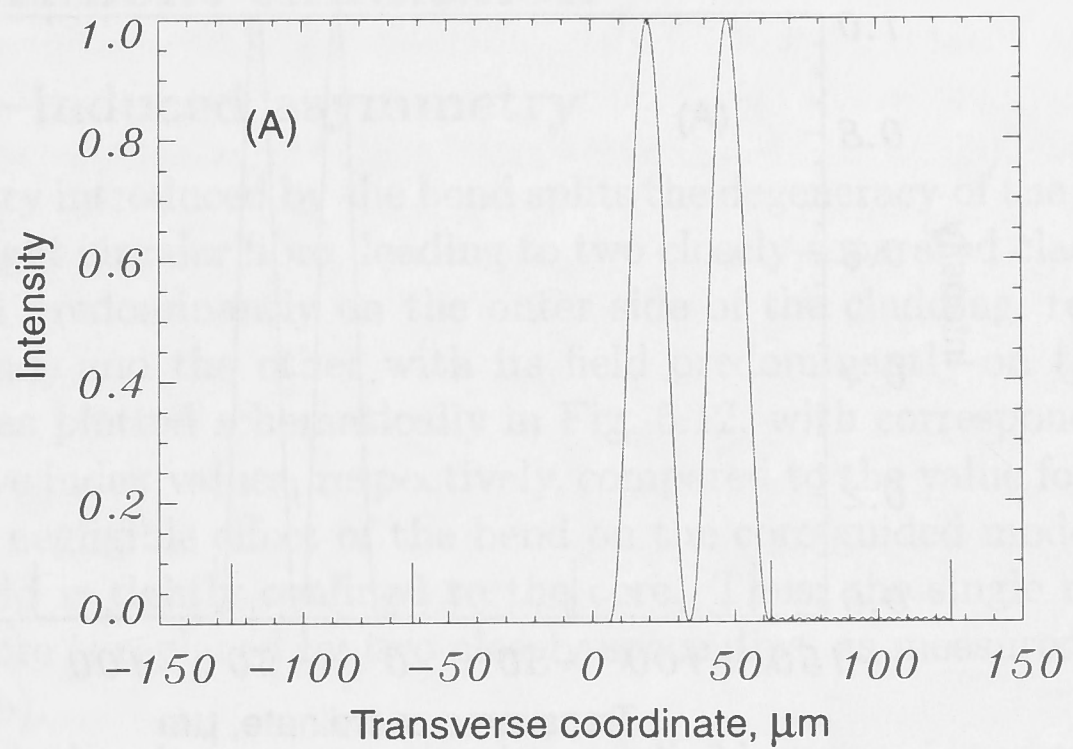


Figure 5.14: Characteristic field evolution of the second-order cladding mode vs. wavelength ($R_b = 150$ cm).

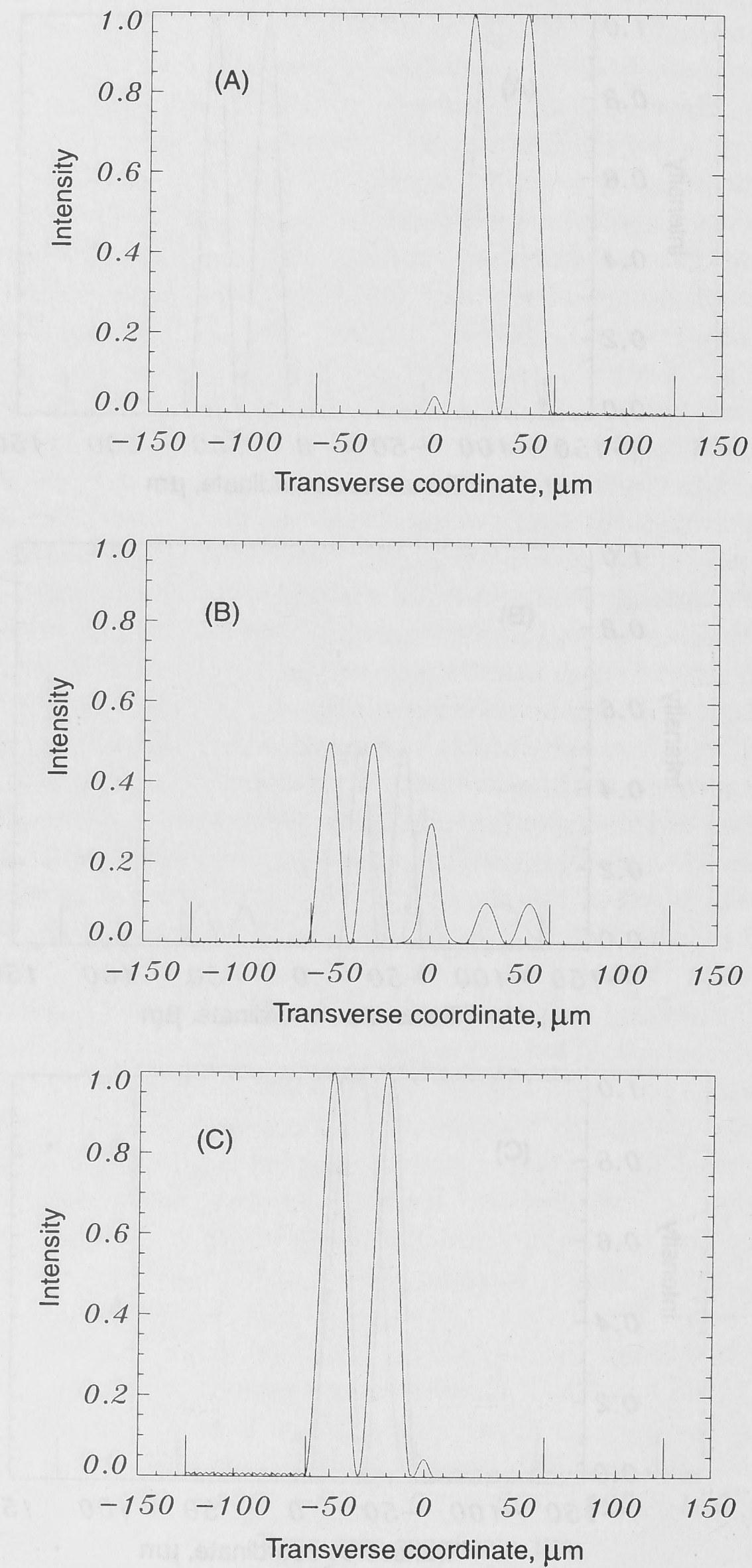


Figure 5.15: Characteristic field evolution of the second-order cladding mode vs. wavelength ($R_b = 50 \text{ cm}$).

5.4 Experiment simulation

5.4.1 Bend-induced asymmetry

The asymmetry introduced by the bend splits the degeneracy of the first cladding mode of the straight circular fibre, leading to two closely-separated cladding modes, one with its field predominantly on the outer side of the cladding, relative to the centre of the bend, and the other with its field predominantly on the inner side of the cladding, as plotted schematically in Fig. 5.12, with correspondingly higher and lower effective index values, respectively, compared to the value for the straight fibre. There is a negligible effect of the bend on the core-guided mode, as at these bend radii its field is tightly confined to the core. Thus, the single resonance dip of the straight fibre is replaced by two closely-spaced dips, as measured for the bent fibre in Fig. 5.3(b).

The effect of the bend on propagation is modelled by assuming a straight waveguide with the transformed profile due to the bend in Fig. 5.7. The modified profile is no longer symmetric about the centre of the waveguide, and numerical solution of the scalar wave equation for the modes of the graded profile leads to the splitting of the first cladding mode. The effective indices for these two modes are plotted in Fig. 5.16 as a function of the bend radius R_b .

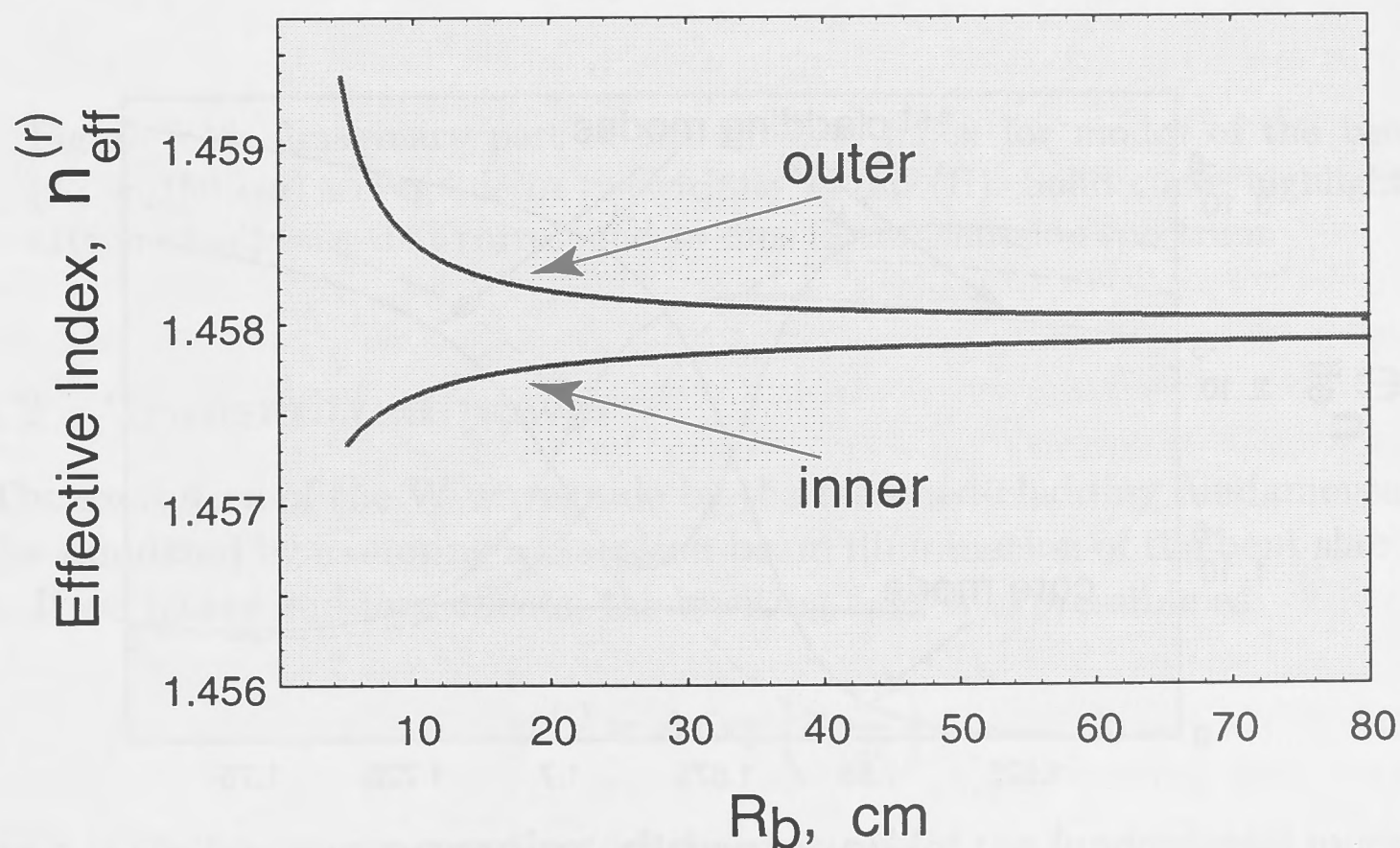


Figure 5.16: Splitting of the first symmetric cladding mode into two asymmetric cladding modes propagating in the inner and outer sides of the bend.

As would be expected, the effective index separation between the two modes increases as the bend radius decreases, and disappears in the straight waveguide limit $R_b \rightarrow \infty$.

With the introduction of only slight bending, e.g. the 150 cm bend radius used in the experimental results of Fig. 5.3, the splitting of the cladding mode is evident from the solid curves in Figs. 5.11 and 5.16. The real parts of the effective index values for the fundamental mode and first cladding mode of the complete equivalent straight waveguide profile in Fig. 5.7 are plotted against wavelength for core index $n_{co} = 1.461$, inner cladding index $n_{ic} = 1.453$, and outer cladding index $n_{oc} = 1.458$. The departure from the straight waveguide solutions denoted by the dashed curves is evident, and three modes are now involved in the region where the two dashed curves come closest together around a wavelength of $1.675 \mu\text{m}$, corresponding to the single dip in Fig. 5.3(a). The closeness of the three solid curves in this region relates to the double dip in Fig. 5.3(b).

Fig. 5.17 plots the respective imaginary parts of the effective indices vs wavelength. Dashed curves denote effective index values for the straight waveguide, showing that the core mode index initially decreases with increasing wavelength and, around 1.68 microns, evolves into the cladding mode, while the cladding mode simultaneously evolves to become the core mode. The evolution of the two dashed curves in the neighbourhood of 1.68 microns wavelength accounts for the single transmission dip in Fig. 5.3(a), while the evolution of the three solid curves accounts for the double dip in Fig. 5.3(b). This wavelength differs from the experimental value in Fig. 5.3 because of the difference in geometries between the circularly symmetric fibre and the symmetric slab waveguide.

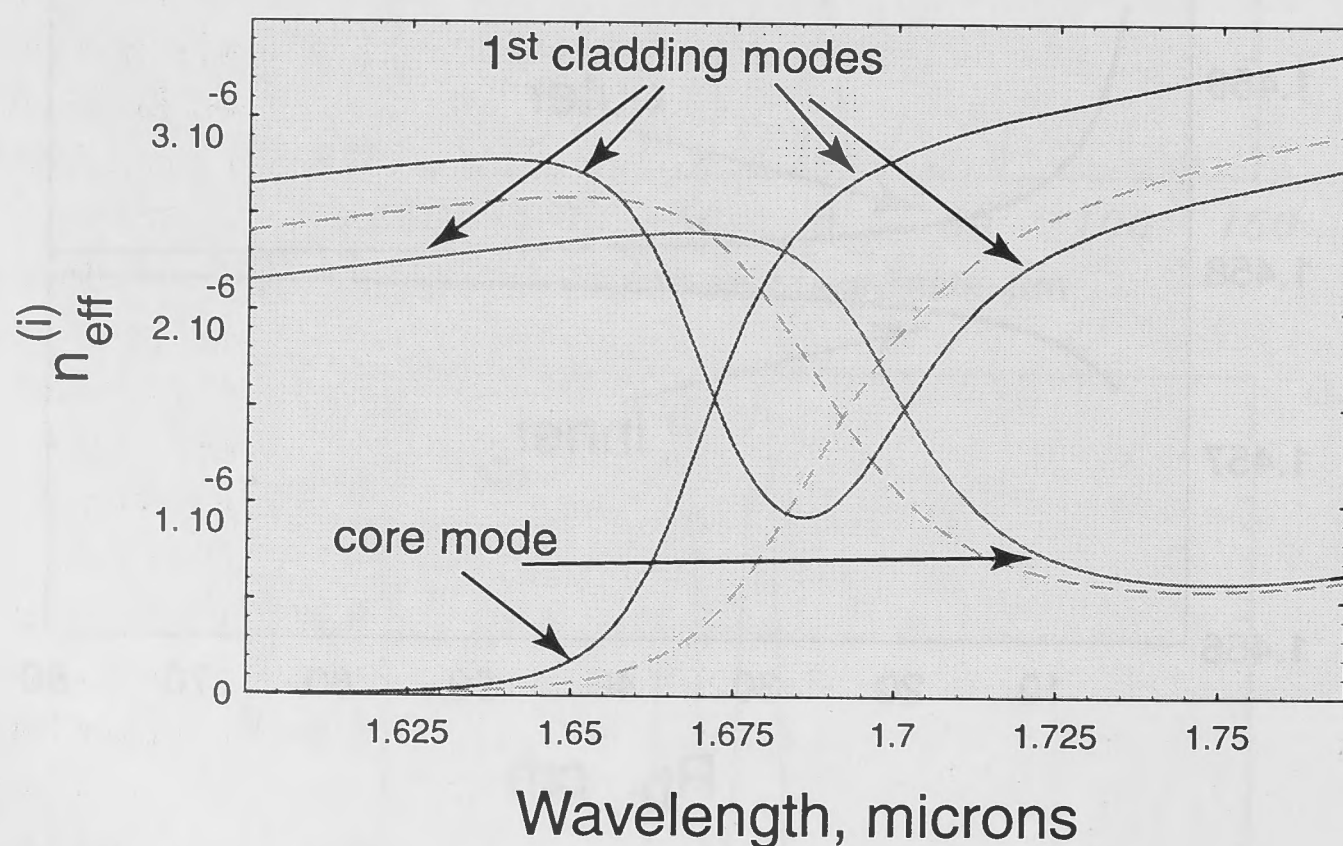


Figure 5.17: Imaginary part of the effective index for modes of the bent (solid curves) and straight (dashed curves) waveguide in the vicinity of dip (I).

Fig. 5.18 shows the dependence of the imaginary parts of the effective indices for the broader wavelength range, covering both the first (I) and second (II) dips areas.

In this plot the core-guided fundamental mode is denoted by the solid curve, with attenuation peaks corresponding to dips in the transmission spectrum. Because of the structure of the higher-order cladding mode fields, addressed in Section 5.3.3, the splitting of the second-order dip is not discernable at $R_b = 150 \text{ cm}$ bend radius.

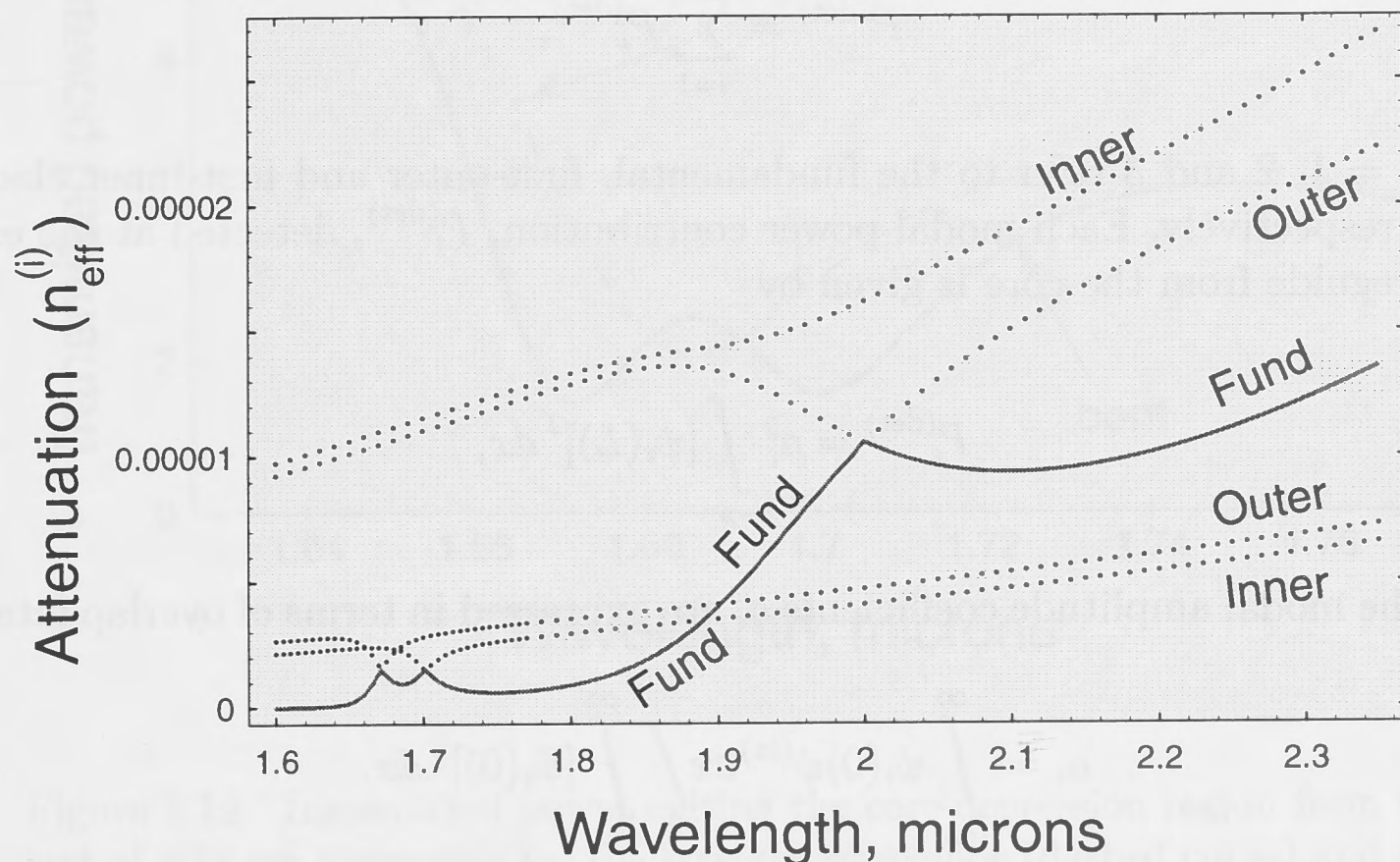


Figure 5.18: Imaginary part of the effective index for modes of the bent ($R_b = 150 \text{ cm}$) waveguide in the vicinity of dip (II). Solid curve highlights attenuation peaks that correspond to dips in transmission spectrum.

5.4.2 Transmitted power

The excitation of the W-waveguide by the matched-cladding fundamental mode can be simulated by assuming a Gaussian beam illumination of the bent slab waveguide. If we ignore end-face effects, the exciting field is expressible as

$$\psi^{(\text{in})} = A \exp\left(-\frac{x^2}{s^2}\right), \quad (5.5)$$

where x is the transverse coordinate s the spot size of the fundamental mode of the matched-cladding waveguide and A a constant. As the spot size of the matched-cladding waveguide does not match that of the W-waveguide, $\psi^{(\text{in})}$ will excite the symmetric waveguide modes, including the fundamental core mode and symmetric cladding modes.

The transmitted power at the end of the waveguide includes the output from the core region and part of the depressed region, in order to simulate the experimental conditions. Consequently, all excited modes which have fields located in the core and depressed region will contribute to the expression for the output power at the

end of a waveguide. However, in order to quantify the splitting of the transmission dip (I) in Fig. 5.3(b), only the contribution from the fundamental core mode, the first inner cladding mode and the first outer cladding mode need to be taken into account. The total detected power will therefore be well approximated by

$$P^{(\text{det})} = \sum_{i=1}^3 P_i^{(\text{det})}, \quad (5.6)$$

where $i = 1, 2$ and 3 refer to the fundamental, first-outer and first-inner cladding modes, respectively. Each modal power contribution, $P_i^{(\text{det})}$, detected at the end of the waveguide from the core is given by

$$P_i^{(\text{det})} = a_i^2 \int_{-\rho}^{\rho} [\psi_i(L)]^2 dx, \quad (5.7)$$

where the modal amplitude coefficients a_i are expressed in terms of overlap integrals

$$a_i = \int_{-\infty}^{\infty} \psi_i(0) \psi^{(\text{in})} dx / \int_{-\infty}^{\infty} [\psi_i(0)]^2 dx, \quad (5.8)$$

$\psi_i(z)$ denotes the attenuated transverse modal field distance z along the waveguide, and $\rho = 3 \mu\text{m}$.

Attenuation along the length of the waveguide is determined by the imaginary part of the modal effective index obtained from the eigenvalue equation. If γ_i denotes the attenuation coefficient of the power of the i -th mode, then $\gamma_i = 2kn_{\text{eff}}^{(i)}$ and $[\psi_i(z)]^2$ is attenuated according to $[\psi_i(z)]^2 = [\psi_i(0)]^2 e^{-\gamma_i z}$. Thus, the detected power can be calculated using the solutions of the scalar wave equation $\psi_i(0)$ at the beginning of the waveguide. Hence

$$\begin{aligned} P_i^{(\text{det})} &= e^{-\gamma_i L} a_i^2 \int_{-\rho}^{\rho} [\psi_i(0)]^2 dx \\ &= e^{-\gamma_i L} \int_{-\rho}^{\rho} [\psi_i(0)]^2 dx \left[\int_{-\infty}^{\infty} \psi_i(0) \psi^{(\text{in})} dx \right]^2 / \left[\int_{-\infty}^{\infty} [\psi_i(0)]^2 dx \right]^2. \end{aligned} \quad (5.9)$$

On substituting Eqn. (5.9) into Eqn. (5.6) and evaluating the resulting expression numerically, this leads to the splitting of the transmission dip (I) in Fig. 5.3(b) as quantified in Fig. 5.19, assuming a waveguide length $L = 18 \text{ cm}$. The dashed curve shows the single transmission dip for the straight waveguide and the solid curve the double dip for the slightly bent waveguide. The estimated relative dip spacing $\delta\lambda/\lambda = 2 \%$ closely matches the experimentally-measured spacing between the double dip (I) in Fig. 5.3(b).

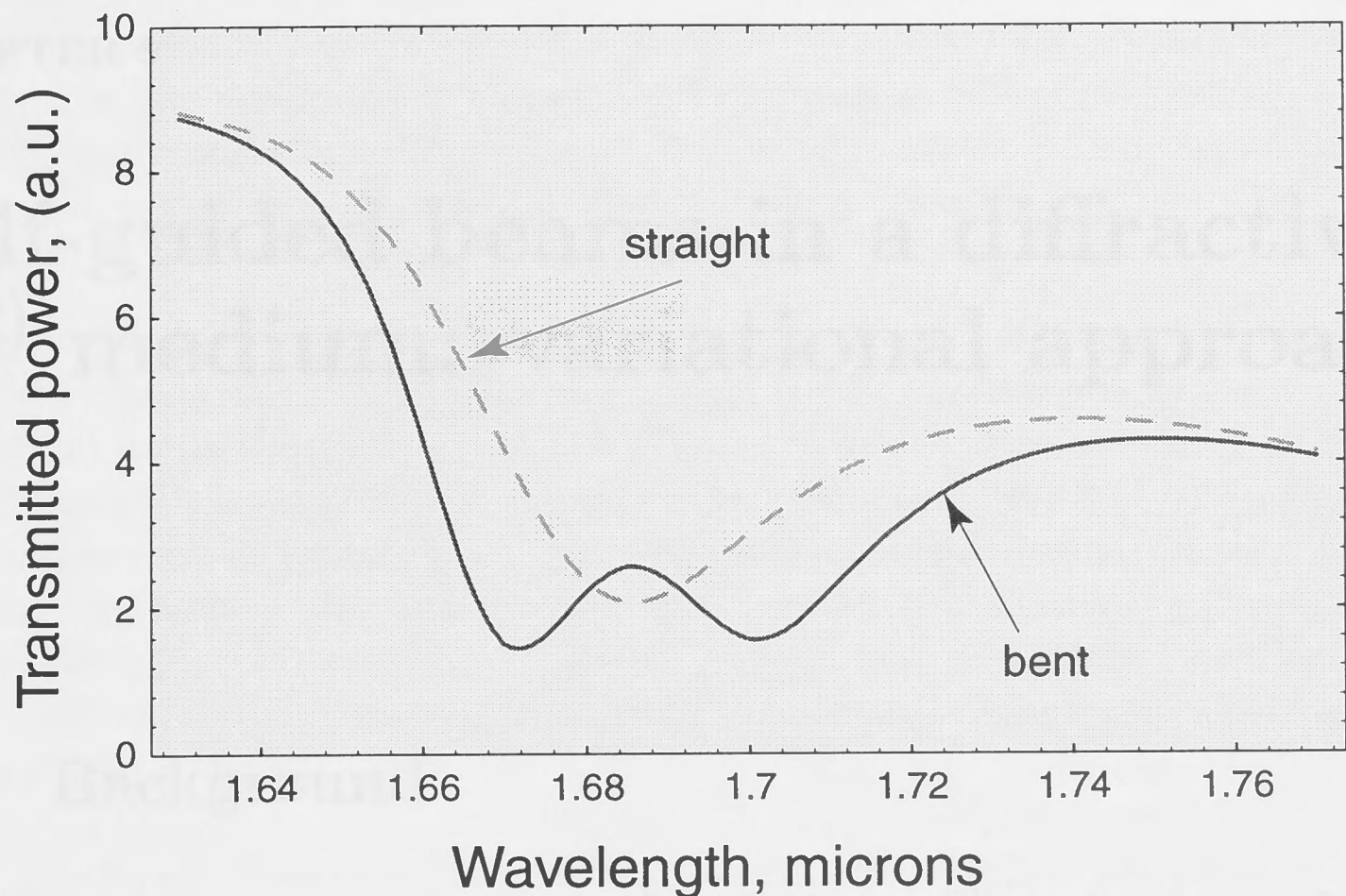


Figure 5.19: Transmitted power exiting the core-depression region from the end of a 18 cm waveguide for the straight waveguide (dashed curve) and the bent waveguide (solid curve).

5.5 Conclusions

In this Chapter we have presented a simple theory of transmission beyond fundamental mode cutoff which depends on breaking of cladding-mode degeneracy in bent W- and depressed cladding single-mode fibres [61, 62]. Bending results in splitting of the symmetrical cladding mode into two asymmetrical cladding modes propagating on the inner and outer sides of the bent cladding, respectively. Splitting of the resonant dips in the transmission spectrum can be attributed to power coupling between the fundamental core mode and these asymmetric cladding modes. Experimental transmission spectra of slightly bent W-fibres have been compared with theoretical results based on a slab waveguide model. In particular, we have shown that relative dip spacing closely matches the experimentally-measured spacing, and the strength and location of the fine-structure features of the resonances depends critically on the fibre bend radius. This suggests a novel practical approach for measuring large bend radii since it avoids the measurements of minute bend loss and relies only on symmetry-breaking effects.

Self-guided beams in a diffractive $\chi^{(2)}$ medium: variational approach

6.1 Background

It is well known that second-order (quadratic or $\chi^{(2)}$) nonlinearities of optical materials without the centre of inversion are responsible for such effects as second harmonic generation (SHG) (see, e.g., [66]). Recent progress in materials with high second-order nonlinearities, including polymeric electro-optical waveguides, has stimulated experimental work to increase, indirectly, effective $\chi^{(3)}$ nonlinearities taking advantages of cascaded second-order effects [17]. Such cascaded nonlinearities can also support intensity-dependent light propagation in the form of parametric self-guided waves (see, e.g., [19, 20, 22, 67–74]).

In this Chapter we demonstrate that localised solutions describing two-wave self-guided beams (spatial optical solitons) in a diffractive nonlinear $\chi^{(2)}$ medium can be well approximated analytically using the simplest ansatz in the form of Gaussian trial functions for a *variational approach* [75, 76]. In particular, for the self-guided beams in $\chi^{(2)}$ slab waveguides we show that, when no exact analytical solutions exist, a variational approach yields Gaussian approximations such that the ratio of the harmonic energy to the total beam energy agrees with the numerically-generated value to within $\sim 0.5\%$. Similar results are obtained for circularly symmetric self-trapped beams in $\chi^{(2)}$ bulk media where the Gaussian approximation is compared with the family of localised solutions found numerically [22, 76].

6.2 Mathematical model

We consider beam propagation in lossless $\chi^{(2)}$ nonlinear media under appropriate conditions for type I SHG (two-wave parametric mixing). In *esu*, the system of equations which describes the interaction of the first fundamental ($\omega_1 = \omega$) and second ($\omega_2 = 2\omega$) harmonics in a *weakly* anisotropic medium with $\chi^{(2)}$ nonlinear

susceptibility have the following form (see [18] for details of derivation):

$$\begin{aligned} 2ik_1 \frac{\partial E_1}{\partial z} + \nabla_{\perp}^2 E_1 + \frac{8\pi\omega_1^2}{c^2} \chi^{(2)} E_2 E_1^* e^{-i\Delta kz} &= 0, \\ 2ik_2 \frac{\partial E_2}{\partial z} + \nabla_{\perp}^2 E_2 + \frac{16\pi\omega_1^2}{c^2} \chi^{(2)} E_1^2 e^{i\Delta kz} &= 0, \end{aligned} \quad (6.1)$$

where E_1 and E_2 are the complex scalar electric field amplitude envelopes, asterisk denotes complex conjugation, $\nabla_{\perp}^2 = \partial^2/\partial x^2$ for the (1+1)-dimensional case of slab waveguide geometry, or $\nabla_{\perp}^2 = \partial^2/\partial x^2 + \partial^2/\partial y^2$ for (2+1)-dimensional bulk media; $\Delta k \equiv (2k_1 - k_2) \equiv 2[n(\omega) - n(2\omega)]\omega/c$ is the wave-vector mismatch between the first and second harmonics, n is the linear refractive index of the medium; z is the longitudinal coordinate parallel to the direction of propagation, x and y are the transverse coordinates, and the $\chi^{(2)}$ coefficient is proportional to the relevant element of the corresponding nonlinear susceptibility tensor. Note, that the system (6.1) is only valid when the spatial walk-off is negligible, although it can also be taken into account if necessary (see, e.g. [18, 20]).

Normalising the transverse coordinates in terms of the initial laser beam radius R_0 (it can be defined in various ways, e.g., as the half-width at the $1/e$ intensity point), then $x \rightarrow R_0 x$, $y \rightarrow R_0 y$. The longitudinal coordinate is normalised in units of the diffraction length[†] $R_d \equiv 2R_0^2 k_1$, i.e. $z \rightarrow R_d z$ and the fields are normalised accordingly to

$$\begin{aligned} E_1 &= \frac{vc^2}{16\pi\omega_1^2 \chi^{(2)} R_0^2} \exp(i\beta z), \\ E_2 &= \frac{wc^2}{8\pi\omega_1^2 \chi^{(2)} R_0^2} \exp[(i(2\beta + \Delta)z)], \end{aligned} \quad (6.2)$$

where $\Delta \equiv \Delta k R_d$, to get the normalised system

$$\begin{aligned} i \frac{\partial v}{\partial z} + \nabla_{\perp}^2 v - \beta v + wv^* &= 0, \\ i\sigma \frac{\partial w}{\partial z} + \nabla_{\perp}^2 w - \sigma(2\beta + \Delta)w + \frac{v^2}{2} &= 0. \end{aligned} \quad (6.3)$$

In the above equations, β is the normalised nonlinearly-induced shift to the propagation constant, and for spatial solitons discussed here $\sigma \equiv k_2/k_1 = 2.0$ since for deriving Eqs. (6.1) we have assumed $\Delta k/k_1 \ll 1$.

To reduce the number of parameters in the system (6.3), it can be rescaled. Using the transformations $v = \tilde{v}\beta$, $w = \tilde{w}\beta$, $z = \tilde{z}/\beta$, $x = \tilde{x}/\sqrt{|\beta|}$, and $y = \tilde{y}/\sqrt{|\beta|}$, we get

$$\begin{aligned} i \frac{\partial \tilde{v}}{\partial \tilde{z}} + r \nabla_{\perp}^2 \tilde{v} - \tilde{v} + \tilde{w}\tilde{v}^* &= 0, \\ 2i \frac{\partial \tilde{w}}{\partial \tilde{z}} + r \nabla_{\perp}^2 \tilde{w} - \alpha \tilde{w} + \frac{\tilde{v}^2}{2} &= 0, \end{aligned} \quad (6.4)$$

[†]For example, if we define R_0 as the half-width at $1/e$ intensity point, then Gaussian-shaped beam $|E_1|^2 \sim \exp[-r^2/R_0^2]$ will spread as $R_0^2(z) = R_0^2(0)[1+(2z/R_d)^2]$ in a linear isotropic medium.

where $\alpha = 4 + 2\Delta/\beta$ and $r \equiv \text{sign}(\beta)$. For the case of spatial bright solitons considered here, $r = +1$.

The two systems (6.3) and (6.4) are equivalent, either of which may be more appropriate for a particular problem. In this Chapter we employ the form (6.4), whereas the system (6.3) is used to describe soliton collisions in Chapter 7. In what follows, we will omit the *tilde* sign in Eqs. (6.4) to simplify notation.

6.3 Solitons in slab $\chi^{(2)}$ waveguides

In case of (1+1)-dimensional slab $\chi^{(2)}$ waveguide (as in Fig. 6.1), the propagation of self-guided waves is described by equations (6.4) in the form

$$\begin{aligned} i\frac{\partial v}{\partial z} + \frac{\partial^2 v}{\partial x^2} - v + wv^* &= 0, \\ 2i\frac{\partial w}{\partial z} + \frac{\partial^2 w}{\partial x^2} - \alpha w + \frac{1}{2}v^2 &= 0. \end{aligned} \quad (6.5)$$

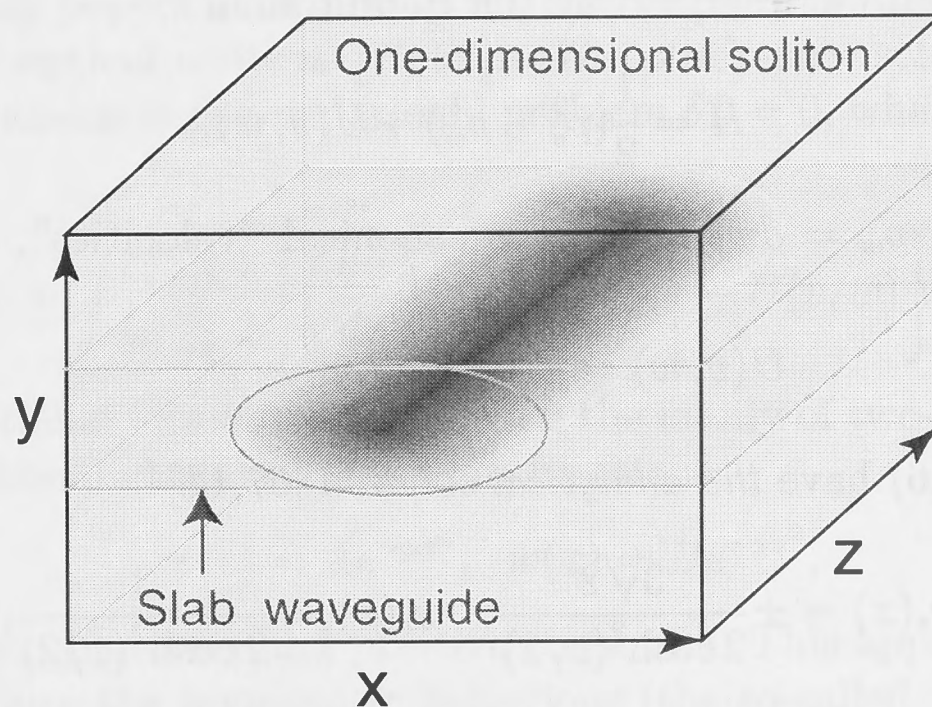


Figure 6.1: The (1+1)-dimensional soliton in a slab waveguide.

For this system, there exists a family of self-guided beams which have been determined numerically [19] using shooting technique outlined in Appendix A.4. This family describes two-wave, stationary localised solutions composed of parametrically coupled field components of the fundamental and second-harmonics. The shapes of these solutions depend on a dimensionless parameter α (see below), which is related to the phase mismatch between the harmonics. The only representative of this family known in analytical form was determined by Karamzin and Sukhorukov for $\alpha = 1$ [67, 68], and subsequently rediscovered by others [71]. The existence of

the family of stationary soliton solutions can be seen in numerical BPM simulations when the initially excited fundamental harmonic generates the second harmonic. Beyond a transition distance, the system evolves into a stationary two-wave state [19, 20, 72]. More recently (1+1)-dimensional $\chi^{(2)}$ solitons have been observed experimentally in LiNbO₃ planar waveguides [77].

6.3.1 Analytical solutions

In our analysis below, we assume near-phase-matched propagation and focus on spatial solitons with $\alpha = O(1)$. For stationary spatially localised solutions of Eqs. (6.5) which do not depend on z , we obtain two coupled ordinary differential equations:

$$\begin{aligned} \frac{d^2 v}{dx^2} - v + vw &= 0, \\ \frac{d^2 w}{dx^2} - \alpha w + \frac{1}{2}v^2 &= 0, \end{aligned} \quad (6.6)$$

where we assume the functions $v(x)$ and $w(x)$ are real and $\alpha > 0$.

These equations can be regarded as the equations of motion for a particle in the plane (v, w) , and can be described by the Hamiltonian

$$H = \frac{1}{2}(p_v^2 + p_w^2) + U(v, w), \quad (6.7)$$

where $p_v = dv/dx$, $p_w = dw/dx$ are the canonical “velocities”, and $U(v, w)$ is an effective potential

$$U(v, w) = \frac{1}{2}(v^2 w - \alpha w^2 - v^2). \quad (6.8)$$

For $\alpha = 1$, Eqs. (6.6) have *the analytical solution* [67, 68]

$$v_s(x) = \pm \frac{3\sqrt{2}}{2 \cosh^2(x/2)}; \quad w_s(x) = \frac{3}{2 \cosh^2(x/2)}, \quad (6.9)$$

An analytical solution of Eqs. (6.6) can be also obtained in the limit of large α . For $\alpha \gg 1$, we can neglect the second-order derivative in the equation for w and find the first term of the asymptotic expansions, $w \approx v^2/2\alpha$, thereby reducing the system of two equations to a single nonlinear Schrödinger (NLS) equation for v [17, 19, 20, 72]. In general, stationary localised solutions of the system (6.5) for $\alpha \gg 1$ can be expressed as an asymptotic series in α^{-1} ,

$$\begin{aligned} v &= \sqrt{\alpha} \left(v_0 + \frac{1}{\alpha} v_1 + \frac{1}{\alpha^2} v_2 + \dots \right), \\ w &= w_0 + \frac{1}{\alpha} w_1 + \frac{1}{\alpha^2} w_2 + \dots \end{aligned} \quad (6.10)$$

Substituting (6.10) into (6.6) and equating coefficients of powers in α^{-1} , we obtain a system of inhomogeneous equations leading to the first and second terms of the asymptotic expansions as follows

$$\begin{aligned}
 v(x) &= \pm 2\sqrt{\alpha} \left[\frac{1}{\cosh x} + \frac{2 \sinh^2 x}{\alpha \cosh^3 x} + O(\alpha^{-2}) \right], \\
 w(x) &= \frac{2}{\cosh^2 x} - \frac{4(5 - 4 \cosh^2 x)}{\alpha \cosh^4 x} + O(\alpha^{-2}).
 \end{aligned}
 \tag{6.11}$$

6.3.2 Variational solutions

As has been shown [19], for $\alpha > 0$ solutions of Eqs. (6.6) corresponding to stationary solitary waves of the Eqs. (6.5) can be found *numerically* as trajectories in the plane (v, w) that separate different regimes of particle motion. Two symmetric separatrix trajectories exist at any value of $\alpha > 0$, which leads to the existence of localised solutions. Compared with numerical solutions, the asymptotic solution (6.11) is a good approximation for $\alpha \gg 1$, but becomes less accurate for $\alpha \sim O(1)$. Accordingly, an approximation method is required for obtaining solutions at smaller values of α . This problem is important for developing a perturbation theory for spatial solitons in dissipative $\chi^{(2)}$ materials [78], and also for simplifying the analysis of beam steering and scattering. Here we describe the family of stationary solutions using a *variational approach*.

There are many papers on applying the Lagrangian variational method to non-linear waves and optical solitons [75, 79]. The stationary solutions described by Eqn. (6.6) are solutions of the variational problem $\delta L = 0$, where the Lagrangian L is given by

$$L = \int_{-\infty}^{+\infty} \left\{ \frac{1}{2} \left[\left(\frac{dv}{dx} \right)^2 + \left(\frac{dw}{dx} \right)^2 \right] - U(v, w) \right\} dx.
 \tag{6.12}$$

We use this variational formalism to describe the family of two-wave bright solitons with fields approximated by two Gaussian functions

$$v(x) = Ae^{-\rho x^2}; \quad w(x) = Be^{-\gamma x^2},
 \tag{6.13}$$

where A, B, ρ and γ are real and positive constants. This approximation does not accurately reproduce the asymptotic behaviour (the so-called ‘‘tails’’) of the exact solutions (6.9) for $\alpha = 1$, because the latter decreases much slower than Gaussian functions for $|x| \gg 1$. Nevertheless, the approximation (6.13) does allow us to make explicit analytical calculations with *different* radii of the fundamental and second harmonic beams. This leads to a good agreement between integral characteristics of approximate analytical solutions and numerical results (see Fig. 6.5). The choice of the trial functions resembles the problem of the internal oscillations of vector solitons in a $\chi^{(3)}$ medium [80] where trial functions similar to the Gaussian form of Eqs. (6.13) were used.

Substituting Eqs. (6.13) into the Lagrangian (6.12), we find a system of four equations for A, B, ρ and γ from the corresponding variational problem $\partial L / \partial a_j = 0$, where $a_j \equiv \{A, B, \rho, \gamma\}$. The resulting equations are

$$A^2 = \frac{(\rho + 1)(2\rho + \gamma)(\gamma + \alpha)}{\sqrt{\rho\gamma}},
 \tag{6.14}$$

$$B = \frac{(\rho + 1)\sqrt{2\rho + \gamma}}{\sqrt{2\rho}}, \quad (6.15)$$

$$\gamma = \frac{4\rho^2}{1 - \rho}, \quad (6.16)$$

where the parameter $\rho(\alpha)$ is the *real positive* root of the cubic equation

$$20\rho^3 + (4 - 3\alpha)\rho^2 + 4\alpha\rho - \alpha = 0. \quad (6.17)$$

This defines $\gamma = \gamma(\alpha)$, $v(0) = A(\alpha)$ and $w(0) = B(\alpha)$ and hence characterises the family of (1+1) spatial solitons. Eqn. (6.17) has the solution $\rho = 1/5$ at $\alpha = 1$, so that $\gamma = 1/5$, $A = 6\sqrt{3}/5 \simeq 2.08$, and $B = 3\sqrt{6}/5 \simeq 1.47$. These values are very close to the amplitudes of the exact solution (6.9), i.e. $v(0) = 3/\sqrt{2} \simeq 2.12$ and $w(0) = 3/2 = 1.5$, and the corresponding relative error is less than 2%.

For $\alpha \neq 1$ the cubic equation (6.17) can be readily solved, and over certain ranges of values of α there can be more than a single *real* root. However, the physical problem under consideration requires the additional condition $\rho < 1$ to ensure $\gamma > 0$, as in Eqn. (6.16). A simple analysis shows that Eqn. (6.17) has only one *real positive* root satisfying this condition. There is a singularity in the dependence $\rho(\alpha)$ at $\alpha = \alpha_1 \approx 29.272$ for the first root, but we have confirmed that in the vicinity of this point and also for $\alpha > \alpha_1$ the real solution is still *unique* provided the condition $\rho < 1$ is satisfied.

This root is plotted in Fig. 6.2 as a function of α for the interval $0 < \alpha \leq 20$.

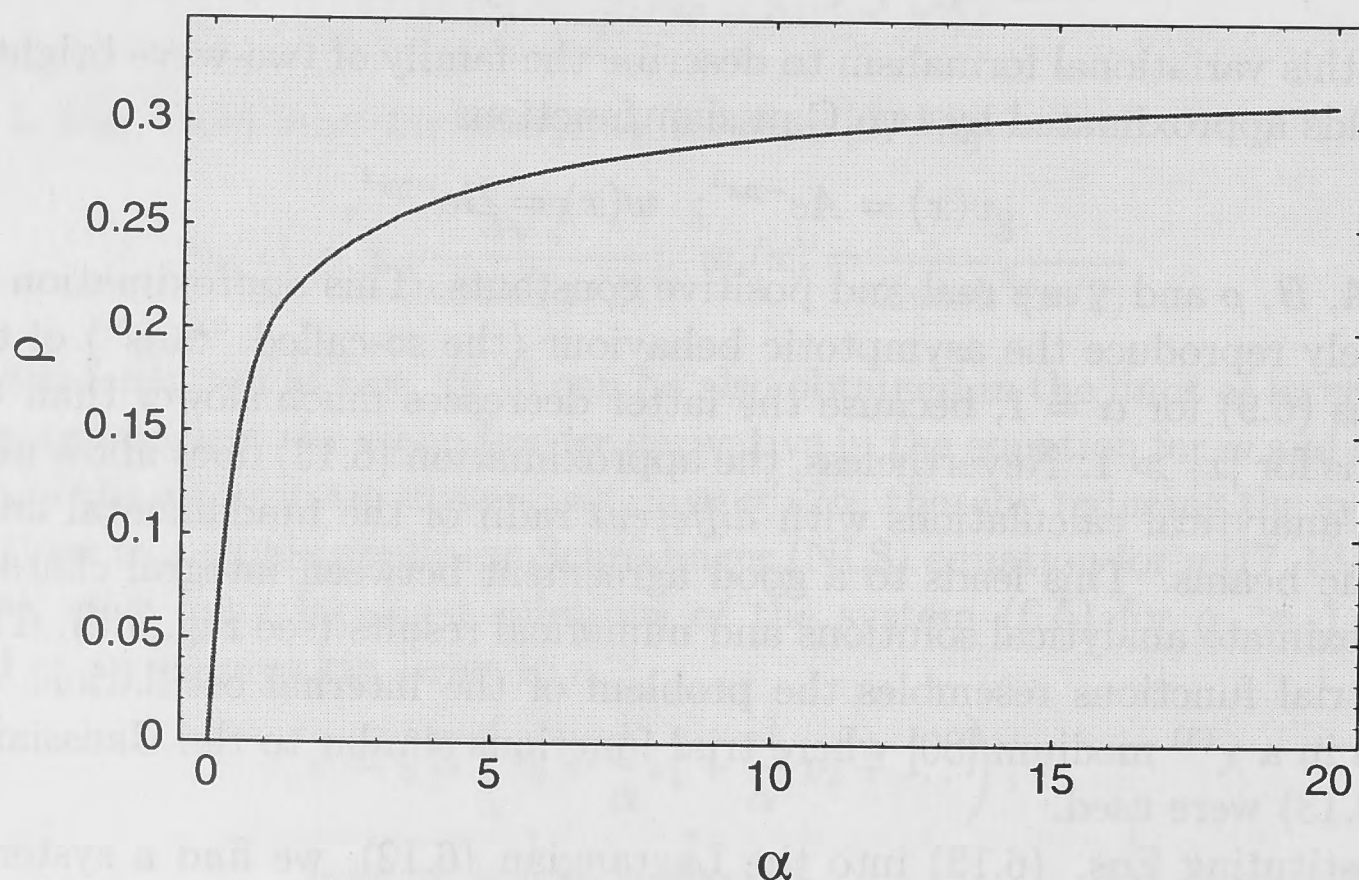


Figure 6.2: Real positive root of Eqn. (6.17) satisfying the condition $\rho < 1$ as a function of the parameter α for the interval $0 < \alpha \leq 20$.

This solution gives approximate profiles of two-wave (1+1)-dimensional bright solitons as defined by Eqs. (6.13) – (6.16). In Fig. 6.3 we compare (for $\alpha = 10$) this approximate variational solutions (dashed curves) with the localised solutions of Eqs. (6.6) (solid curves) found numerically by the shooting technique [19, 76].

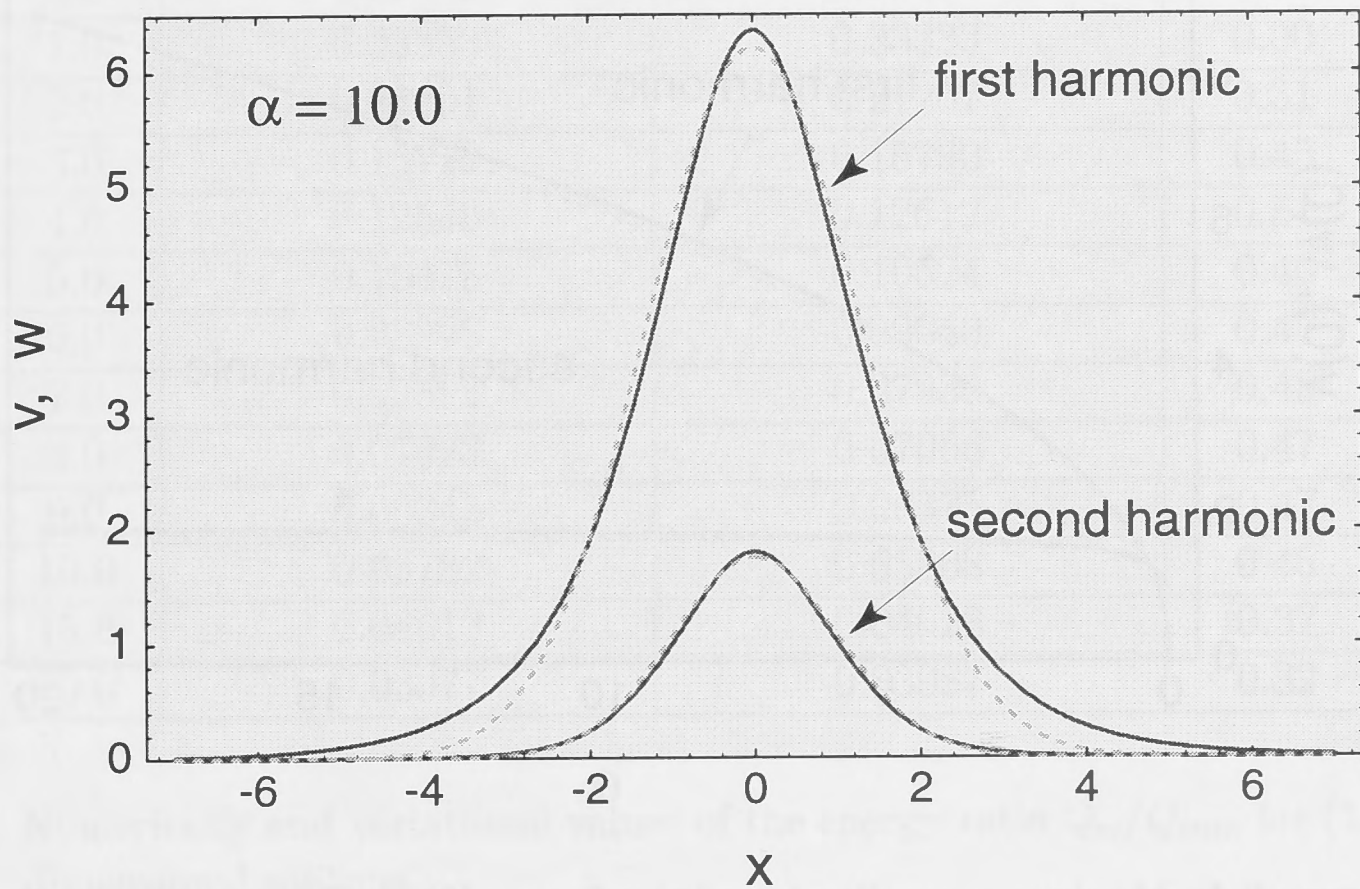


Figure 6.3: Comparison between the numerical solutions (solid curves) and the approximate solutions (6.13)–(6.17) (dashed curves) for $\alpha = 10$ for the soliton profiles of the fundamental and second harmonics in the (1+1)-dimensional case.

There is a good agreement over the range of α -values considered. This is confirmed by comparing the numerical and approximate dependencies of the soliton amplitudes on the parameter α presented in Fig. 6.4. The maximum relative error given by the Gaussian approximations for the amplitudes is less than 3%.

Another way to quantify the accuracy of the variational approach is to compare integral (e.g. energy) characteristics of the solutions because they are less sensitive to the choice of trial functions. In Fig. 6.5 we give the ratio of the field energy in the second harmonic,

$$Q_w = \int_{-\infty}^{+\infty} |w|^2 dx, \quad (6.18)$$

to the energy in both harmonics,

$$Q_{\text{sum}} = \int_{-\infty}^{+\infty} (|v|^2 + |w|^2) dx \quad (6.19)$$

based on the variational solution (6.13)–(6.17) (solid curve) and the exact solutions of the Eqs. (6.6) (opened circles) determined by the shooting technique [19, 76]. Table I gives values from the two methods and the relative error.

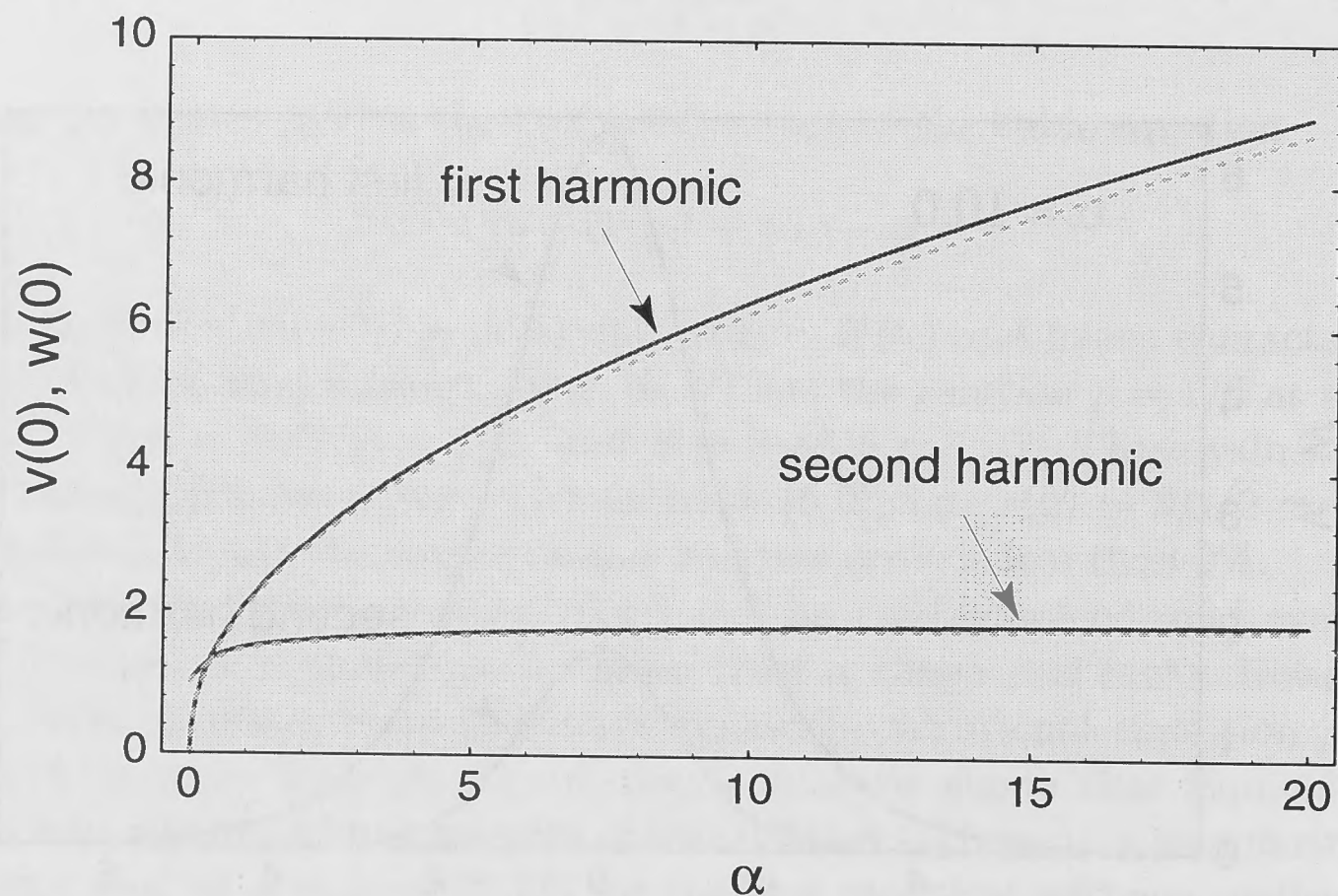


Figure 6.4: Maximum amplitudes of the first, $v(0)$, and second, $w(0)$, harmonics vs. the parameter α ; solid curves - numerical solutions, dashed curves - variational solutions.

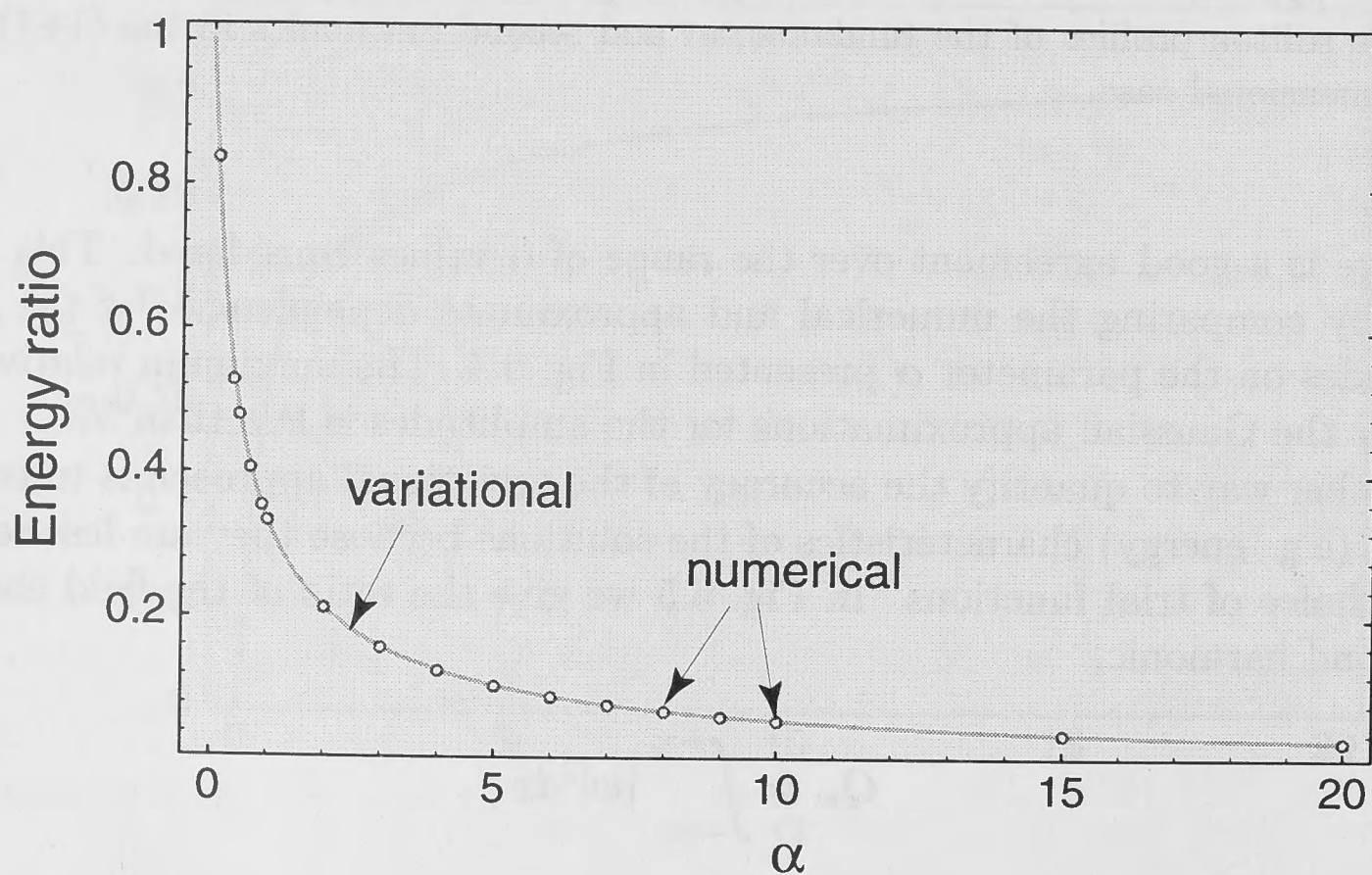


Figure 6.5: Ratio of the energy of the second harmonic, Q_w , to the harmonics' sum energy, Q_{sum} , as a function of the parameter α . Solid curve - variational result, open circles - numerical result.

α	Energy Ratio, Q_w/Q_{sum}		Relative Error, %
	numerical results	variational results	
0.4	0.53014	0.54102	2.05
0.5	0.48069	0.48685	1.28
0.7	0.40710	0.40860	0.37
0.9	0.35450	0.35464	0.04
1.0	0.33333	0.33333	0.00
2.0	0.21201	0.21267	0.31
3.0	0.15719	0.15790	0.45
4.0	0.12548	0.12612	0.51
5.0	0.10476	0.10524	0.46
6.0	0.08998	0.09040	0.47
7.0	0.07892	0.07930	0.48
8.0	0.07033	0.07066	0.47
9.0	0.06345	0.06375	0.47
10.0	0.05782	0.05808	0.45
15.0	0.04013	0.04028	0.37
20.0	0.03077	0.03087	0.32

Table I. Numerically and variational values of the energy ratio Q_w/Q_{sum} for (1+1)-dimensional solitons.

As can be seen from Fig. 6.5 and Table I, the variational approach yields Gaussian approximations of the (1+1) beams such that the ratio of the harmonic energy to the total beam energy equals, with $\sim 0.5\%$ relative error (except for $\alpha \lesssim 0.6$), to the ratio obtained numerically, so that the agreement is excellent.

6.4 Solitons in bulk quadratic media

Development of soliton theory for the (2+1)-dimensional geometry is a problem of fundamental importance which, if solved, could pave the way for the creation of reconfigurable self-guiding structures in bulk $\chi^{(2)}$ materials. We would like to emphasize that for the self-focusing $\chi^{(3)}$ (i.e. Kerr) nonlinearity this problem meets serious difficulties since any self-trapped beam in such media is *unstable* and displays collapse (see, e.g., [81]). In contrary, diffractive quadratic media with wave mixing between the first- and second-harmonic modes due to a $\chi^{(2)}$ nonlinearity are shown to inhibit wave collapse and to support stable solitons [82, 83].

For beams propagating in a bulk $\chi^{(2)}$ medium (as shown in Fig. 6.6) we take into account two transverse coordinates x and y so that Eqs. (6.1), after a similar

renormalisation to that above, take the form

$$\begin{aligned} i\frac{\partial v}{\partial z} + \nabla_{\perp}^2 v - v + v^*w &= 0, \\ 2i\frac{\partial w}{\partial z} + \nabla_{\perp}^2 w - \alpha w + \frac{1}{2}v^2 &= 0, \end{aligned} \quad (6.20)$$

where $\nabla_{\perp}^2 = (\partial^2/\partial x^2, \partial^2/\partial y^2)$, and the parameter α has the same definition as in Section 6.3.

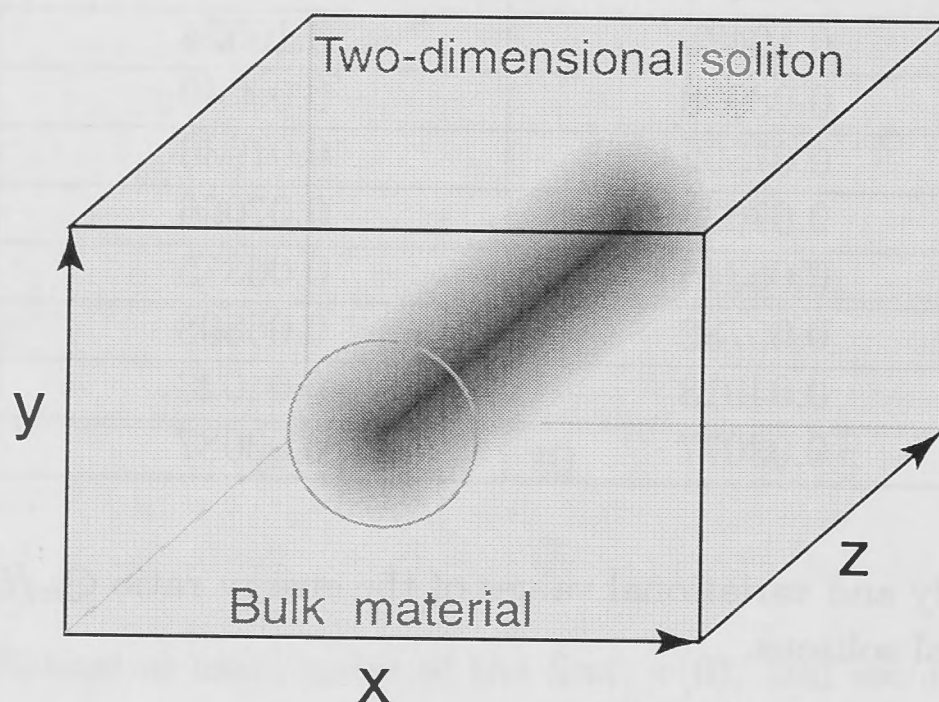


Figure 6.6: A (2+1)-dimensional soliton in a bulk medium.

For the (2+1)-dimensional case, the existence of stable stationary solutions of circular symmetry for the particular case of the exact phase-matched configuration, $k_2 = 2k_1$ (where k_1 and k_2 are the wavenumbers of the fundamental and second harmonics, respectively) has been addressed [69] and a particular (approximate) solution at $\alpha = 1$ found by means of the Hartree approach [71]. More recently it has been shown that in a bulk $\chi^{(2)}$ media there also exists a family of stationary soliton solutions of circular symmetry [22] defined by the dimensionless parameter α , similar to the (1+1) solitons [19]. Formation of (2+1)-dimensional solitons has also been observed in direct numerical simulations analysing beam excitation in a quadratic medium near the resonance between the fundamental and second harmonics [74] and in recent experiments [21, 84, 85].

For the stationary solutions of circular symmetry we omit in Eqs. (6.20) the derivatives in z and consider the envelopes $v(r)$ and $w(r)$ with $r \equiv |\mathbf{r}_{\perp}| = \sqrt{x^2 + y^2}$ as two coordinates in the corresponding mechanical problem with potential

$$U(v, w) = \frac{1}{2}(v^2w - \alpha w^2 - v^2) \quad (6.21)$$

and velocities $\dot{v} \equiv dv/dr$ and $\dot{w} \equiv dw/dr$. The spatially localised solutions of Eqs. (6.20) correspond to special (separatrix) trajectories in the phase space (v, w, \dot{v}, \dot{w}) which start at the point $(v(0), w(0), 0, 0)$ at $r = 0$ and approach asymptotically the point $(0, 0, 0, 0)$ as $r \rightarrow \infty$. These separatrix trajectories and, therefore, the profiles of the (2+1) solitons of circular symmetry, have been found numerically by the shooting and relaxation techniques (see Appendix A.4 for details) for various values of α and are discussed in [22].

Similar to the well-known case of the (2+1)-dimensional solitons of circular symmetry in a Kerr medium (e.g. [86], [78], where Gaussian approximations to the (2+1)-dimensional beam profiles have been used), analytical expressions for the beam profiles in the model (6.20) for *any* value of α have not been found. Nevertheless, these profiles can be found *approximately, and with a good accuracy*, by means of the variational approach. The stationary solutions of Eqs. (6.20) can be treated as extrema points of the Lagrangian with the density

$$\mathcal{L} = \frac{1}{2}[(\nabla_{\perp} v)^2 + (\nabla_{\perp} w)^2 + v^2 + \alpha w^2 - v^2 w], \quad (6.22)$$

i.e. as solutions of the variational problem $\delta L = 0$, where

$$L = \iint \mathcal{L} dx dy. \quad (6.23)$$

To apply the variational approach, we approximate the fields of the soliton family by two Gaussian functions [cf. (6.13)]

$$v(r) = Ae^{-\rho r^2}, \quad w(r) = Be^{-\gamma r^2}, \quad (6.24)$$

where A , B , ρ and γ are constants depending on α and have the same meaning as for the (1+1)-dimensional solitons. Substituting expressions (6.24) into the Lagrangian L , we obtain a system of four equations for A , B , ρ and γ from the corresponding variational problem. The solution for ρ is given implicitly by the cubic equation

$$32\rho^3 + 2\alpha\rho - \alpha = 0, \quad (6.25)$$

from which $\gamma = 4\rho^2$, $B = (1+2\rho)^2$ and $A^2 = \alpha(1+2\rho)^4/8\rho^2$. All of these parameters must be real and positive which determines the appropriate root of Eqn. (6.25).

Similar to the (1+1)-dimensional solitons, Eqn. (6.25) has an exact solution for $\alpha = 1$, $\rho = 1/4$ so that $\gamma = 1/4$, $A = 9\sqrt{2}/4$, $B = 9/4$. For $\alpha \neq 1$ the cubic equation (6.25) can be solved analytically, and for $\alpha > 0$, it always has a single real (positive) root which defines the profiles of the two-wave spatial solitons. Therefore, we can calculate approximately the characteristics of the self-trapped beams *analytically* and compare them with the numerical solutions [22]. This comparison is shown in Fig. 6.7, for soliton profiles with $\alpha = 10$, and in Fig. 6.8, for the soliton amplitudes. The corresponding relative error given by Gaussian approximations is larger than in the case of the (1+1)-dimensional solitons but is below 7%.

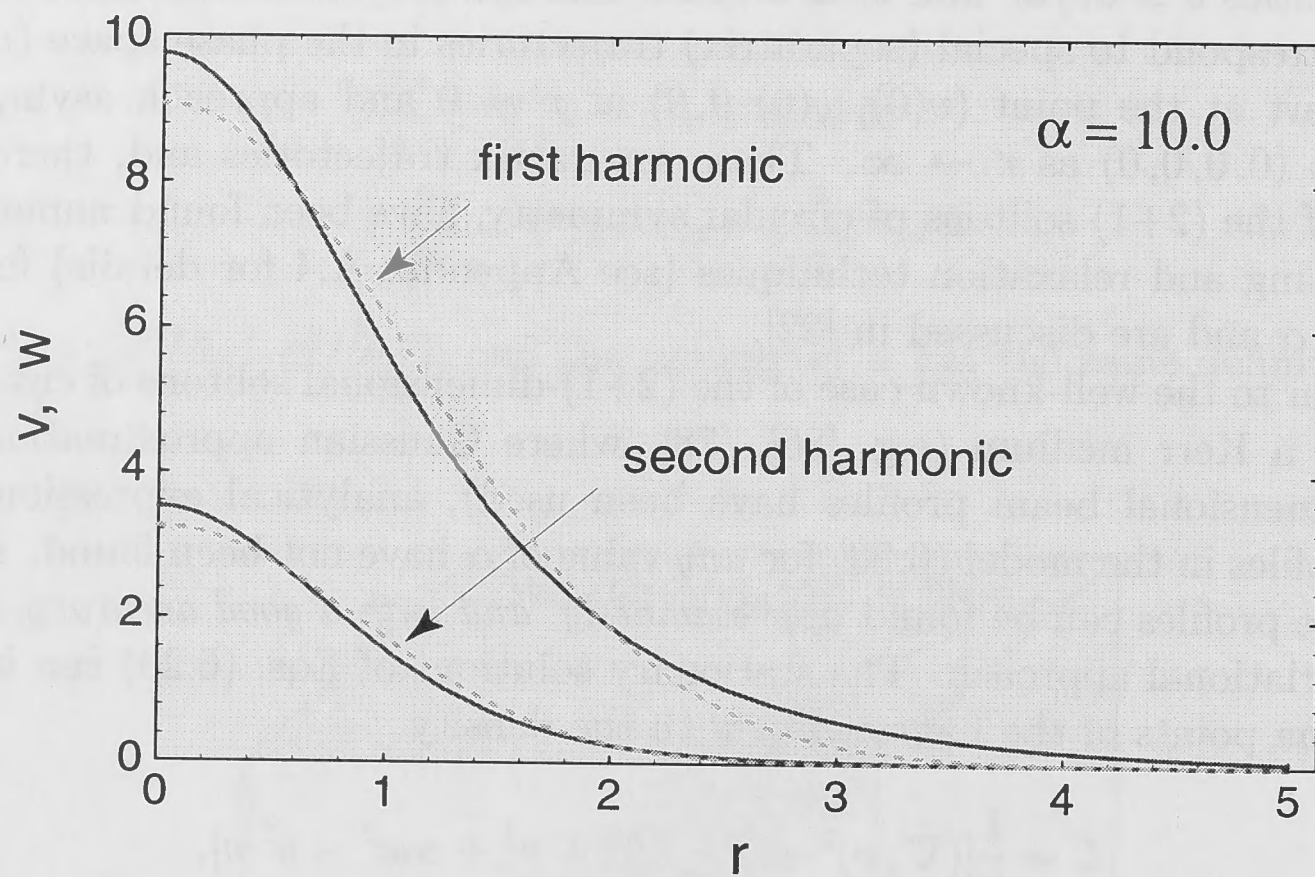


Figure 6.7: Comparison between numerical (solid curves) and variational (dashed curves) solutions for $\alpha = 10$ for the fundamental and second harmonic components of the (2+1)-dimensional solitons. The numerical solutions have been found using the shooting and relaxation techniques [22].

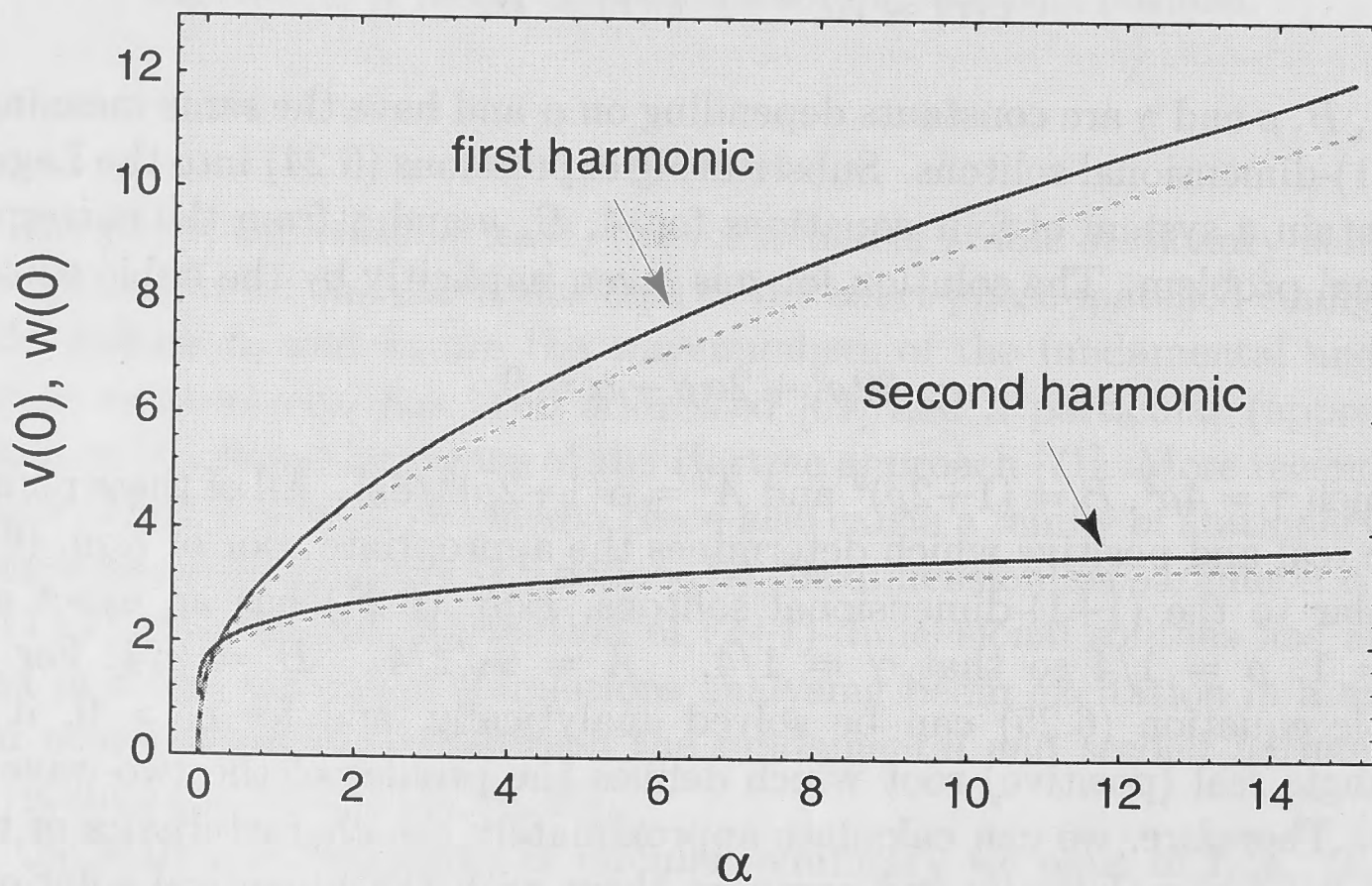


Figure 6.8: Maximum amplitudes of the first, $v(0)$, and second, $w(0)$, harmonics vs. the parameter α ; solid curves - numerical solutions, dashed curves - variational solutions.

We can again quantify the accuracy of the variational solution by calculating the integral characteristics of the energy of the stationary solutions. In Fig. 6.9, we compare the ratio of the field energy in the second harmonic,

$$Q_w = 2\pi \int_0^\infty |w|^2 r dr, \quad (6.26)$$

and the total energy of both harmonics

$$Q_{\text{sum}} = 2\pi \int_0^\infty (|v|^2 + |w|^2) r dr \quad (6.27)$$

using the approximate variational solution (6.24)–(6.25) (solid curve) and the numerical solutions of the system (6.20) (opened circles), obtained by the relaxation technique.

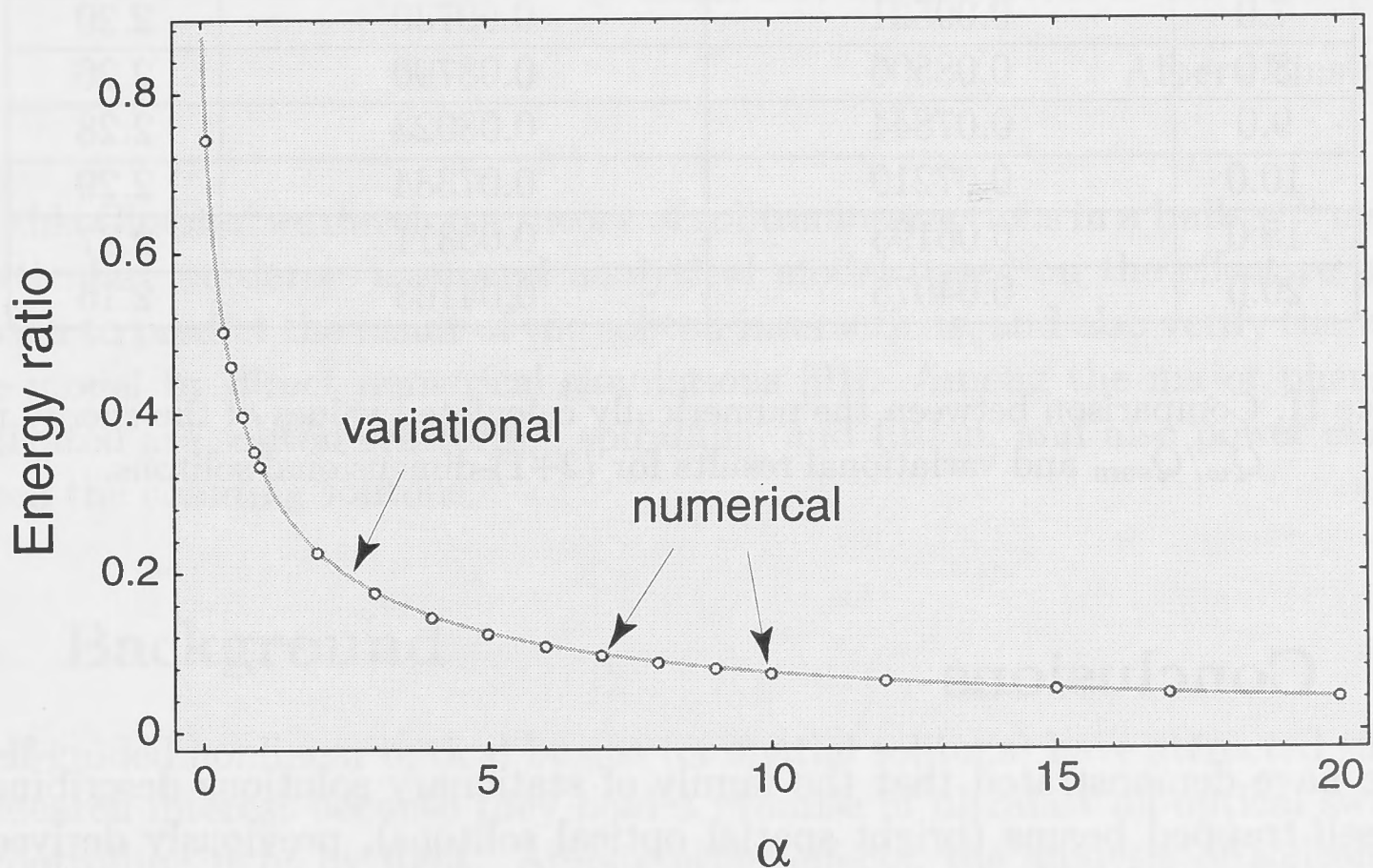


Figure 6.9: Ratio of the energy of the second harmonic, Q_w , to the harmonics' sum energy, Q_{sum} , as a function of the parameter α . Solid curve - variational results, opened circles - numerical results.

Table II presents the energy ratio Q_w/Q_{sum} and the relative error for different values of the parameter α calculated by both approaches. It is clear that for the (2+1) solitons the agreement between the numerical results and Gaussian approximations is quite good, being below 2.5% over the range of α .

α	Energy Ratio, Q_w/Q_{sum}		Relative Error, %
	numerical results	variational results	
0.1	0.74338	0.72528	2.43
0.4	0.50231	0.49559	1.34
0.5	0.45985	0.45508	1.04
0.7	0.39689	0.39471	0.55
0.9	0.35165	0.35108	0.16
1.0	0.33333	0.33333	0.00
2.0	0.22542	0.22773	1.02
3.0	0.17405	0.17672	1.53
4.0	0.14311	0.14572	1.82
5.0	0.12215	0.12460	2.01
6.0	0.10688	0.10915	2.12
7.0	0.09521	0.09730	2.20
8.0	0.08596	0.08790	2.26
9.0	0.07844	0.08023	2.28
10.0	0.07219	0.07384	2.29
15.0	0.05193	0.05311	2.27
20.0	0.04075	0.04163	2.16

Table II. Comparison between the numerically calculated values of the energy ratio Q_w/Q_{sum} and variational results for (2+1)-dimensional solitons.

6.5 Conclusions

We have demonstrated that the family of stationary solutions describing two-wave self-trapped beams (bright spatial optical solitons), previously derived only numerically or known for a particular value of the phase mismatch parameter, can be determined analytically using Gaussian approximations for both (1+1)-dimensional and (2+1)-dimensional solitons with a good accuracy. In particular, we have found very good agreement between the numerical solutions obtained by the shooting or relaxation techniques and approximate (variational) analytical results for the energy ratio between the harmonics. This suggests that the approximate soliton profiles found here could be used in the analytical description of a variety of nonlinear effects, such as analysis of evolution of spatial optical solitons in $\chi^{(2)}$ materials using soliton perturbation theory [79]. These results have found numerous applications and have been used by other researchers [87–90].

Interactions of $\chi^{(2)}$ solitons

You see, wire telegraph is a kind of a very, very long cat. You pull his tail in New York and his head is meowing in Los Angeles. Do you understand this? And radio operates exactly the same way: you send signals here, they receive them there. The only difference is that there is no cat.

Albert Einstein

In this Chapter we develop a theory of soliton interactions in a bulk $\chi^{(2)}$ medium. In particular, we derive a general analytical model based on the effective particle approach to predict the result of the soliton interactions, and also verify the validity of the model by direct numerical simulations [91]. Among the major phenomena investigated are soliton scattering, spiralling, and fusion, and also power exchange between the colliding solitons.

7.1 Background

Self-guided nonlinear optical beams (or spatial solitons) have attracted substantial research interest because they hold a promise of ultrafast all-optical switching and controlling light by light. Among other effects, the analysis of soliton interactions seems to be important for realizing all-optical *nonlinear switching* because solitons are expected to interact (attract, repel, etc.) as effective particles. Spatial $\chi^{(2)}$ solitons are especially attractive for switching, because the nonlinear response of quadratic media occurs on an ultra-fast time scale of femto-seconds (see, e.g., the recent review [92]). Interactions of (1+1)-dimensional quadratic solitons were investigated numerically in [93–97] where it was shown that soliton collisions depend strongly on the initial relative phase between the beams, similar to the case of one-wave non-Kerr solitons described by the generalised Nonlinear Schrödinger equation. Collision-based soliton switching in slab $\chi^{(2)}$ waveguides has been recently observed experimentally [98]. Very similar interactions were observed numerically for head-on collisions of (2+1) dimensional solitons [22, 99, 100][†]. When the relative

[†]Note that unlike (2+1)-dimensional solitons of an ideal Kerr medium, (2+1)-dimensional $\chi^{(2)}$ solitons are stable [22, 101, 102] and have recently been observed experimentally [21, 84, 85].

phase between the two colliding solitons is zero, they attract each other and finally fuse into a single soliton of a larger amplitude. The amplitude of this 'fused' soliton oscillates due to the excitation of a soliton internal mode [103]. However, when the two interacting solitons are significantly out of phase, the interaction between them can be repulsive, and both solitons, after exchanging some energy, survive after the collision.

The most important effects for all-optical switching are non-planar soliton collisions and steering in a bulk medium. Recent experimental discoveries of stable (2+1)-dimensional solitons in different nonlinear media [21, 104–106] initiated the experimental study of fully three-dimensional interactions between solitary beams. In particular, experimental results demonstrating non-planar interaction and spiralling of two incoherent beams in a photorefractive medium have been reported [107]. Similar phenomena are also to be expected for other types of (2+1)-dimensional solitary waves. However, since the first papers on soliton interactions (see, e.g., [108–110]), no systematic theory of non-planar soliton interactions in a bulk medium has been developed so far. In the majority of previous investigations, the analysis has been limited to direct numerical simulations only, which, on their own, is a limited method of analysis, usually inadequate to give *general predictions* or conclusions.

In this Chapter we present a theory of non-planar collisions of optical beams in a bulk nonlinear medium taking the case of (2+1)-dimensional $\chi^{(2)}$ solitons as an important and practical example [91]. In particular, we derive an analytical model describing the soliton scattering, spiralling and fusion, which allows significant simplification of the analysis of beam interactions, and also provides a physical insight. Our derivation is fully presented for the case of (2+1)-dimensional spatial solitons in bulk $\chi^{(2)}$ media. However, it can be easily modified for the much simpler case of (1+1)-dimensional model of soliton interactions. Most of the expressions for the (1+1)-dimensional planar case can be obtained by omitting integration over the second transverse dimension (y), and dependencies on y and C_y in the corresponding (2+1)-dimensional case formulas.

7.2 Mathematical model and integrals of motion

We start from the dimensionless system of equations describing the interaction of the fundamental (v) and second (w) harmonics in a bulk quadratic medium:

$$\begin{aligned} i\frac{\partial v}{\partial z} + \frac{\partial^2 v}{\partial x^2} + \frac{\partial^2 v}{\partial y^2} + wv^* &= 0, \\ i\sigma\frac{\partial w}{\partial z} + \frac{\partial^2 w}{\partial x^2} + \frac{\partial^2 w}{\partial y^2} - \sigma\Delta w + \frac{v^2}{2} &= 0, \end{aligned} \tag{7.1}$$

where $\Delta \equiv z_d\delta k$ is the dimensionless mismatch parameter, and $\sigma \equiv k_2/k_1 = 2.0$ for the case of spatial solitons. The system (7.1) can be obtained from Eqs. (6.1) (see Chapter 6 for derivation details and definitions) in a similar way as Eqs. (6.3). We will call σ and Δ the *system parameters*. These parameters are fixed by the experimental setup. We note, that we use Eqs. (7.1), rather than other forms of

normalised equations (e.g., the form used in [22]), because the former system leads to much simpler equations for soliton interaction.

Although the system (7.1) is not integrable analytically, it possesses several integrals of motion. Three of these integrals of motion are important for our further analysis. They are the energy (or Manley-Rowe) invariant,

$$Q = \int_{-\infty}^{\infty} \int_{-\infty}^{\infty} (|v|^2 + 2\sigma|w|^2) dx dy, \quad (7.2)$$

and the two components of the *vector* momentum

$$P_x = \frac{i}{2} \int_{-\infty}^{\infty} \int_{-\infty}^{\infty} \left\{ \left(v^* \frac{\partial v}{\partial x} - v \frac{\partial v^*}{\partial x} \right) + \sigma \left(w^* \frac{\partial w}{\partial x} - w \frac{\partial w^*}{\partial x} \right) \right\} dx dy,$$

$$P_y = \frac{i}{2} \int_{-\infty}^{\infty} \int_{-\infty}^{\infty} \left\{ \left(v^* \frac{\partial v}{\partial y} - v \frac{\partial v^*}{\partial y} \right) + \sigma \left(w^* \frac{\partial w}{\partial y} - w \frac{\partial w^*}{\partial y} \right) \right\} dx dy. \quad (7.3)$$

The number of integrals of motion of the evolution system is closely related to the number of internal parameters of the respective soliton families [108]. Usually each of the energy- and momentum-type invariants corresponds to the existence of one internal soliton parameter. In this instance we can expect Eqs. (7.1) to have a three-parameter bright soliton family. In order to find this three-parameter family explicitly we represent the v and w components as

$$v(x, y, z) = V(x - C_x z, y - C_y z, z) e^{i\beta z},$$

$$w(x, y, z) = W(x - C_x z, y - C_y z, z) e^{2i\beta z}, \quad (7.4)$$

and then find (e.g., numerically) complex *stationary*, i.e. z -independent, localised solutions of the system

$$\frac{\partial^2 V}{\partial x^2} + \frac{\partial^2 V}{\partial y^2} - iC_x \frac{\partial V}{\partial x} - iC_y \frac{\partial V}{\partial y} - \beta V + WV^* = 0,$$

$$\frac{\partial^2 W}{\partial x^2} + \frac{\partial^2 W}{\partial y^2} - i\sigma C_x \frac{\partial W}{\partial x} - i\sigma C_y \frac{\partial W}{\partial y} - \sigma(2\beta + \Delta)W + \frac{V^2}{2} = 0. \quad (7.5)$$

In Eqs. (7.5), we introduced the real *internal* soliton parameters β , C_x , and C_y , which, in contrast to the *system* parameters σ and Δ , may change during soliton evolution and interactions. The soliton parameter β is the nonlinearly-induced shift of the propagation constant, whereas C_x and C_y are two components of the soliton velocity.

For fixed σ and Δ , the complex stationary soliton solutions of Eqs. (7.5) are defined by values of the *internal* soliton parameters β , C_x , and C_y and can be written down as $V_s(\beta, C_x, C_y)$, $W_s(\beta, C_x, C_y)$. If all possible zero-velocity stationary solitons $V_s(\beta, 0, 0)$, $W_s(\beta, 0, 0)$ are known, then for $\sigma = 2$ we can find all other stationary

solitons of Eqs. (7.5) using the well-known gauge invariance property [22]. Indeed, by direct substitution, one can show that

$$\begin{aligned} V_s(\beta, C_x, C_y) &= V_s \left(\beta - \frac{1}{4}C_x^2 - \frac{1}{4}C_y^2, 0, 0 \right) e^{i(C_x x + C_y y)/2}, \\ W_s(\beta, C_x, C_y) &= W_s \left(\beta - \frac{1}{4}C_x^2 - \frac{1}{4}C_y^2, 0, 0 \right) e^{i(C_x x + C_y y)}. \end{aligned} \quad (7.6)$$

Formulas (7.6) can be used to obtain several important relations between the invariants of Eqs. (7.1) calculated from the soliton solutions $V_s(\beta, C_x, C_y)$ and $W_s(\beta, C_x, C_y)$. Substituting Eqs. (7.6) into the invariants (7.2,7.3), we obtain:

$$\begin{aligned} Q_s(\beta, C_x, C_y) &= Q_s \left(\beta - \frac{1}{4}C_x^2 - \frac{1}{4}C_y^2, 0, 0 \right), \\ P_{xs}(\beta, C_x, C_y) &= -\frac{C_x}{2} Q_s \left(\beta - \frac{1}{4}C_x^2 - \frac{1}{4}C_y^2, 0, 0 \right), \\ P_{ys}(\beta, C_x, C_y) &= -\frac{C_y}{2} Q_s \left(\beta - \frac{1}{4}C_x^2 - \frac{1}{4}C_y^2, 0, 0 \right). \end{aligned} \quad (7.7)$$

In Eqs. (7.7) we use the sub-subscript s to stress that the invariants (7.2) and (7.3) are calculated on the soliton solutions (V_s, W_s). Below, the invariants are always calculated on the soliton solutions (V_s, W_s) and we will omit this sub-subscript for the simplicity of notation. The family of fundamental radially symmetric stationary solitons [22] $V_s(\beta), W_s(\beta)$ has been found in the previous Chapter.

Differentiation of relations (7.7) with respect to β, C_x , and C_y , in turn, leads to the equalities

$$\begin{aligned} \frac{\partial Q}{\partial \beta} &= \frac{\partial \tilde{Q}}{\partial \beta}, \\ \frac{\partial P_x}{\partial C_x} &= -\frac{\tilde{Q}}{2} + \frac{C_x^2}{4} \frac{\partial \tilde{Q}}{\partial \beta}, \\ \frac{\partial P_y}{\partial C_y} &= -\frac{\tilde{Q}}{2} + \frac{C_y^2}{4} \frac{\partial \tilde{Q}}{\partial \beta}, \\ \frac{\partial Q}{\partial C_x} &= \frac{\partial P_x}{\partial \beta} = -\frac{C_x}{2} \frac{\partial \tilde{Q}}{\partial \beta}, \\ \frac{\partial Q}{\partial C_y} &= \frac{\partial P_y}{\partial \beta} = -\frac{C_y}{2} \frac{\partial \tilde{Q}}{\partial \beta}, \\ \frac{\partial P_x}{\partial C_y} &= \frac{\partial P_y}{\partial C_x} = \frac{C_x C_y}{4} \frac{\partial \tilde{Q}}{\partial \beta}, \end{aligned} \quad (7.8)$$

where we use the notation $Q \equiv Q(\beta, C_x, C_y), P_x \equiv P_x(\beta, C_x, C_y), P_y \equiv P_y(\beta, C_x, C_y)$, and $\tilde{Q} \equiv Q \left(\beta - \frac{1}{4}C_x^2 - \frac{1}{4}C_y^2, 0, 0 \right)$.

7.3 Summary of stability results

The full-scale theoretical analysis of the stability of single bright solitons of Eqs. (7.1) is beyond the scope of this Thesis. However, for completeness of the presentation, we present major stability results below. Detailed stability analysis of this and similar problems can be found in [22, 101, 102, 111].

It is possible to show that the parameter surface, separating stable and unstable parameter domains in the phase space (β, C_x, C_y) of the soliton parameters, is defined by the condition

$$\frac{\partial(Q, P_x, P_y)}{\partial(\beta, C_x, C_y)} \equiv \begin{vmatrix} \frac{\partial Q}{\partial \beta} & \frac{\partial Q}{\partial C_x} & \frac{\partial Q}{\partial C_y} \\ \frac{\partial P_x}{\partial \beta} & \frac{\partial P_x}{\partial C_x} & \frac{\partial P_x}{\partial C_y} \\ \frac{\partial P_y}{\partial \beta} & \frac{\partial P_y}{\partial C_x} & \frac{\partial P_y}{\partial C_y} \end{vmatrix} = 0, \quad (7.9)$$

where invariants (7.2) and (7.3) are calculated on the soliton solutions $V_s(\beta, C_x, C_y)$ and $W_s(\beta, C_x, C_y)$. If $\sigma \neq 2$, the gauge invariance would be broken and the threshold condition would have a complicated form. However, for $\chi^{(2)}$ spatial solitons $\sigma = 2$. As a result, we can use the relations (7.8) to simplify the determinant (7.9) to the form

$$\frac{\tilde{Q}^2}{4} \frac{\partial \tilde{Q}}{\partial \beta} = 0. \quad (7.10)$$

Positiveness of \tilde{Q}^2 simplifies the threshold condition even further to $\partial \tilde{Q} / \partial \beta = 0$. The condition for the soliton existence is straightforward to derive too, and it can be expressed as

$$\left(\beta - \frac{1}{4} C_x^2 - \frac{1}{4} C_y^2 \right) > \max \left(0, -\frac{\Delta}{2} \right). \quad (7.11)$$

Using a more elaborate analysis similar to that reported in [101, 102], one can show that for the most interesting case of $\sigma = 2$, the condition of soliton *stability* is given by the simple formula

$$\frac{\partial \tilde{Q}}{\partial \beta} > 0. \quad (7.12)$$

Numerical analysis of the behaviour of the power invariant Q (verified by direct numerical simulations) shows that the unstable $\chi^{(2)}$ spatial solitons can only exist for $\Delta < 0$, whereas for $\Delta \geq 0$ all solitons are stable. This result holds both for (2+1)-dimensional [22] and (1+1)-dimensional [111] cases.

7.4 Soliton interactions: theory versus numerics

In Appendix C, we derive a general system of ordinary differential equations (ODE's) for the soliton parameters, describing the adiabatic interaction of two almost identical solitons in a bulk $\chi^{(2)}$ medium. These equations, Eqs. (C.13), are

simpler than the original model (7.1), but are still too complex to provide immediate physical insight. However, the system (C.13) can be simplified further using additional assumptions.

Let us consider *two initially identical solitons*, which are located symmetrically about the coordinate centre $(0, 0)$ in (x, y) plane, and have opposite initial velocities. In other words, initially $C_x^{(1)} = -C_x^{(2)}$, $C_y^{(1)} = -C_y^{(2)}$. Using these assumptions and the invariant properties (7.8), we can reduce the system (C.13) to the new form:

$$\begin{aligned}
 -\frac{\partial \tilde{Q}^{(1)}}{\partial \beta^{(1)}} \ddot{\phi}^{(1)} + \frac{1}{2} \frac{\partial U}{\partial \phi^{(1)}} &= 0, \\
 -\frac{\partial \tilde{Q}^{(2)}}{\partial \beta^{(2)}} \ddot{\phi}^{(2)} + \frac{1}{2} \frac{\partial U}{\partial \phi^{(2)}} &= 0, \\
 \frac{\tilde{Q}^{(1)}}{2} \ddot{x}^{(1)} + \frac{1}{2} \frac{\partial U}{\partial x^{(1)}} &= 0, \\
 \frac{\tilde{Q}^{(2)}}{2} \ddot{x}^{(2)} + \frac{1}{2} \frac{\partial U}{\partial x^{(2)}} &= 0, \\
 \frac{\tilde{Q}^{(1)}}{2} \ddot{y}^{(1)} + \frac{1}{2} \frac{\partial U}{\partial y^{(1)}} &= 0, \\
 \frac{\tilde{Q}^{(2)}}{2} \ddot{y}^{(2)} + \frac{1}{2} \frac{\partial U}{\partial y^{(2)}} &= 0,
 \end{aligned} \tag{7.13}$$

where the effective potential U is given by the expressions (C.11) and (C.12), in which we formally put all $C_x^{(j)} = 0$ and $C_y^{(j)} = 0$.

7.4.1 Effective particle approach

System (7.13) has the form of the classical mechanics problem for two effective particles interacting in 3-dimensional space. Note, however, that each of these effective particles has a variable anisotropic mass, and $M_\phi^{(j)} \neq M_x^{(j)} = M_y^{(j)}$. In addition, $M_\phi^{(j)} \equiv -2\partial\tilde{Q}^{(j)}/\partial\beta^{(j)}$ is always *negative*, because the stability condition (7.12) for single solitons requires $\partial\tilde{Q}^{(j)}/\partial\beta^{(j)} > 0$.

Now we multiply the first of Eqs. (7.13) by $\partial\tilde{Q}^{(2)}/\partial\beta^{(2)}$, the second of Eqs. (7.13) by $\partial\tilde{Q}^{(1)}/\partial\beta^{(1)}$ and subtract the resulting equations from each other. Repeating similar procedure for other two pairs of equations in the system (7.13), we obtain

$$\begin{aligned}
 M_\phi \ddot{\phi} + \frac{\partial U}{\partial \phi} &= 0, \\
 M_X \ddot{X} + \frac{\partial U}{\partial X} &= 0, \\
 M_Y \ddot{Y} + \frac{\partial U}{\partial Y} &= 0,
 \end{aligned} \tag{7.14}$$

where $M_\phi \equiv -2Q_{\beta^{(1)}}^{(1)}Q_{\beta^{(2)}}^{(2)}/(Q_{\beta^{(1)}}^{(1)} + Q_{\beta^{(2)}}^{(2)})$, $M_X = M_Y \equiv Q^{(1)}Q^{(2)}/(Q^{(1)} + Q^{(2)})$, $\phi \equiv \phi^{(2)} - \phi^{(1)}$, $X \equiv x^{(2)} - x^{(1)}$, and $Y \equiv y^{(2)} - y^{(1)}$.

The reduction from Eqs. (7.13) to Eqs. (7.14) is self-consistent if M_ϕ , M_X , and M_Y depend only on $\Delta\beta \equiv \beta^{(2)} - \beta^{(1)}$ or are constants. In this Subsection we assume all effective masses to be constant, i.e. $M_\phi = M_\phi(\beta_0)$, $M_X = M_X(\beta_0)$, and $M_Y = M_Y(\beta_0)$, where $\beta_0 \equiv \beta^{(1)}(z=0) = \beta^{(2)}(z=0)$. From the physical point of view, this assumption means no power exchange between the solitons. Violation of this assumption and soliton power exchange are addressed in the next Subsection.

Following the standard methods of classical mechanics (see, e.g., [112]), the dimensionality of Eqs. (7.14) can be reduced using cylindrical coordinates (R, ϕ) , where $R \equiv \sqrt{X^2 + Y^2}$ is the relative distance between the interacting beams, X and Y being the separation between solitons in the x and y directions, respectively; and ϕ is the relative phase between the solitons. The final equations can be then presented in the form

$$\begin{aligned} M_\phi \ddot{\phi} + \frac{\partial U_{\text{eff}}}{\partial \phi} &= 0, \\ M_R \ddot{R} + \frac{\partial U_{\text{eff}}}{\partial R} &= 0, \end{aligned} \quad (7.15)$$

which corresponds to the effective two-dimensional Lagrangian

$$L = \frac{1}{2} M_R \dot{R}^2 + \frac{1}{2} M_\phi \dot{\phi}^2 - U_{\text{eff}}(R, \phi), \quad (7.16)$$

We recall that the elements of the effective mass matrix are defined as

$$\begin{aligned} M_R &\equiv \pi \int_0^\infty \{|V(r)|^2 + 2\sigma |W(r)|^2\} r dr, \\ M_\phi &\equiv -2\partial M_R / \partial \beta, \end{aligned}$$

where the integrand is calculated for the one-soliton stationary solutions of radial symmetry. The effective potential energy is defined as

$$U_{\text{eff}}(R, \phi) = \frac{M_R s^2 C_0^2}{4R^2} + U_1(R) \cos(\phi) + U_2(R) \cos(2\phi), \quad (7.17)$$

where the overlap integrals U_1 and U_2 are given by

$$U_1(R) \equiv -2 \int_{-\infty}^{\infty} \int_{-\infty}^{\infty} [W_0^{(2)} V_0^{(2)} V_0^{(1)} + W_0^{(1)} V_0^{(1)} V_0^{(2)}] dx dy,$$

and

$$U_2(R) \equiv - \int_{-\infty}^{\infty} \int_{-\infty}^{\infty} [V_0^{(2)2} W_0^{(1)} + V_0^{(1)2} W_0^{(2)}] dx dy.$$

The impact parameter s defines the distance between the trajectories of noninteracting solitons [see Figs. 7.1 (a)-(c) below], and $C_0 \equiv \dot{R}(z=0)$ is the relative velocity between the solitons prior to the interaction.

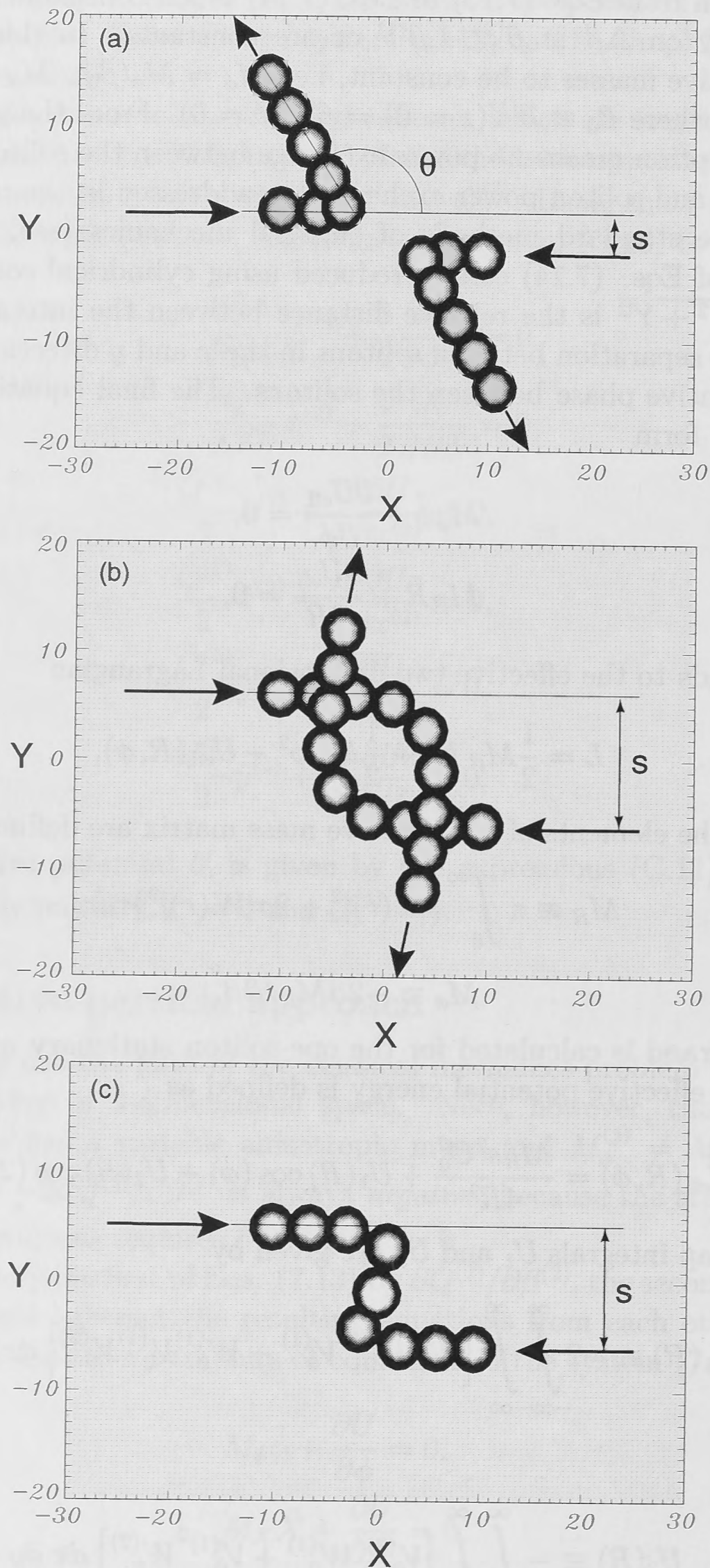


Figure 7.1: Sequences of soliton positions in the (X, Y) plane shown at different propagation distances for (a) soliton scattering ($\phi = \pi$, $s = 3.6$) (b) soliton reflection via spiralling ($\phi = 0$, $s = 11.6$), and (c) soliton fusion ($\phi = 0$, $s = 11.0$). All results are obtained for $\beta = 0.5$, $\Delta = 1.0$ and $C_0 = 0.2$.

When the distance between the interacting solitons is relatively large, the soliton interaction is determined by their tail asymptotics, which can be found analytically (except for constant factors A and B) as $V^{(j)}(r) = (A/\sqrt{r}) \exp(-\sqrt{\beta}r)$ and $W^{(j)}(r) = (B/\sqrt{r}) \exp[-\sqrt{\sigma(2\beta + \Delta)}r]$. The asymptotic expressions for the functions U_1 and U_2 can be also estimated analytically, e.g.,

$$U_1(R) \approx -KA^2 \sqrt[4]{\beta} \exp(-\sqrt{\beta}R)/\sqrt{R},$$

where the positive parameter K is fitted numerically. We found that for a large range of parameters Δ and β , $K \approx 20.855$. The situation with $U_2(R)$ is more complicated. For $\sqrt{\sigma(\Delta + 2\beta)} \leq 2\sqrt{\beta}$, the potential $U_2(R) \sim \exp[-\sqrt{\sigma(\Delta + 2\beta)}R]$, whereas for $\sqrt{\sigma(\Delta + 2\beta)} > 2\sqrt{\beta}$, the potential $U_2(R) \sim \exp[-2\sqrt{\beta}R]$. In both cases further numerical fitting is necessary. For the combination of parameter values discussed in this Thesis ($\Delta = 1$, $\beta = 0.5$) our fitting formulas have the following forms:

$$\begin{aligned} U_1(R) &= -2330.0 \exp(-0.7071R)/\sqrt{R}, \\ U_2(R) &= -8216.0 \exp(-1.4142R). \end{aligned} \tag{7.18}$$

The effective mechanical model defined by the Lagrangian (7.16) can be used to generate a physical picture of soliton dynamics predicting the outcome of soliton collisions [91]. Importantly, interaction forces depend strongly on the relative phase ϕ . For simplicity, we concentrate on the case when $U_2 \ll U_1$ (which is always true for $\Delta > 0$) and $\phi = 0, \pi$. In the case of out-of-phase collisions ($\phi = \pi$), the “centrifugal force”, defined by the first term of the effective potential U_{eff} , and the direct interaction force, defined by the second term $U_1(R) \cos(\phi)$, are both *repulsive*. Therefore, the effective particle cannot reach the force centre, i.e. solitons cannot fuse [see Fig. 7.2 (a)]. The interaction scenario is very different for in-phase soliton collisions ($\phi = 0$). An interplay between a repulsive “centrifugal” force and an attractive interaction force leads to two qualitatively different regimes schematically shown in Fig. 7.2 (b). For low relative velocities (or sufficiently large s) solitons cannot overcome the centrifugal potential barrier, and they spiral about each other. At higher velocities (or smaller s) soliton fusion can occur.

The numerical analysis used the standard split-step BPM, which is described in Appendix A.2. Our direct numerical modelling of Eqs. (7.1) confirmed the predictions of the approximate model given by the Lagrangian (7.16). Figures 7.1 (a)-(c) present the characteristic examples of the soliton interaction including soliton scattering (a), soliton spiralling (b), and soliton fusion (c). All types of the soliton interactions predicted by the analytical model have been observed in the numerical results [91]. To make quantitative comparison, we integrated the dynamical model for the relative coordinate and phase following from Eqn. (7.16), applying the techniques of the well-known scattering theory of classical mechanics [112]. Figure 7.3 compares the results of our analytical model with direct numerical experiment showing the dependence of the scattering angle θ on the soliton impact parameter s . Good agreement is found even for the case of initial relative velocity $C_0 = 0.2$.

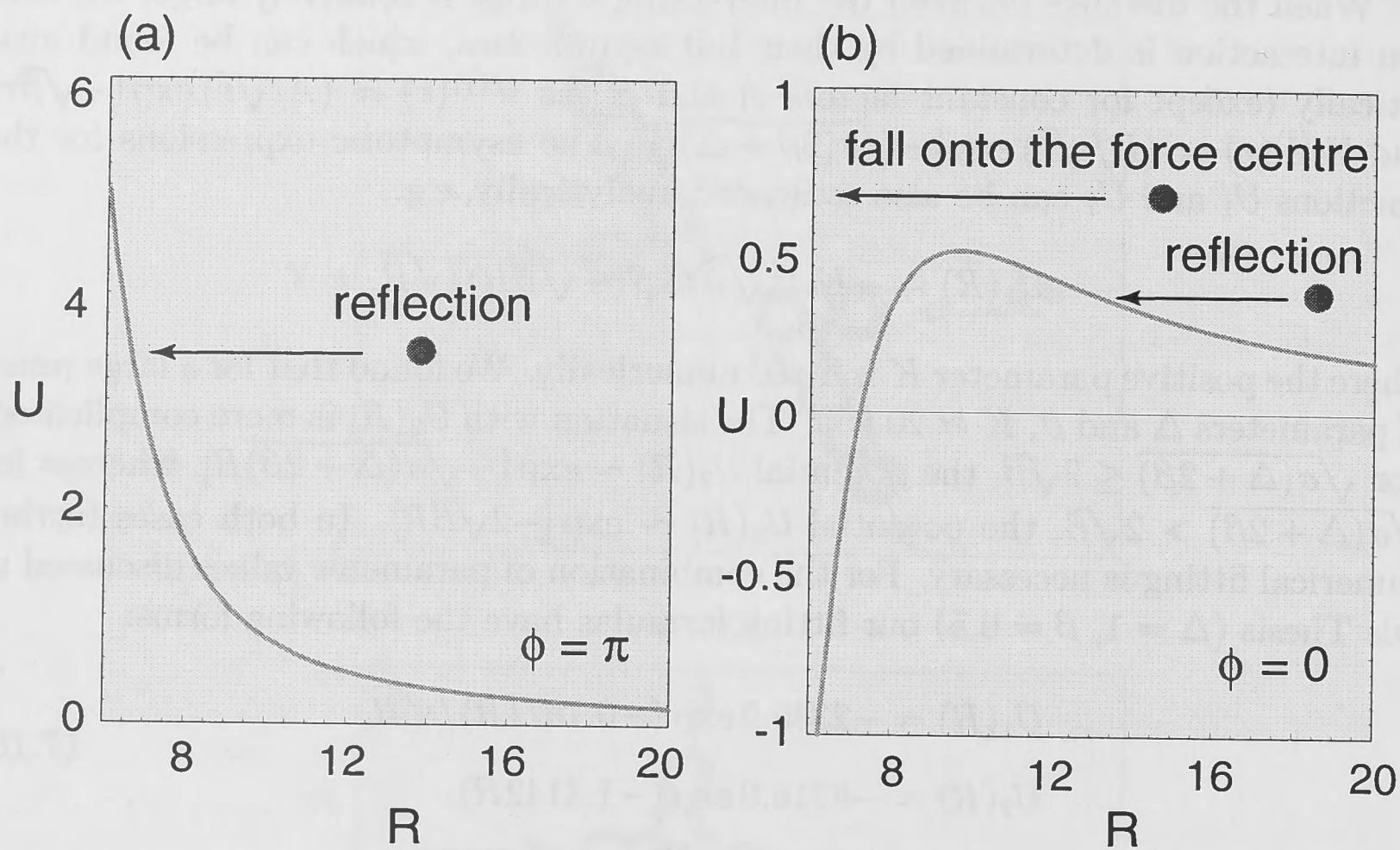


Figure 7.2: Qualitative sketch of the effective interaction potential $U_{\text{eff}}(R, \phi)$ for (a) out-of-phase interaction ($\phi = \pi$) (b) in-phase interaction ($\phi = 0$).

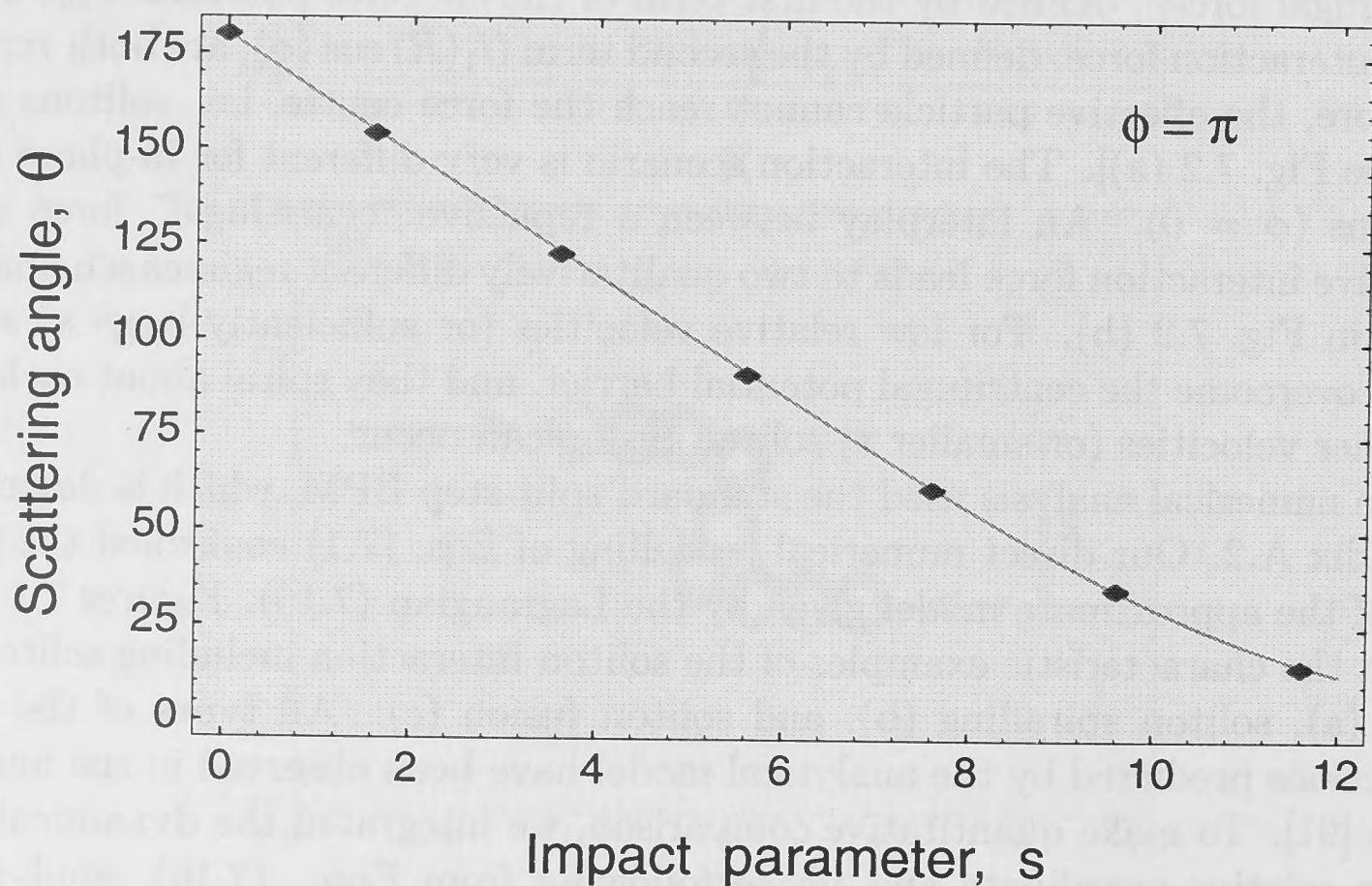


Figure 7.3: Soliton scattering angle θ vs. impact parameter s [see definitions in Fig. 7.1(a)] for out-of-phase collisions. Solid line - analytical results, diamonds - results of numerical simulations. Results are obtained for $\beta = 0.5$, $\Delta = 1.0$, and $C_0 = 0.2$.

7.4.2 Power exchange between colliding solitons

To describe the power exchange between the interacting solitons, we approximate $Q^{(1)}$ and $Q^{(2)}$ as linear functions of $\beta^{(1)}$ and $\beta^{(2)}$, respectively. This leads to the following dependences of $Q^{(1)}$ and $Q^{(2)}$ on $\Delta\beta$ [$\Delta\beta \equiv \beta^{(2)} - \beta^{(1)}$]:

$$\begin{aligned} Q^{(1)} &= Q - \frac{1}{2} \frac{\partial Q}{\partial \beta} \Delta\beta, \\ Q^{(2)} &= Q + \frac{1}{2} \frac{\partial Q}{\partial \beta} \Delta\beta, \end{aligned} \quad (7.19)$$

where $\beta \equiv (\beta^{(2)} + \beta^{(1)})/2$ and $Q \equiv Q^{(1)}(\beta) = Q^{(2)}(\beta)$. Equations (7.19) are consistent with the total energy conservation: $Q^{(1)} + Q^{(2)} = 2Q = \text{const}$. Using Eqs. (7.19) we find that

$$\begin{aligned} M_\phi &= -Q_\beta = \text{const}, \\ M_X &= M_Y = Q/2 - (1/8)Q_\beta^2(\Delta\beta)^2. \end{aligned} \quad (7.20)$$

Thus for small changes of relative phase ϕ (implying that $\Delta\beta = \dot{\phi}$ is also small) all masses M_ϕ , M_X , and M_Y are constants, correct to order $(\Delta\beta)^2$. These qualitative arguments show why we assume masses to be constants in Eqs. (7.14).

We can calculate the small power exchange between harmonics by simply integrating Eqs. (7.15), and measuring $\Delta\beta \equiv \dot{\phi}$ at some z sufficiently far beyond the collision region. In general, after the interaction $\Delta\beta \neq 0$ for any soliton collision with initial $\phi \neq 0, \pi$. The exchanged power is then given by

$$\Delta Q = \frac{\partial Q}{\partial \beta} \Delta\beta, \quad (7.21)$$

where $\partial Q/\partial \beta$ is calculated for any of two identical solitons prior to their interaction. Figures 7.4 and 7.5 give an example of soliton collision with significant power exchange.

It is evident from Fig. 7.4 that, after the collision, the relative soliton velocity has increased. This can be readily explained using dynamical invariants of Eqs. 7.15. Consider the total energy of the two particles approaching each other from sufficiently large distance:

$$H_{\text{in}} = \frac{1}{2} M_R \dot{R}^2 + \frac{1}{2} M_\phi \dot{\phi}^2. \quad (7.22)$$

In Eqn. (7.22) we neglected the potential energy of interaction $U_{\text{eff}}(R, \phi)$. The total energy H_{out} far after the interaction has the same form as H_{in} and must retain the same value as before the interaction. Accordingly, since $\dot{\phi}^2 > 0$ and $M_\phi < 0$, the growth of $\dot{\phi}$ has to be compensated for by the growth of relative velocity \dot{R} .

To verify our theoretical predictions we compared the power exchange results given by Eqn. (7.21) with the results of direct numerical modelling (see Figure 7.6). Surprisingly Fig. 7.6 demonstrates that Eqn. (7.21) can give approximately correct results even when significant soliton power exchange occurs, and the condition $\Delta\beta \ll 1$ is violated.

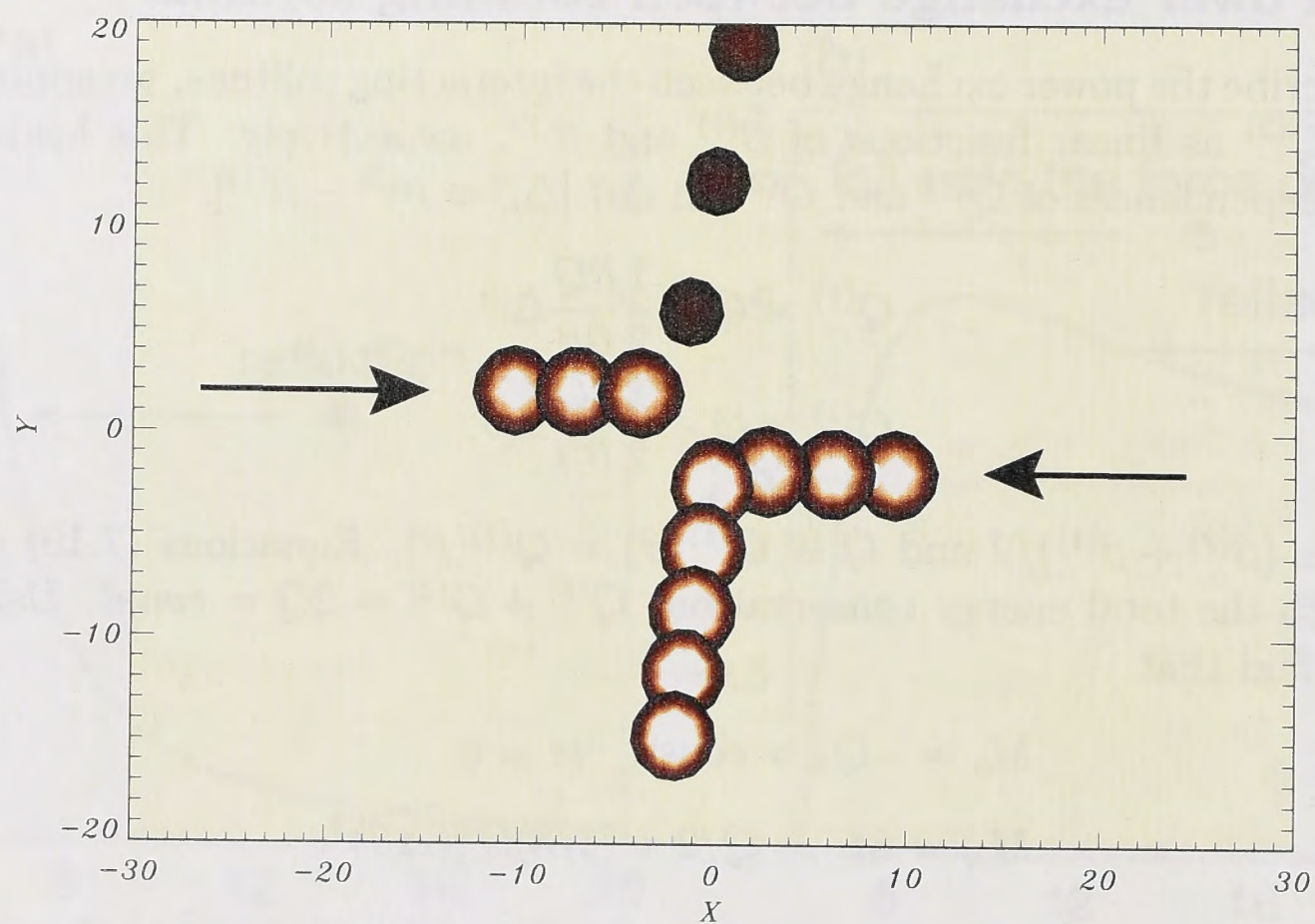


Figure 7.4: Sequences of soliton positions in (X, Y) plane shown at different propagation distances for soliton scattering ($\phi = \pi/8$, $s = 3.2$) with significant power exchange. All results are obtained for $\beta = 0.5$, $\Delta = 1.0$, and $C_0 = 0.4$.

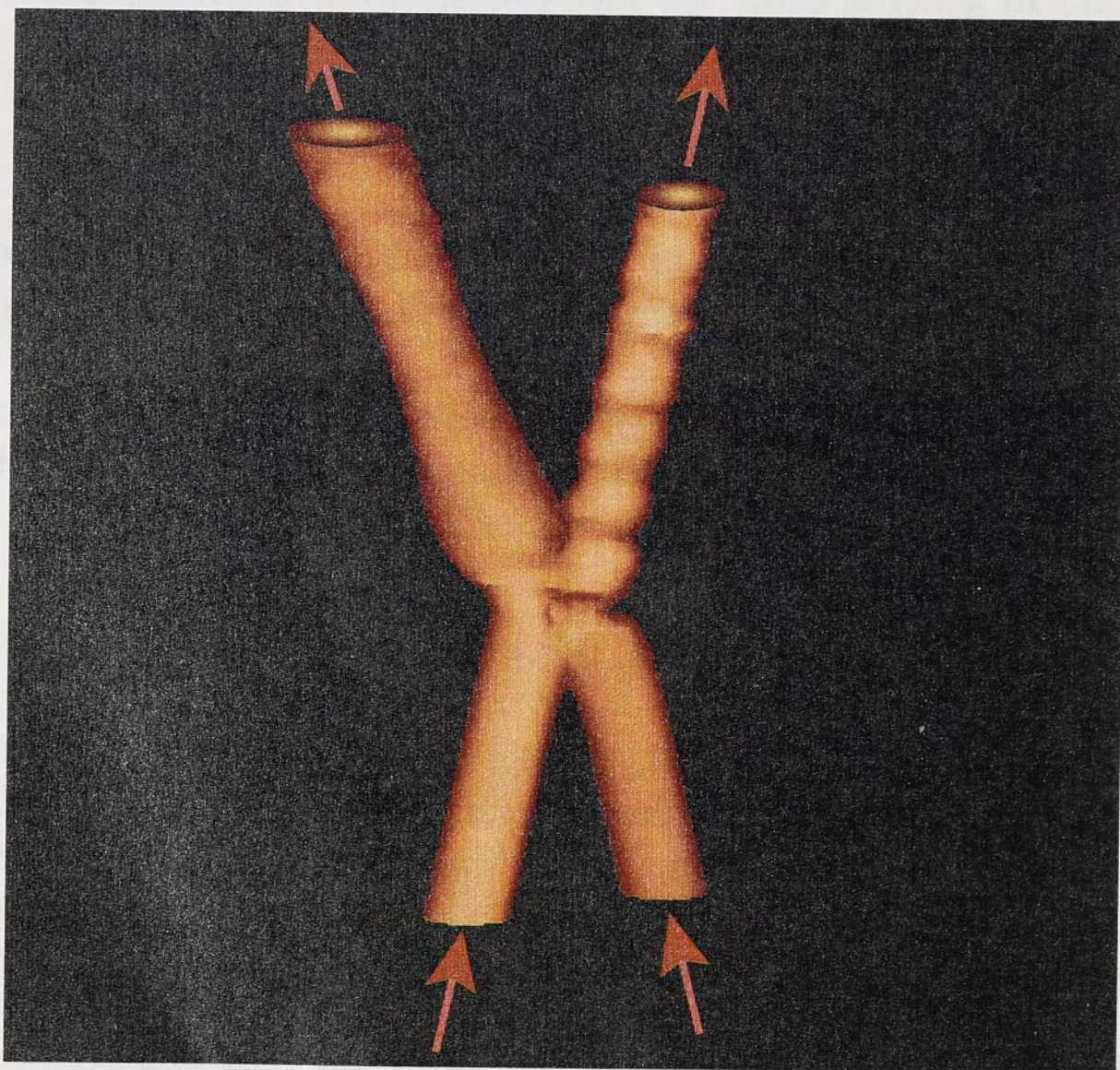


Figure 7.5: Three-dimensional view of soliton interaction with significant power exchange. The parameters are the same as in Fig. 7.4.

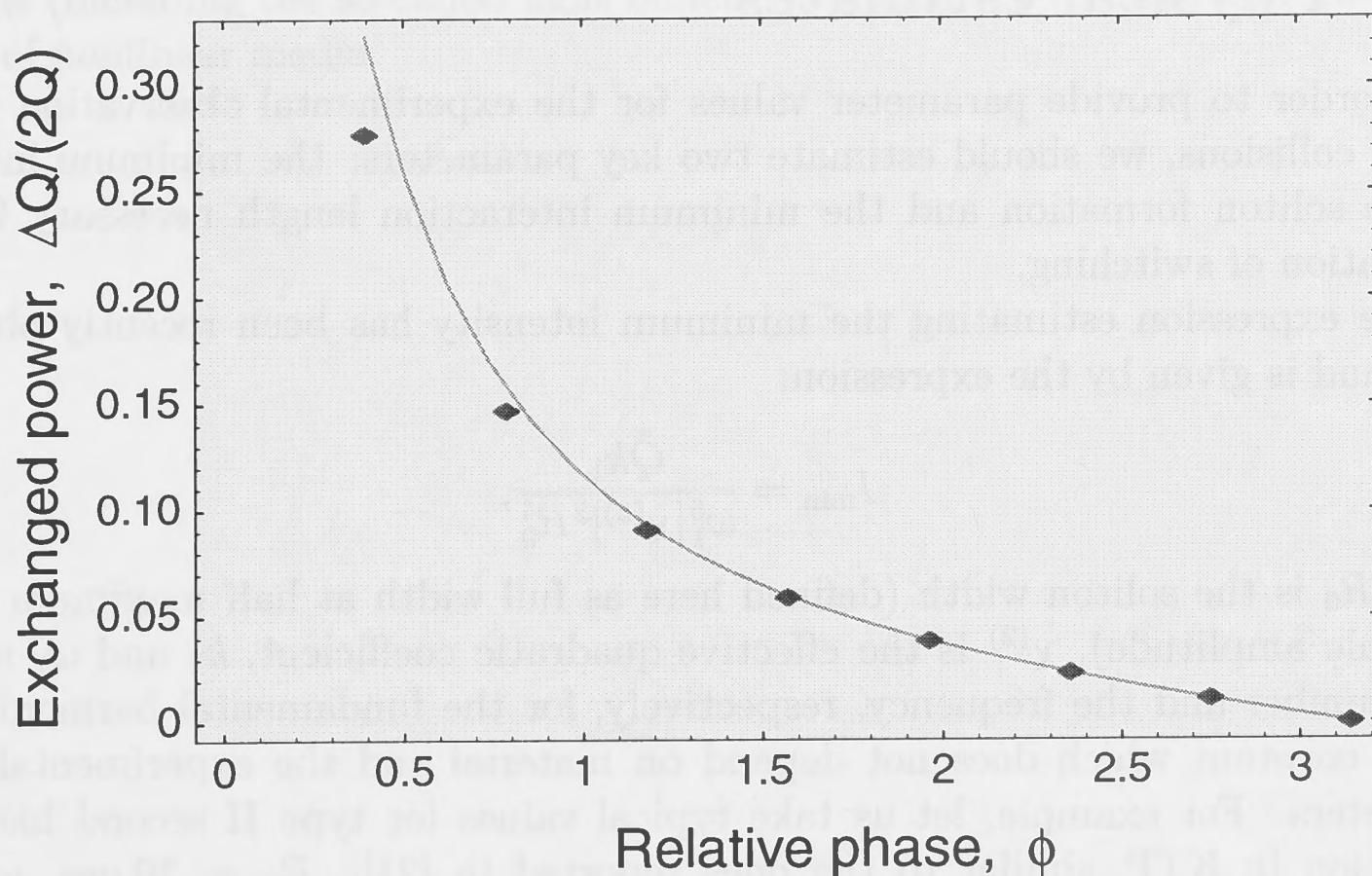


Figure 7.6: Normalised exchanged power between the solitons $\Delta Q/(2Q)$ vs. relative phase ϕ . Solid line - analytical results, diamonds - results of numerical simulations. Results are for $s = 3.6$, $\beta = 0.5$, $\Delta = 1.0$, and $C_0 = 0.2$.

7.5 Stability of spiralling configurations

Using the analytical model, we can investigate a possibility of stable spiralling configurations (or bound states) similar to those observed for incoherently interacting photorefractive solitons [107]. For two (2+1)-dimensional $\chi^{(2)}$ solitons interacting coherently with a positive phase mismatch and $U_1 \gg U_2$, the model (7.16) predicts the existence of a local minimum of the effective interaction potential $U_{\text{eff}}(R)$ at $\phi = 0$ and $R_0 \sim 1$. However, the approximate model (7.16) is valid only for weakly overlapping solitons when R is large and, therefore, this minimum is physically unrealisable, being located in the region of soliton fusion. In the opposite situation of negative phase matching, U_1 and U_2 may become comparable and we find a shallow local minimum of the potential $U_{\text{eff}}(R)$ at $\phi = \pi$ and $R_0 \gg 1$. A spiralling configuration of two solitons corresponding to such a local minimum would be stable if both mass coefficients in the energy (7.16) were positive. Unfortunately, stability of single solitons involved in the interaction always requires that $M_\phi < 0$ [see the condition (7.12)], and therefore this extremum is a *saddle point* in the space (R, ϕ) meaning that no stable bound states of coherently interacting $\chi^{(2)}$ solitons are possible. Indeed, we have not been able to observe such states in direct numerical modelling of Eqs. (7.1). We expect this to be a rather general phenomenon valid for other types of solitary waves interacting coherently, which, however, has not been previously addressed in literature.

7.6 Physical estimates

In order to provide parameter values for the experimental observation of $\chi^{(2)}$ soliton collisions, we should estimate two key parameters: the minimum intensity for the soliton formation and the minimum interaction length necessary for the observation of switching.

The expression estimating the minimum intensity has been recently obtained [113], and is given by the expression:

$$I_{\min} = \frac{\tilde{Q}k_1}{\omega_1^5[\chi^{(2)}]^2 R_0^4}, \quad (7.23)$$

where R_0 is the soliton width (defined here as full width at half maximum for E_2 harmonic amplitude), $\chi^{(2)}$ is the effective quadratic coefficient, k_1 and ω_1 are the wave number and the frequency, respectively, for the fundamental harmonic, and \tilde{Q} is a constant which does not depend on material and the experimental setup parameters. For example, let us take typical values for type II second harmonic generation in KTP, similar to the ones reported in [21]: $R_0 = 10 \mu m$, $\omega_1/c = 6.13 \times 10^4 \text{ cm}^{-1}$, $k_1 = 10.5 \mu m^{-1}$ and $\chi^{(2)} = 6 \text{ pm/V}$. Using the formalism of [113], we obtain $I_{\min} \approx 14.0 \text{ GW cm}^{-2}$ for (2+1)-dimensional solitons.

Our numerical results indicate, that the minimum interaction length L_{\min} necessary for switching is about 10 normalised propagation distance units, i.e. is of the order of 10 diffraction lengths (see the previous Chapter, Section 6.2 for the definition of diffraction length R_{dif}). Again, taking the experimental parameters as $R_0 = 10 \mu m$ and $k_1 = 10.5$, we can calculate that $R_{\text{dif}} \approx 2 \text{ mm}$. Thus the minimum necessary crystal length in physical units is $L_{\min} = 10R_{\text{dif}} \approx 2 \text{ cm}$.

We point out that our values of I_{\min} and L_{\min} give an estimate from below. Our calculations are based on the assumption that the laser beams initially match exactly each of the corresponding soliton components. Breaking this condition, e.g., generating $\chi^{(2)}$ solitons without seeding of the second harmonic, should slightly increase the required threshold intensity and interaction length. On the other hand, the use of new materials and/or phase-matching techniques (as in [114]) can lead to much higher values of effective $\chi^{(2)}$ parameter, which, in turn, significantly decreases I_{\min} , or (if R_0 is decreased) L_{\min} .

7.7 Conclusions

In this Chapter we have analysed non-planar collisions of (2+1)-dimensional $\chi^{(2)}$ solitons and demonstrated a controllable soliton-based all-optical switching [91] determined by the initial soliton states, i.e. the soliton velocities, the relative phase, and the impact parameter. We have derived an effective mechanical model [91] which provides a physical description of elastic soliton collisions in terms of an effective particle. This model has been fully confirmed by the results of direct numerical simulations. The phenomenon of $\chi^{(2)}$ soliton scattering may find its applications in ultra-fast all-optical signal processing and switching in a bulk medium. Our approach can be readily generalised for analysing interactions of higher-dimensional

solitons (including the so-called light bullets [115–117]) in $\chi^{(2)}$ materials and other types of nonlinear media.

Numerical methods

Computers can figure out all kinds of problems, except the things in the world that just don't add up.

James Magary

This chapter contains brief descriptions of all the numerical methods used throughout the thesis. As we saw earlier, most of the problems addressed in this thesis have no exact analytical solutions, and, therefore, need to be solved numerically. A variety of techniques for solving ODE's and PDE's was employed to study linear optical waveguides (Chapters 2–5), as well as nonlinear self-guiding phenomena (Chapters 6–7), with emphasis on mode solvers and beam propagation methods. Some numerical methods, e.g. the Fourier Decomposition Method, are intrinsically linear and can only be applied to linear waveguide problems, whereas beam propagation schemes can be tailored to tackle both linear and nonlinear evolution dynamics.

A.1 Fourier Decomposition Method (FDM)

The Fourier Decomposition Method is used to find approximate solutions of linear eigenvalue-eigenvector problems, such as the scalar wave equation (2.5),

$$\left(\frac{\partial^2}{\partial x^2} + \frac{\partial^2}{\partial y^2} + k^2 n^2(x, y) - \beta^2 \right) \psi = 0. \quad (\text{A.1})$$

The FDM has been described in detail in [30]. This powerful approach allows us to calculate modal fields and corresponding propagation constants of arbitrarily shaped linear dielectric waveguides, but is particularly attractive for analyzing square- or rectangular-core waveguides. It relies on the expansion of the field in a two-dimensional Fourier series, which is used to convert the scalar wave equation into a matrix eigenvalue-eigenvector equation. To facilitate calculation of the matrix elements, the waveguide geometry is approximated by a number of rectangles, each of constant refractive index.

Application to the twin cores in Fig. 2.7 is a straightforward generalisation, starting with the definition of the bounding rectangular domain of sides L_x and L_y , as shown in Fig. A.1. The symmetrically-placed domain is assumed to be large

solitons (including the so-called light solitons) in a medium of nonlinear media. $\chi^{(2)}$ is a tensor of rank 2, and its components are antisymmetric with respect to the last two indices. The expression for the nonlinear polarization is given by

$$P_i = \epsilon_0 \chi_{ijk} E_j E_k \quad (7.23)$$

where ϵ_0 is the permittivity of free space, E_j and E_k are the components of the electric field, and χ_{ijk} is the second-order susceptibility tensor. The tensor χ_{ijk} is antisymmetric with respect to the last two indices, $\chi_{ijk} = -\chi_{ikj}$. The expression for the nonlinear polarization is given by

where ϵ_0 is the permittivity of free space, E_j and E_k are the components of the electric field, and χ_{ijk} is the second-order susceptibility tensor. The tensor χ_{ijk} is antisymmetric with respect to the last two indices, $\chi_{ijk} = -\chi_{ikj}$. The expression for the nonlinear polarization is given by

where ϵ_0 is the permittivity of free space, E_j and E_k are the components of the electric field, and χ_{ijk} is the second-order susceptibility tensor. The tensor χ_{ijk} is antisymmetric with respect to the last two indices, $\chi_{ijk} = -\chi_{ikj}$. The expression for the nonlinear polarization is given by

where ϵ_0 is the permittivity of free space, E_j and E_k are the components of the electric field, and χ_{ijk} is the second-order susceptibility tensor. The tensor χ_{ijk} is antisymmetric with respect to the last two indices, $\chi_{ijk} = -\chi_{ikj}$. The expression for the nonlinear polarization is given by

Numerical methods

Computers can figure out all kinds of problems, except the things in the world that just don't add up.

James Magary

This chapter contains brief descriptions of all the numerical methods used throughout the thesis. As we saw earlier, most of the problems addressed in this thesis have no exact analytical solutions, and, therefore, need to be treated numerically. A variety of techniques for solving ODE's and PDE's was employed to study linear optical waveguides [Chapters 2-5], as well as nonlinear self-guiding phenomena [Chapters 6-7], with emphasis on mode solvers and beam propagation methods. Some numerical methods, e.g. the Fourier Decomposition Method, are *intrinsically linear* and can only be applied to linear waveguide problems, whereas beam propagation schemes can be tailored to tackle both linear and nonlinear evolution dynamics.

A.1 Fourier Decomposition Method (FDM)

The Fourier Decomposition Method is used to find approximate solutions of linear eigenvalue-eigenvector problem, such as the scalar wave equation (2.5):

$$\left\{ \frac{\partial^2}{\partial x^2} + \frac{\partial^2}{\partial y^2} + k^2 n^2(x, y) - \beta^2 \right\} \psi = 0. \quad (\text{A.1})$$

The FDM has been described in detail in [30]. This powerful approach allows us to calculate modal fields and corresponding propagation constants of arbitrarily shaped linear dielectric waveguides, but is particularly attractive for analysing square- or rectangular-core waveguides. It relies on the expansion of the field in a two-dimensional Fourier series, which is used to convert the scalar wave equation into a matrix eigenvalue-eigenvector equation. To facilitate calculation of the matrix elements, the waveguide geometry is approximated by a number of rectangles, each of constant refractive index.

Application to the twin cores in Fig. 2.7 is a straightforward generalisation, starting with the definition of the bounding rectangular domain of sides L_x and L_y , as shown in Fig. A.1. The symmetrically-placed domain is assumed to be large

enough so that the two waveguide cores can be located in the centre of the domain with a wide cladding between the cores and the nearest boundary, and the modal field can be taken to be zero along the four edges.

The modal fields of the even and odd supermodes (or local supermodes) of the twin core coupler can then be expressed as a double summation over the complete set of orthonormal eigenfunctions of the scalar wave equation, i.e. Eqn. (A.1). Thus

$$\psi(x, y) = \frac{2}{\sqrt{L_x L_y}} \sum_{m=1}^{N_m} \sum_{n=1}^{N_n} a_{mn} \sin\left(\frac{m\pi x}{L_x}\right) \sin\left(\frac{n\pi y}{L_y}\right), \quad (\text{A.2})$$

where the a_{mn} are constants, and the integers N_m and N_n are large enough to ensure convergence of the series. The basis functions

$$\psi_{mn}(x, y) = \frac{2}{\sqrt{L_x L_y}} \sin\left(\frac{m\pi x}{L_x}\right) \sin\left(\frac{n\pi y}{L_y}\right) \quad (\text{A.3})$$

obey the usual orthonormality relation

$$\int \int_{A_\infty} \psi_{mn}(x, y) \psi_{pq}(x, y) dx dy = \delta_{mn,pq}. \quad (\text{A.4})$$

Substitution of the expansion (A.2) into Eqn. (2.5), with the twin square-core refractive-index profile for $n(x, y)$, multiplication by ψ_{pq} , and integration over the infinite cross-section leads to a linear $N_m \times N_n$ homogeneous matrix equation for the a_{mn} .

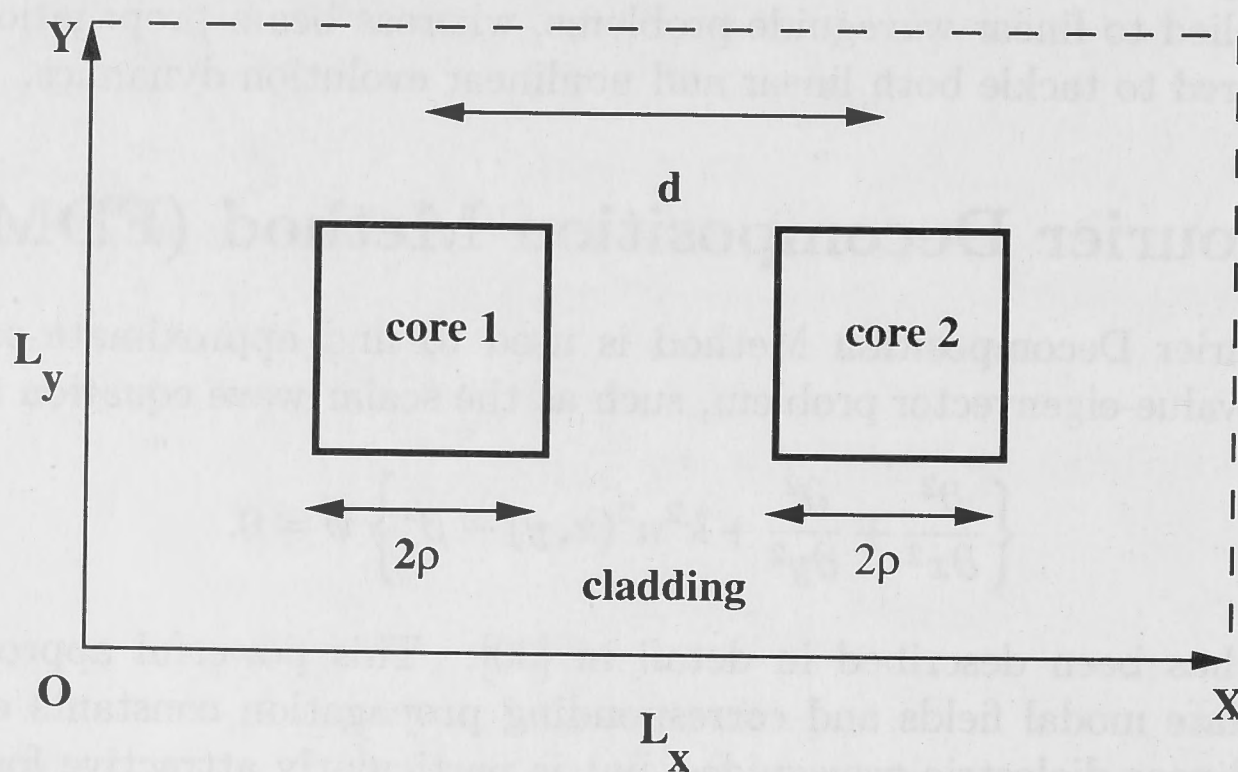


Figure A.1: Configuration of boundaries for the FDM. L_x and L_y are the sides of the numerical domain in the (x, y) plane, d is the separation between the core axes, and each core has sides 2ρ .

The eigenvalue equation for the propagation constants of the supermodes corresponds to the vanishing of the determinant of the matrix. This procedure is carried out numerically using standard library routines [118].

A.2 Beam Propagation Method (BPM)

Suitable numerical beam propagation schemes can be classified into two broad categories known as

- finite-difference methods [119–121] and
- pseudospectral methods [12, 122].

Generally speaking, finite-difference methods work faster for most linear problems and pseudospectral methods are preferable for nonlinear tasks, e.g. homogeneous nonlinear equations like the system (6.5). The method that is used extensively in this thesis is known as the *split-step Fourier method* [122, 123] or *split-step beam propagation method* (BPM). The straightforward implementation of multi-dimensional linear propagation and the fast speed of this method for nonlinear evolution, compared with most of finite-difference methods, can be attributed to the use of the split-step Fourier method based on the Fast-Fourier-Transform (FFT) algorithm [118]. This section gives a basic description of the split-step BPM and its attributes for linear and nonlinear cases; more advanced discussions are presented in [12, 122, 123].

A.2.1 Linear BPM

Analysing the equation (A.1), we can only find stationary (i.e. z -independent) solutions. If we want to consider the evolution of some arbitrary initial pulse-like condition $\psi(x, y)$ in z , then we should start with the scalar Helmholtz equation:

$$\left\{ \frac{\partial^2}{\partial z^2} + \frac{\partial^2}{\partial x^2} + \frac{\partial^2}{\partial y^2} + k^2 n^2 \right\} E = 0, \quad (\text{A.5})$$

where $E = E(x, y, z)$ is one of the transverse field components, k is the free-space wavenumber and $n = n(x, y, z)$ is the refractive index profile.

Within the paraxial approximation, we can express the field as a product of a slowly-varying amplitude envelope $A(x, y, z)$ and a rapidly oscillating phase term:

$$E(x, y, z) = A(x, y, z) e^{i k n_{\text{cl}} z}, \quad (\text{A.6})$$

where n_{cl} is the cladding index. Substituting the above expression into (A.5), we obtain the following equation:

$$\frac{\partial^2 A}{\partial z^2} + 2i k n_{\text{cl}} \frac{\partial A}{\partial z} + \frac{\partial^2 A}{\partial x^2} + \frac{\partial^2 A}{\partial y^2} + k^2 (n^2 - n_{\text{cl}}^2) A = 0 \quad (\text{A.7})$$

Omitting the second-order derivative in z and using the fact that $n \approx n_{\text{cl}}$ in the weak-guidance approximation, this leads to

$$i \frac{\partial A}{\partial z} = \frac{1}{2k n_{\text{cl}}} \left(-\frac{\partial^2}{\partial x^2} - \frac{\partial^2}{\partial y^2} \right) A - k(n - n_{\text{cl}}) A, \quad (\text{A.8})$$

which is also called the *two-dimensional non-stationary linear Schrödinger equation*.

To understand the concepts underlying the split-step Fourier method, it is useful to write Eqn. (A.8) in the form

$$\frac{\partial A}{\partial z} = (\hat{D} + \hat{W})A \quad (\text{A.9})$$

where \hat{D} is a differential operator that accounts for diffraction in a linear medium and \hat{W} is an operator that governs the effect of the waveguide profile on pulse propagation. These operators are given by

$$\hat{D} = \frac{i}{2kn_{\text{cl}}} \left\{ \frac{\partial^2}{\partial x^2} + \frac{\partial^2}{\partial y^2} \right\}, \quad (\text{A.10a})$$

$$\hat{W} = ik(n - n_{\text{cl}}). \quad (\text{A.10b})$$

In general, diffraction and focusing due to the waveguide act together along the length of the waveguide. The split-step Fourier method obtains an approximate solution by assuming that in propagating the optical field over a small distance h , the diffractive and focusing effects can be taken to act independently. More specifically, propagation from z to $z+h$ is carried out in two steps. In the first step, diffraction acts alone, and $\hat{W} = 0$ in Eqn. (A.9). In the second step, the waveguide acts alone, and $\hat{D} = 0$ in Eqn. (A.9). Mathematically this is equivalent to setting

$$A(x, y, z+h) = \exp[h\hat{W}] \exp[h\hat{D}]A(x, y, z). \quad (\text{A.11})$$

The execution of the exponential operation $\exp[h\hat{D}]$ is best performed in Fourier space using the prescription

$$\exp[h\hat{D}]B(x, y, z) = \{F^{-1} \exp[h\hat{D}(i\omega_x + i\omega_y)]F\}B(x, y, z), \quad (\text{A.12})$$

where F denotes the Fourier-transform operation, $\hat{D}(i\omega_x + i\omega_y)$ is obtained from Eqn. (A.10a) by replacing $\partial/\partial x$ by $i\omega_x$ and $\partial/\partial y$ by $i\omega_y$, and ω_x and ω_y are the frequencies in the Fourier domain.

After expressing the envelope $A(x, y, z)$ in a two-dimensional Fourier series

$$A(x, y, z) \approx \sum_{m=-\frac{N}{2}+1}^{N/2} \sum_{n=-\frac{N}{2}+1}^{N/2} \tilde{A}_{mn}(z) \exp\left[\frac{2\pi i}{L}(mx + ny)\right], \quad (\text{A.13})$$

the exponential operator $\exp[h\hat{D}]$ becomes

$$\exp\left[ih \frac{k_x^2 + k_y^2}{2k}\right], \quad (\text{A.14})$$

where L is the side of the square numerical domain in the (x, y) plane, $k_x = 2\pi m/L$ and $k_y = 2\pi n/L$.

Knowing the initial condition $A(x, y, z)$ on a discrete mesh of step sizes Δx and Δy , the Fourier coefficients \tilde{A}_{mn} are calculated using the Fourier transform of the initial condition $A_{pq} = A(p\Delta x, q\Delta y)$:

$$\tilde{A}_{mn}(z) = \frac{1}{N^2} \sum_{p=0}^{N-1} \sum_{q=0}^{N-1} A_{pq}(z) \exp \left[-\frac{2\pi i}{L} (mp + nq) \right] \quad (\text{A.15})$$

Then the exponential operator (A.14) is applied and solution transformed back from the Fourier space using (A.13). Multiplying by the ‘‘focusing’’ correction $\exp[h\hat{W}]$ finishes the step and yields the solution $A_{pq}(z+h)$. By repeating this procedure the initial field is propagated along the waveguide.

Although the split-step Fourier method is accurate to third order in the step size h [124], care should be taken in defining exact core dimensions to avoid errors due to discretisation in the transverse (x, y) plane.

A.2.2 Nonlinear BPM

Nonlinear generalisation of the split-step BPM is straightforward. The only modification is that for the nonlinear case (especially for a *system* of nonlinear equations) the operator W cannot be presented in simple analytic form (A.10b). Numerical methods should be used instead. Here, as an example, we describe a nonlinear BPM algorithm for the system (6.5).

Suppose that we know the forms of $\{v(x), w(x)\}$ for some z_0 . The integration step will be completed if we calculate $\{v(x), w(x)\}$ at $z_0 + \Delta z$ ($\Delta z \ll 1$). At the first stage of the integration we solve the decoupled system

$$i \frac{\partial v}{\partial z} + \frac{\partial^2 v}{\partial x^2} = 0; \quad 2i \frac{\partial w}{\partial z} + \frac{\partial^2 w}{\partial x^2} = 0. \quad (\text{A.16})$$

Equations (A.16) can be solved using the Fourier transform method [125]:

$$\begin{aligned} v(x, z_0 + \Delta z) &= \hat{F}^{-1} e^{-ik_x^2 \Delta z} \hat{F} v(x, z_0), \\ w(x, z_0 + \Delta z) &= \hat{F}^{-1} e^{-ik_x^2 \Delta z / 2} \hat{F} v(x, z_0), \end{aligned} \quad (\text{A.17})$$

where k_x is a Fourier space variable conjugated to x and \hat{F} and \hat{F}^{-1} denote forward and backward Fourier transform operators, respectively. It is straightforward to implement the solution (A.17) numerically for the functions v and w on a discrete mesh x_i , using a FFT algorithm for \hat{F} and \hat{F}^{-1} operations.

After the first stage is finished, we consider the remaining terms in Eqs. (6.5):

$$i \frac{dv}{dz} - v + wv^* = 0; \quad 2i \frac{dw}{dz} - \alpha w + \frac{v^2}{2} = 0. \quad (\text{A.18})$$

In Eqs. (A.18), the ODE's relating to different mesh points x_i are decoupled from each other. Accordingly, for any initial $\{v(x_n, z_0), w(x_n, z_0)\}$ the corresponding $\{v(x_n, z_0 + \Delta z), w(x_n, z_0 + \Delta z)\}$ are obtained numerically using the classical fourth-order Runge-Kutta method (which is consistent in terms of the orders of accuracy

with any version of the split-step algorithm) [118]. This is facilitated by taking $v(x_i)$ and $w(x_i)$ of the (A.17) of the first stage calculations as the initial conditions for the second stage Runge-Kutta integration. The integration of Eqs. (A.18) concludes a single Δz step, and then the two-stage process is repeated as often as required. This process of integration of PDE initial value problems in evolution parameter z is often referred to as the *propagation* of an initial input along the z coordinate.

Finally we make several comments concerning the split-step BPM:

- The accuracy of the method can be improved, if at the initial step in z (and only at the initial step), we calculate the solution (A.17) using $\Delta z/2$ instead of Δz (see the discussion in Ref. [12]).
- Due to peculiarities of the FFT algorithm, the number of mesh points x_i should be equal to a power of 2. We have found that a 512-point mesh on the interval $-50 < x < 50$, and $\Delta z = 0.005$ step size usually provide a sufficient accuracy for soliton related integrations. In the $(2 + 1)$ -dimensional case, we used 256×256 -point mesh in the domain $-30 < x < 30$, $-30 < y < 30$ and $\Delta z = 0.01$
- The split-step Fourier method automatically imposes *periodic* boundary conditions. Sometimes *absorbers* at mesh points close to the boundaries of the integration interval should be included to prevent radiation reflecting back into the area of soliton propagation.

A.3 Transfer Matrix Approach plus Staircase Approximation

There seems to be an abundant amount of literature on various methods of modal analysis. Among them the Transfer Matrix Approach [52–54, 126] is probably one of the simplest to implement, still providing excellent results as far as accuracy, applicability and computing speed are concerned. In this Appendix we present this method closely following the description given in Ref. [52]. For the specific application of Transfer Matrix Approach to a curved waveguide the reader is referred to Ref. [53]. The Staircase Approximation technique is based on the approximation of the non-homogeneous index of refraction [e.g. $n' = n e^{u/R_b}$ in Chapter 4, Eqn. (4.13), Fig. 4.8] by a large number of small steps of constant refractive index. The approximate profile is then solved by means of the transfer matrix method itself.

In essence, the transfer matrix approach is a simple method of matrix multiplication for obtaining real and imaginary parts of the propagation constants, as well as field configurations and power attenuation coefficients for various modes of a planar waveguide structure which may have media of complex refractive indices. It has been applied to quantify bend losses and absorption losses in Chapters 4 and 5. The main advantage of this technique is that it only involves straightforward 2×2 matrix multiplication.

We first consider a layered structure as shown in Fig. A.2. For a plane wave incident at an angle θ_1 , the electric field in each medium may be written in the form

$$\begin{aligned} \mathcal{E}_i = & \hat{\mathbf{e}}_i^+ E_i^+ e^{i\Delta_i} \exp[i(\omega t - k_i \cos \theta_i x - \beta z)] \\ & + \hat{\mathbf{e}}_i^- E_i^- e^{-i\Delta_i} \exp[i(\omega t + k_i \cos \theta_i x - \beta z)], \end{aligned} \quad (\text{A.19})$$

where $\Delta_1 = \Delta_2 = 0$, $\Delta_3 = k_3 d_2 \cos \theta_3$, $\Delta_4 = k_4 (d_2 + d_3) \cos \theta_4$, $k_i = k_0 n_i = \omega n_i / c$ and $\beta = k_1 \sin \theta_1 = k_2 \sin \theta_2 = \dots = k_4 \sin \theta_4$ is an invariant of the system; $\hat{\mathbf{e}}_i^+$ and $\hat{\mathbf{e}}_i^-$ represent the unit electric field polarisation vectors, and E_i^+ and E_i^- are the electric field amplitudes of waves propagating in the downward and upward directions (see Fig. A.2), respectively. The expressions for the phase terms Δ_i are introduced to simplify the form of the transfer matrix at each interface.

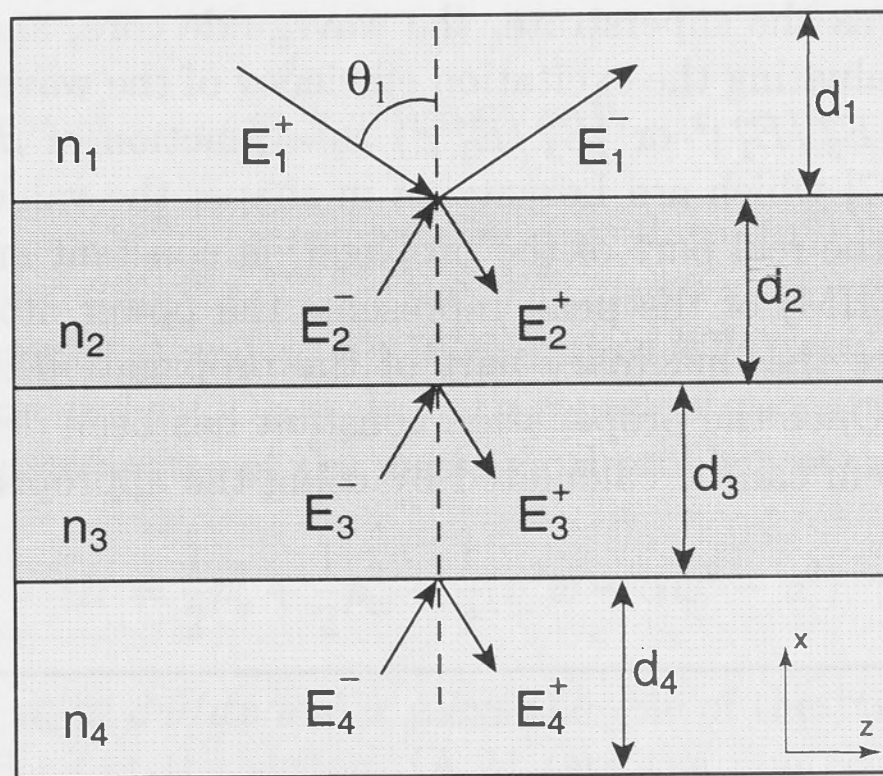


Figure A.2: Incidence of a plane wave at an angle θ_1 in a multilayered medium.

On applying the appropriate boundary conditions at the interfaces we can obtain

$$\begin{pmatrix} E_1^+ \\ E_1^- \end{pmatrix} = S_1 \begin{pmatrix} E_2^+ \\ E_2^- \end{pmatrix} = \dots = S_1 S_2 S_3 \begin{pmatrix} E_4^+ \\ E_4^- \end{pmatrix}, \quad (\text{A.20})$$

where

$$S_i = \frac{1}{t_i} \begin{pmatrix} e^{i\delta_i} & r_i e^{i\delta_i} \\ r_i e^{-i\delta_i} & e^{-i\delta_i} \end{pmatrix} \quad (\text{A.21})$$

and r_i and t_i represent, respectively, the amplitude reflection and transmission coefficients at the i -th interface; $\delta_i = k_i d_i \cos \theta_i$.

For the TE polarisation

$$r_i = \frac{n_i \cos \theta_i - n_{i+1} \cos \theta_{i+1}}{n_i \cos \theta_i + n_{i+1} \cos \theta_{i+1}}, \quad (\text{A.22})$$

$$t_i = \frac{2n_i \cos \theta_i}{n_i \cos \theta_i + n_{i+1} \cos \theta_{i+1}}. \quad (\text{A.23})$$

Obviously, for a wave incident from the first medium, there would be no upward propagating wave in the last medium, and thus for the structure shown in Fig. A.2, $E_4^- = 0$. Using this condition, and using (A.20) and (A.21) one can readily calculate the fields in terms of E_1^+ .

In order to use the above matrix method in determining the propagation characteristics of planar waveguides, the second, third, and fourth media in Fig. A.2 may be interpreted as the superstrate, the waveguide core, and the substrate, respectively. Upon evaluating the excitation efficiency of the wave in the waveguiding layer (i.e. $\eta(\beta) = |E_3^+/E_1^+|^2$ or $|E_3^-/E_1^+|^2$) as a function of β , one would obtain resonance peaks [127] which are Lorentzian in shape; the value of β at which the peaks appear gives the real part of the propagation constant and the full width at half maximum (FWHM) of the peak represents the power attenuation coefficient γ which is just twice the imaginary part of the propagation constant [see Chapter 4, Eqn. (4.20)]. Once the propagation constant has been determined, the fields throughout the system can be calculated by using the appropriate matrices at the interfaces.

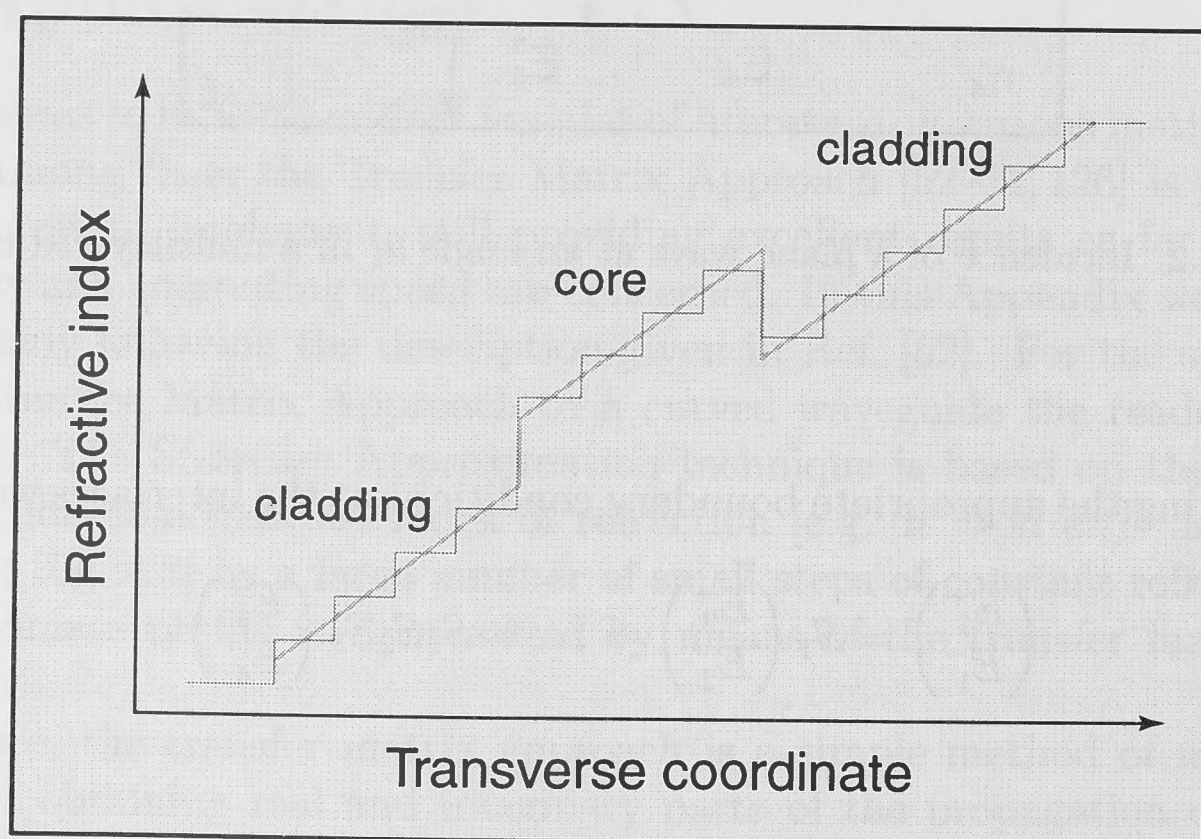


Figure A.3: The staircase approximation. The original refractive index (thick line) is approximated by a large number of small steps with a constant index of refraction (thin line).

Although the transfer matrix technique described above is quite general and can be applied to study slab waveguides with arbitrary graded refractive index profiles, it requires the nonuniform structure to be divided into homogeneous layers (as shown in Figure A.3). The total number of such layers depends on how rapidly the index profile changes; a large number may be needed to obtain convergence. We have applied the present method in Chapters 4 and 5 to study bent planar waveguides, which are characterised by an effective exponential profile (4.13) shown in Fig. 4.8(b). This method can be used in the analysis of any practical slab waveguiding structure.

A.4 Shooting and Relaxation Methods

Stationary solutions of Eqs. (6.5) are described by the system of two second order ODE's

$$\begin{aligned}\frac{\partial^2 v}{\partial x^2} - v + wv &= 0, \\ \frac{\partial^2 w}{\partial x^2} - \alpha w + \frac{v^2}{2} &= 0,\end{aligned}\tag{A.24}$$

for the real functions $v(x)$ and $w(x)$. Equations (A.24) can also be presented as a system of four first order ODE's. In both representations $v(x)$ and $w(x)$ can be considered as two coordinates of the mechanical problem with Hamiltonian

$$H = \frac{1}{2}p_v^2 + \frac{1}{2}p_w^2 + \frac{1}{2}(v^2w - \alpha w^2 - v^2),\tag{A.25}$$

where $p_v \equiv dv/dx$, $p_w \equiv dw/dx$ and x plays the role of the "time" variable.

Localised solutions of the system (A.24) are the nontrivial separatrix trajectories in the four-dimensional phase space (v, w, p_v, p_w) . These trajectories start at the point $(v^{(1)}, w^{(1)}, 0, 0)$ at $x = -\infty$ and approach asymptotically the point $(v^{(2)}, w^{(2)}, 0, 0)$ for $x \rightarrow \infty$. In the case of bright solitons $v^{(1)} = w^{(1)} = v^{(2)} = w^{(2)} = 0$. The question of finding these separatrix trajectories is a particular case of a general mathematical problem, which is called the *two point boundary value problem*. As the terminology indicates, for this problem boundary conditions are to be satisfied at two points – usually starting and ending values of the integration interval. Formally, soliton-related two point boundary value problems are defined on the infinite interval $(-\infty, \infty)$ [or $(0, \infty)$ if symmetry conditions are imposed], but they can always be reformulated in a finite interval by taking into account soliton asymptotics for large absolute values of x . Two major numerical methods of solving two point boundary value problems are known. A description of them (including working code examples) is given in [118]. In addition, [128–132] also contain useful information.

In the *shooting method*, we choose values for all of the dependent variables at one boundary. These values must be consistent with any boundary conditions for *that* boundary, but otherwise are arranged to depend on arbitrary free parameters

whose values we initially guess. After that, we integrate the ODE's by initial value methods, e.g. by Runge-Kutta [118]), to the other boundary. In general, we find discrepancies from the required values there. Using multidimensional root-finding procedures, we adjust the free parameters at the starting point to minimise the discrepancies at the other boundary point. If we integrate the differential equations to follow the trajectory of a shot from a gun to a target, then choosing the initial conditions corresponds to aiming. The shooting method provides a systematic approach of taking a set of "ranging" shots that allow us to improve the accuracy of "hitting" the target.

The *relaxation method* uses a different approach. The ODE's are replaced by finite-difference equations on a mesh of points that covers the range of integration. A trial solution consists of values for the dependent variables at each mesh point, *not* satisfying the desired finite-difference equations, nor necessarily satisfying the required boundary conditions. The iteration, called *relaxation*, consists of adjusting all the values on the mesh in such a way to bring them into successively closer agreement with the finite-difference equations and, simultaneously, with the boundary conditions. For example, if the problem involves four coupled equations of the first order, e.g. Eqs. (A.24), and a mesh of one hundred points, we must first guess and then improve four hundred variables representing the solution. Good initial guesses are the secret of efficient relaxation methods. When we search for a continuous (in α) soliton family, we have to solve Eqs. (A.24) many times, each time with a slightly different value of α . In this case, the previous solution is a good initial guess when the parameter is changed and the asymptotic solutions (6.11) [or the exact solution Eqn. (6.9)] can be successfully used as starting points to follow the continuous soliton families.

Comparing the two methods, we note that the relaxation method works better than the shooting method for finding solitons of simple shape (e.g. single radiationless solitons). In the case of bound states of radiating solitons, which oscillate in the central part and do not form continuous families, the shooting method is preferable. In general, we follow the advice of [118]: starting a new problem, it is always better to shoot first, and only then relax. Almost all the results of Chapter 6 (which are related to ODE integration) have been initially obtained by shooting [20].

APPENDIX B

Fractional Coupled Power

In this Appendix we present a general formalism of *coupled mode theory*, applied in this Thesis to two different physical phenomena:

- power exchange between the cores of optical couplers, quantified in Chapter 3;
- power coupling between the modes of bent optical fibres, addressed in Chapter 4.

According to coupled local-mode theory [5, Sectns. 27–3, 29–9], the equations describing power transfer dynamics in both cases are mathematically equivalent and can be written in the following general form:

$$\begin{cases} \frac{db_1}{dz} - i(\beta_1 + D_{11})b_1 = iD_{12}b_2, \\ \frac{db_2}{dz} - i(\beta_2 + D_{22})b_2 = iD_{21}b_1. \end{cases} \quad (\text{B.1})$$

Below we will define the physical parameters for each case and outline the way of solving the above system of equations.

B.1 Power exchange in a coupler

Here we present details of the coupled equations used to describe propagation in both the uniform central region and the curved input and output arms of a planar coupler (see Figure 3.1). Assuming that the coupler is weakly guiding, the scalar transverse electric field $\psi(x, y, z)$ in a coupler with longitudinal coordinate z parallel to the direction of propagation, and coordinates x and y in the cross-section can be represented approximately by

$$\psi(x, y, z) = b_1(z)\psi_1(x, y) + b_2(z)\psi_2(x, y). \quad (\text{B.2})$$

Note that here $\psi(x, y, z)$ is a complex field envelope at a fixed frequency, $\psi_1(x, y)$ and $\psi_2(x, y)$ are the scalar electric fields of the fundamental modes of each of two waveguides comprising the coupler in isolation from the other, and $b_1(z)$ and $b_2(z)$

are the z -dependent coefficients of the normalised local-modes of cores 1 and 2 in isolation.

According to coupled local-mode theory, the normalised coefficients $b_1(z)$ and $b_2(z)$ contain both the z -dependent amplitude and phase, such that $|b_1|^2 + |b_2|^2 = 1$, and determine the output powers in each core of a slowly varying, nonuniform coupler at cross-section z : $|b_1(z)|^2 = P_2(z)$ and $|b_2(z)|^2 = P_3(z)$. We note that Equation (B.2) is an accurate approximation to the field of the coupler provided that

$$\left| \frac{\int_{-\infty}^{+\infty} \psi_1(x, y) \psi_2(x, y) dx dy}{\sqrt{\int_{-\infty}^{+\infty} \psi_1^2(x, y) dx dy \int_{-\infty}^{+\infty} \psi_2^2(x, y) dx dy}} \right| \ll 1 \quad (\text{B.3})$$

which holds for all examples considered in this Thesis.

The coefficients $b_1(z)$ and $b_2(z)$ satisfy the pair of coupled equations (B.1), where β_1 is the propagation constant of the fundamental mode of the first isolated waveguide, β_2 is the propagation constant of the second isolated waveguide, and D_{ij} are coupling coefficients, which are determined by overlap integrals:

$$D_{ij} = k \frac{\int_{A_\infty} (n - n_i) \Psi_i \Psi_j dA}{\int_{A_\infty} \Psi_i^2 dA}. \quad (\text{B.4})$$

In the above definition n and n_i denote the refractive index profiles of the coupler and i -th core in isolation, respectively, k being the wavenumber. In the bulk geometry A_∞ corresponds to the integration over the whole (x, y) coupler cross-section, $dA = dx dy$. In planar case the integration is carried out over the transverse coordinate $-\infty < x < +\infty$, $dA = dx$.

In the present case, $D_{11} \ll \beta_1$, $D_{22} \ll \beta_2$ and $D_{12} \approx D_{21}$. Accordingly, for the power transfer dynamics in the coupler, equations B.1 can be simplified to

$$\begin{cases} \frac{db_1}{dz} - i\beta_1 b_1 = iC(z)b_2, \\ \frac{db_2}{dz} - i\beta_2 b_2 = iC(z)b_1, \end{cases} \quad (\text{B.5})$$

where the z -dependent coupling coefficient, $C(z) = D_{12} = D_{21}$, is expressible as

$$C(z) = \frac{\sqrt{\{\beta_+(z) - \beta_-(z)\}^2 - (\beta_1 - \beta_2)^2}}{2}. \quad (\text{B.6})$$

in terms of the propagation constants β_+ and β_- of the two supermodes of the coupler.

As we require information only about the powers exiting ports 2 and 3, a more convenient way to express the coupled equations (B.5) is to introduce the (real) Stokes parameters S_0 , S_1 , S_2 and S_3 defined by

$$\begin{aligned} S_0 &= |b_1|^2 + |b_2|^2, \\ S_1 &= |b_1|^2 - |b_2|^2, \\ S_2 &= b_1 b_2^* + b_2 b_1^*, \\ S_3 &= -i(b_1 b_2^* - b_2 b_1^*), \end{aligned} \quad (\text{B.7})$$

where the asterisks denote the complex conjugate. Substituting Eqs. (B.7) into Eqs. (B.5) and rearranging, we obtain an equivalent system of equations describing the power transfer dynamics in terms of the Stokes parameters [38]:

$$\begin{aligned} \frac{dS_0}{dz} &= 0, \\ \frac{dS_1}{dz} &= 2C(z)S_3, \\ \frac{dS_2}{dz} &= -(\beta_1 - \beta_2)S_3, \\ \frac{dS_3}{dz} &= (\beta_1 - \beta_2)S_2 - 2C(z)S_1. \end{aligned} \quad (\text{B.8})$$

Assuming that unit power is initially launched into core 1 and zero power is launched into core 2, power conservation leads to the result $S_0 = P_2(z) + P_3(z) = 1$ so that $S_1 = P_2(z) - P_3(z) = 1 - 2P_3(z)$. In the uniform central region of the coupler, the coupling coefficient is constant, so Eqs. (B.8) are readily integrated, and we obtain the following solutions for $P_2(z)$ and $P_3(z)$ [5, Sectn. 18–20]:

$$\begin{cases} P_2 = 1 - F^2 \sin^2\left(\frac{C}{F}L_c\right), \\ P_3 = F^2 \sin^2\left(\frac{C}{F}L_c\right), \end{cases} \quad (\text{B.9})$$

where

$$F^2 = 1 - \left(\frac{\beta_1 - \beta_2}{\beta_+ - \beta_-}\right)^2, \quad (\text{B.10})$$

$$\frac{C}{F} = \frac{\beta_+ - \beta_-}{2}, \quad (\text{B.11})$$

and L_c is the length of the central section of the coupler.

For the general case of a coupler which comprises the uniform central region together with the curved input and output cores, the parameter C becomes z -dependent. In this case the fractional coupled power, $P_3(z)$, along the length of the coupler has to be determined by solving Eqs. (B.8) numerically. The Fourier Decomposition Method (see Appendix A.1) is used to find the propagation constants for both the fundamental mode of each core and the supermodes of the composite coupler, from which $C(z)$ is determined via Eqn. (B.6).

B.2 Power exchange between modes of a bent fibre

Under certain resonance conditions, a small perturbation of the fibre (e.g. bending with radius of curvature varying along the bend) leads to the transfer of large proportion of total power between only two modes of the complete set of modes of the unperturbed fibre. If we ignore the weak power transfer to all other modes, the set of coupled mode equations (B.1) describes arbitrary power transfer between the two forward-propagating resonant modes.

In our case $b_1(z)$ and $b_2(z)$ are the coefficients of the normalised core and cladding modes, involved in the power exchange process, $\beta_1(z)$ and $\beta_2(z)$ are the propagation constants of the core and cladding modes of the unperturbed (straight) fibre, respectively, and the z -dependent coupling coefficient, $D_{ij}(z)$, is expressed as:

$$D_{ij} = \frac{k}{2n_{co}} \frac{\int_{A_\infty} (n^2 - \bar{n}^2) \Psi_i \Psi_j dA}{\int_{A_\infty} \Psi_i^2 dA}. \quad (\text{B.12})$$

In the above definition n and \bar{n} denote the refractive index profiles of perturbed (bent) and unperturbed (straight) fibre, respectively, Ψ_i and Ψ_j being solutions of the scalar wave equation for the unperturbed fibre, which are involved in power exchange. In the bulk geometry A_∞ corresponds to the integration over the (x, y) plane, $dA = dx dy$. In planar case the integration is carried out over the transverse coordinate $-\infty < x < +\infty$, $dA = dx$.

To solve the coupled equations (B.1), we again introduce the Stokes parameters (B.7) and obtain an equivalent system of equations:

$$\begin{aligned} \frac{dS_0}{dz} &= [D_{12}(z) - D_{21}(z)] S_3, \\ \frac{dS_1}{dz} &= [D_{12}(z) + D_{21}(z)] S_3, \\ \frac{dS_2}{dz} &= -[\beta_1 + D_{11}(z) - \beta_2 - D_{22}(z)] S_3, \\ \frac{dS_3}{dz} &= [D_{12}(z) - D_{21}(z)] (S_0 + S_1) - [\beta_2 + D_{22}(z) - \beta_1 - D_{11}(z)] S_2 - 2D_{12}(z) S_1. \end{aligned} \quad (\text{B.13})$$

Assuming that unit power is initially in the core mode, the second mode is not excited, and $D_{12}(z) \approx D_{21}(z)$, we obtain $S_0 = P_1(z) + P_2(z) = 1$ so that $S_1 = P_1(z) - P_2(z) = 1 - 2P_2(z)$. It is then straightforward to determine the fractional coupled power, $P_2(z)$, transferred to the cladding mode along the length of the fibre by solving Eqs. (B.13) numerically.

Derivation of adiabatic equations of soliton interaction

The harmony of the world is made manifest in Form and Number, and the heart and soul and all the poetry of Natural Philosophy are embodied in the concept of mathematical beauty.

– On Growth and Form [1917], Epilogue
Sir D'Arcy Wentworth Thompson

In the derivation of the soliton interaction equations, which describe the adiabatic evolution of two solitons, we follow the scheme suggested in [108], but with a few modifications to increase the efficiency of the derivation procedure. We also generalise the method, taking the second transverse direction into account.

To derive the simplified evolution model, we look for a solution of Eqs. (7.1) in the two-soliton form:

$$v \equiv v^{(1)} + v^{(2)} = V^{(1)}(x - x^{(1)}, y - y^{(1)}, Z) e^{i\phi^{(1)}} + V^{(2)}(x - x^{(2)}, y - y^{(2)}, Z) e^{i\phi^{(2)}},$$

$$w \equiv w^{(1)} + w^{(2)} = W^{(1)}(x - x^{(1)}, y - y^{(1)}, Z) e^{2i\phi^{(1)}} + W^{(2)}(x - x^{(2)}, y - y^{(2)}, Z) e^{2i\phi^{(2)}},$$

where superscripts (1) and (2) denote first and second solitons, respectively, $Z = \varepsilon z$ ($\varepsilon \ll 1$), and $\phi^{(j)}(z)$, $x^{(j)}(z)$, and $y^{(j)}(z)$ are soliton phases and coordinates, given by

$$\begin{aligned} \phi^{(j)}(z) &= \int_0^z \beta^{(j)}(Z') dz' + \phi_0^{(j)}, \\ x^{(j)}(z) &= \int_0^z C_x^{(j)}(Z') dz' + x_0^{(j)}, \\ y^{(j)}(z) &= \int_0^z C_y^{(j)}(Z') dz' + y_0^{(j)}. \end{aligned} \tag{C.1}$$

where $j = 1, 2$. Note, that we allow soliton parameters $\beta^{(j)}$, $C_x^{(j)}$, and $C_y^{(j)}$ to vary adiabatically during soliton interaction, whereas $\phi_0^{(j)}$, $x_0^{(j)}$, and $y_0^{(j)}$ are constants defining the initial soliton positions and phases.

Now we express $V^{(j)}$ and $W^{(j)}$ in the form of asymptotic series:

$$\begin{aligned} V^{(j)}(x, y, z) &= V_0^{(j)}[x, y, \beta^{(j)}(Z), C_x^{(j)}(Z), C_y^{(j)}(Z)] + \sum_{n=1}^{+\infty} \varepsilon^n V_n^{(j)}(x, y, z), \\ W^{(j)}(x, y, z) &= W_0^{(j)}[x, y, \beta^{(j)}(Z), C_x^{(j)}(Z), C_y^{(j)}(Z)] + \sum_{n=1}^{+\infty} \varepsilon^n W_n^{(j)}(x, y, z). \end{aligned} \quad (\text{C.2})$$

Substituting Eqs. (C.2) into Eqs. (7.1) we collect terms of the same order in ε . We assume that in the lowest (zeroth) order, the solitons are located far from each other and the equations for the soliton 1 and the soliton 2 are not coupled. Zero-order soliton shapes $V_0^{(j)}, W_0^{(j)}$ are given by the localised solutions of

$$\begin{aligned} \frac{\partial^2 V_0^{(j)}}{\partial x^2} + \frac{\partial^2 V_0^{(j)}}{\partial y^2} - iC_x^{(j)} \frac{\partial V_0^{(j)}}{\partial x} - iC_y^{(j)} \frac{\partial V_0^{(j)}}{\partial y} - \beta^{(j)} V_0^{(j)} + W_0^{(j)} V_0^{(j)*} &= 0, \\ \frac{\partial^2 W_0^{(j)}}{\partial x^2} + \frac{\partial^2 W_0^{(j)}}{\partial y^2} - i\sigma C_x^{(j)} \frac{\partial W_0^{(j)}}{\partial x} - i\sigma C_y^{(j)} \frac{\partial W_0^{(j)}}{\partial y} - \sigma(2\beta^{(j)} + \Delta) W_0^{(j)} + \frac{V_0^{(j)2}}{2} &= 0, \end{aligned}$$

with initial phases $\phi_0^{(j)}$, and initial positions $x_0^{(j)}, y_0^{(j)}$ ($j = 1, 2$).

In order to have a self-consistent perturbation scheme, we have to assume that the influence of interacting solitons on each other arises from first-order effects in ε . This leads to two coupled subsystems of equations, which define the first-order correction to the shape of soliton 1 due to soliton 2, and vice-versa. The analysis of each of these subsystems can be done separately and is virtually identical. Below we present the full-scale analysis for the first-order correction to the shape of the soliton 1. This is given by:

$$\begin{aligned} \hat{L}^{(1)} \begin{pmatrix} V_1^{(1)} \\ W_1^{(1)} \\ V_1^{(1)*} \\ W_1^{(1)*} \end{pmatrix} &= i\dot{\beta}^{(1)} \begin{pmatrix} -V_{0\beta^{(1)}}^{(1)} \\ -\sigma W_{0\beta^{(1)}}^{(1)} \\ V_{0\beta^{(1)}}^{(1)*} \\ \sigma W_{0\beta^{(1)}}^{(1)*} \end{pmatrix} + i\dot{C}_x^{(1)} \begin{pmatrix} -V_{0C_x^{(1)}}^{(1)} \\ -\sigma W_{0C_x^{(1)}}^{(1)} \\ V_{0C_x^{(1)}}^{(1)*} \\ \sigma W_{0C_x^{(1)}}^{(1)*} \end{pmatrix} + i\dot{C}_y^{(1)} \begin{pmatrix} -V_{0C_y^{(1)}}^{(1)} \\ -\sigma W_{0C_y^{(1)}}^{(1)} \\ V_{0C_y^{(1)}}^{(1)*} \\ \sigma W_{0C_y^{(1)}}^{(1)*} \end{pmatrix} - \\ &- \frac{1}{\varepsilon} \begin{pmatrix} W_0^{(2)} V_0^{(2)*} e^{i[\phi^{(2)} - \phi^{(1)}]} \\ (1/2) V_0^{(2)2} e^{2i[\phi^{(2)} - \phi^{(1)}]} \\ W_0^{(2)*} V_0^{(2)} e^{-i[\phi^{(2)} - \phi^{(1)}]} \\ (1/2) V_0^{(2)*2} e^{-2i[\phi^{(2)} - \phi^{(1)}]} \end{pmatrix}, \end{aligned} \quad (\text{C.3})$$

where dot denotes the derivative with respect to Z , subscripts $\beta^{(1)}, C_x^{(1)}$, and $C_y^{(1)}$ stand for partial derivatives with respect to $\beta^{(1)}, C_x^{(1)}$, and $C_y^{(1)}$, respectively. Note

that we introduce the factor $1/\varepsilon$ in front of the last column of system (C.3) to stress that each of terms of this last column is of the order ε . The linear differential operator $\hat{L}^{(1)}$ is given by

$$\hat{L}^{(1)} = \begin{pmatrix} A & V_0^{(1)*} & W_0^{(1)} & 0 \\ V_0^{(1)} & B & 0 & 0 \\ W_0^{(1)*} & 0 & C & V_0^{(1)} \\ 0 & 0 & V_0^{(1)*} & D \end{pmatrix} \quad (\text{C.4})$$

where

$$\begin{aligned} A &\equiv \frac{\partial^2}{\partial x^2} + \frac{\partial^2}{\partial y^2} - iC_x^{(1)} \frac{\partial}{\partial x} - iC_y^{(1)} \frac{\partial}{\partial y} - \beta^{(1)}, \\ B &\equiv \frac{\partial^2}{\partial x^2} + \frac{\partial^2}{\partial y^2} - iC_x^{(1)} \frac{\partial}{\partial x} - iC_y^{(1)} \frac{\partial}{\partial y} - \sigma[2\beta^{(1)} + \Delta], \\ C &\equiv \frac{\partial^2}{\partial x^2} + \frac{\partial^2}{\partial y^2} + iC_x^{(1)} \frac{\partial}{\partial x} + iC_y^{(1)} \frac{\partial}{\partial y} - \beta^{(1)}, \\ D &\equiv \frac{\partial^2}{\partial x^2} + \frac{\partial^2}{\partial y^2} + iC_x^{(1)} \frac{\partial}{\partial x} + iC_y^{(1)} \frac{\partial}{\partial y} - \sigma[2\beta^{(1)} + \Delta]. \end{aligned}$$

The system (C.3) has nontrivial localised solutions only if the certain solvability conditions are satisfied [108], which means that the right-hand-side of Eqs. (C.3) should be orthogonal to all possible localised solutions of the corresponding homogeneous system [i.e. the system (C.3) with zero right hand side].

We use the conventional assumption that the homogeneous system $\hat{L}^{(1)T}(V_h^{(1)}, W_h^{(1)}, V_h^{(1)*}, W_h^{(1)*}) = 0$ has only three linearly independent localised solutions

$$\begin{aligned} V_{h1}^{(1)} &= iV_0^{(1)}; & W_{h1}^{(1)} &= i\sigma W_0^{(1)}; & V_{h1}^{(1)*} &= -iV_0^{(1)*}; & W_{h1}^{(1)*} &= -i\sigma W_0^{(1)*}, \\ V_{h2}^{(1)} &= V_{0x}^{(1)}; & W_{h2}^{(1)} &= W_{0x}^{(1)}; & V_{h2}^{(1)*} &= V_{0x}^{(1)*}; & W_{h2}^{(1)*} &= W_{0x}^{(1)*}, \\ V_{h3}^{(1)} &= V_{0y}^{(1)}; & W_{h3}^{(1)} &= W_{0y}^{(1)}; & V_{h3}^{(1)*} &= V_{0y}^{(1)*}; & W_{h3}^{(1)*} &= W_{0y}^{(1)*}, \end{aligned} \quad (\text{C.5})$$

each of which corresponds to a certain internal symmetry of Eqs. (7.1). In Eqs. (C.5) subscripts x and y stand for partial derivatives with respect to x and y , respectively.

We can express each of three solvability conditions for the system (C.3) in the explicit form

$$\int_{-\infty}^{\infty} \int_{-\infty}^{\infty} \left[V_{hj}^{(1)*} V_{rhs}^{(1)} + W_{hj}^{(1)*} W_{rhs}^{(1)} + V_{hj}^{(1)} V_{rhs}^{(1)*} + W_{hj}^{(1)} W_{rhs}^{(1)*} \right] dx dy = 0, \quad (\text{C.6})$$

where $j = 1, 2, 3$ and $V_{rhs}^{(1)}$, $W_{rhs}^{(1)}$, $V_{rhs}^{(1)*}$, and $W_{rhs}^{(1)*}$ stand for first, second, third, and fourth rows of the right hand side of Eqs. (C.3), respectively.

Calculation of the integrals in the solvability conditions (C.6) leads to the result

$$\begin{aligned} \dot{\beta}^{(1)} \frac{\partial Q^{(1)}}{\partial \beta^{(1)}} + \dot{C}_x^{(1)} \frac{\partial P_x^{(1)}}{\partial \beta^{(1)}} + \dot{C}_y^{(1)} \frac{\partial P_y^{(1)}}{\partial \beta^{(1)}} - \frac{\partial U^{(1)}}{\partial \phi^{(1)}} &= 0, \\ \dot{\beta}^{(1)} \frac{\partial Q^{(1)}}{\partial C_x^{(1)}} + \dot{C}_x^{(1)} \frac{\partial P_x^{(1)}}{\partial C_x^{(1)}} + \dot{C}_y^{(1)} \frac{\partial P_y^{(1)}}{\partial C_x^{(1)}} - \frac{\partial U^{(1)}}{\partial x^{(1)}} &= 0, \\ \dot{\beta}^{(1)} \frac{\partial Q^{(1)}}{\partial C_y^{(1)}} + \dot{C}_x^{(1)} \frac{\partial P_x^{(1)}}{\partial C_y^{(1)}} + \dot{C}_y^{(1)} \frac{\partial P_y^{(1)}}{\partial C_y^{(1)}} - \frac{\partial U^{(1)}}{\partial y^{(1)}} &= 0, \end{aligned} \quad (\text{C.7})$$

where the invariants (7.2,7.3) are calculated on the zero-order soliton approximations $V_0^{(1)}$, $W_0^{(1)}$ and the function $U^{(1)}$ is given by

$$U^{(1)} = -\text{Re} \int_{-\infty}^{\infty} \int_{-\infty}^{\infty} \left[2W_0^{(2)} V_0^{(2)*} V_0^{(1)*} e^{i(\phi_2 - \phi_1)} + V_0^{(2)2} W_0^{(1)*} e^{2i(\phi_2 - \phi_1)} \right] dx dy. \quad (\text{C.8})$$

Note that in Eqs. (C.7) and everywhere below, dot denotes the derivative with respect to z , not Z ! This enables us to cancel out $1/\varepsilon$ factors, which otherwise would appear in front of the $U^{(1)}$ -terms.

Equations (C.7) and (C.8) describe the dynamics of soliton 1 under the influence of the soliton 2. In the exactly the same way, we can obtain the equations describing the dynamics of the soliton 2 under the influence of soliton 1. They have the form of Eqs. (C.7,C.8) with all superscripts rotated according to $1 \leftrightarrow 2$.

We now make the second major assumption, requiring the two interacting solitons to have almost the same internal soliton parameters β , C_x , and C_y . In other words, we assume that $|\beta^{(2)} - \beta^{(1)}| \sim \varepsilon$, $|C_x^{(2)} - C_x^{(1)}| \sim \varepsilon$, $|C_y^{(2)} - C_y^{(1)}| \sim \varepsilon$. Taking this assumption into account, it is straightforward to show that $U^{(1)} = U^{(2)} = (1/2)U \equiv (1/2)[U^{(1)} + U^{(2)}]$ to order ε . Using the gauge invariance formulas (7.6), the *effective interaction potential* U can be expressed as

$$U = U_1 \cos(\phi) + U_2 \cos(2\phi), \quad (\text{C.9})$$

where

$$\phi \equiv [C_x^{(1)} x^{(1)} - C_x^{(2)} x^{(2)} + C_y^{(1)} y^{(1)} - C_y^{(2)} y^{(2)}] / 2 + \phi^{(2)} - \phi^{(1)}, \quad (\text{C.10})$$

$$U_1 \equiv -2 \int_{-\infty}^{\infty} \int_{-\infty}^{\infty} \left[\tilde{W}_0^{(2)} \tilde{V}_0^{(2)} \tilde{V}_0^{(1)} + \tilde{W}_0^{(1)} \tilde{V}_0^{(1)} \tilde{V}_0^{(2)} \right] dx dy, \quad (\text{C.11})$$

and

$$U_2 \equiv - \int_{-\infty}^{\infty} \int_{-\infty}^{\infty} \left[\tilde{V}_0^{(2)} \tilde{V}_0^{(2)} \tilde{W}_0^{(1)} + \tilde{V}_0^{(1)} \tilde{V}_0^{(1)} \tilde{W}_0^{(2)} \right] dx dy. \quad (\text{C.12})$$

In the expressions (C.11) and (C.12), we use the notation

$$\begin{aligned}\tilde{V}_0^{(j)}(\beta^{(j)}, C_x^{(j)}, C_y^{(j)}; x, y) &\equiv V_0^{(j)}(\beta^{(j)} - \frac{C_x^{(j)2}}{4} - \frac{C_y^{(j)2}}{4}, 0, 0; x - x^{(j)}, y - y^{(j)}), \\ \tilde{W}_0^{(j)}(\beta^{(j)}, C_x^{(j)}, C_y^{(j)}; x, y) &\equiv W_0^{(j)}(\beta^{(j)} - \frac{C_x^{(j)2}}{4} - \frac{C_y^{(j)2}}{4}, 0, 0; x - x^{(j)}, y - y^{(j)}),\end{aligned}$$

where $j = 1, 2$.

Using the definitions (C.1), we obtain the final system of ordinary differential equations describing the adiabatic interaction of two almost identical solitons in the bulk $\chi^{(2)}$ medium

$$\begin{aligned}\ddot{\phi}^{(1)} \frac{\partial Q^{(1)}}{\partial \beta^{(1)}} + \ddot{x}^{(1)} \frac{\partial P_x^{(1)}}{\partial \beta^{(1)}} + \ddot{y}^{(1)} \frac{\partial P_y^{(1)}}{\partial \beta^{(1)}} - \frac{1}{2} \frac{\partial U}{\partial \phi^{(1)}} &= 0, \\ \ddot{\phi}^{(1)} \frac{\partial Q^{(1)}}{\partial C_x^{(1)}} + \ddot{x}^{(1)} \frac{\partial P_x^{(1)}}{\partial C_x^{(1)}} + \ddot{y}^{(1)} \frac{\partial P_y^{(1)}}{\partial C_x^{(1)}} - \frac{1}{2} \frac{\partial U}{\partial x^{(1)}} &= 0, \\ \ddot{\phi}^{(1)} \frac{\partial Q^{(1)}}{\partial C_y^{(1)}} + \ddot{x}^{(1)} \frac{\partial P_x^{(1)}}{\partial C_y^{(1)}} + \ddot{y}^{(1)} \frac{\partial P_y^{(1)}}{\partial C_y^{(1)}} - \frac{1}{2} \frac{\partial U}{\partial y^{(1)}} &= 0, \\ \ddot{\phi}^{(2)} \frac{\partial Q^{(2)}}{\partial \beta^{(2)}} + \ddot{x}^{(2)} \frac{\partial P_x^{(2)}}{\partial \beta^{(2)}} + \ddot{y}^{(2)} \frac{\partial P_y^{(2)}}{\partial \beta^{(2)}} - \frac{1}{2} \frac{\partial U}{\partial \phi^{(2)}} &= 0, \\ \ddot{\phi}^{(2)} \frac{\partial Q^{(2)}}{\partial C_x^{(2)}} + \ddot{x}^{(2)} \frac{\partial P_x^{(2)}}{\partial C_x^{(2)}} + \ddot{y}^{(2)} \frac{\partial P_y^{(2)}}{\partial C_x^{(2)}} - \frac{1}{2} \frac{\partial U}{\partial x^{(2)}} &= 0, \\ \ddot{\phi}^{(2)} \frac{\partial Q^{(2)}}{\partial C_y^{(2)}} + \ddot{x}^{(2)} \frac{\partial P_x^{(2)}}{\partial C_y^{(2)}} + \ddot{y}^{(2)} \frac{\partial P_y^{(2)}}{\partial C_y^{(2)}} - \frac{1}{2} \frac{\partial U}{\partial y^{(2)}} &= 0.\end{aligned}\tag{C.13}$$

In the (1+1)-dimensional case, the derivation procedure can be readily modified and leads to a similar set of equations

$$\begin{aligned}\ddot{\phi}^{(1)} \frac{\partial Q^{(1)}}{\partial \beta^{(1)}} + \ddot{x}^{(1)} \frac{\partial P_x^{(1)}}{\partial \beta^{(1)}} - \frac{1}{2} \frac{\partial U}{\partial \phi^{(1)}} &= 0, \\ \ddot{\phi}^{(1)} \frac{\partial Q^{(1)}}{\partial C_x^{(1)}} + \ddot{x}^{(1)} \frac{\partial P_x^{(1)}}{\partial C_x^{(1)}} - \frac{1}{2} \frac{\partial U}{\partial x^{(1)}} &= 0, \\ \ddot{\phi}^{(2)} \frac{\partial Q^{(2)}}{\partial \beta^{(2)}} + \ddot{x}^{(2)} \frac{\partial P_x^{(2)}}{\partial \beta^{(2)}} - \frac{1}{2} \frac{\partial U}{\partial \phi^{(2)}} &= 0, \\ \ddot{\phi}^{(2)} \frac{\partial Q^{(2)}}{\partial C_x^{(2)}} + \ddot{x}^{(2)} \frac{\partial P_x^{(2)}}{\partial C_x^{(2)}} - \frac{1}{2} \frac{\partial U}{\partial x^{(2)}} &= 0,\end{aligned}\tag{C.14}$$

where appropriate changes in the definitions of invariants and the effective interaction potential have been made.

Using the definitions (C.1), we obtain the final system of ordinary differential equations describing the adiabatic interaction of two almost identical solitons in the X^2 medium

$$\begin{aligned} \dot{a}_1 &= -\frac{1}{2} \frac{d}{dt} \ln \left(\frac{C_1}{C_2} \right) + \dots \\ \dot{a}_2 &= -\frac{1}{2} \frac{d}{dt} \ln \left(\frac{C_2}{C_1} \right) + \dots \end{aligned} \quad (C.8)$$

where $\gamma = 1, 2$. In the (1+1)-dimensional case, the interaction is described by a set of equations which leads to a similar set of equations as presented in eq. (C.8) and (C.9).

$$\dot{a}_1 = -\frac{1}{2} \frac{d}{dt} \ln \left(\frac{C_1}{C_2} \right) + \dots \quad (C.9)$$

$$\dot{a}_2 = -\frac{1}{2} \frac{d}{dt} \ln \left(\frac{C_2}{C_1} \right) + \dots \quad (C.10)$$

where appropriate changes in the definitions of invariants and the effective interaction potential have been made.

$$\dot{a}_1 = -\frac{1}{2} \frac{d}{dt} \ln \left(\frac{C_1}{C_2} \right) + \dots \quad (C.11)$$

Bibliography

- [1] S. E. Miller. Integrated optics: an introduction. *Bell Syst. Tech. J.*, **48(7)**, 2059–2068, (1969).
- [2] S. Valette, S. Renard, H. Denis, J. P. Jadot, A. Fournier, P. Philippe, P. Gidon, A. M. Grouillet, and E. Desgranges. Si-based integrated optics technologies. *Solid State Technol.*, **32**, 69–74, (1989).
- [3] M. Kawachi. Silica waveguides on silicon and their application to integrated-optic components. *Opt. and Quantum Electron.*, **22**, 391–416, (1990).
- [4] A. Takagi, K. Jinguji, and M. Kawachi. Design and fabrication of broad-band silica-based optical waveguide couplers with asymmetric structure. *IEEE J. Quantum Electron.*, **28**, 848–855, (1992).
- [5] A. W. Snyder and J. D. Love. *Optical Waveguide Theory*. Chapman and Hall, London, 1983.
- [6] G. I. Stegeman, E. M. Wright, N. Finlayson, R. Zanoni, and C. T. Seaton. Third order nonlinear integrated optics. *J. Lightwave Technol.*, **6**, 953–970, (1988).
- [7] S. M. Jensen. The nonlinear coherent coupler. *IEEE J. Quantum Electron.*, **QE-18**, 1580–1583, (1982).
- [8] S. R. Friberg, A. M. Weiner, Y. Silberberg, B. G. Sfez, and P. S. Smith. Femtosecond switching in a dual-core-fiber nonlinear coupler. *Opt. Lett.*, **13**, 904–906, (1988).
- [9] Y. Baek, R. Schiek, and G. I. Stegeman. All-optical switching in a hybrid Mach-Zehnder interferometer as a result of cascaded second-order nonlinearity. *Opt. Lett.*, **20**, 2168–2170, (1995).
- [10] P. Li Kam Wa, P. N. Robson, J. S. Roberts, M. A. Pate, and J. P. R. David. All-optical switching between modes of GaAs/GaAlAs multiple quantum well waveguide. *Appl. Phys. Lett.*, **52**, 2013–2014, (1988).
- [11] A. Hasegawa and F. Tappert. Transmission of stationary nonlinear optical pulses in dispersive dielectric fibers. *Appl. Phys. Lett.*, **23**, 142–144, (1973).

- [12] G. P. Agrawal. *Nonlinear Fiber Optics*. Academic Press, New York, 1995.
- [13] N. Kikuchi, S. Sasaki, and K. Sekine. 10 Gb/s dispersion-compensated transmission over 2245 km conventional fibres in a recirculating loop. *Electron. Lett.*, **31**, 375–377, (1995).
- [14] N. Kikuchi and S. Sasaki. Fibre nonlinearity in dispersion-compensated conventional fibre transmission. *Electron. Lett.*, **32**, 570–572, (1996).
- [15] A. W. Snyder, D. J. Mitchell, L. Poladian, and F. Ladouceur. Self-induced optical fibers: Spatial solitary waves. *Opt. Lett.*, **16**, 21–23, (1991).
- [16] M. Schubert and B. Wilhelmi. *Nonlinear Optics and Quantum Electronics*. Wiley, New York, 1986.
- [17] R. DeSalvo, D. J. Hagan, M. Sheik-Bahae, G. I. Stegemen, and E. W. Van Stryland. Self-focusing and self-defocusing by cascaded second-order effects in KTP. *Opt. Lett.*, **17**, 28–30, (1992).
- [18] C. R. Menyuk, R. Schiek, and L. Torner. Solitary waves due to $\chi^{(2)} : \chi^{(2)}$ cascading. *J. Opt. Soc. Am. B*, **11**, 2434–2443, (1994).
- [19] A. V. Buryak and Yu. S. Kivshar. Spatial optical solitons governed by quadratic nonlinearity. *Opt. Lett.*, **19**, 1612–1614, (1994). Erratum, *Opt. Lett.*, 20:1080, 1995.
- [20] A. V. Buryak and Yu. S. Kivshar. Solitons due to second harmonic generation. *Phys. Lett. A*, **197**, 407–412, (1995).
- [21] W. E. Torruellas, Z. Wang, D. J. Hagan, E. W. VanStryland, G. I. Stegeman, L. Torner, and C. R. Menyuk. Observation of two-dimensional spatial solitary waves in a quadratic medium. *Phys. Rev. Lett.*, **74**, 5036–5039, (1995).
- [22] A. V. Buryak, Yu. S. Kivshar, and V. V. Steblina. Self-trapping of light beams and parametric solitons in diffractive quadratic media. *Phys. Rev. A*, **52**, 1670–1674, (1995).
- [23] R. Schiek, Y. Baek, and G. I. Stegeman. One-dimensional spatial solitary waves due to cascaded second-order nonlinearities in planar waveguides. *Phys. Rev. E*, **53**, 1138–1141, (1996).
- [24] M. G. F. Wilson and G. A. Teh. Tapered optical couplers. *IEEE Trans. Microwave Theory Tech.*, **23**, 85–92, (1975).
- [25] G. Giroult-Matlakowski, C. Charles, A. Durandet, R. W. Boswell, S. Armand, H. M. Persing, A. J. Perry, P. D. Lloyd, S. R. Hyde, and D. Bogsanyi. Deposition of silicon dioxide films using the helicon diffusion reactor for integrated optics applications. *J. Vac. Sci. Technol. A*, **12**, 2754–2761, (1994).

- [26] A. W. Snyder. Asymptotic expressions for eigenfunctions and eigenvalues of dielectric or optical fibers. *IEEE Trans. Microwave Theory Tech.*, **MTT-17**, 1130–1138, (1969).
- [27] F. Ladouceur, I. M. Skinner, and J. D. Love. Single-mode square- and rectangular-core waveguides. *IEE Proceedings-J*, **137**, 253–260, (1991).
- [28] F. Ladouceur and J. D. Love. *Silica-based Buried Channel Waveguides and Devices*. Chapman and Hall, London, 1996.
- [29] S. R. Nagel, J. B. MacChesney, and K. L. Walker. *Optical Fiber Communications*, volume 1. Academic Press, Orlando, 1985.
- [30] C. H. Henry and B. H. Verbeek. Solution of the scalar wave equation for arbitrarily shaped dielectric waveguides by two-dimensional Fourier analysis. *J. Lightwave Technol.*, **7**, 308–313, (1989).
- [31] C. Charles, G. Giroult-Matlakowski, R. W. Boswell, A. Goullet, G. Turban, and C. Cardinaud. Characterization of silicon dioxide films deposited at low pressure and temperature in a helicon diffusion reactor. *J. Vac. Sci. Technol. A*, **11**, 2954–2963, (1993).
- [32] N. Takato, T. Kominato, A. Sugita, K. Jinguji, H. Toba, and M. Kawachi. Silica-based integrated optic Mach-Zehnder multi/demultiplexer family with channel spacing of 0.01–250 nm. *IEEE J. Sel. Areas Commun.*, **8**, 1120–1127, (1990).
- [33] D. B. Mortimore. Wavelength-flattened fused couplers. *Electron. Lett.*, **21**, 742–743, (1985).
- [34] F. Gonthier, D. Ricard, S. Lacroix, and J. Bures. Wavelength-flattened 2×2 splitters made of identical single-mode fibers. *Opt. Lett.*, **16**, 1201–1203, (1991).
- [35] A. Takagi, K. Jinguji, and M. Kawachi. Wavelength characteristics of (2×2) optical channel-type directional couplers with symmetric or nonsymmetric coupling structures. *J. Lightwave Technol.*, **10**, 735–746, (1992).
- [36] R. Hereth and G. Schiffner. Broad-band optical directional couplers and polarization splitters. *J. Lightwave Technol.*, **7**, 925–930, (1989).
- [37] J. D. Love and V. V. Steblina. Highly broadband buried channel couplers. *Electron. Lett.*, **30**, 1853–1855, (1994).
- [38] S. J. Hewlett, J. D. Love, and V. V. Steblina. Analysis and design of highly-broadband planar evanescent couplers. *Opt. and Quantum Electron.*, **28**, 71–81, (1996).

- [39] A. Ankiewicz, A. W. Snyder, and X.-H. Zheng. Coupling between parallel optical fiber cores – critical examination. *J. Lightwave Technol.*, **LT-4**, 1317–1323, (1986).
- [40] J. D. Love and A. Ankiewicz. Cutoff in single-mode optical fibre couplers. *Electron. Lett.*, **20**, 362–363, (1984).
- [41] J. D. Love and A. Ankiewicz. Modal cutoffs in single- and few-mode fibre couplers. *J. Lightwave Technol.*, **LT-3**, 100–110, (1985).
- [42] S. J. Hewlett, F. Ladouceur, and J. D. Love. Second-mode cut-off in rectangular-core couplers using the Fourier Decomposition Method. *Opt. and Quantum Electron.*, **27**, 987–994, (1995).
- [43] S. J. Hewlett and F. Ladouceur. Fourier Decomposition Method applied to mapped infinite domains: scalar analysis of dielectric waveguides down to modal cut-off. *J. Lightwave Technol.*, **LT-13**, 375–383, (1995).
- [44] V. V. Steblina, J. D. Love, and F. Ladouceur. Supermode analysis of fibre bend loss. In *20-th Australian Conference on Optical Fibre Technology*, volume 20, pages 67–70, Coolum Beach, Queensland, Australia, 1995.
- [45] E. G. Neumann. Curved dielectric optical waveguides with reduced transition losses. *IEEE Proceedings Part-H*, **129**, 278–280, (1982).
- [46] A. J. Harris and P. F. Castle. Bend loss measurements on high numerical aperture single-mode fibers as a function of wavelength and bend radius. *J. Lightwave Technol.*, **LT-4**, 34–40, (1986).
- [47] I. A. White. Radiation from bends in optical waveguides: the volume-current method. *IEE J. Microwaves, Opt. & Acoust.*, **3**, 186–188, (1979).
- [48] W. A. Gambling, H. Matsumura, and C. M. Ragdale. Field deformation in a curved single-mode fibre. *Electron. Lett.*, **14**, 130–132, (1978).
- [49] D. Marcuse. Field deformation and loss caused by curvature of optical fibres. *J. Opt. Soc. Am.*, **66**, 311–320, (1976).
- [50] M. Heiblum and J. H. Harris. Analysis of curved optical waveguides by conformal transformation. *IEEE J. Quantum Electron.*, **QE-11**, 75–83, (1975).
- [51] P. Moon and D. I. Spencer. *Field theory handbook: including coordinate systems, differential equations and their solutions*. Springer-Verlag, Berlin; New York, 1988.
- [52] A. K. Ghatak, K. Thyagarajan, and M. R. Shenoy. Numerical analysis of planar optical waveguides using matrix approach. *J. Lightwave Technol.*, **LT-5**, 660–667, (1987).

- [53] K. Thyagarajan, M. R. Shenoy, and A. K. Ghatak. Accurate numerical method for the calculation of bending loss in optical waveguides using a matrix approach. *Optics Letters*, **12**, 296–298, (1987).
- [54] F. Ladouceur. Transfer matrix method. In *Light Numerical Recipes*, <http://rsphysse.anu.edu.au/~fjl124/web/solvers/mls/mls.html>, 1996.
- [55] D. Marcuse. *Light Transmission Optics*. Van Nostrand Reinhold, New York, 1973.
- [56] A. Tomita and D. Marcuse. Mode coupling loss in single-mode fibers with depressed inner cladding. *J. Lightwave Technol.*, **LT-1**, 449–452, (1983).
- [57] P. L. François and C. Vassalo. Finite cladding effects in W fibers: a new interpretation of leaky modes. *Applied Optics*, **22**, 3109–3120, (1983).
- [58] W. M. Henry, J. D. Love, and G.-D. Peng. Anomalous loss in depressed-cladding and W-fibres. *Opt. and Quantum Electron.*, **25**, 409–416, (1993).
- [59] E. A. J. Marcatili. Bends in optical dielectric guides. *Bell Syst. Tech. J.*, **48**, 2013–2132, (1969).
- [60] E. F. Kuester and D. C. Chang. Surface-wave radiation loss from curved dielectric slabs and fibres. *IEEE J. Quantum Electron.*, **QE-11**, 903–907, (1975).
- [61] V. V. Steblina, J. D. Love, R. H. Stolen, and J-S. Wang. Cladding mode degeneracy in bent W-fibres beyond cutoff. *Opt. Commun.*, (1998). In press.
- [62] V. V. Steblina, J. D. Love, R. H. Stolen, and J-S. Wang. Bends in depressed-cladding and W-fibres: modal degeneracy. *J. Lightwave Technol.*, (1997). Submitted.
- [63] S. J. Garth. Mode behaviour on bent planar dielectric waveguides. *IEE Proc.-Optoelectron.*, **142**, 115–120, (1995).
- [64] J. Chilwell and I. Hodgkinson. Thin-film field-transfer matrix theory of planar multilayer waveguides and reflection from prism-loaded waveguides. *J. Opt. Soc. Am. A*, **1**, 742–753, (1984).
- [65] L. M. Walpita. Solutions for planar optical waveguide equations by selecting zero elements in a characteristic matrix. *J. Opt. Soc. Am. A*, **2**, 595–602, (1985).
- [66] Y. P. Shen. *The Principles of Nonlinear Optics*. John Wiley, New York, 1984. Chap. 7 and references therein.

- [67] Y. N. Karamzin and A. P. Sukhorukov. Nonlinear interaction of diffracted light beams in a medium with quadratic nonlinearity: mutual focusing of beams and limitation on the efficiency of optical frequency converters. *JETP Lett.*, **20**, 339–342, (1974). Also available in Russian: *Pis'ma ZhETF*, **20**, 734–739, (1974).
- [68] Y. N. Karamzin and A. P. Sukhorukov. Mutual focusing of high-power light beams in media with quadratic nonlinearity. *Sov. Phys. JETP*, **41**, 414–420, (1976). Also available in Russian: *Zh. Eksp. Teor. Fiz.*, **68**, 834–847, (1975).
- [69] A. A. Kanashov and A. M. Rubenchik. On diffraction and dispersion effect on three wave interaction. *Physica D*, **4**, 122–134, (1981).
- [70] R. Schiek. Nonlinear refraction caused by cascaded second-order nonlinearity in optical waveguide structures. *J. Opt. Soc. Am. B*, **10**, 1848–1855, (1993).
- [71] K. Hayata and M. Koshiba. Multidimensional solitons in quadratic nonlinear media. *Phys. Rev. Lett.*, **71**, 3275–3278, (1993). *Phys. Rev. Lett.*, **72**, 178, (1994)(E).
- [72] L. Torner, C. R. Menyuk, and G. I. Stegeman. Excitation of solitons with cascaded $\chi^{(2)}$ nonlinearities. *Opt. Lett.*, **19**, 1615–1617, (1994).
- [73] A. V. Buryak and Yu. S. Kivshar. Twin-hole dark solitons. *Phys. Rev. A*, **51**, R41–R44, (1995).
- [74] L. Torner, C. R. Menyuk, W. E. Torruellas, and G. I. Stegeman. Two-dimensional solitons with second-order nonlinearities. *Opt. Lett.*, **20**, 13–15, (1995).
- [75] D. Anderson. Variational approach to nonlinear pulse propagation in optical fibers. *Phys. Rev. A*, **27**, 3135–3145, (1983).
- [76] V. V. Steblina, Yu. S. Kivshar, M. Lisak, and B. A. Malomed. Self-guided beams in diffractive $\chi^{(2)}$ medium: variational approach. *Opt. Commun.*, **118**, 345–352, (1995).
- [77] Y. Baek, R. Schiek, and G.I. Stegeman. Spatial solitons caused by cascaded second-order nonlinearity in a LiNbO_3 planar waveguide. In *QELS 95. Summaries of Papers Presented at the Quantum Electronics and Laser Science Conference*, volume 16, pages vii+279, 76–77, Optical Society of America, Washington D.C., USA, 1995.
- [78] D. Anderson, M. Bonnedal, and M. Lisak. Self-trapped cylindrical laser beams. *Phys. Fluids*, **22**, 1838–1840, (1979).
- [79] Yu. S. Kivshar and B. A. Malomed. Dynamics of solitons in nearly integrable systems. *Rev. Mod. Phys.*, **61**, 763–915, (1989).

- [80] D. J. Kaup, B. A. Malomed, and R. S. Tasgal. Internal dynamics of a vector soliton in a nonlinear optical fiber. *Phys. Rev. E*, **48**, 3049–3053, (1993).
- [81] J. J. Rasmussen and K. Rypdal. Blow-up in nonlinear Schroedinger equations. I. A general review. *Physica Scripta*, **33**, 481–497, (1986).
- [82] L. Berge, V. K. Mezentsev, J. J. Rasmussen, and J. Wyller. Formation of stable solitons in quadratic nonlinear media. *Phys. Rev. A*, **52**, R28–R31, (1995).
- [83] L. Berge, O. Bang, J. J. Rasmussen, and V. K. Mezentsev. Self-focusing and solitonlike structures in materials with competing quadratic and cubic nonlinearities. *Phys. Rev. E*, **55**, 3555–3570, (1997).
- [84] M. T. G. Canva, R. A. Fuerst, D. Baboiu, G. I. Stegeman, and G. Assanto. Quadratic spatial soliton generation by seeded downconversion of a strong harmonic pump beam. *Opt. Lett.*, **22**, 1683–1685, (1997).
- [85] R. A. Fuerst, M. T. G. Canva, D. Baboiu, and G. I. Stegeman. Properties of type II quadratic solitons excited by imbalanced fundamental waves. *Opt. Lett.*, **22**, 1748–1750, (1997).
- [86] R. Y. Chiao, E. Garmire, and C. H. Townes. Self-trapping of optical beams. *Phys. Rev. Lett.*, **13**, 479–480, (1964).
- [87] B. A. Malomed, D. Anderson, A. Berntson, M. Florjanczyk, and M. Lisak. Decay of parametric solitons in a lossy medium with quadratic nonlinearity. *Pure and Appl. Optics*, **5**, 941–946, (1996).
- [88] V. M. Agranovich, S. A. Darmanyan, O. A. Dubovsky, A. M. Kamchatnov, E. I. Ogievetsky, T. Neidlinger, and P. Reineker. Fermi resonance solitary wave on the interface between two layers of organic semiconductors. *Phys. Rev. B*, **53**, 15451–15454, (1996).
- [89] C. B. Clausen, P. L. Christiansen, and L. Torner. Perturbative approach to the interaction of solitons in quadratic nonlinear media. *Opt. Commun.*, **136**, 185–192, (1997).
- [90] V. M. Agranovich, S. A. Darmanyan, A. M. Kamchatnov, T. A. Leskova, and A. D. Boardman. Variational approach to solitons in systems with cascaded $\chi^{(2)}$ nonlinearity. *Phys. Rev. E*, **55**, 1894–1898, (1997).
- [91] V. V. Steblina, A. V. Buryak, and Yu. S. Kivshar. Scattering and spiralling of solitons in a bulk quadratic medium. *Opt. Lett.*, **23**, 156–158, (1998).
- [92] G.I. Stegeman, D.J. Hagan, and L. Torner. $\chi^{(2)}$ cascading phenomena and their applications to all-optical signal processing, mode-locking, pulse compression and solitons. *J. Opt. Quantum Electron.*, **28**, 1691–1740, (1996).

- [93] M. J. Werner and P. D. Drummond. Simulton solutions for the parametric amplifier. *J. Opt. Soc. Am. B*, **10**, 2390–2393, (1993).
- [94] D. M. Baboiu, G. I. Stegeman, and L. Torner. Interaction of one-dimensional bright solitary waves in quadratic media. *Opt. Lett.*, **20**, 2282–2284, (1995).
- [95] C. Etrich, U. Peschel, F. Lederer, and B. Malomed. Collision of solitary waves in media with a second-order nonlinearity. *Phys. Rev. A*, **52**, R3444–R3447, (1995).
- [96] M. Haelterman, S. Trillo, and P. Ferro. Multiple soliton bound states and symmetry breaking in quadratic media. *Opt. Lett.*, **22**, 84–86, (1997).
- [97] D. M. Baboiu and G. I. Stegeman. Solitary-wave interactions in quadratic media near type I phase-matching conditions. *J. Opt. Soc. Am. B*, **14**, 3143–3150, (1997).
- [98] Y. Baek, R. Schiek, G. I. Stegeman, I. Baumann, and W. Sohler. Interactions between one-dimensional quadratic solitons. *Opt. Lett.*, **22**, 1550–1552, (1997).
- [99] G. Leo, G. Assanto, and W. E. Torruellas. Intensity-controlled interactions between vectorial spatial solitary waves in quadratic nonlinear media. *Opt. Lett.*, **22**, 7–9, (1997).
- [100] G. Leo, G. Assanto, and W. E. Torruellas. Beam pointing control with spatial solitary waves in quadratic nonlinear media. *Opt. Commun.*, **134**, 223–226, (1997).
- [101] A. V. Buryak, Yu. S. Kivshar, and S. Trillo. Stability of three-wave parametric solitons in diffractive quadratic media. *Phys. Rev. Lett.*, **77**, 5210–5213, (1996).
- [102] A. V. Buryak and Yu. S. Kivshar. Multistability of three-wave parametric self-trapping. *Phys. Rev. Lett.*, **78**, 3286–3289, (1997).
- [103] C. Etrich, U. Peschel, F. Lederer, B. Malomed, and Yu. S. Kivshar. Origin of the persistent oscillations of solitary waves in nonlinear quadratic media. *Phys. Rev. E*, **54**, 4321–4324, (1996).
- [104] G.C. Duree, J.L. Shultz, G.J. Salamo, M. Segev, A. Yariv, B. Crosignani, P. Di Porto, E.J. Sharp, and R.R. Neurgaonkar. Observation of self-trapping of an optical beam due to the photorefractive effect. *Phys. Rev. Lett.*, **71**, 553–556, (1993).
- [105] V. Tikhonenko, J. Christou, and B. Luther-Davies. Spiraling bright spatial solitons formed by the breakup of an optical vortex in a saturable self-focusing medium. *J. Opt. Soc. Am. B*, **12**, 2046–2052, (1995).

- [106] V. Tikhonenko, J. Christou, and B. Luther-Davies. Three dimensional bright spatial soliton collision and fusion in a saturable nonlinear medium. *Phys. Rev. Lett.*, **76**, 2698–2701, (1996).
- [107] M. Shih, M. Segev, and G. Salamo. Three-dimensional spiraling of interacting spatial solitons. *Phys. Rev. Lett.*, **78**, 2551–2554, (1997).
- [108] K. A. Gorshkov and L. A. Ostrovsky. Interactions of solitons in nonintegrable systems: direct perturbation method and applications. *Physica D*, **3**, (1981).
- [109] V. I. Karpman and V. V. Solov'ev. A perturbational approach to the two-soliton systems. *Physica D*, **3**, 487–502, (1981).
- [110] L. Poladian, A.W. Snyder, and D.J. Mitchell. Spiralling spatial solitons. *Opt. Commun.*, **85**, 59–62, (1991).
- [111] D. E. Pelinovsky, A. V. Buryak, and Yu. S. Kivshar. Instability of solitons governed by quadratic nonlinearities. *Phys. Rev. Lett.*, **75**, 591–595, (1995).
- [112] H. Goldstein. *Classical Mechanics*. Addison-Wesley, Massachusetts, 1980.
- [113] A. V. Buryak, Yu. S. Kivshar, and S. Trillo. Parametric spatial solitary waves due to type II second-harmonic generation. *J. Opt. Soc. Am. B*, **14**, 3110–3118, (1997).
- [114] G. D. Miller, R. G. Batchko, W. M. Tulloch, D. R. Weise, M. M. Fejer, and R. L. Byer. 42%-efficient single-pass CW second-harmonic generation in periodically poled lithium niobate. *Opt. Lett.*, **22**, 1834–1836, (1997).
- [115] D. E. Edmundson and R. H. Enns. Fully three-dimensional collisions of bistable light bullets. *Opt. Lett.*, **18**, 1609–1611, (1993).
- [116] D. E. Edmundson and R. H. Enns. Particlelike nature of colliding three-dimensional optical solitons. *Phys. Rev. A*, **51**, 2491–2498, (1995).
- [117] B. Malomed, P. Drummond, H. He, A. Berntson, D. Anderson, and M. Lisak. Spatiotemporal solitons in multidimensional optical media with a quadratic nonlinearity. *Phys. Rev. E*, **56**, 4725–4735, (1997).
- [118] W. H. Press, S. A. Teukolsky, W. T. Vetterling, and B. P. Flannery. *Numerical Recipes in C: The Art of Scientific Computing*. Cambridge University Press, Cambridge, 1992.
- [119] Y. Chung and N. Dagli. An assessment of Finite Difference Beam Propagation Method. *IEEE J. Quantum Electron.*, **QE-26**, 1335–1339, (1990).
- [120] P. C. Lee, D. Schulz, and E. Voges. Three-dimensional finite difference beam propagation algorithms for photonic devices. *J. Lightwave Technol.*, **10**, 1832–1838, (1992).